TUM School of Computation, Information and Technology
Technische Universität München

Unified Force-Sensitive Robot Mechatronics

Pneumatic Robots - Electromagnetic Prostheses - Cable-Driven Exoskeletons

Dipl.-Ing. Alexander Tödtheide

Vollständiger Abdruck der von der TUM School of Computation, Information and Technology der Technischen Universität München zur Erlangung des akademischen Grades eines

Doktors der Ingenieurwissenschaften (Dr.-Ing.)

genehmigten Dissertation.

Vorsitz:
Prof. Dr.-Ing. Eckehard Steinbach

Prüfer der Dissertation:
1. Prof. Dr.-Ing. Sami Haddadin
2. Prof. Dr.-Ing. Tamim Asfour
3. Prof. Dr. Dr. h.c. Robert Riener

Die Dissertation wurde am 9. November 2022 bei der Technischen Universität München eingereicht und durch die TUM School of Computation, Information and Technology am 15. Mai 2023 angenommen.

Acknowledgment

First of all, I want to thank Sami Haddadin for providing this exceptional education and for giving me the opportunity to work with amazing cutting-edge robotics technology. In particular, I want to thank him for the many skills I have learned, from robotics technology, over to scientific writing and the presentation of scientific results – many of which I presented at well-respected international conferences and in front of significant personalities from industry, politics and research. But most importantly, I want to thank him for the many opportunities of developing tactile robotic systems, completely from scratch, using cutting-edge robotics technology. He gave me the freedom and trust to work on many aspects within the robot development, including modeling, control and mechanical design, which then finally led to this thesis. He provided valuable feedback in many personal meetings and motivated me to design highly-integrated, miniaturized robotic devices. He guided me towards the submission of highly respected conferences and journals that I look back on with pride and gratitude. Finally, I also want to thank him for the challenging projects under tight deadlines, which helped me to become the engineer and scientist that I am today.

Also, I want to thank my colleagues, many of them close companions, with whom I worked with under tight deadlines and night sessions. In particular, I want to thank Erfan Shahriari, Johannes Kühn, Johannes Ringwald, Ali Baradaran, Nico Mannsfeld, Hugo Tadashi Muniz Kussaba, Elisabeth Jensen, Dennis Knobbe, Fernando Diaz Ledezma, Andreas Kurz, Moritz Schappler, Jonathan Vorndamme and Torsten Lilge. In this respect, a special thanks to Edmundo Pozo Fortonić for developing and maintaining the electronics of the latest prosthesis prototype II and the exoskeleton. Thanks to Robin Grahammer and Burak Güner for assembling and soldering the hardware of prototype II and the exoskeleton. Thanks to Andreas Kurz for building the electronics of the pneumatic testbeds. Thank you Jaesug Jung for proofreading the manuscript. Also, I want to thank the team of Franka Emika GmbH for providing outstanding mechatronic components, infrastructure and maintenance support for the development of prototype I. Thanks to Erfan Shahriari and Ali Baradaran for providing the robot setup for measuring the reaction wrenches at the exoskeleton. Thanks to Xiao Chen, Hamid Sadeghian and Abdeldjallil Naceri for programming and operating the Panda robot in the teleoperation experiments with the exoskeleton. Also, thanks to QB Robotics Srl for providing the softhand pro 2 for the prosthetic devices, as used in prototype I and II.

Also, I would like to thank the programs and institutions that funded this research, namely the Alfried Krupp von Bohlen und Halbach Foundation, the LongLeif GaPa GmbH (Project Y, grant no. 5140953), the project ReconCycle under grant no. 871352, the Research of the Federal Republic of Germany (BMBF) by funding the project AI.D under the Project Number 16ME0539K and the European Union's Horizon 2020 SoftPro Grant No 688857l.

Finally and most importantly, I want to thank my beloved wife, my parents and my family who supported me with unlimited motivation, love and patience.

Zusammenfassung

Heutige Roboter zeichnen sich nicht nur durch hohe Präzision in der industriellen Fertigung aus, sondern können auch sensitiv Kontaktkräfte messen, erkennen und auf diese reagieren. Diese neuen Eigenschaften haben einen Paradigmenwechsel weg von positionsgeregelten Industrierobotern oder einfachen kollaborativen Robotern hin zu "Soft and Tactile Robotics" eingeleitet. Dies hat unter anderem dazu geführt, dass Roboter nicht mehr aus Sicherheitsgründen in Käfigen operieren müssen, sondern in direkter Nähe zum Menschen arbeiten können. Die Technologie ist mittlerweile so ausgereift, dass sogenannte "Soft and Tactile Robots" heutzutage in großen Stückzahlen Einsatz in unterschiedlichsten Branchen finden.

Für diese Robotersysteme hat sich ein Antriebskonzept durchgesetzt, welches auf Drehmomentsensoren zur Nachgiebigkeits- und Kraftregelung sowie Kontakterkennung, Wellgetrieben mit hohen Untersetzungen, und bürstenlosen Gleichstrommotoren mit hoher Drehmomentdichte basiert. Für die Grundregelung dieser Robotersysteme wird eine Kombination aus einer (dem Menschen nachempfundenen) Impedanz- und Kraftregelung sowie einer unterlagerten Drehmomentregelung verwendet.

Die wissenschaftliche Hypothese dieser Arbeit besteht darin, zu zeigen, dass komplexe Robotersysteme mit aktiver Nachgiebigkeits- und Kraftregelung systematisch unter Verwendung eines verallgemeinerten mechatronischen Entwicklungs- und Syntheseframeworks entworfen werden können. Das Framework wird erfolgreich an drei Robotersystemen validiert, die, basierend auf unterschiedlichen Aktoren, Sensoren und Transmissionskonzepten, implementiert und experimentell getestet werden. Der Schlüssel zum Verständnis dieses Konzepts ist i) die mathematische Abstraktion des Aktorsystems zur idealen Drehmomentquelle durch die Verwendung einer zur Aktorik passenden Kraft-/Drehmomentregelung, sowie ii) eine zur Kinematik passenden nichtlinearen Vorwärts- und Rückwärtstransformation. Die Folge daraus ist ein "Hardware Abstraction Layer", der die genaue physikalische Funktionsweise des Aktormoduls verbirgt bzw. auf ein systemisches Berechnungskonzept generalisiert und somit dessen Verwendung und Analyse vereinfacht. Ähnliche Abstraktionskonzepte sind bekanntermaßen im Chip Design zu finden, mit welchen die Ansteuerung von Milliarden Transistoren über Hochsprachen wie C ermöglicht wurde. In diesem Sinne ist das Finden und Anwenden von funktionalen und mathematisch beschreibbaren Abstraktionsebenen auch immer mit technischem Fortschritt verbunden.

Diese Formulierung wird im nächsten Schritt zur Aufstellung eines verallgemeinerten Mechatronikdesignkonzepts für kraftsensitive und nachgiebige mechatronische Systeme erweitert. Damit lassen sich Robotersysteme mit unterschiedlichen Aktortechnologien und Kinematiken nach ein und demselben "Baukastenprinizip" modellieren, simulieren, regeln und auslegen. Folglich spielt dieser Ansatz seine Stärke bei Robotersystemen mit speziellen Anforderungen aus (wie z.B. tragbare Systeme und Systeme mit neuartiger Aktorik), bei welchen nicht auf Erfahrung aus Vorentwicklungen zurückgegriffen werden kann.

In dieser Arbeit wird das o.g. Designkonzept zunächst auf sehnenbasierte und pneumatische Robotersysteme, sowie im folgenden auf tragbare, elektromechanische Systeme mit gemischt seriell/parallelen Kinematiken erweitert. Durch die große Anzahl bestehender Aktortechnologien und Transmissionen können naturgemäß nicht alle Kombinationen berücksichtigt werden. Jedoch wurden äußerst unterschiedliche und damit auch aussagekräftige Systeme ausgewählt und zur Validierung des erarbeiteten Entwurfskonzept in vielfältigen Simulationen, Implementierungen und Experimenten herangezogen.

Die Arbeit gliedert sich dabei in zwei logische Teile: Während zunächst das o.g. Mechatronikentwurfskonzept auf alternative Antriebssysteme (sehnenbetriebene Pneumatiksysteme) angewandt wird, werden mit dem gleichen Entwicklungsansatz neue Robotersysteme mit besonderen Anforderungen in Form von Prothesen und Exoskeletten unter dem Paradigma der “Soft and Tactile Robotics“ entworfen und realisiert.

Ein weiteres Ziel ist dabei die gleichzeitige Erforschung von neuen Anwendungsfeldern und Einsatzmöglichkeiten für diese "Soft and Tactile Robotics" im Bereich pneumatischer Robotik, Prothetik und Exoskeletten. Die Untersuchungen an pneumatischen Systemen zielen darauf ab, gängige Reglerkonzepte

der “Soft and Tactile Robotics“ von elektromechanischen Systemen auf pneumatische Antriebe zu übertragen. Besonders hervorzuheben sind die zwei Generationen an entwickelten Unterarmprothesen, deren Entwicklung sowohl das mechanische Design einer spezialisierten Kinematik, als auch die dazu passenden Regelungsmethoden beinhaltet. Der finale Prothesenprototyp die "Artifical Neuromuscular Prosthesis" (ANP) imitiert das neuromuskuläre System des Menschen im Sinne eines Körperbewusstseins, Kontaktbewusstseins, einer menschenähnlichen Reaktion auf Kontakte und einer menschenähnlichen Kinematik. Dies wird ermöglicht durch eine in der Robotik üblichen, mathematischen vollständigen Modellierung der Starrkörperdynamik, die bisher einzigartig in der Prothetik ist. Die ANP ist sich somit ihrer mechanischen Zustände “bewusst”, kann ihr Eigengewicht für beliebige Oberarmpositionen kompensieren, schätzt Kontakte und kann ihre Gelenksteifigkeit einstellen. Des Weiteren wurde ein mechatronisches Schulter-Exoskelett entwickelt, welches durch einen aktiven Prothesenschaft die Belastung am Oberarmstumpf reduzieren kann. Das System zeichnet sich durch die intuitive Steuerung aus, welche durch Methoden der "Soft and Tactile Robotics" realisiert wurde. Die Arbeit zeigt eine erste Machbarkeitsstudie dieses neuartigen Prothesengesamtsystems, welche durch experimentelle und simulative Studien untermauert wird.

Die Arbeit untergliedert sich wie folgt:

Kapitel 1 leitet in die Arbeit ein. Es wird die Motivation zur Arbeit bzw. zur Erforschung von neuen Mechatronikansätzen in der taktilen Robotik vorgestellt und der spezifische Beitrag zum Stand der Forschung herausgearbeitet. Dabei wird das Mechatronikentwurfskonzept für kraftsensitive und nachgiebige mechatronische Systeme skizziert, welches in Kapitel 3 weiter ausgeführt wird.

Kapitel 2 führt durch den Stand der Technik. Ausgehend von taktilen Robotern, die als "Goldstandard" angesehen werden, wird unter der Variation der Antriebstechnologie auf Vorarbeiten im Bereich pneumatische und hydraulische Roboter eingegangen. Diese Übersicht dient der Einordnung von Kapitel 4. Im Anschluss wird der Stand der Technik in der Armprothetik und der Exoskelette, die eine spezielle Anwendung von Robotersystemen sind, vorgestellt. Dies wiederum dient der Einordnung von Kapitel 5 und 6.

Kapitel 3 führt in die Grundlagen für die Methoden zur Modellierung und Regelung der untersuchten Robotersysteme ein. Neben der Modellierung sogenannter floating base Systeme, wird auch die Modellierung und Regelung von sehnenbasierten Systemen beschrieben. Der Abschnitt "Soft and tactile Robotics" erklärt die grundsätzlichen Regelkreise und Methoden. Zusammen mit dem Ansatz aus Kapitel 1 wird in diesem Kapitel das Mechatronikentwurfskonzept für kraftsensitive und nachgiebige mechatronische Systeme mathematisch beschrieben, sodass die Funktionsweise eines verallgemeinerten Mechatronik-Entwurfs für unterschiedliche Aktortypen, Transmissionen und Kinematiken ersichtlich wird.

Im Folgenden wird das Mechatronikentwurfskonzept auf pneumatische Aktorik (Part I), Prothesen (Part II) und Exoskelette (Part III) angewendet. Bei allen Systemen werden sehnenbasierte Transmissionskonzepte in der Roboterstruktur verwendet.

Kapitel 4 (Part I) beschäftigt sich mit der Erforschung von pneumatischen Aktoren im genannten methodischen Rahmen und dem Transfer von Methoden der "Soft and Tactile Robotics" auf die Pneumatik. Ausgehend von einem antagonistischen 1-Degrees Of Freedom (dof) System, welches dem Aufbau der menschlichen Muskeln nachempfunden wurde, wird ein 2-dof Handgelenk und ein pneumatisches Robotersystem mit 7-dof vorgestellt und modelliert. Dabei werden Systeme mit steigender Anzahl an Freiheitsgraden untersucht, um die Generalisierbarkeit des Mechatronikentwurfskonzepts zu überprüfen – aber auch um die grundsätzlichen Potentiale pneumatischer Technologie aufzuzeigen. Abschließend wird eine Simulation einer Leichtbauroboterkinematik mit pneumatischen Aktoren durchgeführt, um Regelung und Aktorik für gängige Roboterstrukturen zu untersuchen.

Kapitel 5 (Part II) widmet sich der Erforschung neuer Anwendungsfelder für taktile Robotersysteme mit dem Fokus auf der Entwicklung eines neuartigen, körper- und kontakt-”bewussten” Prothesensystems. Das Kapitel beschreibt ein neues Paradigma in der Prothesenentwicklung und leitet daraus notwendige, technische Spezifikationen ab. Die Realisierung der technischen Vorhaben erfolgt über zwei Prototypen (unter Anwendung des o.g. Mechatronikentwurfskonzepts) mit steigender Funktionalität und optimiertem Design. Im Anschluss daran werden die Konstruktionslösungen vorgestellt und die geforderten Systemeigenschaften experimentell validiert.

Kapitel 6 (Part III) trägt auch zur Erforschung neuartiger Robotersysteme für die Prothetik bei. Zum Schutz des Armstumpfes wird ein Schulterexoskelett konzipiert, welches das Gewicht der Prothese trägt und als "aktiver Prothesenschaft" interpretiert werden kann. Entsprechend der Definition des Entwurfs-Paradigmas werden die technischen Spezifikationen des Schulterexoskeletts abgeleitet. Dem modellbasierten Mechatronikentwurfskonzepts dieser Arbeit folgend, wird ein aktiv geregeltes Simulationsmodell von Exoskelett und Mensch vorgestellt, welches zur weiteren Systemauslegung und Entwicklung verwendet wird. Die Konstruktionslösung wird vorgestellt und die geforderten Systemeigenschaften werden in Experimenten und Simulationen validiert.

Kapitel 7 fasst die Ergebnisse dieser Arbeit zusammen und beschreibt zukünftige Aufgabenfelder.

Abstract

Modern day robots not only deliver high precision in industrial manufacturing, but can also sensitively measure, detect and respond to contact forces. These new features have initiated a paradigm shift away from position-controlled industrial robots or simple collaborative robots towards "Soft and Tactile Robotics".

Among other things, this has lead to robots that no longer have to operate in cages for safety reasons, but can work in close proximity to humans. The technology has reached such a mature state that so-called "Soft and Tactile Robotics" are now used in large numbers within a wide range of industries. For these robot systems, a drive concept has been established, which is based on strain-wave gearings with high reduction ratios, brushless DC motors with high torque density and torque sensors as used for compliance control, force control and contact detection. The fundamental control principle of these robots is based on a combination of impedance control, force control and subordinated torque control schemes.

The scientific hypothesis of this dissertation is that complex robotic systems with active compliance and force control can be systematically designed under a unified mechatronic design and synthesis framework. The framework is successfully validated by three distinct robotic devices that were designed, based on various actuation, sensing, transmission concepts, implemented and experimentally tested. The key to understanding this concept is i) the mathematical abstraction of the actuator system as ideal torque source through the use of a force/torque controller that matches the actuator technology, and ii) suitable forward and backward non-linear transformations for arbitrary transmission principles. The result is a "hardware abstraction layer" that obscures the exact physical operation of the actuator module, generalizes the mathematical description, thus simplifying its use and analysis. Similar abstraction concepts are found in chip design, which have enabled the control of billions of transistors via high-level languages such as C. In this sense, finding and applying functional and mathematically describable levels of abstraction is also often associated with technical progress.

This formulation will be extended in the next step to establish a generalized mechatronic design concept for force-sensitive and compliant mechatronic systems. This allows robot systems with different actuator technologies and kinematics to be modeled, simulated, controlled and designed according to one and the same "modular principle". Consequently, this approach shows its strength in robot systems with special requirements (e.g. portable systems, systems with novel actuators), where no or very little experience from previous developments exists.

In this thesis, the above design concept is first extended to tendon-driven and pneumatically-actuated robots, and subsequently, to wearable, electromechanical systems with mixed serial/parallel kinematics. Due to the large number of existing actuator technologies and transmissions, not all combinations can be considered. However, highly diverse and thus also meaningful systems were selected and used to validate the developed design concept in a variety of simulations, implementations and experiments.

The work is divided into two logical parts: first, the above mechatronics design concept is applied to alternative actuation systems (i.e tendon driven pneumatic systems), and second, the same approach is used for designing new robotic systems in the form of prostheses and exoskeletons under the paradigm of "Soft and Tactile Robotics" using the same development approach.

A further goal is the simultaneous exploration of new fields of application and possible use cases for "Soft and Tactile Robotics" in the area of pneumatic robotics, prosthetics and exoskeletons. The investigations on pneumatic systems aim to systematically transfer common controller concepts of "Soft and Tactile Robotics" from electromechanical to pneumatic actuators. Particularly noteworthy are the two generations of developed forearm prostheses, whose design includes both the specialized mechanical solution as well as the suitable control methods. The final prosthesis prototype, the Artificial Neuromuscular Prosthesis (ANP), mimics the human neuromuscular system in terms of body awareness, contact awareness, human-like contact response, and human-like kinematics. This is achieved by a mathematical complete modeling of rigid-body dynamics

common in robotics, which is currently unique in prosthetics. The ANP is thus "aware" of its mechanical states, can compensate its own weight for arbitrary upper arm positions, estimate contacts, and can adjust its joint stiffness. Furthermore, a mechatronic shoulder exoskeleton was developed that can reduce stress on the humeral stump through an active prosthetic socket. The system is characterized by intuitive control, which was realized by methods from "Soft and Tactile Robotics". The paper shows a first feasibility study of this novel prosthetic exoskeleton-based concept, which is validated by experimental and simulative studies.

The thesis is structured as follows:

Chapter 1 introduces the motivation for researching new mechatronics approaches in tactile robotics and elaborates the specific contribution to the state of the art. By this, the mechatronics design concept for force-sensitive and compliant mechatronic systems is outlined, which is further elaborated in Chapter 3.

Chapter 2 takes the reader through the state of the art. Starting with tactile robots, which are considered the "gold standard," preliminary work on pneumatic and hydraulic robots are discussed. This is followed by a presentation of the state of the art in arm prosthetics and exoskeletons, which are in fact specific robot system applications. This in turn serves to classify Chapters 5 and 6.

Chapter 3 introduces the methods for modeling and control of the investigated robotic systems. In addition to the modeling of so-called floating- and fixed-base systems, the modeling and control of tendon-based systems is described. The section "Soft and tactile Robotics" explains the basic control schemes and methods in modern robotic systems. Together with the approach from Chapter 1, this chapter mathematically describes the mechatronics design concept for force-sensitive and compliant mechatronic systems, such that a generalized mechatronics design for different actuator types, transmissions, and kinematics becomes possible.

Subsequently, the mechatronic design concept is applied to pneumatic actuators (Part I), prostheses (Part II), and exoskeletons (Part III). Tendon-based transmission concepts are used in the robotic structure for the majority of systems.

Chapter 4 (Part I) deals with the exploration of pneumatic actuators in the aforementioned methodological framework and transferring "Soft and Tactile Robotics" to pneumatics. Starting with an antagonistic system, inspired by the structure of human muscles, a 2-Degrees Of Freedom (dof) wrist and a 7-dof pneumatic robot are investigated. Systems with increasing number of degrees of freedom are researched to verify the generalizability of the mechatronic design concept - but also to specifically demonstrate the fundamental potentials of pneumatic technology.

Chapter 5 (Part II) is devoted to exploring new application areas for tactile robotic systems, focusing on the development of a novel body- and contact-aware prosthetic system. The chapter describes a new paradigm in prosthesis development and derives necessary, technical specifications from it. The realization of the technical requirements is done by two prototypes (using the aforementioned mechatronic design concept), whereas the later prototype stands out by a more optimized design and more functionalities. Subsequently, the design solutions are presented and the required system properties are validated experimentally.

Chapter 6 (Part III) also contributes to the exploration of novel robotic systems for prosthetics. A shoulder exoskeleton is designed to protect the residual limb of an amputee for the case of a transhumeral amputation. This device carries the weight of the prosthesis and can be interpreted as an active prosthetic socket. After defining the design paradigm, the technical specifications of the shoulder exoskeleton are derived. Following the model-based mechatronics design concept of this thesis, an actively controlled simulation model of exoskeleton and human is presented, which is used for further system design and development. The design solution is presented and the required system properties are validated through experiments and simulations.

Chapter 7 summarizes and clarifies the results of this work and describes future tasks and applications.

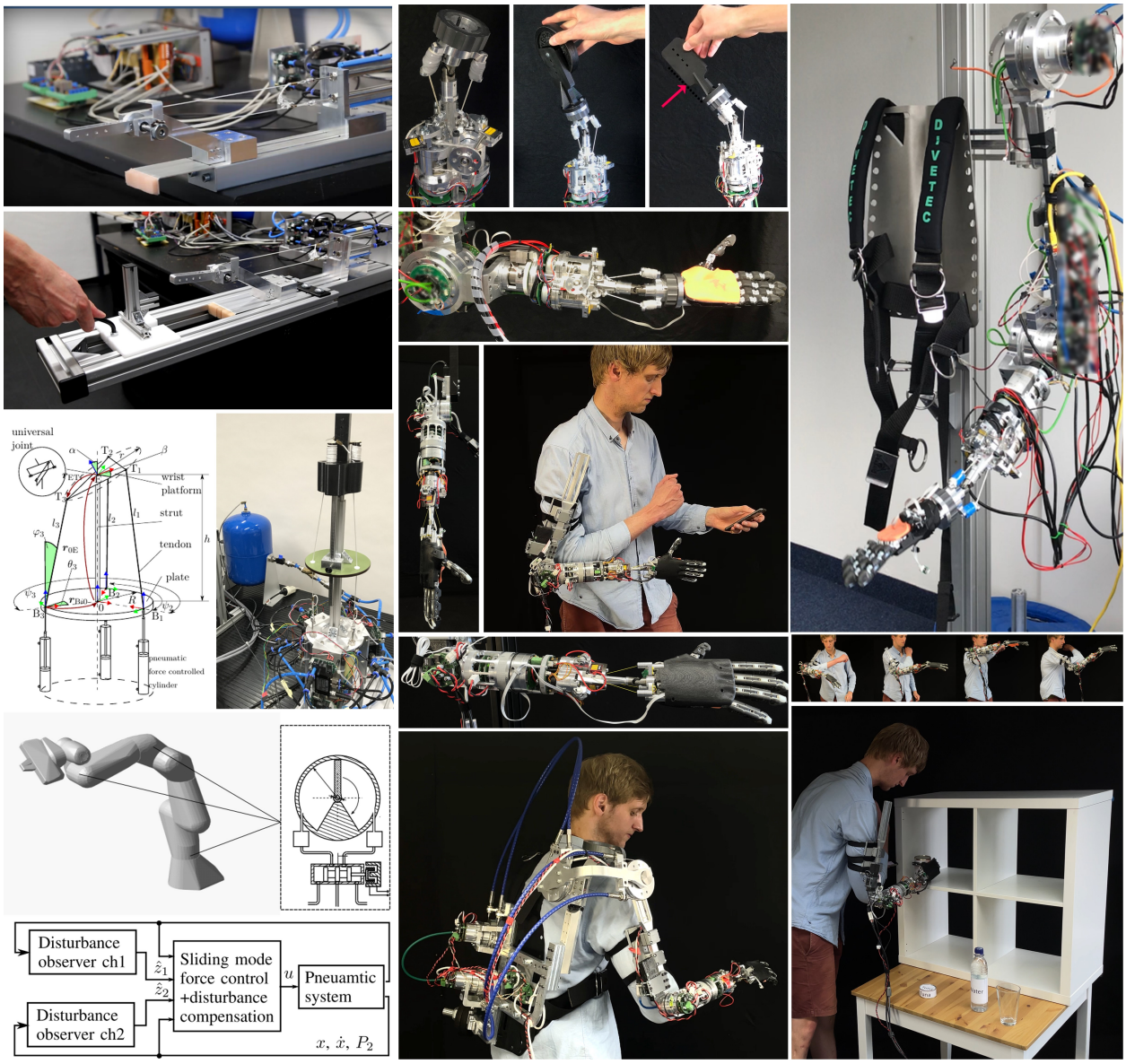

Figure 1 Impressions of this thesis

Publications

The publications to which the author has contributed throughout this thesis are listed below. Figure 1 depicts the structure of the thesis including the publications upon which this thesis was written. Furthermore, the overall flow between the chapters, such as the technological transfer, is depicted which is indicated by the horizontal arrows.

International Journals

- **A. Tödtheide**, E. Pozo Fortunić, J. Kühn, E. Jensen, and S. Haddadin, "A Transhumeral Prosthesis with an Artificial Neuromuscular System: Sim2Real-Guided Design, Modeling and Control", *International Journal of Robotics Research (IJRR)*, 2023, *accepted*.
- **A. Tödtheide**, E. Pozo Fortunić, J. Kühn, E. Jensen, and S. Haddadin, "A Wearable Force-Sensitive and Body-Aware Exoprosthesis for a Transhumeral Prosthesis Socket", *IEEE Transactions on Robotics (T-RO)*, 2023.
- **A. Tödtheide** and S. Haddadin, "CPA-Wrist: Compliant Pneumatic Actuation for Antagonistic Tendon Driven Wrists", *IEEE Robotics and Automation Letters (RA-L)*, 2018.
- **A. Tödtheide**, T. Lilge, and S. Haddadin, "Antagonistic Impedance Control for Pneumatically Actuated Robot Joints", *IEEE Robotics and Automation Letters (RA-L)*, 2016.
- N. Seppich, N. Tacca, K. Chao, M. Akim, D. Hidalgo-Carvajal, E. Fortunić, **A. Tödtheide**, J. Kühn and S. Haddadin, "CyberLimb: A Novel Robotic Prosthesis Concept with Shared and Intuitive Control", *Journal of NeuroEngineering and Rehabilitation (JNER)*, 2022.
- J. Kühn, T. Hu, **A. Tödtheide**, E. Pozo Fortunić, E. Jensen, and S. Haddadin "Seamless Limb-Driven Prostheses: The Synergy-Complement Control Approach", Nature Machine Intelligence, 2022, *under review*.
- J. Kühn, T. Hu, **A. Tödtheide**, E. Pozo Fortunić, A. Melone, E. Jensen, C. Herneth and S. Haddadin "Approaching Asimov's Third Law: Superhuman Protective Robot Reflexes for Touch and Heat", Nature Machine Intelligence, *in preparation*.

International Conferences

1. **A. Tödtheide**, X. Chen, H. Sadeghian, A. Naceri and S. Haddadin, "A Tactile Exoskeleton for Teleoperation: An Application in Elderly Care Robotics", *IEEE Conference on Robotics and Automation (ICRA)*, 2023, London, United Kingdom.
2. **A. Tödtheide**, J. Kühn, E. Pozo Fortunić and S. Haddadin, "An Integrated, Force-Sensitive, Impedance Controlled, Tendon-Driven Wrist: Design, Modeling, and Control", *IEEE-RAS International Conference on Humanoid Robots (Humanoids)*, 2015, Munich, Germany.
3. **A. Tödtheide**, E. Shahriari and S. Haddadin, "Tank Based Unified Torque/Impedance Control for a Pneumatically Actuated Antagonistic Robot Joint", *IEEE Conference on Robotics and Automation (ICRA)*, 2017, Singapore, Singapore.

4. J. Vorndamme, M. Schappler, **A. Tödtheide** and S. Haddadin, "Soft robotics for the hydraulic atlas arms: Joint Impedance Control with Collision Detection and Disturbance Compensation", *IEEE/RSJ International Conference on Intelligent Robots and Systems (IROS)*, 2016, Daejeon, Korea.

5. M. Schappler, J. Vorndamme, **A. Tödtheide**, D. Conner, O. von Stryk and S. Haddadin, "Modeling, Identification and Joint Impedance Control of the Atlas Arms", *IEEE-RAS International Conference on Humanoid Robots (Humanoids)*, 2015, Nancy, France.

6. **A. Tödtheide**, H. Kussaba, and S. Haddadin, "Nonlinear Disturbance Observer for Pneumatic Systems: Algorithm and Application to Sliding Mode Force Control", *in preparation*.

Workshops

1. **A. Tödtheide**, J. Kühn and S. Haddadin, "Proprio-and Exteroceptive Reflexes for a Pneumatically Actuated Finger based on the Artificial Robot Nervous System", *IEEE Conference on Robotics and Automation*, ICRA 2017 all-day workshop on "The robotic sense of touch: from sensing to understanding", 2017, Singapore, Singapore.

2. **A. Tödtheide**, T. Lilge and S. Haddadin, "Compliant Interaction with an Antagonistic Pneumatically Controlled Robot Joint", Human-friendly Robots, 2015, Munich, Germany.

Thesis

The results of the diploma thesis

1. **A. Tödtheide** "Development, Modeling and Control of Pneumatic Drives for an Anthropomorphic Robot Hand", *Diploma Thesis*, 2015, Institut für Regelungstechnik, Leibniz Universität Hannover

were used in **A. Tödtheide** et al., "Antagonistic impedance control for pneumatically actuated robot joints", *IEEE Robotics and Automation Letters (RA-L)*, 2016 and parts were utilized in Chapter 4.

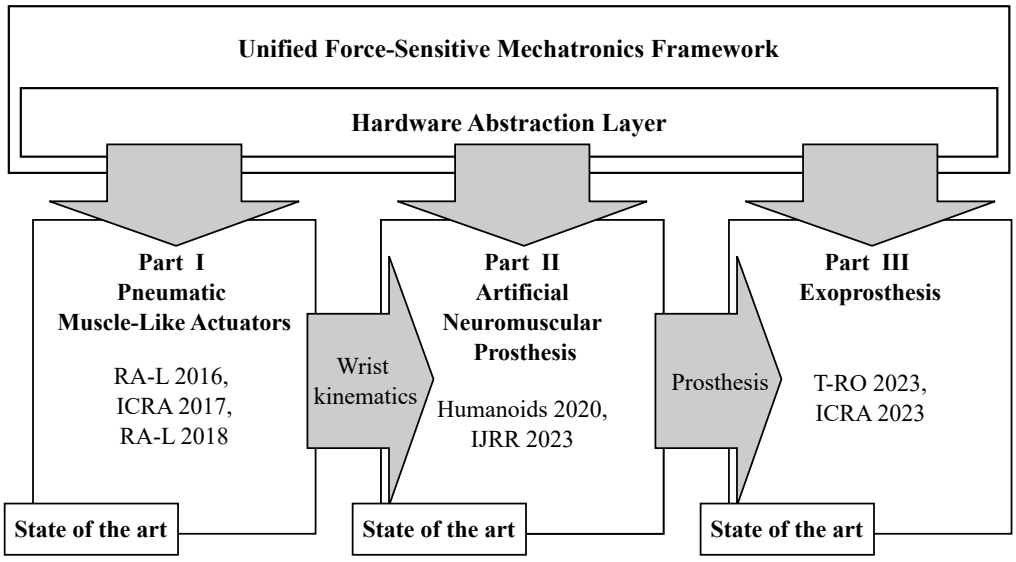

Figure 1 Content and structure of the thesis as based on the listed publications

Contents

List of Symbols

Frames

b	Frame of the robot base
W	Frame of the world
x	Frame of an arbitrary location
j	Frame of body j

General symbols

$\hat{\square}$	Estimated units
${}^{j}\boldsymbol{I}_{j}$	Inertia tensor of body j expressed the frame j
${}^{\mathrm{b}}\boldsymbol{A}_{j}$	Rotation matrix of rigid body j expressed in b
${}^{\mathrm{b}}\boldsymbol{T}_{j}$	Transformation matrix of rigid body j expressed in b
${}^{\mathrm{b}}\mathcal{F}$	6-dof Wrench expressed in b
${}^{\mathrm{b}}\boldsymbol{F}$	Vector of forces expressed in b
${}^{\mathrm{b}}\boldsymbol{g}$	Vector of gravity expressed in b
${}^{\mathrm{b}}\boldsymbol{M}$	Vector of moments expressed in b
$\boldsymbol{D}$	Controller Damping matrix
$\boldsymbol{J}$	Jacobian matrix
$\boldsymbol{K}$	Controller gain matrix
Ω	Quaternion
$\boldsymbol{\omega}$	Vector of angular velocity
$\boldsymbol{\tau}$	Vector of joint torques
$\boldsymbol{\tau}_{\mathrm{a}}$	Vector of actuator torques
$\boldsymbol{\tau}_{\mathrm{c}}$	Vector of generalized forces
$\boldsymbol{\varphi}$	Vector of orientation in RPY coordinates
$\boldsymbol{C}$	Coriolis matrix
$\boldsymbol{F}_{\mathrm{t}}$	Vector of tendon forces
$\boldsymbol{g}$	Vector of gravitational torques
$\boldsymbol{h}$	Tendon extension function vecotor

$\boldsymbol{J}_\mathrm{t}$ Tendon Jacobian matrix

$\boldsymbol{M}$ Mass matrix

$\boldsymbol{P}$ Binary switching matrix

$\boldsymbol{q}$ Joint angle

$\boldsymbol{q}_\mathrm{a}$ Actuator joint angle

$\boldsymbol{q}_\mathrm{c}$ Generalized coordinate of the floating-base robot

$\boldsymbol{r}$ Cartesian vector

$\boldsymbol{s}$ Vector of the first moment

$\boldsymbol{t}$ Vector of translation

b Width

h Height

i_g Gear ratio

l Length

r Radius

Pneumatics

α Flow attenuation

$\dot{m}$ Mass flow

Ψ Flow function

A Area

c_f Discharge coefficient

L Stroke length

P Chamber pressure

R Specific gas constant

T Chamber temperature

u Valve voltage

V Chamber volume

x_s Spool position

x Piston position

1 Introduction

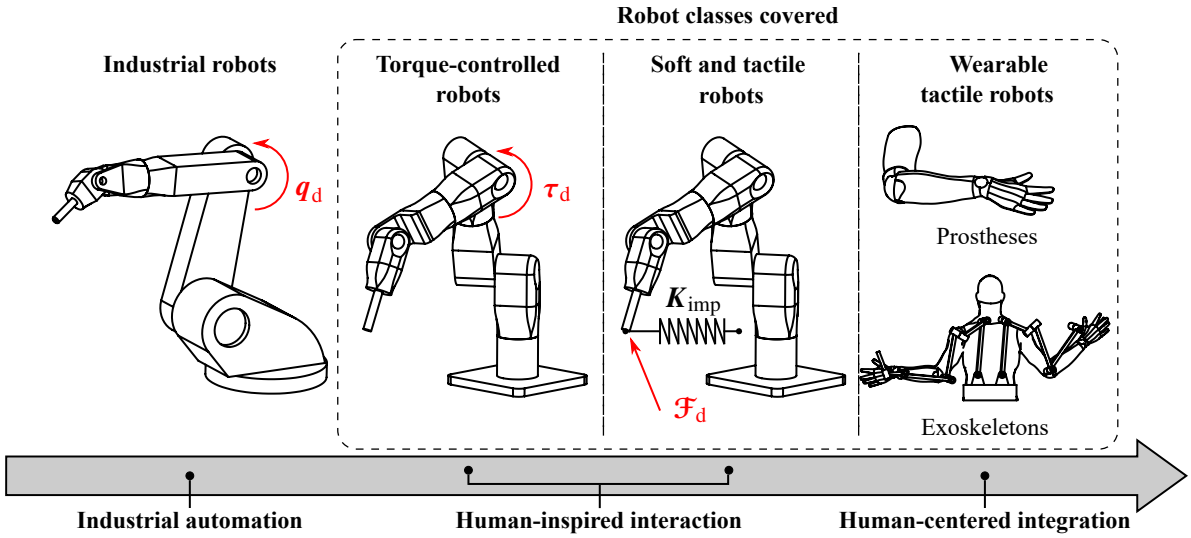

Figure 1.1 From mechatronics for industrial robot automation to mechatronics for human-centered robotics

1.1 Motivation

Evolving advances in robotics have led to establishing the technology in industry, and interestingly in society, providing novel applications, use cases and devices. In particular, modern robot applications have been developed, which are neither stationary nor repetitively-moving, but rather force-sensitive, interactive, autonomously learning and possibly wearable, e.g., through robotic exoskeletons and prostheses. These robots are characterized by their human-inspired and human-centered design, see Fig. 1.1, which was in essence enabled by a paradigm shift from industrial towards soft and tactile robots [1]. The essential feature of soft and tactile robots is their high-performance torque-level control in combination with accurate dynamic models, including their drive-train. This enables the designer i) to impose a desired mechanical behavior in software, ii) to solely control the robot via interaction forces, and iii) to detect and respond to environmental forces. These properties have revolutionized how robots interact with the environment and have resulted in many modern day applications such as collaborative robots, haptic devices and exoskeletons.

To date, these robots are realized by well-established mechatronic design approaches. Typically, soft and tactile robots are based on serial kinematics with electromechanical actuators, being flanged at the rotary joint axes of the robot, containing gears, torque sensors, Brushless Direct Current (BLDC) motors and motor electronics.

However, this well established and successful approach still has limitations that need to be addressed:

1. torque sensors and gears are complex, still relatively expensive and prone to mechanical impacts when mounted, which limits the use cases of state-of-the-art robotic systems in terms of dynamic contacts,

2. the existing structural design approach of soft and tactile robots is not straightforward – particularly for wearable robotic systems.

To overcome the aforementioned challenges, the goal of this thesis is to develop an alternative mechatronic approach for i) robot structures, ii) transmission elements and iii) actuation concepts, however with the same

technology background (i.e., drive-train and control algorithms) as used for soft and tactile robots. As the development of robots is cost-intensive and the implementation of new features is potentially risky, a unified simulation-based mechatronic development framework is proposed and introduced, which was designed to ensure a working robot prototype from scratch instead of thorough numerous design and prototype iterations.

This framework was used for advancing the design space in other areas such as

1. human-like pneumatic actuators,
2. upper-limb prosthetics and
3. exoskeletons,

thereby demonstrating the strength and variety of the framework. This approach is described in more detail below.

1.2 Approach

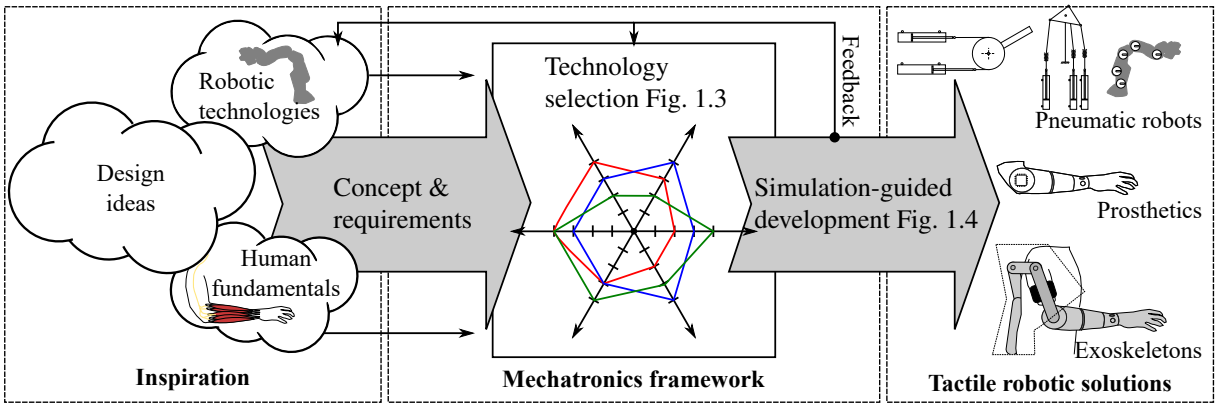

Figure 1.2 Development pipeline for tactile robotic systems

In this thesis, a model-based development approach is developed that can be used to design soft and tactile robot systems with different i) transmissions, ii) actuation concepts iii) and robot kinematics[1] by a unified mathematical framework. In this context, it is worth mentioning that the key characteristics of soft and tactile robots (in contrast to industrial robots) are force/torque sensors in the joints combined with suitable control schemes.

The core ideas of the development framework are to

1. algorithmize state-of-the-art control concepts from soft and tactile robots, i.e., gravity compensation, impedance control, etc., assuming a cascaded structure of joint torque and impedance control,
2. introduce actuator abstractions, which represent the actuator as torque source, regardless of the specific actuation principle, being realized by an actuator-tailored force/torque controller,
3. introduce transmission abstractions, i.e., for tendons, gears, spools, which provide actuator- and joint level-mappings, by mathematical back and forward transformations to provide joint-level control for complex actuation concepts.

Consequently, a variety of system configurations can be modeled, controlled and designed in principle. The overall development pipeline of the framework is depicted in Fig. 1.2, which is split into three phases: *inspiration*, *mechatronics framework* and *tactile robotics solutions*. In the phase *inspiration*, the fundamental

[1] Parallel structures can be designed, as long as the parallel elements add up to the main serial structure, and as long as these can be considered massless.

design idea of the robot is created. State-of-the-art knowledge from soft and tactile robotics and human neuromechanics may be considered, as these domains provide existing and working design concepts from technical or biological system perspective. A technical example for such a biological-inspired technical design might be the kinematics of industrial robots, which was inspired by the anatomy of human limbs.

Three main biological inspirations utilized are as follows.

1. Tendon-driven design, inspired by human tendons, allows for a remote actuation of robot joints. With this, more lightweight structures with an optimized Center Of Mass (COM) can be designed.

2. Inherent compliance in the actuation, inspired by the flexibility of human muscles and tendons, allows for releasing/storing energy and for mitigating impacts. This property is particularly exploited by using pneumatic actuators.

3. Backdrivability of the actuator, inspired by the low-friction properties of human muscles, allows for a seamless interaction with the environment. This property is utilized by using both pneumatic actuators and electromechanical geared systems when operated in torque control mode.

After forming the idea of the robot, the concept and requirements are defined, which are the inputs for the subsequent mechatronic framework.

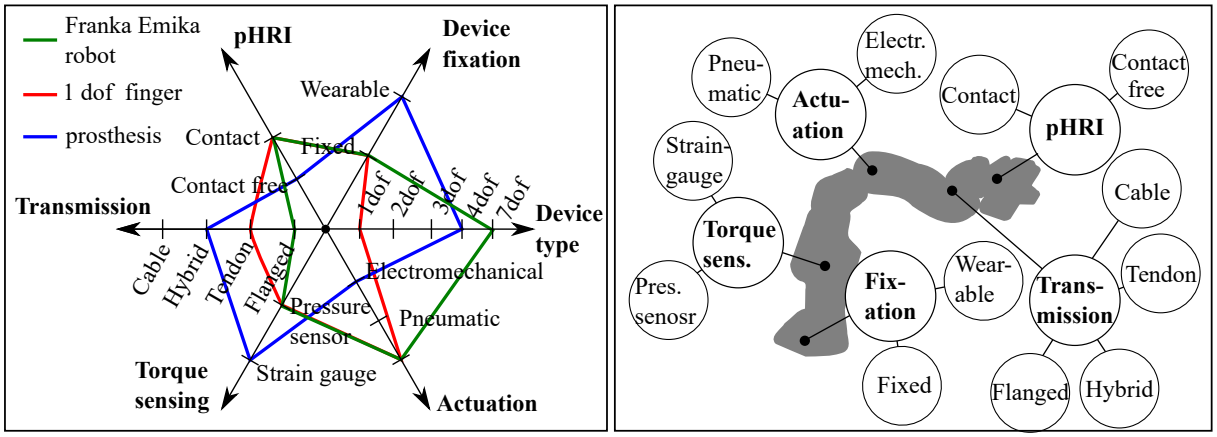

Figure 1.3 Morphological chart and robot concept showing space of possible design variants

The mechatronics framework, see Fig. 1.2, consists of the *technology selection* and the *simulation-guided development pipeline*. The technology selection covers the space of existing technologies used in this thesis, see Fig. 1.3. Here, the features of chosen systems are illustrated by the green, red and blue lines in the morphological chart. The features and categories of the morphological chart were mainly determined in the phase *inspiration* as illustrated by the small arrows in Fig. 1.2.

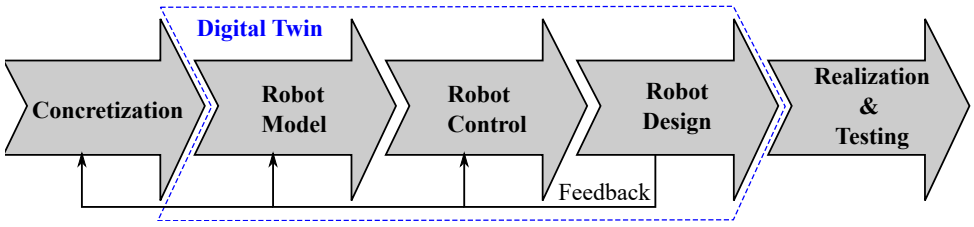

Figure 1.4 Simulation-guided development pipeline

Based on the chosen technology from the morphological chart, the simulation-guided development of the robot is performed, see Fig. 1.4. This pipeline starts with the *concretization* of the design fulfilling the necessary steps between the choice of technologies from Fig. 1.3 towards a kinematic, sensing and actuation concept.

A *digital twin* of the robot device is elaborated, which includes the modeling, control and mechanical design in a computer aided environment, see Fig. 1.4.

Robot Model: The *robot model* includes the following components and processes: i) A rigid-body model of the robot that is derived from a symbolic analysis of the mechanism structure and the fundamental equations of mechanics, i.e., Newton-/Euler and Lagrange. The outcome is then transferred to numerical robot models representing the differential equations of the robot. This allows for the modeling of both fixed- and floating-base kinematics. ii) The transmission elements are derived and added to the model by a symbolic analysis of the transmission structure. iii) The actuation is considered by two different approaches. First, the actuation of electromechanical systems is abstracted as an idealized torque source. Second, the actuation of pneumatic systems is expressed by a thermodynamics model, which includes the effects of the pressure evolution, the in-/outflow of pressurized air and the valve behavior.

Robot Control: The *robot controller* includes state-of-the-art control methods such as actuator force/torque control, impedance control and momentum observation for contact monitoring. While the actuator force/torque controller serves as system boundary for the *Actuator Abstraction Layer (AAL)*, the mathematical transformations of the transmissions allows for the *Transmission Abstraction Layer (TAL)*. This enables joint-side control of the robot despite the complex transmission structure between joint and actuation. All aforementioned methods are generalized and standardized, as they are based on the same mathematical foundation for each robot in the framework of this thesis.

Robot Design: Part of the *digital twin* is also the mechanical design formalized by a computer-aided design software. This allows for specializing the geometry of the robot with respect to required dimensions and loads, provided by simulation, before the device is realized. These methods are also used for extracting loads on actuation and structure in different simulation scenarios. After the successful design, the device is realized and tested.

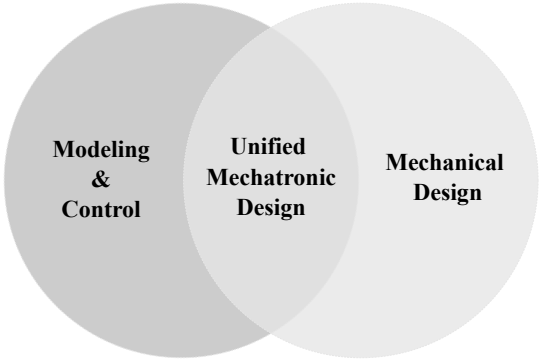

Figure 1.5 Unified mechatronics design

In the final step, the *digital twin* simulation allows for testing, validating, parameterizing and iterating different control and model approaches before a robot device is realized.

The proposed unified mechatronic design approach defines the modeling and control part as the central crystallization point in the systematic robot development. This is because, the systematic modeling and control ensures key functionality of the robot and allows for deriving the necessary properties of sensors, actuators and controllers. As will be shown throughout the course of this thesis, the proposed approach then allows for developing complex robotic systems with minimum number of prototypes.

In summary, the aim of this thesis is to provide a general, modular and parameterizable mathematical design framework applied to a number of complex robotic systems, covering the modeling and control, as well as the mechanical design of the robot, see Fig. 1.5. This work does not aim for general design rules of robotic geometries and integration on a component level. This work also does not aim for a fully automated design framework. Rather, it provides systematic processes, simulation tools and guidelines by, which advanced specialized tactile robotic prototypes can be developed in a minimum number of hardware prototypes.

1.3 Contribution

In the following, the specific contributions of this thesis are proposed.

Unified Force-Sensitive Mechatronics Design: This thesis provides a framework for the design and control of soft and tactile robots with various actuation concepts, transmission technologies and kinematic structures, which are simulatively and experimentally verified for selected systems. While previous works also focused on a simulation-driven design approach for robot co-simulation-based software/controller design [2] [3] [4], and mechatronic design [5] [6] [7] [8], [9], [10], [11], to the best of the author's knowledge, this thesis is the first work that investigates a model-based design-approach for soft and tactile robotic systems. Even though the utilized technologies of the framework (i.e., pneumatics, electromechanical actuation, inherently compliant and tendon-based systems) have individually been researched extensively, they have neither been described nor validated by a holistic robotics design framework, especially not in terms of soft and tactile robotic mechatronics and control.

By the application of the framework, further contributions were obtained in pneumatics, prosthetics and exoskeletons, as described below.

Pneumatics: In the field of pneumatic actuation, the major contribution of this thesis is a systematic transfer of state-of-the-art soft and tactile robotics methodologies to pneumatically actuated robots, impedance control, momentum observation, unified force/impedance control and joint torque control. While the modeling and control of pneumatic cylinders is an existing and well researched technology, methods for soft and tactile robotics have not – to the best of the author's knowledge – been systematically investigated for pneumatics to date. Following the design of tactile electromechanical actuators, equivalent pneumatic joint designs with the corresponding sensors, actuators and controllers are proposed. With this, novel human-inspired, tendon-driven robot joint designs for 1-dof and 2-dof are introduced, which are validated in simulation and experiment. In addition, the control concepts are validated on a 7-dof robot simulation, providing a concept evaluation and a preliminary step towards the development of a 7-dof pneumatic robot using the development design framework. Most noticeably, pneumatic-level force-controllers and pneumatic-level disturbance observers are presented. On this basis, joint torques, joint impedances, contact losses and actuator-level forces can be successfully controlled for pneumatically driven robots. Disturbance joint torques and disturbance actuator pressure variations (such as leakages) can also be successfully observed. Consequently, a full real world model and accurate control of the pneumatic joint becomes possible from a soft and tactile perspective.

Prosthetics: This work provides contributions to the development of upper-limb prostheses in i) *development approach*, ii) *prostheses features*, and iii) *mechatronic solution*.

- *Development approach:* This work provides a novel development approach for upper limb prostheses, which is based on core features of the human motor control system. First, key features and systematic working principles of the body are identified. Second, a human-inspired control scheme is elaborated, governing the mechatronic system design, including sensors, actuators and controllers. This corresponds to the human body by considering the state of the art in soft, tactile and humanoid robotics. Third, a digital-twin simulation of the prosthesis is developed based on the unified force-sensitive mechatronics design of this thesis by which every feature of the prosthesis is developed, optimized and tested in simulation before the device has built. This step enables the development of advanced robotic prostheses at a reduced number of physical prototypes.

- *Prostheses features:* The intention of the aforementioned development approach is to provide human-like features to upper-limb prostheses. The hypothesis is that a prosthesis, which was developed along core design principles of the human body, also provides more human-like characteristics. In particular, these cover i) body awareness, ii) contact awareness, iii) human-like contact response, and iv) human-like kinematics. By this, natural features lost through amputation, may be reestablished

by the artificial prosthetic device. This is a significant paradigm change in prosthetic features, which generally has not been considered to date.

- *Mechatronic solution:* This thesis provides the highly-integrated Artificial Neuromuscular Prosthesis (ANP), which stands out for its i) 4-dof human-like elbow-to-wrist kinematics, ii) torque-controlled robot joints and iii) an Inertial Measurement Unit (IMU), measuring the orientation of the device to calculate internal models in real-time – all provided at a small size and a weight of 1.7 kg. The prosthesis is equipped with an Artificial Neuromuscular Controller, which is designed in accordance with the human body. The system is equipped with joint impedance control, a floating-base rigid-body model and a floating-base momentum observer, which is the state-of-the-art knowledge in human motor control. Modeling and control methods, known from soft, tactile and humanoid robotics, are transferred to upper-limb prosthetics. Finally, the functionality of the device and the control methods are validated in human-in-the-loop experiments.

Exoskeletons: A novel exoskeleton-based method for attaching a prosthesis to the human is proposed. Commonly, prosthetic systems are attached to the human by various passive interfaces, which however are either invasive and/or quite unpleasant and exhaustive for the user. In this thesis, the first wearable active prosthesis socket, which is realized by a tactile shoulder exoskeleton, is proposed. While the idea of an active socket, denoted *exoprosthesis*, was conceptualized in [12], [13], a full implementation of the concept remained open. The potential and feasibility of the active socket is investigated by i) the development of a first exoskeleton prototype, ii) the development of tactile controllers, iii) multi-body simulations for a stress analysis on the human body and iv) an experimental controller evaluation including human-in-the-loop tests. A further contribution is the mechanical design of the asymmetric, tactile exoskeleton, which provides a balanced and ergonomic improved COM, realized by a contralateral remote actuator placement.

1.4 Outline

The thesis is structured as follows. Chapter 2 describes the state of the art in tactile robotics, fluid robots, upper-limb prosthetics and exoskeletons. Chapter 3 covers the framework proving the mathematical methods of this thesis. Chapter 4 deals with pneumatic muscle-like actuators applied to various robot systems. Chapter 5 focuses on novel human-inspired methods for upper-limb prostheses. Chapter 6 deals with the *exoprosthesis* being an active socket, realized by a shoulder exoskeleton. Chapter 7 concludes the work.

2 State of the art

In this chapter, the state of the art of the related work is presented, which was written based on [14], [15], [16], [17], [18], [19], [20].

2.1 From Soft to Tactile Robot Design

The success of modern robot technology was initiated by the automation of motion in the automobile industry. These industrial robots were designed to perform high-speed repetitive motions with high absolute, repetitive accuracy, robustness and durability [21]. However, due to their large weight, high speed and their pure position control approach [22], these robots are obviously very dangerous to humans. For this reason, safety fences or other barriers prevent the human from entering the workspace of the robot in industrial environments [23].

Lightweight Robots Due to the demand for more flexible use cases of robots such as force feedback systems and collaborating robots (e.g. in health care, space robotics) [24], a paradigm shift from industrial to collaborative, and finally, to soft and tactile robots occurred, with particular focus on lightweight design. In this regard, soft and tactile robots were developed in order to provide a safe operation in unknown and unstructured environments, especially in the presence of people [25]. This means that the robot must not be harmful for itself, for its environment and for people, on a physical level. This refers mainly to contacts or collisions. This fact was already conceptualized within the "Three Laws of Robotics" by Isaac Asimov in 1954 [26] who inspired roboticists to elaborate solutions for robot safety [27] and proposed international safety standards for robot applications such as the ISO10218.

Design Paradigms The design of a safer robot requires a complete reconsideration of the design in contrast to classical industrial robotics. Common design strategies include low weight and inertia [22], [25], [28], [1], [29], backdrivability of the actuation [29], [25], [28], low impedance [30], [31] torque-controlled joints [28], [21], [24] and alternating compliant and tactile system response [25], [21], [1].

Two paradigm shifts dominated the research on robotic actuation over the last twenty years [1]. While classical industrial robots include a rigidly position controlled drive-train, the first paradigm shift happened by the use of torque sensing and control across the entire robot [22], [21], which in fact were already introduced in the 1980s [32]. This enables the measurements of environmental and contact forces, and was later the key to soft [24] and tactile control [33, 34]. The second paradigm shift happened by the use of inherently compliant elements in the drive-train to mitigate impacts, to store energy and to generally improve the performance of the robot [35]. These robots typically utilize a combination of passive and active compliance. These two paradigms will be further discussed below, though acknowledging that the latter is still only used in research, not real-world applications.

2.1.1 Structural Design

The structural design has a major influence on the robot performance and safety. For this reason, first attempts implemented soft covers on the robot structure to mitigate the impact energy [28], [36], which, however, turned out to be impractical. Another structural approach is to reduce the mass and inertia in order to minimize the kinetic energy of the robot [29]. Lightweight metals and composite materials became standard in the design of soft robots [22], [1], [21], which also gave them the name lightweight robots. E.g., the LWR III is reported to have a load-to-weight-ratio of $1 : 1$ [21], presumably measured for the static

case. Still, this ratio remains a magnitude higher compared to human limbs. The only reported robot with human-like weight and inertia is the LIMS robot [29]. Apart from a lightweight structure, an efficient and lightweight drive-train contributes to a low weight and inertia robot, as discussed below.

2.1.2 Rigid Drive-train

State-of-the-art torque-controlled robot joints for soft and tactile robots generally include a highly reducing strain-wave gear, a BLDC and a torque sensor [28]. Angular measurements may either be performed on joint-side, limb-side or both. BLDCs are preferred in such robots over Direct Current (DC) motors as these are more efficient and provide a higher torque density. Electronics of lightweight robots are implemented at the robot actuator to reduce weight and wiring [21]. In the following subsection, gear and torque sensor are discussed in more detail.

Strain-Wave Gear A Strain-wave gear, as used in a robot, is in essence a differential gear with three elements, namely *wave generator*, *flex spline* and *circular spline*. In contrast to spur gears or planetary gears, a strain wave gear is based on a different working principle as explained by the subsequent actuation at the *wave generator* with the output on the *circular spline*. When the *wave generator* performs a rotary motion, its oval shape deforms the enclosing *flex spline*. As *flex spline* and *circular spline* include small teeth, which are in interaction with each other, the rise and fall of the tooth motion, imposed by the *wave generator*, affects a reduction of speed and the amplification of torque at the output of the gear, i.e the *circular spline*. As the components of a strain-wave gear are magnitudes smaller and lighter than spur gears or planetary gears, strain-wave gears are a key enabler for obtaining a lightweight robotic actuator that strives for a high power density [28]. In contrast to typical high speed motions of classical industrial robots, the actuators for lightweight robots were usually designed for moderate velocity [21]. Such a decrease in task space velocity allows for higher gear ratios and also higher joint torques. Thus, lighter robot structures can be achieved.

Joint Torque Sensor The joint torque sensor in a soft robotic actuator is used for measuring the sum of link-side and environmental interaction torques. They are typically realized using strain-gauge-based [21] or optical approaches [37]. Most importantly, the torque sensor is used for damping oscillations, scaling the motor inertia and enabling soft robotics control [21], [24]. In combination with joint level torque control, it provides an active backdrivability to the robot [25] and direct interaction with the Lagrangian mechanics on a torque-level. The consequence of the joint torque control is that any desired mechanical behavior such as gravity compensation, impedance and stiffness can be imposed on the robot structure by active control. Link-side torque measurements have turned out to be essential for tactile control as well as motor-side measurements, and are highly biased by friction and stiction of the gear. This means that in principle, link-side torque sensors are not necessary as long as low-friction drive-trains and motor-side torque measurements are available [28].

Actuator Placement The placement of the actuation plays a fundamental role in the design of a robot. The design and placement of the actuation can be realized by a

- *joint collocated modular*, or
- *remote tendon-driven*

approach [38], [39]. In the *joint collocated modular* approach, the actuators are flanged directly at the joint axes by using modular actuators. In a *remote tendon-driven* design, the actuators are placed at a remote location, proximal to the robot base [29], which can be used to reduce the weight and inertia of the structure to obtain higher accelerations and velocities. Tendon-driven joints are mostly actuated by a bio-inspired antagonistic arrangement similar to human muscles [1]. Most commercially available collaborative soft and tactile robots are realized by a modular design [34], [34]. Examples for tendon driven robots can be found in [40], [41], [29]. Furthermore, *remote tendon-driven* designs are commonly used in anthropomorphic robot hands [42], [43], [44], [45].

2.1.3 Flexible Drive-train

The aforementioned drive-train concepts from the previous section may be practically considered rigid. The limitation of this design is most apparent when hard collisions occur [46], [47], [48], [1], [49]. Due to the limited backdrivability of the strain-wave gearing[1], the impact energy can hardly be dissipated and may destroy torque sensors or gears. Even a high-sampling torque controller cannot prevent the hardware from getting damaged [48], [50], even though active compliance and the flexibility of the robot structure are still protective for the drive-train. Furthermore, when comparing the robot to human performance in terms of control bandwidth, human motion is generally faster [42] and more efficient. Humans use the co-contraction of their antagonistically arranged compliant neuromechanical apparatus to increase the performance in terms of speed and impact resilience. This fact is also enabled by the ability of the muscles to store energy like a mechanical spring [51].

Inherent Compliance For these reasons, a second paradigm shift in robotics occurred towards robots containing passive elements with inherent compliance [23] targets to improve collision robustness and to achieve human-like manipulation and locomotion [52]. The ability to store and release energy allows for novel applications such as running and throwing [53], [54], [27], [1], [55]. Often, this concept is implemented as antagonistically arranged inherently compliant elements placed between actuator and robot joint. In fact, this is essentially a bio-inspired concept based on the design of human muscles [1].

Series Elastic Actuators The most straightforward design to recreate the aforementioned elastic behavior utilizes mechanical springs between actuator and joint. This system is called a Series Elastic Actuator (SEA) [1], [56]. While these actuators provide a good impact robustness, their disadvantages are a significantly reduced bandwidth, lower position accuracy and no possibility to adjust the actuator stiffness.

VSA and VIA For this reason, Variable Stiffness Actuators (VSA) [57], [1], [58], [59], [60] and Variable Impedance Actuators (VIA) were introduced [52], [25]. There, an additional actuator is used in the actuation of a single robotic joint for pretensioning internal springs and for changing the mechanical joint stiffness. In contrast to position or torque controlled actuators, SEA, VSA and VIA were inspired from a set equilibrium point of view on design level [52], [54]. As a consequence, these actuators showed improved performance [61] in terms of energy efficiency [54], impact robustness [50], [42], and dynamics [35], [62], [63], [64]. One of the most advanced robots utilizing VIAs, is the DLR's hand arm system (hasy) [65]. On the downside, VSAs and VIAs come at the cost of an increased number of actuators and increased complexity, which has turned out to problematic in achieving high practical robustness and performance. Finally, joint- and actuator-sided measurements, allow for the measurement of the joint deflection, which is used to measure the torque based on the identified stiffness properties [66].

Pneumatic Actuators Another approach for realizing a VIA are pneumatic actuators. Bicci and Tonietti reported to use double actuated cylinders or antagonistically arranged pneumatic muscle actuators to obtain a VIA exploiting the compressibility of air [25]. Pneumatic actuators achieve similar properties as VIAs and VSAs, however with less mechanical components in the drive-train. However, they come along with increased complexity due to the need for compressors, pressure tanks and air conditioning systems. Pneumatic actuators are considered as an alternative actuation principle to reach similar behavior to SEA, VSA and VIA based on electromechanical technology.

2.1.4 Active Compliance Control

The main difference in the control of an industrial robot and the control of a soft and tactile robot is that the environment has to be considered partially unknown for the latter case. This fact requires a control strategy

[1] In a collision, first the stiction and friction needs to be overcome before the actuator starts moving.

governing how to deal with unforeseen interactions and collisions by measuring and controlling interaction forces [27].

On the hardware side, compliant and tactile control requires either joint torque measurements [22] or Cartesian force/torque sensors [67], [68]. Historically, the development of tactile interaction controllers occurred as follows [27]: The initial approaches focused on force control [69], and hybrid position and force control [70], and the latter approaches focused on active compliance [71] and stiffness control [72].

In the 1980s, the nowadays most widely adapted control approach for soft robots, namely impedance control, was proposed by Neville Hogan [73]. Later, this concept was extended to flexible joints in [74], [75], [24] providing a significant performance improvement for high controller stiffnesses in contrast to rigid-joint approaches for lightweight robots. A unification of force and impedance control, solving the stability issues of hybrid position and force controlled robots, was proposed in [76]. This approach provides a fully tactile controller as end effector impedances and end effector contact forces can be set and controlled simultaneously.

In general, impedance control makes the robot behave like a second order mass spring damper system. As a consequence, not only the robot position but also its impedance behavior is actively controlled. In terms of robot safety, impedance behavior makes the robot compliant, mitigates interaction forces and increases perceived robot safety. The impedance controller is based on a cascaded control cycle with an outer impedance loop and an inner torque or force control loop taking the commands from the impedance controller [28]. In contrast to other controllers (such as hybrid position/force control [70]), impedance control provides a stable system behavior, as shown by a passivity analysis in [74]. Impedance control has also been realized for VSAs and VIAs [65] containing antagonistic and nonlinear inherent stiffness properties. In this setting, the actual achieved stiffness is a combination of inherent and active compliance [61]. Also, joint torque measurements are obtained by measuring the elongation of the compliant element.

In the following section, fluid actuation such as pneumatic and hydraulic systems are discussed.

2.2 Fluidic Robot Design

Fluid actuators can be categorized into pneumatic and hydraulic systems. While hydraulic actuators utilize fluids (mostly oil or water), pneumatic actuators utilize pressurized gases such as air. Both technologies are further discussed below.

2.2.1 Pneumatic Robots

Pneumatics actuators show inherent physical compliance due the compressibility of air and provide backdrivable actuation due to their simple working principle. They are able to produce high speeds, are robust against shocks, can store energy and have a compliance, which can be physically adjusted by the chamber pressure. These properties also make pneumatic actuators a potential candidate for implementing VSAs and VIAs. For electromechanical drives, however, the aforementioned properties can only be achieved by additional compliant elements and actuators, while pneumatic actuators require a supply of purified, pressurized air.

System Components Pneumatic drives commonly consist of a pneumatic actuator, one or two valves, position sensors, pressure sensors and valve drivers/controllers. The two most common types of pneumatic drives are pneumatic cylinders (linear and rotary) and Pneumatic Muscle Actuator (PMA).

Pneumatic Cylinders Linear or rotary pneumatic cylinders contain a piston or vane, which are driven by a pressure difference between one or two neighboring pneumatic chambers [77]. There are different single chamber designs, dual chamber designs, rodless designs or reluctance springs cylinders [78]. Another important factor is the seal, which mitigates the leakage and serves as a bearing for the motion. The seals can either be optimized for low leakage or low friction, whereas the low friction seals generally improve the physical interaction [25]. Due to the clear geometry of the chamber and piston and the well-known thermodynamics effects, a mathematical state-space model of pressure and temperature of the cylinder

Table 2.1 Comparing properties, modeling and control of PMA and pneumatic cylinders.

	PMA	Pneumatic cylinders
Stroke length	Short	Long
Model approach	Data driven	Analytical
Dynamics	Slow	Fast
Force sensing	Load cell	Pressure sensing
Output force	High	Medium
Modeling	[83], [84] [85], [86]	[79], [88], [89]
Position control	[90], [91], [92], [93]	[94], [95], [96],[96]
Force/torque control	[97]	[98], [99], [100], [89], [101], [81]
Force&Stiffness control	[102], [103]	[104], [105], [106], [107]
Impedance control (linear)	N.A.	[108]
Impedance control (rotary)	[109], [110]	N.A.

chambers can be derived [79]. For modeling and control, mostly isotherm reduced order models are used [80] [81], [82].

Pneumatic Muscle Actuators The PMA has become very popular in robotics research due to the similar appearance to human muscles. These actuators consist of a rubber bladder, which is surrounded by textile fabric. Different modifications of this actuator type exist [83], [84] [85], [86]. The original concept was invented in the 1950s by Joseph McKibben, a physician trying to help polio patients [87]. However, this design approach was more frequently used for research application in the 1980s. As the PMA can only produce pulling forces, it is usually setup with an antagonistic configuration. The actuator can be made of cheap materials, can be easily manufactured and can produce high forces. However, PMAs are considered to be slow in dynamics, to have a short stroke length and to have a hysteresis effect making them hard to control. The properties of PMAs and pneumatic cylinders are further compared in Tab. 2.1.

Pneumatic Valves Another central element of a pneumatic system are the valves, which are generally characterized as proportional valves [107], [81] or switching (on/off) valves [111]. While proportional valves have a quasi-linear relation between input signal and choke area, switching valves adjust the amount of air-flow via the switching frequency. Valves are categorized according to their possible states and number of inputs (e.g. 5/3, 3/2, 2/2) where the first number denotes the number of ports and the second number denotes the number of states. In robotics, 5/3 valves are used to couple the inflow and the outflow of neighboring chambers [81] while some works equip every chamber with a valve to obtain an extra controllable degree of freedom per actuator [106], [108].

Sensing Position, pressure and force sensing are the most common signals for pneumatic cylinders and PMAs. The position can either be measured on actuator or joint level. For PMAs, joint-level measurements are generally performed. For PMAs and pneumatic cylinders the chamber pressure is commonly measured. Force measurements are obtained from pressure measurements and the geometry for cylinders, while PMAs often require extra load cells [110], [103].

Control In the manufacturing industry, pneumatic cylinders are often utilized in simple on/off switching control states. The control of pneumatic cylinders and PMAs gained much interest in the 2000s. In research, position, force [98] and stiffness control are the most commonly used control concepts. As PID controllers and linear approaches provided limited performance [94], a breakthrough in pneumatics control was achieved by nonlinear control approaches [94]. In particular, nonlinear sliding mode control has found many applications for both pneumatic cylinders and PMAs [96]. Table 2.1 lists state-of-the-art modeling and control approaches for PMAs and pneumatic cylinders.

Applications Typical pneumatic applications are devices for medical rehabilitation [112], [113], [114], surgery [115], prosthetics [116], [117] exoskeletons [118], [119], [120] humanoids [121], [122], [114], [123], [124], [125], [126], [127], walking robots [128], [129] and lightweight robots [125], [130], [124]. Generally, pneumatic systems do not seem to be so widespread in commercial products as in electromechanical systems. A technological pioneer in pneumatics is the German company Festo, which has developed numerous bio-inspired and pneumatic robots [125]. In 2022, Festo introduced a robotic lightweight robot with rotary pneumatic cylinders showing the commercial potential of this technology.

2.2.2 Hydraulic Robots

Hydraulic and pneumatic actuators share very similar actuation technology. Both rotary and linear cylinders, solenoid and proportional valves can be found for hydraulic actuation systems [78]. There is also an equivalent technology for PMAs using fluids called hydro fluid muscle [131], [132], [133]. In contrast to pneumatic actuators, hydraulic actuators are driven by a fluid such as oil or water in a closed-loop fluid cycle, pressurized at supply pressures between 70 and 200 bar. As a result, hydraulic actuators can generate high torques and have an excellent power-to-weight ratio. In contrast to pneumatic systems, they have hardly any inherent compliance as the used fluids are generally incompressible. The downside is that leakage and human safety remain largely unresolved problems when dealing with hydraulic systems.

Nevertheless, hydraulic actuation has found many applications in mobile humanoid and bio-inspired robotics. The humanoid robot DB [134] and SARCOS [135], [136] provide torque control. Another torque controlled humanoid is the TaeMu [137]. Other well-known commercial hydraulic robots are Boston Dynamic's Patman and Atlas robot [138], [139], whereas Atlas was investigated in various publications after the DARPA Robotics Challenge from 2015 [140], [141], [142], [143]. Further bio-inspired hydraulic robots are the Boston Dynamics Bigdog [144] and the torque-controlled quadruped robot HyQ [145].

2.3 Upper-Limb Prostheses

Modern upper-limb prostheses are wearable, complex robotic devices. In the following section, the state of the art in upper-limb prostheses is outlined, focusing on elbow-to-wrist-mechanics.

Design Approach In recent decades, different design strategies have been developed in arm prosthetics with the aim of providing the best user experience for the amputee. This is commonly understood to be a balance between functionality, weight and size. Typical requirements for the design of a mechatronic prosthesis include high payload at high Load-to-Weight ratio [146] and human-like appearance [147] (i.e., human-like kinematics, motion, size and texture) – all of which reflect fundamental features of the human body. Finally, a key factor for achieving small, lightweight actuators with high output torque is the use of electromechanical actuators combined with high gear ratios [148, 146, 149].

Commercial Prostheses Typically, commercial transhumeral prostheses are equipped with an active elbow, a single active dof in the wrist (and possibly one additional passive wrist dof) together with a modular hand. Examples for commercial devices are the UtahArm and Wrist Rotator by Motion Control (Motion Control, Inc., Salt Lake City, Utah, USA) [150], the Dynamic Arm and Michaelangelo Hand/Wrist by Ottobock (Ottobock SE & Co. KGaA, Duderstadt, Germany) [147], the Boston Digital Arm (Liberating Technologies Inc., Hollison, MA, USA) [151] and the Touch Bionics iLimb Wrist (Ossur hf, Reykjavic, Iceland) [152].Devices with Flexion/Extension (F/E) include the KS-Bionic Hand by Kesheng Prostheses (Shanghai Kesheng Prosthetic Technology Co., Shanghai, China) [153] and the Powered Flexion Wrist by Fillauer Motion Control (Fillauer Europe AB, Sollentuna, Sweden) [150]. In contrast to the aforementioned systems for which wrist modules cannot be combined with Supination/Pronation (P/S), the LUKE Arm (Mobious Bionics LLC, Manchester, NH, USA) [154] has this ability.

Research Prosthesis Wrists: To date, wrists are still rare in prosthetics although a full 3-dof wrist is required to obtain human-like kinematics and dexterity. Due to the three intersecting axes of the wrist, it is challenging to find a small, lightweight solution that provides a sufficiently high torque. Finding a solution to this problem, without making too many compromises, becomes more and more difficult with increasing degrees of freedom. Consequently, most systems focus on wrists with 1-dof, either in the form of F/E or Supination/Pronation (P/S) [155, 146]. Two dof and 3-dof wrists are closely related since any wrist that provides 2-dof via F/E and Radial/Ulnar Deviation (R/U) can be easily extended to a 3-dof wrist by a P/S wrist rotator.

One straightforward design strategy in 2-dof or 3-dof wrists is to place the actuators in a serial order [156] and to minimize the dimensions to human size [148, 146, 149]. For [148, 149], high torques of at least 8 Nm were achieved, even though rather low efficiency was reported [148]. Furthermore, the resulting wrist kinematics contained an offset between the rotation axes, which is $\approx 5-6$ times larger than that of a human wrist [157]. The use of bevel gears to provide P/S and F/E was reported in [156, 158], but these methods have generally provided low torque to date. Also, parallel kinematics, using rods, were applied [159]. Another rod-based design provides a comparably high torque of up to 8 Nm [160]. To the best of the author's knowledge, only [149] provides torque sensing, which is essential for any active compliance control methods, but may increase the weight and the size of the device.

Research Prostheses (Elow to Wrist): The following section examines the state of the art in transhumeral prosthetic systems with a special focus on designs that include wrists.

A transhumeral prosthetic system with a 1-dof wrist (P/S) and one 1-dof elbow (F/E) was proposed in [155]. The work focuses on a mechanical design solution, which fits into an anthropomorphic forearm model. For that, a BLDC was placed at the center of the forearm, actuating the elbow via three chain and cable-driven stages. The maximum elbow torque is listed as 16 Nm and the gear ratio is listed as 35. The P/S wrist actuator consists of several spur and worm gears providing a torque of up to 2.6 Nm and gear ratios of up to 1900:1. The weight of the whole arm is less than 2 kg.

A transhumeral prosthetic system with a 2-dof wrist (P/S, F/E) is the Luke Deka arm [161]. The focus of the authors was to develop robust and cutting edge robotics for commercial prostheses. The modular prosthesis is distributed by the company Mobius Bionics LLC and is available for shoulder, humeral and radial amputation and contains a hand. A prior research variant of that system was proposed by Resnik et al. in [161]. The authors show novel, high-level user control modes using IMUs, foot-controls and sEMGs. The patent [162] provides further information about the mechanical design of the wrist and of the hand.

Another highly advanced prosthetic system with a 2-dof wrist (and hand) is the Rehabilitation Institute Of Chicago (RIC) arm described in [146]. The system consists of a 3-dof arm and a 2-dof hand. The focus of the RIC arm lies in providing miniaturized mechatronics for extra small body dimensions without sacrificing too many degrees of freedom and functionality. This was achieved by extraordinary mechatronic design solutions and high gear ratios. Despite the multistage gears, high efficiencies were achieved.

The modular prosthetic limb Modular Prosthesis Limb (MPL) is the first reported full transhumeral system with a 3-dof wrist (with additional R/U) [149]. It also includes a 10-dof hand [163, 164, 149]. The goal of this project was to develop a cutting-edge prosthetic arm with human-like kinematics, torque and sensory feedback in an anthropomorphic form factor. In fact, the MPL is the first and only reported system utilizing torque sensing and impedance control. Still no performance or working principle were provided. The MPL has been developed since 2007 in several project phases (exploring various actuation concepts) by 50 collaborating research institutes. To date, three official prototypes have been developed. In general, the MPL joints use multi-stage gears consisting of cyclonic and planetary gears in order to obtain high torques. This is similar to the concept of the RIC arm. The modular wrist consists of a serial RRR kinematics with a human-like form factor, similar to [148, 146]. The motor for F/E is implemented in the palm of the hand.

The above paragraph provide an overview about mechatronics of transhumeral prostheses as well as standalone prosthesis wrist modules. The following sections examine how the prostheses – proposed in this thesis – contribute to novel semi-autonomy algorithms and state-of-the-art control methods for upper-limb prostheses.

HMIs and Autonomy: Human machine interfaces HMI and semi-autonomy algorithms for prostheses are closely related due in part to the level of (semi-)autonomy for connecting two potential extremes: on the one hand, direct HMI-based control (common in most prostheses today), and on the other hand, full automation (robots).

A common HMI in upper limb prostheses is Surface Electromyography (sEMG) [165, 146]. Sequential control is the current standard sEMG method in prostheses, which allows the user to control each joint individually while the other joints are kept constant [166, 146, 167]. In combination with Targeted Muscle Reinnervation (TMR) surgery [168] and pattern recognition algorithms, multiple channels can also be controlled simultaneously [169, 170]. Alternatively, sEMG may be combined with additional input signals coming, for example, from IMUs [171, 167] or external switches, such as foot pedals [161]. Some attempts were made for implementing coordinated control of all prosthesis joints based on human-inspired synergies [167, 172, 13] or residual limb-driven techniques. Brain computer interfaces, such as Electroencephalogram (EEG), are also reported for prosthesis control [173, 174]. The coordinated control and EEG-based approaches have so far been implemented in research systems due to challenges with individualization, robustness and generalized use for further translation.

Within the area of semi-autonomous algorithms, the playback of prerecorded skills (trajectories) was shown in [12, 149]. Semi-autonomous task planning supported by multi-modal sensor information, such as computer vision, bio-signals, and motion capturing was proposed in [175]. A similar approach was applied in [176] to provide a shared autonomy framework with grasping prediction. A semi-autonomy bimanual interaction was established in [177]. Semi-autonomous algorithms for prostheses, such as visual servoing and trajectory teaching and playback, were shown in [12]. The work also showed a concept for a gravity-compensated, impedance and torque controlled *exoprosthesis*, but this was shown on a comparably large 2-dof prosthesis. Semi-autonomous prosthesis state estimation, prediction, and prosthesis reflexes were proposed in [13].

2.4 Upper-Limb Exoskeletons

Finally, the state of the art in upper-body exoskeleton is summarized below.

Applications

Upper limb exoskeletons have been developed for various purposes, such as power augmentation [178, 179], rehabilitation [180, 181, 182, 183, 184], teleoperation [185, 186], haptic interaction [187, 186, 188] and assistance [189, 190, 191]. Over the last 20 years, hundreds of upper limb exoskeletons have been developed and listed in reviews for general [192, 193, 194, 195, 196, 197] and for medical applications [198, 199]. These reviews demonstrate not only the challenges, solutions and systems, but also reflect the popularity of the technology.

Classification

Exoskeletons may be classified according to many factors, including their type of actuation, power transmission, dof, link configuration, control method, applied body part and application [193]. Electric motors are the most frequently utilized actuation technology, while some systems also use pneumatic [200] or hydraulic actuators [201]. Gears, cables, linkages and belt drives are utilized for power transmission. Regardless of the particular design, a general problem in upper limb exoskeletons is the limited torque density of available actuation technology [195, 202, 203]. Therefore, high torque exoskeletons are rather large while small exoskeletons provide little torque [202]. Most upper limb exoskeletons use serial kinematics, while parallel and hybrid configurations are also frequently utilized [193].

Control

Exoskeletons are designed to ensure a safe and responsive interaction with the human and the environment [195]. As the human body is physically connected to the exoskeleton control cycle, the human intention needs to be measured for enabling user-level control. This can either be achieved by cognitive or by physical human robot interaction (cHRI, pHRI) [193, 195]. In HRI, biological signals such as sEMG [204, 188, 178, 183] or Electroencephalogram [188, 205, 206] are transformed into suitable signals controlling the robot. In HRI, the exoskeleton can be guided via interaction wrenches, requiring measurement or estimation. In addition, gravity and Coriolis compensations [207, 208, 181, 178] can be applied to compensate for rigid body mechanical effects. Impedance [209, 210, 211, 192] and admittance behavior [212, 213, 214] are generally recommended if a compliant interaction is required [215, 195, 216]. These can be further classified according to their specific control objective into *assistance*, *correction*, and *guidance* modes [195].

Shoulder Exoskeletons: Human Anatomy

Shoulder exoskeletons are a subclass of upper limb exoskeletons and are of special interest for this thesis. Many challenges in the design of these systems arise from the complex human shoulder kinematics, as discussed in the next section. The human shoulder has a highly intricate anatomic structure with complex kinematics. The glenohumeral joint, (often referred to as the “shoulder joint" [217]), can be well described as a simple ball-and-socket joint, which is able to provide a spherical motion around the Instantaneous Center Of Rotation (ICR). The location of the ball-and-socket joint ICR can move in Cartesian space, constrained by the anatomy of the clavicle (collarbone) and scapula (shoulder blade)[2]. In fact, glenohumeral joint rotation is usually coupled with its ICR motion.

Shoulder Exoskeletons: Design

A major challenge in the design of shoulder exoskeletons is complementing human kinematics. The simplest possible design involves assuming a fixed ICR. Most shoulder exoskeletons utilize an RRR serial gimbal mechanism with three rotational axes [182], such as [218, 219, 220]. Even though this approach is common, it suffers from a limited workspace and the chance of singularities [182, 221]. Others, such as [208, 222, 223, 202, 188, 224], have developed solutions for tracking a moving ICR. This was achieved by a parallelogram kinematics on the back [208], a 3-dof parallel kinematics with linear actuators [222], a complex parallelogram kinematics [202] or additional active degrees of freedom [224, 188].

Other important design factors for shoulder exoskeletons are to avoid colliding structures and to match the human workspace. A RRR shoulder exoskeleton with a bearing at the central humerus for internal/external rotation, which provides a larger workspace than naive RRR designs, was shown in [189]. This problem was approached in [180] by placing the shoulder abduction/adduction actuator at the lower back. Further solutions include a double parallelogram for internal/external rotation [225], a nested gimbal design [203] or an externally located serial kinematic structure, carrying the shoulder exoskeleton [226, 227]. Passive elements can also be used to extend the usable workspace [228]. In this regard, a passive double parallelogram for internal/external rotation [209] and a passive scissor mechanism [221] were proposed. In general, the most targeted solutions to shoulder kinematics and workspace challenges are often achieved at the expense of increased weight, complexity and larger dimensions, which is likely the reason why the majority of systems is not mobile today.

Rigid, Wearable, Powered Upper Limb Devices

Many state-of-the-art upper limb exoskeletons, such as CADEN 7 [226], ABLE [229], ArMin III [181], HARMONY [230] and LIMPACT [202], are high-performance, however, non-wearable. In turn, many wearable systems were developed using a variety of approaches, such as soft exosuits [231, 232, 233, 234, 235], passive exoskeletons e.g., with gravitational springs [236, 237], and passive exoskeletons for industrial

[2]This includes the scapulothoracic articulation, the acromioclavicular joint, and the sternoclavicular joint.

applications [238, 239, 240, 241]. Rigid, wearable, powered upper limb exoskeletons are of the class, which is most comparable to the device proposed in this thesis [242], [243], [244], [188], [245], [225], [189], [209], [246], [228], [218], [247]. These listed systems include a complete arm structure and contain (at least) a shoulder module. Some systems include other active and/or passive joints, such as elbow, wrist, and hand joints. Most devices[3] have a weight $< 7\,\text{kg}$ except for [243]. The different systems were developed for various applications, therefore, the target torque and power requirements are obviously not fully comparable. All aforementioned systems, apart from [245, 218], provide control via pHRI, utilizing force or torque sensor measurements.

2.5 Summary

This chapter sets forth the foundation for the different research areas of this thesis. The following chapters apply the technological background of soft and tactile robots in Sec. 2.1. The background in fluid robots is of special interest for the development of pneumatic robots in Chapter 4. The background in prosthetics, see Sec. 2.3, is necessary for the developments in Chapter 5. Finally, the background in exoskeletons is essential for understanding the methods and results addressed in Chapter 6. In the next chapter, the model and control framework is proposed.

[3] The systems provide shoulder torques between 4 Nm and 18 Nm. The maximum human shoulder torque is listed to be 60 Nm for internal/external rotation, 115 Nm for abduction/adduction, and 134 Nm for flexion/extension [213].)

3 Modeling and Control

In this chapter, the modeling and control framework is introduced, which is utilized for the development of all mechatronic systems of this work. The sections of this chapter define the main components of the framework to model the behavior of developed robots. It contains rigid body modeling (Sec. 3.1), soft robotics and tactile controllers (Sec 3.2), an *Actuator Abstraction Layer (AAL)* (Sec. 3.3) and a *Transmission Abstraction Layer (TAL)* (Sec. 3.4). Submodules and submodule variants are defined in the subsections, respectively.

The framework design was derived from the driving questions.

- What are commonalities and differences in modeling and control for robotic systems with various actuator types, and transmission technologies?
- Is there a mathematical approach allowing the modeling, control and design by an overarching generalizing framework?

The modular approach of this work provides possible solutions to these questions.

For the first question, it is important to consider the underlying rigid body model either as a fixed or floating-base structure depending on whether the robot is mounted to the ground or a wearable device is used. Based on state-of-the-art soft robotics controller design, the systems are equipped with a suitable model-based compensation of the rigid body dynamics, an impedance controller for active compliance control and a momentum observer to estimate external torques – or generalized forces.

For evaluating actuation and transmissions under the first question, novel abstraction layers are proposed and used for the controller design. These allow to implement actuators and structures of varying complexity, which are obscured by the abstraction layer. With this, a modular design of the different robot systems becomes possible. Therefore, the particular actuator and transmission mechanisms are introduced. Specifically, electromechanical actuators (utilizing BLDCs + strain-wave gearing + torque sensing) and pneumatic actuators (utilizing pneumatic cylinders + high-speed solenoids + pressure sensors) are used. The considered transmissions are directly flanged actuators, an antagonistic setup with two tendons per joint and an antagonistic design setup with three tendons for two joints. This chapter was written based on [18], [14], [16], [17] and [20].

3.1 Rigid Body Modeling

First, the general floating-base model of a serial kinematics is derived and subsequently simplified to the fixed base model.

3.1.1 Floating-Base

The systems in this work incorporate serial chain kinematic structures. Other kinematic concepts such as tree structures or kinematic loops are not part of this work but may be applied under the same framework.

Kinematics

The floating-base system is assumed to consist of a serial chain kinematics with $i = 1 \dots m$ joints $\boldsymbol{q} \in \mathbb{R}^{m \times 1}$ and $j = 1 \dots n$ rigid bodies, with $\boldsymbol{q}$ denoting the generalized coordinate of the system. Its forward kinematics can be described via the transformation matrices

$$ {}^{\mathrm{b}}\boldsymbol{T}_j(\boldsymbol{q}) = {}^{\mathrm{b}}\boldsymbol{T}_1(\boldsymbol{q}) {}^{1}\boldsymbol{T}_2(\boldsymbol{q}) \dots {}^{j-1}\boldsymbol{T}_j(\boldsymbol{q}) \tag{3.1} $$

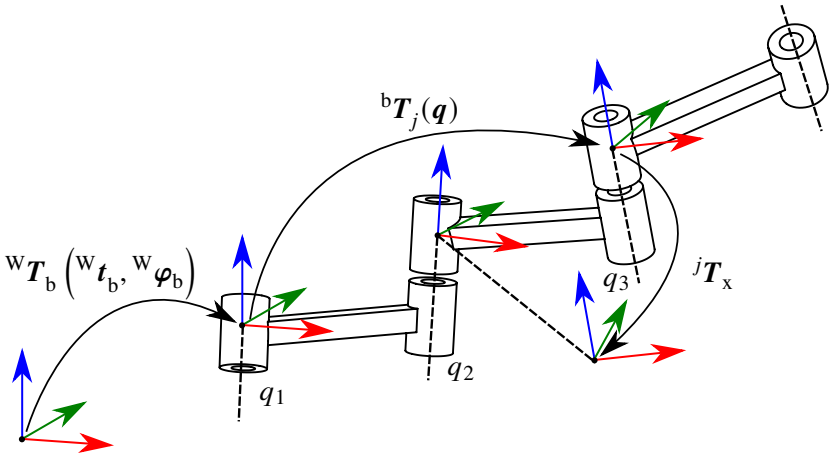

Figure 3.1 Serial floating-base kinematics structure

corresponding to the rigid body coordinate frame (j) expressed in base coordinates of frame (b), see Fig. 3.1. In this work, the serial chain kinematics is obtained by modifying Denavit-Hartenberg parameters [248] (DH). A floating-base description of kinematics (3.1) expressed in world coordinates (W) is

$$ {}^{\mathrm{W}}\boldsymbol{T}_{\mathrm{x}} = {}^{\mathrm{W}}\boldsymbol{T}_{\mathrm{b}}\,{}^{\mathrm{b}}\boldsymbol{T}_j(\boldsymbol{q})\,{}^{j}\boldsymbol{T}_{\mathrm{x}} \tag{3.2} $$

$$ {}^{\mathrm{W}}\boldsymbol{T}_{\mathrm{b}} = \begin{pmatrix} {}^{\mathrm{W}}\boldsymbol{A}_{\mathrm{b}}\left({}^{\mathrm{W}}\boldsymbol{\varphi}_{\mathrm{b}}\right) & {}^{\mathrm{W}}\boldsymbol{t}_{\mathrm{b}} \\ \boldsymbol{0} & 1 \end{pmatrix}, \tag{3.3} $$

with ${}^{\mathrm{W}}\boldsymbol{T}_{\mathrm{b}}$ being the transformation matrix of the floating-base and ${}^{j}\boldsymbol{T}_{\mathrm{x}}$ being the transformation matrix to a frame (x), which is attached to an arbitrary frame (j) along the kinematic structure (3.1). The coordinates of the floating-base

$$ {}^{\mathrm{W}}\boldsymbol{t}_{\mathrm{b}} \in \mathbb{R}^{3\times 1}, {}^{\mathrm{W}}\boldsymbol{\varphi}_{\mathrm{b}} \in \mathbb{R}^{3\times 1} \tag{3.4} $$

for translation and rotation are expressed in world coordinates (W). In this work, all orientations are expressed by the Roll Pitch Yaw convention (RPY). ${}^{\mathrm{W}}\boldsymbol{A}_{\mathrm{b}} \in \mathrm{SO}(3)$ denotes the associated rotation matrix, which is assumed to be defined for all transformation matrices ${}^{\mathrm{W}}\boldsymbol{T}_{\mathrm{b}}$. Thus, the generalized coordinate vector of the floating-base serial chain is

$$ \boldsymbol{q}_{\mathrm{c}} = \begin{pmatrix} {}^{\mathrm{W}}\boldsymbol{t}_{\mathrm{b}}{}^{T} & {}^{\mathrm{W}}\boldsymbol{\varphi}_{\mathrm{b}}^{T} & \boldsymbol{q}^{T} \end{pmatrix}^{T} \in \mathbb{R}^{(6+m)\times 1}. \tag{3.5} $$

Finally, the locations of every limb[1] is described as

$$ {}^{\mathrm{W}}\boldsymbol{T}_j\left(\boldsymbol{q}_{\mathrm{c}}\right) = \begin{pmatrix} {}^{\mathrm{W}}\boldsymbol{A}_j\left({}^{\mathrm{W}}\boldsymbol{\varphi}_j\right) & {}^{\mathrm{W}}\boldsymbol{t}_j \\ \boldsymbol{0} & 1 \end{pmatrix} \tag{3.6} $$

with ${}^{\mathrm{W}}\boldsymbol{t}_j$ being the translational position of frame j, ${}^{\mathrm{W}}\boldsymbol{A}_j$ the orientation matrix of frame j, and ${}^{\mathrm{W}}\boldsymbol{\varphi}_j$ the corresponding orientation vector.

Differential kinematics

Floating-base Jacobian matrices are required to compute an interaction between the floating body and its environment. The floating-base Jacobian $\boldsymbol{J}(\mathrm{x}, \boldsymbol{q}_{\mathrm{c}})$ of an arbitrary frame ${}^{\mathrm{W}}\boldsymbol{T}_{\mathrm{x}}$ allows for mapping external

[1] Required for the calculation of the dynamics.

generalized forces $\boldsymbol{\tau}_{\text{ext}}$ and Cartesian wrenches ${}^{\text{W}}\boldsymbol{\mathcal{F}}_{\text{ext}}$, as well as generalized velocities $\dot{\boldsymbol{q}}_{\text{c}}$ and Cartesian velocities via $\left({}^{\text{W}}\dot{\boldsymbol{t}}_{\text{x}} \quad {}^{\text{W}}\boldsymbol{\omega}_{\text{x}}\right)^T$ as

$$\boldsymbol{\tau}_{\text{ext,c}} = \boldsymbol{J}^T(\text{x}, \boldsymbol{q}_{\text{c}}) {}^{\text{W}}\boldsymbol{\mathcal{F}}_{\text{ext}}, \quad \begin{pmatrix} {}^{\text{W}}\dot{\boldsymbol{t}}_{\text{x}} \\ {}^{\text{W}}\boldsymbol{\omega}_{\text{x}} \end{pmatrix} = \boldsymbol{J}(\text{x}, \boldsymbol{q}_{\text{c}}) \dot{\boldsymbol{q}}_{\text{c}}. \tag{3.7}$$

with $\boldsymbol{\tau}_{\text{ext,c}} = \left({}^{\text{W}}\boldsymbol{F}_{\text{b,ext}}{}^T \quad {}^{\varphi}\boldsymbol{M}_{\text{b,ext}}{}^T \quad \boldsymbol{\tau}_{\text{ext}}^T\right)^T$, where ${}^{\text{W}}\boldsymbol{F}_{\text{b,ext}}$, ${}^{\varphi}\boldsymbol{M}_{\text{b,ext}}$ and $\boldsymbol{\tau}_{\text{ext}}$ are external forces and moments of the base and external joint torques. ${}^{\varphi}\boldsymbol{M}_{\text{b,ext}}$ is described in a twisted coordinate frame φ which can be transformed to world coordinates using (3.11). The translational and angular velocities ${}^{\text{W}}\dot{\boldsymbol{t}}_{\text{x}}$ and ${}^{\text{W}}\boldsymbol{\omega}_{\text{x}}$ are related to the associated transformation matrix ${}^{\text{W}}\boldsymbol{T}_{\text{x}}$. The external wrench

$${}^{\text{W}}\boldsymbol{\mathcal{F}}_{\text{ext}} = \left({}^{\text{W}}\boldsymbol{F}_{\text{ext}}{}^T \quad {}^{\text{W}}\boldsymbol{M}_{\text{ext}}{}^T\right)^T \in \mathbb{R}^{6\times 1} \tag{3.8}$$

consists of the force ${}^{\text{W}}\boldsymbol{F}_{\text{ext}} \in \mathbb{R}^{3\times 1}$ acting at ${}^{\text{W}}\boldsymbol{t}_{\text{x}}$ and the moment ${}^{\text{W}}\boldsymbol{M}_{\text{ext}} \in \mathbb{R}^{3\times 1}$.

The analytic floating-base Jacobian may be obtained by setting up translational and rotational components from (3.2) as

$$\begin{aligned} f\left(\boldsymbol{q}_c\right) &= \left({}^{\text{W}}\boldsymbol{T}_{\text{x}(1..3,4)}{}^T \quad \boldsymbol{\alpha}_{\text{RPY}}\left({}^{\text{W}}\boldsymbol{T}_{\text{x}(1..3,1..3)}\right)^T\right)^T, \\ &= \left({}^{\text{W}}\boldsymbol{t}_{\text{x}}{}^T \quad {}^{\text{W}}\boldsymbol{\varphi}_{\text{x}}^T\right)^T, \end{aligned} \tag{3.9}$$

with $\boldsymbol{\alpha}_{\text{RPY}} \in \mathbb{R}^{1\times 3}$ being an operator for obtaining RPY orientation angles [249] from a rotation matrix ${}^{\text{W}}\boldsymbol{A}_{\text{x}}$ where ${}^{\text{W}}\boldsymbol{t}_{\text{x}}{}^T$ is the translational and ${}^{\text{W}}\boldsymbol{\varphi}_{\text{x}}^T$ is the rotational component of ${}^{\text{W}}\boldsymbol{T}_{\text{x}}$. The geometric Jacobian $\boldsymbol{J}(\text{x}, \boldsymbol{q}_{\text{c}}) \in \mathbb{R}^{6\times(6+m)}$ of the chosen contact frame ${}^{\text{W}}\boldsymbol{T}_{\text{x}}$ is obtained from partial derivative as

$$\boldsymbol{J}(\text{x}, \boldsymbol{q}_{\text{c}}) = \begin{pmatrix} \boldsymbol{I}_{6\times 6} & \boldsymbol{0}_{6\times 3} \\ \boldsymbol{0}_{3\times 6} & \boldsymbol{J}_{\omega}\left(\boldsymbol{\varphi}_{\text{x}}\right) \end{pmatrix} \frac{\partial f\left(\boldsymbol{q}_{\text{c}}\right)}{\partial \boldsymbol{q}_{\text{c}}}, \tag{3.10}$$

where $\boldsymbol{J}_{\omega}(\boldsymbol{\varphi})$ denotes the twist matrix

$$\boldsymbol{J}_{\omega} = \begin{pmatrix} 1 & 0 & \sin(\varphi_2) \\ 0 & \cos(\varphi_1) & -\sin(\varphi_1)\cos(\varphi_2) \\ 0 & \sin(\varphi_1) & \cos(\varphi_1)\cos(\varphi_2) \end{pmatrix} \in \mathbb{R}^{3\times 3} \tag{3.11}$$

from [250] using the orientation angles $\boldsymbol{\varphi} = (\varphi_1, \varphi_2, \varphi_3)^T$.

Dynamics

The dynamics of the serial chain kinematics is either derived by the Lagrangian equations or via the Newton/Euler approach [251]. From the Lagrange function

$$L = T - U, \tag{3.12}$$

the kinetic energy T and potential energy U of the system are required. The former consists of the sum of rotational and translational energy of each body j as

$$T = \sum_{j=1}^{n} \frac{1}{2}\left({}^j\boldsymbol{\omega}_j{}^T {}^j\boldsymbol{I}_j {}^j\boldsymbol{\omega}_j + m_j {}^j\dot{\boldsymbol{t}}_j{}^T {}^j\dot{\boldsymbol{t}}_j + 2 {}^j\dot{\boldsymbol{t}}_j{}^T \left({}^j\boldsymbol{\omega}_j \times {}^j\boldsymbol{s}_j\right)\right). \tag{3.13}$$

It contains the angular velocity ${}^{j}\boldsymbol{\omega}_j$ and translational velocity ${}^{j}\dot{\boldsymbol{t}}_j$ of body j described in the coordinates of frame j. Additionally, it contains the limb mass m_j and the inertia tensor ${}^{j}\boldsymbol{I}_j$ of body j described in the coordinates of j with respect to the origin of frame j. The inertia tensor can be further described as

$$ {}^{j}\boldsymbol{I}_j = \begin{pmatrix} XX_j & XY_j & XZ_j \\ XY_j & YY_j & YZ_j \\ XZ_j & YZ_j & ZZ_j \end{pmatrix}, \tag{3.14} $$

with XX_j, YY_j and ZZ_j being the inertia parameters around the main axes, and XY_j, XZ_j and YZ_j the deviation moments. The reference frame for the kinetic energy may be described in any coordinate system of use. In order to formulate (3.14) with constant entries it is beneficial to describe the kinetic energy in a body frame. In general, it is common to describe the kinetic energy with respect to the center of mass, simplifying (3.13). In this work, the kinetic energy is described with respect to frame j according to MDH-parameters [251]. With this, the robot model can be described in linear coordinates, which is very useful for robot identification. As a consequence, the mass and the center of mass cannot be independently obtained. This fact is expressed by the first moment

$$ {}^{j}\boldsymbol{s}_j = (mX, mY, mZ)^T = m_j {}^{j}\boldsymbol{r}_{j,\mathrm{C}_j}, \tag{3.15} $$

of body j in coordinates of j. The related parameters mX, mY and mZ denote the first moment in x, y and z direction, respectively. Consequently, all mechanical parameters for a single rigid body j are

$$ \left\{ XX_j, YY_j, ZZ_j, XY_j, XZ_j, YZ_j, mX_j, mY_j, mZ_j, m_j \right\}. \tag{3.16} $$

The linear and rotational velocities can be described as

$$ {}^{j}\dot{\boldsymbol{t}}_j = {}^{j}\boldsymbol{A}_{\mathrm{W}} {}^{\mathrm{W}}\dot{\boldsymbol{t}}_j, \quad {}^{j}\boldsymbol{\omega}_j = {}^{j}\boldsymbol{A}_{\mathrm{W}} {}^{\mathrm{W}}\boldsymbol{\omega}_j \text{ with } \begin{pmatrix} {}^{\mathrm{W}}\dot{\boldsymbol{t}}_j & {}^{\mathrm{W}}\boldsymbol{\omega}_j \end{pmatrix}^T = \boldsymbol{J}(j, \boldsymbol{q}_\mathrm{c}) \dot{\boldsymbol{q}}_\mathrm{c}, \tag{3.17} $$

where $\boldsymbol{J}(j, \boldsymbol{q}_\mathrm{c})$ is the Jacobians related to frame ${}^{\mathrm{W}}\boldsymbol{T}_j$.

The potential energy of the system is then

$$ U = -\sum_{j=1}^{n} \left({}^{\mathrm{W}}\boldsymbol{g}^T \left(m_j {}^{\mathrm{W}}\boldsymbol{t}_j + {}^{\mathrm{W}}\boldsymbol{A}_j {}^{j}\boldsymbol{s}_j \right) \right), \tag{3.18} $$

where ${}^{\mathrm{W}}\boldsymbol{g}$ is the direction of the gravity vector.

Finally, (3.1)-(3.18) are used for calculating the Lagrange equation [249]

$$ \frac{\mathrm{d}}{\mathrm{d}t} \left(\frac{\partial L}{\partial \dot{\boldsymbol{q}}_\mathrm{c}} \right) - \frac{\partial L}{\partial \boldsymbol{q}_\mathrm{c}} = \boldsymbol{\tau}_\mathrm{c}, \tag{3.19} $$

which can be further developed into the floating-base robot dynamics form

$$ \boldsymbol{M}(\boldsymbol{q}_\mathrm{c}) \ddot{\boldsymbol{q}}_\mathrm{c} + \boldsymbol{C}(\boldsymbol{q}_\mathrm{c}, \dot{\boldsymbol{q}}_\mathrm{c}) \dot{\boldsymbol{q}}_\mathrm{c} + \boldsymbol{g}(\boldsymbol{q}_\mathrm{c}) = \boldsymbol{\tau}_\mathrm{c} + \boldsymbol{\tau}_{\mathrm{ext,c}} \tag{3.20} $$

with $\boldsymbol{M}(\boldsymbol{q}_\mathrm{c}) \in \mathbb{R}^{(6+m)\times(6+m)}$ being the mass matrix, $\boldsymbol{C}(\boldsymbol{q}_\mathrm{c}, \dot{\boldsymbol{q}}_\mathrm{c}) \in \mathbb{R}^{(6+m)\times(6+m)}$ the Coriolis matrix, $\boldsymbol{g}(\boldsymbol{q}_\mathrm{c}) \in \mathbb{R}^{(6+m)\times 1}$ the vector of gravitational influences and $\boldsymbol{\tau}_{\mathrm{ext,c}} \in \mathbb{R}^{(6+m)\times 1}$ the vector of external generalized forces. The generalized joint forces are expressed as $\boldsymbol{\tau}_\mathrm{c} = \begin{pmatrix} {}^{\mathrm{W}}\boldsymbol{F}_\mathrm{b}{}^T & {}^{\varphi}\boldsymbol{M}_\mathrm{b}{}^T & \boldsymbol{\tau}^T \end{pmatrix}$ with ${}^{\mathrm{W}}\boldsymbol{F}_\mathrm{b} \in \mathbb{R}^{3\times 1}$ and ${}^{\varphi}\boldsymbol{M}_\mathrm{b} \in \mathbb{R}^{3\times 1}$ being the forces and moments of the base, and $\boldsymbol{\tau} \in \mathbb{R}^{m\times 1}$ being the joint torques. ${}^{\mathrm{W}}\boldsymbol{F}_\mathrm{b}$ and

${}^{\varphi}\boldsymbol{M}_{\mathrm{b}}$ are zero as the base is not actuated. The matrices from (3.20) can be further subdivided into block matrices

$$\boldsymbol{M}(\boldsymbol{q}_{\mathrm{c}}) = \begin{pmatrix} \boldsymbol{M}_{\mathrm{b,b}}(\boldsymbol{q}_{\mathrm{c}}) & \boldsymbol{M}_{\mathrm{b,j}}(\boldsymbol{q}_{\mathrm{c}}) \\ \boldsymbol{M}_{\mathrm{j,b}}(\boldsymbol{q}_{\mathrm{c}}) & \boldsymbol{M}_{\mathrm{j,j}}(\boldsymbol{q}_{\mathrm{c}}) \end{pmatrix}, \tag{3.21}$$
$$\boldsymbol{C}(\boldsymbol{q}_{\mathrm{c}}, \dot{\boldsymbol{q}}_{\mathrm{c}}) = \begin{pmatrix} \boldsymbol{C}_{\mathrm{b}}(\boldsymbol{q}_{\mathrm{c}}, \dot{\boldsymbol{q}}_{\mathrm{c}}) \\ \boldsymbol{C}_{\mathrm{j}}(\boldsymbol{q}_{\mathrm{c}}, \dot{\boldsymbol{q}}_{\mathrm{c}}) \end{pmatrix}, \boldsymbol{g}(\boldsymbol{q}_{\mathrm{c}}) = \begin{pmatrix} \boldsymbol{g}_{\mathrm{b}}(\boldsymbol{q}_{\mathrm{c}}) \\ \boldsymbol{g}_{\mathrm{j}}(\boldsymbol{q}_{\mathrm{c}}) \end{pmatrix},$$

where subscripts b and j denote base or joint influence, respectively.

Base Orientation

The forward dynamics of the system for plant simulation is obtained by numerically integrating $\ddot{\boldsymbol{q}}$, $\ddot{\boldsymbol{t}}_{\mathrm{b}}$ and $\ddot{\boldsymbol{\varphi}}_{\mathrm{b}}$ over time. While the rotational velocity

$${}^{\mathrm{W}}\dot{\boldsymbol{\varphi}}_{\mathrm{b}} = \int_0^{\tau_{\mathrm{c}}} {}^{\mathrm{W}}\ddot{\boldsymbol{\varphi}}_{\mathrm{b}} \mathrm{dt} \tag{3.22}$$

can be obtained easily by numerical integration, the orientation of the robot base is computed by numerically solving[2] the well known differential equation [252]

$${}^{\mathrm{W}}\dot{\boldsymbol{A}}_{\mathrm{b}} = \begin{pmatrix} 0 & -\omega_{\mathrm{b,z}} & \omega_{\mathrm{b,y}} \\ \omega_{\mathrm{b,z}} & 0 & -\omega_{\mathrm{b,x}} \\ -\omega_{\mathrm{b,y}} & \omega_{\mathrm{b,x}} & 0 \end{pmatrix} {}^{\mathrm{W}}\boldsymbol{A}_{\mathrm{b}}, \tag{3.23}$$

with

$${}^{\mathrm{W}}\boldsymbol{A}_{\mathrm{b}}(t) = \int_0^{\tau_{\mathrm{c}}} {}^{\mathrm{W}}\dot{\boldsymbol{A}}_{\mathrm{b}}(t) \mathrm{dt}. \tag{3.24}$$

The angular velocity ${}^{\mathrm{W}}\boldsymbol{\omega}_{\mathrm{b}}$ in (3.23) may then be obtained by

$$\begin{pmatrix} {}^{\mathrm{W}}\dot{\boldsymbol{t}}_{\mathrm{b}} \\ {}^{\mathrm{W}}\boldsymbol{\omega}_{\mathrm{b}} \end{pmatrix} = \boldsymbol{J}(\mathrm{b}, \boldsymbol{q}_{\mathrm{c}}^{*}) \boldsymbol{q}_{\mathrm{c}}^{*}, \text{ with } \boldsymbol{q}_{\mathrm{c}}^{*} = \begin{pmatrix} {}^{\mathrm{W}}\dot{\boldsymbol{t}}_{\mathrm{b}}^{T} & {}^{\mathrm{W}}\dot{\boldsymbol{\varphi}}_{\mathrm{b}}^{T} & \boldsymbol{0} \end{pmatrix}^{T}, \tag{3.25}$$

with $\boldsymbol{J}(\mathrm{b}, \boldsymbol{q}_{\mathrm{c}})$ being the floating-base Jacobian of the base frame ${}^{\mathrm{W}}\boldsymbol{T}_{\mathrm{b}}$.

3.1.2 Fixed-Base

The fixed-base model is considered as a special case of the floating-base model and is derived as shown below. For the fixed-base model, ${}^{\mathrm{W}}\boldsymbol{t}_{\mathrm{b}}$ and ${}^{\mathrm{W}}\boldsymbol{\varphi}_{\mathrm{b}}$ are constant and thus removed from the generalized coordinates

$$\boldsymbol{q}_{\mathrm{c}} = \begin{pmatrix} {}^{\mathrm{W}}\cancel{\boldsymbol{t}_{\mathrm{b}}^{T}} & {}^{\mathrm{W}}\cancel{\boldsymbol{\varphi}_{\mathrm{b}}^{T}} & \boldsymbol{q}^{T} \end{pmatrix}^{T} \tag{3.26}$$
$$\Rightarrow \boldsymbol{q}_{\mathrm{c}} \hat{=} \boldsymbol{q} \tag{3.27}$$

For simplicity, the base frame is chosen to be

$${}^{\mathrm{W}}\boldsymbol{T}_{\mathrm{b}} = \begin{pmatrix} 1 & 0 & 0 & 0 \\ 0 & 1 & 0 & 0 \\ 0 & 0 & 1 & 0 \\ 0 & 0 & 0 & 1 \end{pmatrix}, \tag{3.28}$$

[2] This equation has to be applied as ${}^{\mathrm{W}}\boldsymbol{\varphi}_{\mathrm{b}} \neq \int_0^{\tau_{\mathrm{c}}} {}^{\mathrm{W}}\dot{\boldsymbol{\varphi}}_{\mathrm{b}} \mathrm{dt}$.

leading to the following kinematics model

$$
\begin{aligned}
{}^{\mathrm{W}}\boldsymbol{T}_{\mathrm{x}} &= {}^{\mathrm{W}}\boldsymbol{T}_{\mathrm{b}}\,{}^{\mathrm{b}}\boldsymbol{T}_{j}(\boldsymbol{q})\,{}^{j}\boldsymbol{T}_{\mathrm{x}} && (3.29)\\
&= {}^{\mathrm{W}}\boldsymbol{T}_{j}(\boldsymbol{q})\,{}^{j}\boldsymbol{T}_{\mathrm{x}}. && (3.30)
\end{aligned}
$$

After applying (3.30) on (3.1)-(3.19), the robot dynamics for a fixed-base equates to

$$
\boldsymbol{M}(\boldsymbol{q})\ddot{\boldsymbol{q}} + \boldsymbol{C}(\boldsymbol{q},\dot{\boldsymbol{q}})\dot{\boldsymbol{q}} + \boldsymbol{g}(\boldsymbol{q}) = \boldsymbol{\tau} + \boldsymbol{\tau}_{\mathrm{ext}}, \tag{3.31}
$$

with $\boldsymbol{M}(\boldsymbol{q}) \in \mathbb{R}^{m\times m}$ being the mass matrix, $\boldsymbol{C}(\boldsymbol{q},\dot{\boldsymbol{q}}) \in \mathbb{R}^{m\times m}$ the Coriolis matrix, $\boldsymbol{g}(\boldsymbol{q}) \in \mathbb{R}^{m\times 1}$ the vector of gravitational influences and $\boldsymbol{\tau}_{\mathrm{ext}} \in \mathbb{R}^{m\times 1}$ the vector of external generalized forces.

3.2 Soft Robotics and Tactile Control

The following section introduces state-of-the-art control concepts for robotic systems. In particular, three main components are considered, namely i) rigid body model compensation, ii) joint impedance control and iii) the momentum observer for disturbance monitoring.

3.2.1 Rigid Body Compensation

In this work, the rigid body model-based compensation structure

$$
\boldsymbol{\tau}_{\mathrm{ff}} = \hat{\boldsymbol{C}}(\boldsymbol{q},\dot{\boldsymbol{q}})\dot{\boldsymbol{q}} + \hat{\boldsymbol{g}}(\boldsymbol{q}) \tag{3.32}
$$

is mainly used. It contains the estimated Coriolis torques $\hat{\boldsymbol{C}}(\boldsymbol{q},\dot{\boldsymbol{q}}) = \boldsymbol{C}(\boldsymbol{q},\dot{\boldsymbol{q}})$ and the estimated gravity vector $\hat{\boldsymbol{g}}(\boldsymbol{q}) = \boldsymbol{g}(\boldsymbol{q})$. A compensation of inertia effects [253] is not considered in this work. The closed-loop behavior for a fixed-base model is obtained by inserting (3.32) in (3.31), neglecting quantization discretization and friction, and assuming the agreement of measured and actual joint angles as well as ideal torque control $\boldsymbol{\tau}_{\mathrm{ff}} = \boldsymbol{\tau}$. This leads to

$$
\boldsymbol{M}(\boldsymbol{q})\ddot{\boldsymbol{q}} = \boldsymbol{\tau}_{\mathrm{ext}}. \tag{3.33}
$$

This means that the system does not accelerate to the extent that no external torques $\boldsymbol{\tau}_{\mathrm{ext}}$ act on the system.

The same approach can be performed for a floating-base system (3.20) by applying floating-base model compensation

$$
\boldsymbol{\tau}_{\mathrm{ff}} = \hat{\boldsymbol{C}}_{\mathrm{j}}(\boldsymbol{q}_{\mathrm{c}},\dot{\boldsymbol{q}}_{\mathrm{c}})\dot{\boldsymbol{q}}_{\mathrm{c}} + \hat{\boldsymbol{g}}_{\mathrm{j}}(\boldsymbol{q}_{\mathrm{c}}) \tag{3.34}
$$

with the estimated Coriolis matrix $\hat{\boldsymbol{C}}_{\mathrm{j}}(\boldsymbol{q}_{\mathrm{c}},\dot{\boldsymbol{q}}_{\mathrm{c}})$ and the estimated gravity vector $\hat{\boldsymbol{g}}_{\mathrm{j}}(\boldsymbol{q}_{\mathrm{c}})$. In contrast to (3.32), Coriolis and gravity vector are taken from the submatrices (3.22). These were derived from the generalized coordinate $\boldsymbol{q}_{\mathrm{c}}$, see (3.5). Consequently, base orientation ${}^{\mathrm{W}}\boldsymbol{\varphi}_{\mathrm{b}}$ and translation ${}^{\mathrm{W}}\boldsymbol{t}_{\mathrm{b}}$ are also considered within the model as shown below

$$
\begin{pmatrix} \boldsymbol{M}_{\mathrm{b,b}}(\boldsymbol{q}_{\mathrm{c}}) & \boldsymbol{M}_{\mathrm{b,j}}(\boldsymbol{q}_{\mathrm{c}}) \\ \boldsymbol{M}_{\mathrm{j,b}}(\boldsymbol{q}_{\mathrm{c}}) & \boldsymbol{M}_{\mathrm{j,j}}(\boldsymbol{q}_{\mathrm{c}}) \end{pmatrix} \begin{pmatrix} {}^{\mathrm{W}}\ddot{\boldsymbol{t}}_{\mathrm{b}} \\ {}^{\mathrm{W}}\ddot{\boldsymbol{\varphi}}_{\mathrm{b}} \\ \ddot{\boldsymbol{q}} \end{pmatrix} + \begin{pmatrix} \boldsymbol{C}_{\mathrm{b}}(\boldsymbol{q}_{\mathrm{c}},\dot{\boldsymbol{q}}_{\mathrm{c}}) \\ \boldsymbol{0} \end{pmatrix} \dot{\boldsymbol{q}}_{\mathrm{c}} + \begin{pmatrix} \boldsymbol{g}_{\mathrm{b}}(\boldsymbol{q}_{\mathrm{c}}) \\ \boldsymbol{0} \end{pmatrix} = \boldsymbol{\tau}_{\mathrm{ext,c}}. \tag{3.35}
$$

The last row of (3.35) shows that Coriolis and gravity influences are compensated for $\boldsymbol{q}$. However, an acceleration of the base translation or orientation leads to joint acceleration. Based on the aforementioned concept, the acceleration of the base on the joints may be compensated by

$$
\boldsymbol{\tau}_{\mathrm{d}} = \hat{\boldsymbol{M}}_{\mathrm{j,b}}(\boldsymbol{q}_{\mathrm{c}}) \begin{pmatrix} {}^{\mathrm{W}}\ddot{\boldsymbol{t}}_{\mathrm{b}} \\ {}^{\mathrm{W}}\ddot{\boldsymbol{\varphi}}_{\mathrm{b}} \end{pmatrix}, \tag{3.36}
$$

however, requiring practically non accessible measurements of ${}^{\mathrm{W}}\ddot{\boldsymbol{t}}_{\mathrm{b}}$ and ${}^{\mathrm{W}}\ddot{\boldsymbol{\varphi}}_{\mathrm{b}}$. After applying the model compensations, the robotic systems essentially act with zero gravity, as in space. That is why this mode is also called zero-g control. On top of this basic control mode, an impedance controller is constructed for motion and compliance control.

3.2.2 Joint Impedance Control

The assumed controller is a joint level impedance controller

$$\boldsymbol{\tau}_{\mathrm{d}} = \boldsymbol{K}_{\mathrm{imp}}(\boldsymbol{q} - \boldsymbol{q}_{\mathrm{d}}) + \boldsymbol{D}_{\mathrm{imp}}(\dot{\boldsymbol{q}} - \dot{\boldsymbol{q}}_{\mathrm{d}}) + \boldsymbol{\tau}_{\mathrm{ff}} \tag{3.37}$$

with $\boldsymbol{K}_{\mathrm{imp}} \in \mathbb{R}^{m\times m}$ and $\boldsymbol{D}_{\mathrm{imp}} \in \mathbb{R}^{m\times m}$ being the desired stiffness and damping matrices and $\boldsymbol{q}_{\mathrm{d}}$ the desired joint angles. A diagonal damping approach [254] is applied for damping design

$$\boldsymbol{D}_{\mathrm{imp}} = \sqrt{\hat{\boldsymbol{M}}(\boldsymbol{q})\boldsymbol{D}_{\Psi}}\sqrt{\boldsymbol{K}_{\mathrm{imp}}} + \sqrt{\boldsymbol{K}_{\mathrm{imp}}(\boldsymbol{q})\boldsymbol{D}_{\Psi}}\sqrt{\hat{\boldsymbol{M}}(\boldsymbol{q})}. \tag{3.38}$$

It serves as the decoupling of the generalized coordinates and adjustment of the actual damping along a unified damping matrix $\boldsymbol{D}_{\Psi}$.

The closed-loop behavior of the overall system is

$$\boldsymbol{M}(\boldsymbol{q})\ddot{\boldsymbol{q}} + \boldsymbol{D}_{\mathrm{imp}}\dot{\boldsymbol{q}} + \boldsymbol{K}_{\mathrm{imp}}\boldsymbol{q} = \boldsymbol{\tau}_{\mathrm{ext}} + \boldsymbol{K}_{\mathrm{imp}}\boldsymbol{q}_{\mathrm{d}} + \boldsymbol{D}_{\mathrm{imp}}\dot{\boldsymbol{q}}_{\mathrm{d}}, \tag{3.39}$$

i.e., a mass-spring-damper behavior with adjustable active compliance and damping.

3.2.3 Momentum Observer

The generalized momentum observer from [255] is used for estimating external joint torques. Here, the observer is adapted to utilize the floating base model components as [256]

$$\hat{\boldsymbol{\tau}}_{\mathrm{ext}} = K_{\mathrm{O}}\left(\int_0^T \left(\boldsymbol{\tau} - \boldsymbol{\beta}(\boldsymbol{q}_{\mathrm{c}}, \dot{\boldsymbol{q}}_{\mathrm{c}}) - \hat{\boldsymbol{\tau}}_{\mathrm{ext}}\right)\mathrm{d}t - \hat{\boldsymbol{M}}_{\mathrm{j,j}}(\boldsymbol{q}_{\mathrm{c}})\dot{\boldsymbol{q}}\right), \tag{3.40}$$

with

$$\boldsymbol{\beta}(\boldsymbol{q}_{\mathrm{c}}, \dot{\boldsymbol{q}}_{\mathrm{c}}) = \hat{\boldsymbol{C}}_{\mathrm{j}}(\boldsymbol{q}_{\mathrm{c}}, \dot{\boldsymbol{q}}_{\mathrm{c}}) + \hat{\boldsymbol{g}}_{\mathrm{j}}(\boldsymbol{q}_{\mathrm{c}}) - \dot{\hat{\boldsymbol{M}}}_{\mathrm{j,j}}(\boldsymbol{q}_{\mathrm{c}})\dot{\boldsymbol{q}}. \tag{3.41}$$

A fixed-base formulation with a similar notation may be found in [257].

3.3 Actuator Abstraction Layer

In this section, the developed *Actuator Abstraction Layer (AAL)* is described. After introducing the concept, modeling and force control for the used actuation technologies, including the fundamentals of pneumatic and electromechanical actuation, are reviewed.

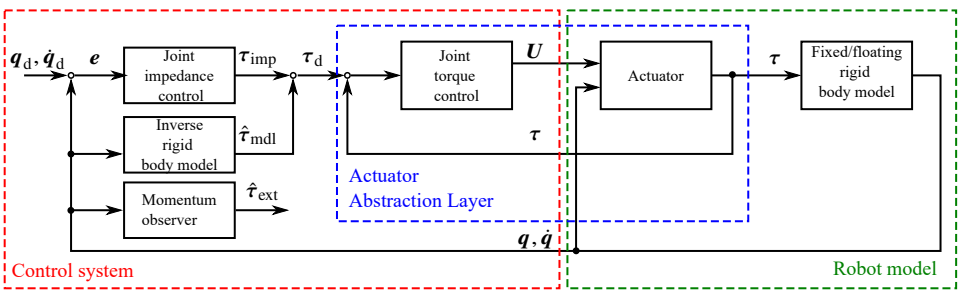

Figure 3.2 Control scheme with the actuator abstraction layer

3.3.1 Concept

In this work, the actuators of a robot are considered to be an ideal torque source. A torque source means that the actuator delivers any torque $\boldsymbol{\tau}$, which is commanded via a desired torque $\boldsymbol{\tau}_\mathrm{d}$. This concept has been utilized for pneumatic [14], hydraulic [258] and electromechanical robots [21].

Here, the combination of torque controller and actuator is integrated and interfaced by the *Actuator Abstraction Layer (AAL)*, see Fig. 3.2, encapsulating the actual functionality and mechatronic technology of the underlying actuator. With this concept, the control scheme from Fig. 3.2 is compatible and conceptually modular to various actuation technologies such as electromechanical, pneumatic or hydraulic actuation.

Generally, it is assumed from the design point of view that the inherent dynamic behavior of the actuator is eliminated to the greatest extent by the underlying torque controller. However, fundamental characteristics of the actuator such as inherent compliance, backdrivability, friction and stiction are generally not be fully compensated by the control due to limited bandwidth and limited controller accuracy.

Finally, the concept of the force and torque source are shown graphically in the simulation results under Fig. 3.4. The left side of the figure shows the simulation of a direct drive torque-controlled electromechanical actuator. The right side of the figure shows a pneumatic force controlled actuator. Torque steps of 1 Nm and a force of 10 N are desired by the controller. It can be seen that both forces and torques are regulated correctly, despite the position change in row two and the disturbances in row three. Furthermore, real world effects such as a different rise-time and different reactions on external forces and torques can be observed, respectively.

The following section describes electromechanical and pneumatic actuation.

3.3.2 Electromechanical Actuation

The electromechanically driven systems used in this work are controlled by a cascaded controller structure of current and torque control using BLDCs. The modeling and control of BLDCs is complex, contains many nonlinearities, and requires high sampling frequencies. In general, the control of BLDCs is a well understood problem for reliable and mature technology. In order to explain the torque source concept for electromechanical systems, a simple torque controlled electromechanical direct current motor (DC motor) is analyzed below.

Modeling

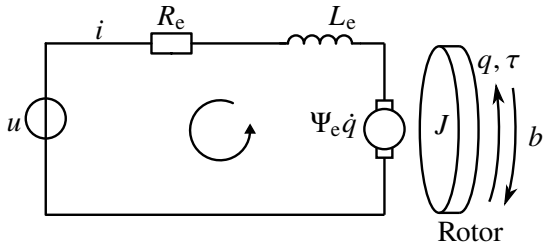

Figure 3.3 Electrical scheme of a DC motor excited by a permanent magnet

The scheme of the DC motor circuit is depicted in Fig. 3.3. The electrical function can be understood by applying Kirchhoff's law to the mesh circuit, resulting in

$$L_\mathrm{e}\dot{i} + R_\mathrm{e} i = u - w, \tag{3.42}$$

where u denotes the input voltage, i the current, R_e the resistance and L_e. A back-EMF acts on the circuit

$$w = \Psi_\mathrm{e}\dot{q}, \tag{3.43}$$

where Ψ_e is the flux and where q the motor angle, counteracting the motion. The rotor of the DC motor can be described by the differential equation

$$I\ddot{q} + b\dot{q} = \tau + \tau_{\text{ext}}, \tag{3.44}$$

where J is the rotor inertia, b the viscous damping and τ_{ext} an external torque. The torque generated by the motor τ can be further described by

$$\tau = c_{\text{T}} i, \tag{3.45}$$

with c_{T} being the torque constant.

Torque Control

In this basic illustrative example, torque control of the actuator is performed by current control, given that the relation between current and torque is known from (3.45). For this, the control error is defined as

$$e = i_{\text{d}} - i = \frac{\tau_{\text{d}}}{c_{\text{T}}} - i. \tag{3.46}$$

A Proportional-Integral (PI) controller may be used to control the current as

$$u = K_{\text{P}} e + K_{\text{I}} \int_0^\infty e \, \mathrm{d}t. \tag{3.47}$$

The resulting behavior is depicted in Fig. 3.4 (left). It can be seen that the controlled system delivers the demanded torque robust to actuation position changes and external disturbances.

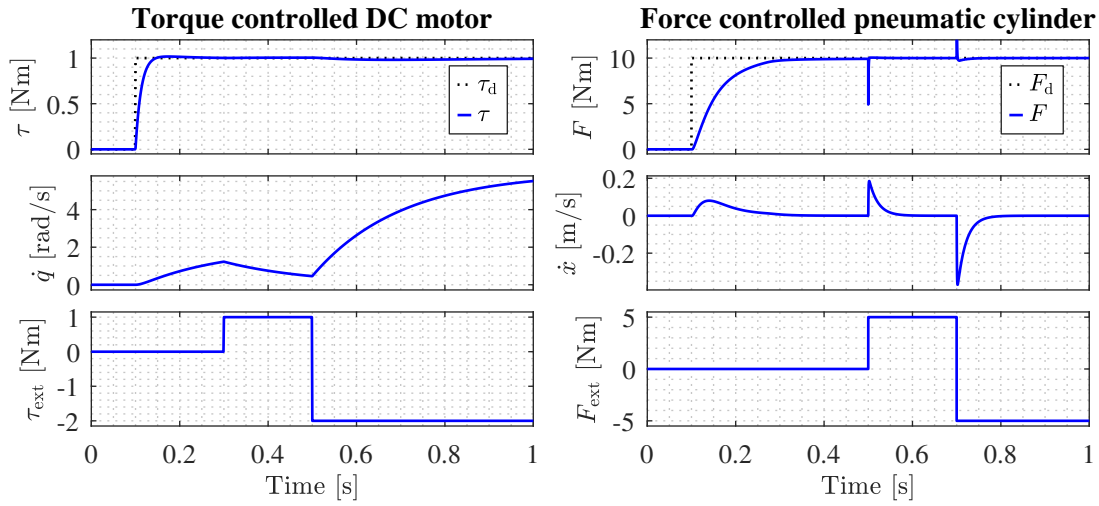

Figure 3.4 Simulation of torque controlled DC motor and force controlled pneumatic actuator serving as force or torque source, respectively. The pneumatic cylinder is equipped with a spring damper system as load.

The following section outlines the basic modeling and control dynamics of the utilized pneumatic systems.

3.3.3 Pneumatic Actuation

Modeling

In this work, linear and rotary pneumatic cylinders actuated by a proportional 5/3 valve[3] are considered, see Fig. 3.5. In the linear cylinder, a piston moves in direction x, driven by the pressure difference between P_1

[3]The number 5 stands for the number of ports and 3 represents the number of possible states of the valve.

and P_2 of the surrounding chambers. In a rotary cylinder, a vane separates the two chambers, enabling a rotary motion around q by a pressure difference in the chambers. Both drives are equipped with pressure sensors for each chamber, respectively. A proportional 5/3 valve couples the inflow and outflow of air from the supply pressure to the chambers or from the chambers to ambiance. The proportional valves enable a quasi-linear shift of the spool position x_s.

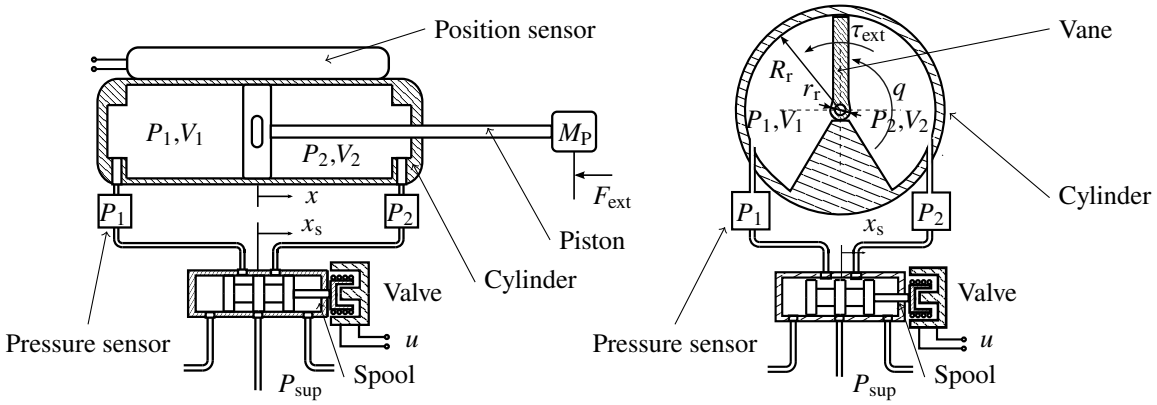

Figure 3.5 Technical drawings of linear and rotary pneumatic cylinders

A model of a double actuated pneumatic cylinder in combination with a proportional 5/3 valve was introduced in [81]. The pressure dynamics of a pneumatic chamber is given by

$$\dot{P} = \frac{R\sqrt{T_{\text{atm}}}}{V} \overbrace{(\alpha_{\text{in}}\dot{m}_{\text{in}} - \alpha_{\text{ex}}\dot{m}_{\text{out}})}^{\dot{m}_{\text{v}}} - \alpha_{\text{mt}}\frac{P}{V}\dot{V}, \tag{3.48}$$

with P being the chamber pressure, V the chamber volume depending on the piston position x, T_{atm} being a constant ambiance temperature, R being the specific gas constant of air and $\dot{m}_{\text{in}}$ and $\dot{m}_{\text{out}}$ being in and out flowing masses. α_{in}, α_{ex}, α_{mt} are dimensionless attenuation factors close to 1, affecting the pressure evolution of charging, discharging and cylinder motion.

The mass flow from and to the valve is $\dot{m}_{\text{v}i}$ (which includes inflowing and outflowing mass $\dot{m}_{\text{in}}$ and $\dot{m}_{\text{out}}$), and is further modeled by

$$\dot{m}_X = c_{\text{f}} A_{\text{m},X} P_{\text{u}} \Psi(P_{\text{d}}/P_{\text{u}}), \tag{3.49}$$

with c_{f} being a discharge coefficient of the valve and X a placeholder for $X = \{\text{in}, \text{out}\}$. $\Psi(P_{\text{d}}/P_{\text{u}})$ is the flow function

$$\Psi(P_{\text{d}}/P_{\text{u}}) = \begin{cases} \sqrt{\frac{2\gamma}{RT_{\text{u}}(\gamma-1)}\left[\left(\frac{P_{\text{d}}}{P_{\text{u}}}\right)^{\frac{2}{\gamma}} - \left(\frac{P_{\text{d}}}{P_{\text{u}}}\right)^{\frac{\gamma+1}{\gamma}}\right]} & \frac{P_{\text{d}}}{P_{\text{u}}} \geq P_{\text{krit}} \\ \sqrt{\frac{\gamma}{RT_{\text{u}}}\frac{2}{\gamma+1}^{\frac{\gamma+1}{\gamma-1}}} & \frac{P_{\text{d}}}{P_{\text{u}}} < P_{\text{krit}}, \end{cases} \tag{3.50}$$

with γ being the heat capacity ratio of air. $P_{\text{krit}} = 2/(\gamma+1)^{\gamma/(\gamma-1)}$ denotes the critical pressure. P_{d}, P_{u} and T_{u} are downstream and upstream pressures as well as the upstream temperature. P_{u}, T_{u} and P_{d} are assigned by case distinction depending on the pressures P_1, P_2, atmospheric pressure P_{atm} and supply pressure P_{sup} for each pressure potential, respectively.

For the considered system, a coupling between inflow and outflow of the neighboring chambers exists due to the use of a 5/3 valve. For instance, when chamber 1 is connected to supply pressure, chamber 2 is connected to ambiance and vice versa. This is expressed by the following substitution

$$A_{\text{v}1} := A_{\text{m,in}1} = A_{\text{m,out}2},\ A_{\text{v}2} := A_{\text{m,out}1} = A_{\text{m,in}2} \tag{3.51}$$

Table 3.1 Linear and rotary pneumatic cylinder models

	Linear cylinder	Rotary cylinder
Coordinate	x	q
Volume	$V_i = V_{0i} + (A_i L/2 \pm A_i x)$	$A_{\text{eq}} = \frac{b}{2}\left(r_{\text{ro}}^2 - r_{\text{ri}}^2\right)$ $V_i = V_{0i} \pm A_{\text{eq}}(q - q_0)$
Force/torque	$F = P_1 A_1 - P_2 A_2 - P_{\text{atm}} A_{\text{r}}$	$\tau = A_{\text{eq}}\,(P_2 - P_1)$

in (3.49) for chamber 1 and 2 and in- and outflow. The choke area function of the valve $A_{\text{v}i}$, depicted in Fig. 3.6, may be calculated by a geometric approach [81] or approximated by a suitable modeling function. In this work, piecewise linear splines are used[4] (indicated by the gray vertical lines in Fig. 3.6).

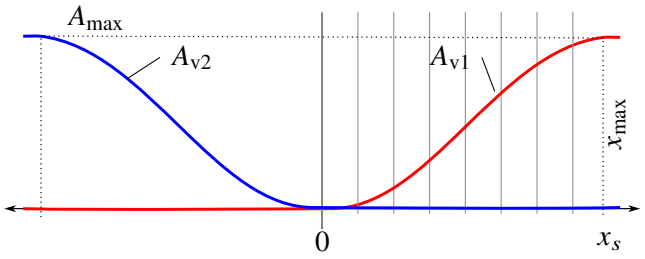

Figure 3.6 Qualitative shape of valve orifice function $A_{\text{v}i}$

Between spool position x_{s} and input voltage u, the following 1st order dynamics with time constant τ and gain c_{vv} is considered.

$$\tau \dot{x}_s + x_s = c_{\text{vv}} u. \tag{3.52}$$

Both linear and rotary cylinders can be modeled by (3.48) to (3.52), see Tab. 3.1. The motion of the linear cylinder is described in the coordinate x, while the rotary cylinder is described by the angle q, see Fig. 3.5. The volume of the linear cylinder is calculated based on the facing surfaces A_1 and A_2, the maximum stroke length L and the motion x. It yields $A_2 = A_1 - A_r$ with A_r being the area of rod entering chamber 2. The volume of the rotary cylinder is based on the cylinder width b, the maximum radius r_{ro} and the minimum radius r_{ri} of a chamber. Both rotary and liner cylinder models contain a dead volume V_{0i}, which is independent from the stroke. The force, which is generated by the linear actuator is F, while the torque generated by the rotary cylinder is τ. The parameter A_{eq} is a geometric constant. q_0 is used to shift the zero position of the rotary cylinder. The derivation of the kinematics of the rotary cylinder can be found in the Appendix A.1.2 .

Force and Torque Control

The pneumatic force and torque controllers in this work are based on a nonlinear sliding mode force controller for pneumatic cylinders with a 5/3 proportional valve from [81]. The torque controller for rotary cylinders was derived along the linear case. A first order sliding mode controller requires the definition of a so-called sliding surface $s(t)$, which is essentially the control error for the first-order controller as it can be seen in the first row of Tab. 3.2. Furthermore, the derivative of $s(t)$ is required, containing $\dot{P}_1$ and $\dot{P}_2$. $\dot{P}_1$ and $\dot{P}_2$ are substituted with the chamber models (3.48). Next, this equation needs to be solved for the system input. Given that there are two inputs A_{v1} and A_{v2}, which cannot both be present at the same time, a case distinction for $s(t) < 0$ and $s(t) > 0$ is made by either including A_{v1} or A_{v2}. These equations contain the flow-functions Ψ_{P2Pa}, Ψ_{PsP1}, Ψ_{P1Pa} and Ψ_{PsP2} using (3.50) and represent the mass flows between P_2 and P_{atm}, P_{sup} and P_1,

[4] This approach is chosen as high accuracy can be obtained by choosing many intervals and the inverse functions can be calculated easily for nonlinear control due to its piece wise linearity. Identification results from [14] were used.

Table 3.2 Force and torque control of linear and rotary cylinders using a sliding mode controller from [81].

	Linear cylinder	Rotary cylinder
Control error	$s(t) = \tilde{F} = F - F_\mathrm{d}$	$s(t) = \tilde{\tau} = \tau - \tau_\mathrm{d}$
Approach	$\dot{s}(t) = \dot{\tilde{F}} = \dot{P}_1 A_1 - \dot{P}_2 A_2 - \dot{F}_\mathrm{d}$	$\dot{s}(t) = \dot{\tilde{\tau}} = A_\mathrm{eq}\left(\dot{P}_2 - \dot{P}_1\right) - \dot{\tau}_\mathrm{d}$
Control law $s(t) < 0$	$A_\mathrm{m,eq} \widehat{=} A_\mathrm{v1} = \ldots$ $+(\dot{F}_\mathrm{d} + A_1(+(\dot{V}_1 P_1 \alpha_\mathrm{mt})/V_1)$ $-A_2(-(\dot{V}_2 P_2 \alpha_\mathrm{mt})/V_2))/((A_2 c_\mathrm{pn} P_2 \alpha_\mathrm{ex} \Psi_\mathrm{P2Pa})/V_2$ $+(A_1 c_\mathrm{pn} P_\mathrm{sup} \alpha_\mathrm{in} \Psi_\mathrm{PsP1})/V_1)$	$A_\mathrm{m,eq} \widehat{=} A_\mathrm{v1} = \ldots$ $+(A_\mathrm{eq} \dot{V}_1 P_1 V_2 \alpha_\mathrm{mt} - \dot{\tau}_\mathrm{d} V_1 V_2$ $+A_\mathrm{eq} \dot{V}_2 P_2 V_1 \alpha_\mathrm{mt})/(A_\mathrm{eq} K_f (P_2 V_1 \alpha_\mathrm{ex} \dot{m}_\mathrm{P2Pa}$ $+P_\mathrm{sup} V_2 \alpha_\mathrm{in} \dot{m}_\mathrm{PsP1}))$
Control law $s(t) > 0$	$A_\mathrm{m,eq} \widehat{=} A_\mathrm{v2} = \ldots$ $-(\dot{F}_\mathrm{d} + A_1(+(\dot{V}_1 P_1 \alpha_\mathrm{mt})/V_1)$ $-A_2(-(\dot{V}_2 P_2 \alpha_\mathrm{mt})/V_2))/((A_1 c_\mathrm{pn} P_1 \alpha_\mathrm{ex} \Psi_\mathrm{P1Pa})/V_1$ $+(A_2 c_\mathrm{pn} P_\mathrm{sup} \alpha_\mathrm{in} \Psi_\mathrm{PsP2})/V_2)$	$A_\mathrm{m,eq} \widehat{=} A_\mathrm{v2} = \ldots$ $-(A_\mathrm{eq} \dot{V}_1 P_1 V_2 \alpha_\mathrm{mt} - \dot{\tau}_\mathrm{d} V_1 V_2$ $+A_\mathrm{eq} \dot{V}_2 P_2 V_1 \alpha_\mathrm{mt})/(A_\mathrm{eq} K_f (P_1 V_2 \alpha_\mathrm{ex} \dot{m}_\mathrm{P1Pa}$ $+P_\mathrm{sup} V_1 \alpha_\mathrm{in} \dot{m}_\mathrm{PsP2}))$

P_1 and P_atm, as well as P_sup and P_2, assuming a correct allocation of up- and downstream pressures. Finally, $c_\mathrm{pn} = c_\mathrm{f} R \sqrt{T_\mathrm{atm}}$ is a combination of parameters for simplicity. The solved equations for the different case distinctions are depicted in the last two rows of Tab. 3.2.

The calculated equivalent area $A_\mathrm{m,eq}$ is inserted into the inverse function of the valve area, see Fig. 3.6, as

$$x_\mathrm{s,eq} = A_\mathrm{v}^{-1}(A_\mathrm{m,eq}). \tag{3.53}$$

For this, the linear splines from Fig. 3.6 enable a straightforward interval based calculation of the inverse function. The equivalent voltage is obtained by the static relation (3.52) as

$$u_\mathrm{eq} = \frac{x_\mathrm{s,eq}}{c_\mathrm{vv}}. \tag{3.54}$$

The final output voltage of the controller becomes

$$u = u_\mathrm{eq} - K_\mathrm{pn1} \,\mathrm{sat}\left(\frac{s(t)}{K_\mathrm{pn2}}\right), \tag{3.55}$$

with the saturation function sat() and the gain parameters K_pn1 and K_pn2. The controller input F_d or τ_d directly affects $s(t)$, (3.55) and the equations from Tab. 3.2. The controller output is u. A dynamic simulation of the full force controlled linear actuator is depicted in Fig. 3.4 (right).

3.4 Transmission Abstraction Layer

This section introduces the novel concept of a *Transmission Abstraction Layer (TAL)*. Depending on the robot design, the specific actuation may either be flanged at the robot joint or placed in a remote location. In the latter case, transmissions are used to transfer the actuator force/torque to the robot joints. Common transmission methods are tendons, rods, shafts and gears. This work focuses in particular on tendon-driven, belt-driven and hybrid structures. Inherent deliberate compliance such as mechanical springs are not considered in this work as the key focus centers around mechanically rigid actuation. Thus, the inherent compliance of the pneumatic system is considered to be part of the actuation system, and not the transmission.

3.4.1 Concept

The control of tendon-driven structures requires specialized mathematical methods [259]. This section utilizes the existing approaches to achieve a *Transmission Abstraction Layer (TAL)*. The intention of the

abstraction layer is to allow the same control approaches for tendon-driven/hybrid tendon-driven structures as well as for directly joint driven structures, e.g. from Sec. 3.3.

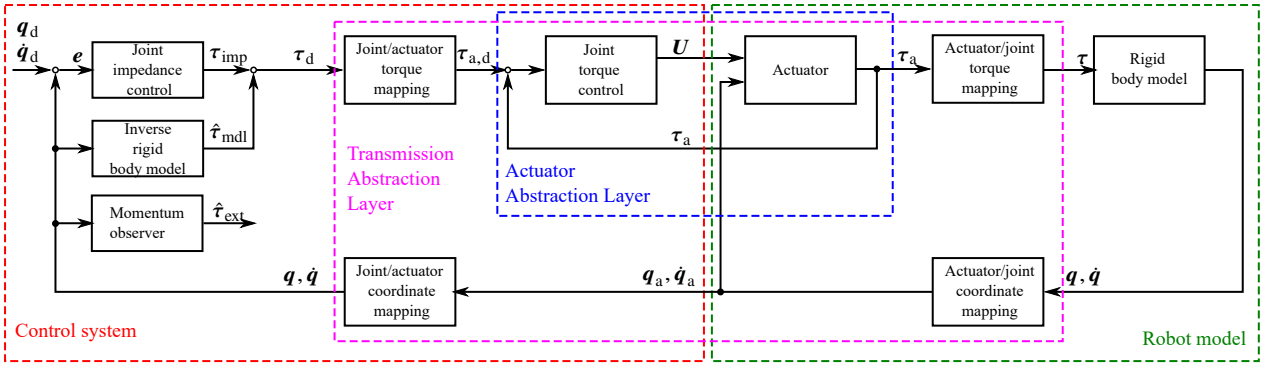

Figure 3.7 Control scheme with actuator and transmission abstraction layers

Figure 3.7 depicts an update of the modeling and control framework from Fig. 3.2 with a *TAL*. Let us consider the exemplary tendon driven robot finger from Fig. 3.8. Tendon forces F_{t1}, F_{t2}, F_{t3}, F_{t4} apply the torque τ_1 and τ_2 to the joints q_1 and q_2. This fact is modeled by the *Actuator/joint torque mapping* and defines the generalized actuator forces $\boldsymbol{\tau}_a = (F_{t1}, F_{t2}, \dots)^T$, which are generated by the force/torque controlled actuation, see Fig. 3.7. In the system, the link-side joint angles $\boldsymbol{q}$ cannot be measured directly but in actuation coordinates $\boldsymbol{q}_a$. This can be modeled by an *Actuator/joint coordinate mappings*, which transforms joint coordinates $\boldsymbol{q}$ to actuator coordinates $\boldsymbol{q}_a$, incorporating the tendon extensions h_1, h_2, h_3 and h_4, see Fig. 3.8. These two mappings describe the tendon-driven *Robot model*, together with rigid body and actuator model from Sec. 3.1 and Sec. 3.3, respectively.

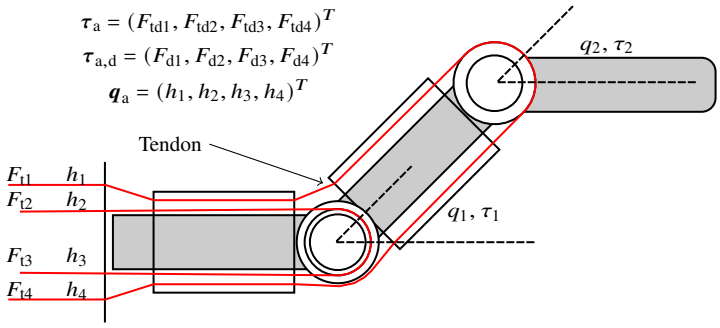

Figure 3.8 Exemplary tendon-actuated robot finger [259]

The control of the tendon-driven robot requires further mathematical mappings. When using controller (3.37), the desired joint torque $\boldsymbol{\tau}_d$ is commanded, see Fig. 3.7. As robot joints are not actuated directly, the *Joint/actuator torque mapping* is required to calculate the desired tendon forces $\boldsymbol{F}_{t,d}$ for a desired joint torque $\boldsymbol{\tau}_d$. These tendon forces are listed in the vector $\boldsymbol{\tau}_{a,d}$ whose entries are the desired values of the underlying actuator force/torque controller. In addition, model compensation and controller (3.37) require measurements of $\boldsymbol{q}$ and $\dot{\boldsymbol{q}}$ respectively. These are calculated based on actuator coordinates $\boldsymbol{q}_a$ with the help of the *Joint/actuator coordinate mapping*. In summary, both the *AAL* and the *TAL* are encapsulating combinations of hardware and software components and are thus a mechatronic system.

Further relevant applications and design approaches for the *TAL* are shown below.

1. If all joints are actuated directly at the joint, all aforementioned mappings reduce to 1 and $\boldsymbol{\tau} \hat{=} \boldsymbol{\tau}_a$ and $\boldsymbol{q} \hat{=} \boldsymbol{q}_a$. Consequently, Fig. 3.7 becomes Fig. 3.2.

2. The interface between *Control system* and *Robot model* shows the signals, which are transmitted between the software and the physical system, i.e., $\boldsymbol{U}, \boldsymbol{\tau}_a, \boldsymbol{q}_a$. Consequently, a realistic model of sensors

and actuators can be obtained. Furthermore, the resulting controller can be directly implemented on the specific hardware system, as sensor and actuator interfaces have already been considered in simulation.

3. A modular and systematic simulation becomes possible.
   a) All mappings of the *AAL* may be replaced by 1 if the actuation specifications are not of interest.
   b) All mappings of the *TAL* may be replaced with 1 if the specific transmission specification are not of interest. Thus, the higher-level impedance controller and the model compensation may be developed independently from the transmission models. Note this does not refer to the control theoretic aspects such as stability or the robustness analysis, which is not the focus of this work.
4. Mappings may be validated against each other. A series connection of *Joint/actuator torque mapping* and *Actuator/joint torque mapping*, and *Joint/actuator coordinate mapping* and *Actuator/joint coordinate mapping* should result in the same numerical value.

The followign section describes the mathematical methods for mappings.

3.4.2 Kinematic Mappings

Tendon-driven systems may be described by an analytical approach from [259]. For this, the length of each tendon of the robot is modeled geometrically by the *extension function*

$$\boldsymbol{h}(\boldsymbol{q}) \in \mathbb{R}^p, \tag{3.56}$$

where p is the number of tendons. The partial derivative of (3.56) along the joint coordinates $\boldsymbol{q}$ leads to the tendon Jacobian

$$\boldsymbol{J}_\mathrm{t}(\boldsymbol{q}) = \frac{\partial \boldsymbol{h}(\boldsymbol{q})}{\partial \boldsymbol{q}}^T. \tag{3.57}$$

This Jacobian allows for a mapping between generalized actuator forces $\boldsymbol{\tau}_\mathrm{a}$ and joint torques $\boldsymbol{\tau}$ via

$$\boldsymbol{\tau} = \boldsymbol{J}_\mathrm{t}\boldsymbol{\tau}_\mathrm{a}. \tag{3.58}$$

Furthermore, the velocities of joint and actuator coordinates can be calculated by

$$\dot{\boldsymbol{q}} = \boldsymbol{J}_\mathrm{t}^{\dagger T}(\boldsymbol{q})\dot{\boldsymbol{q}}_\mathrm{a}, \tag{3.59}$$

where $\boldsymbol{J}_\mathrm{t}^\dagger$ is the right pseudo-inverse of $\boldsymbol{J}_\mathrm{t}(\boldsymbol{q})$ and the actuator velocity by

$$\dot{\boldsymbol{q}}_\mathrm{a} = \boldsymbol{J}_\mathrm{t}{}^T(\boldsymbol{q})\dot{\boldsymbol{q}}. \tag{3.60}$$

The joint coordinates $\boldsymbol{q}$ can then be obtained by an online optimization [260], [17]

$$\underset{\boldsymbol{q}}{\text{minimize}}\ (\hat{\boldsymbol{h}}(\boldsymbol{q}) - \boldsymbol{h}) \tag{3.61}$$

with $\hat{\boldsymbol{h}}(\boldsymbol{q})$ being the modeled and $\boldsymbol{h}$ being the measured tendon elongation.

Desired generalized tendon forces can be computed by [261]

$$\boldsymbol{\tau}_\mathrm{a,d} = \boldsymbol{J}_\mathrm{t}^{+}(\boldsymbol{q})\boldsymbol{\tau}_\mathrm{d} + \boldsymbol{\tau}_\mathrm{a,p}, \tag{3.62}$$

where $\boldsymbol{\tau}_\mathrm{a,p}$ is a generalized pretension force. As tendons can only transmit pulling forces, it has to be ensured that the tendon forces always remain positive. For mass-less rod-driven structures on the other hand, both positive and negative forces may be applied.

In [17], a new tendon distribution algorithm

$$\begin{aligned} \min_{\boldsymbol{\tau}_{\mathrm{a,d}}} \quad & \sum_{k=1}^{p} \tau_{\mathrm{a,d},k} \\ & \text{such that} \\ & \boldsymbol{\tau}_{\mathrm{a,d}} \geq \boldsymbol{\tau}_{\mathrm{a,p}} \\ & \boldsymbol{J}_{\mathrm{t}}(\boldsymbol{q})\boldsymbol{\tau}_{\mathrm{a}} = \boldsymbol{\tau} \end{aligned} \tag{3.63}$$

was proposed, which is based on linear programming and solves the tendon problem at 1 kHz. Figure 3.9 gives an overview of all mappings from Fig. 3.7.

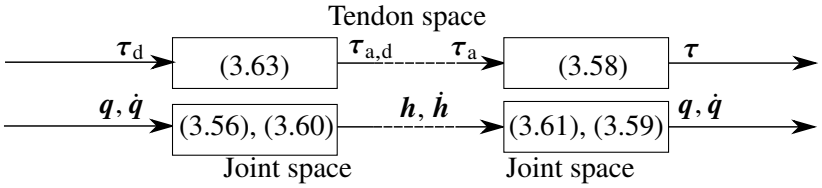

Figure 3.9 Actuator-/joint-level mapping

After examining the fundamentals of transmissions, the specific transmission mechanism of this work including mathematical modeling are introduced.

3.4.3 Transmission Mechanisms

The following section evaluates the transmission mechanisms incorporated into this work. First, the *flanged actuator* is used within the prostheses prototype I and II as elbow and forearm joint, see Chapter 5. Next, the *Belt and Bowden cables actuation* is used for the shoulder exoskeleton, see Chapter 6. Subsequently, the *tendon actuation 1-Degrees Of Freedom* and *2-Degrees Of Freedom* is used for the pneumatic testbeds, see Chapter 4. Finally, the *hybrid Tendon/Non-Tendon Actuation* is used for prosthesis prototype I and II from Chapter 5 utilizing the aforementioned *2-Degrees Of Freedom tendon actuation*.

Flanged Actuator – 1-Degrees Of Freedom

The most simple transmission is a directly flanged torque controlled actuator, see Fig. 3.10. In this case, the joint torque τ acts directly on the rigid body dynamics as described in (3.20) and (3.31). Consequently, $\tau = \tau_{\mathrm{a}}$ and $q = q_{\mathrm{a}}$.

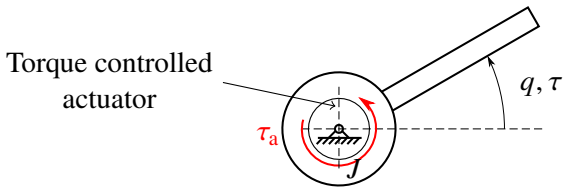

Figure 3.10 Flanged actuator

Belt and Bowden Cable Actuation – 1-Degrees Of Freedom

A typical belt and a Bowden cable transmission are depicted in Fig. 3.11. For both transmission types, the torque controlled actuator is placed remotely and cables are used to transmit the force and torque to the robot joint. In contrast to the Belt mechanism, the Bowden cable allows for a variable placement of the actuators

as the inner cable is guided by the outer, flexible pipes of the Bowden cables. For the kinematics of both transmission types, it yields

$$q = \frac{r_{\text{in}}}{r_{\text{out}}} q_{\text{a}} \text{ and } \tau = \frac{r_{\text{out}}}{r_{\text{in}}} \tau_{\text{a}}, \tag{3.64}$$

where r_{out} and r_{in} are the spool radii of driven and driving spool.

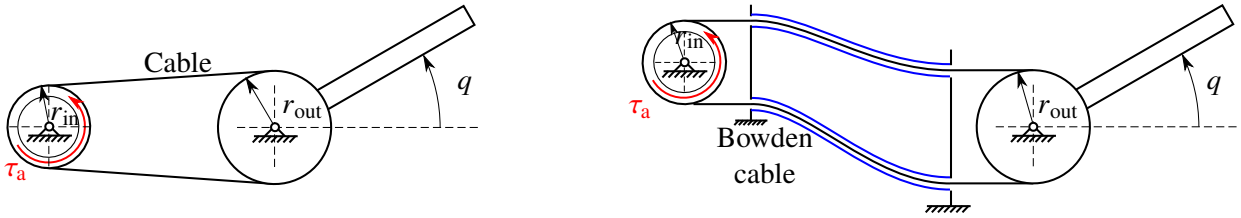

Figure 3.11 Belt and Bowden cable actuation

Antagonistic Tendon Actuation – 1-Degrees Of Freedom

An antagonistically actuated robot joint is depicted in Fig. 3.12. In contrast to the belt transmission, each tendon can be controlled individually by tendon forces F_{t1} and F_{t2} respectively. The variables of the joints

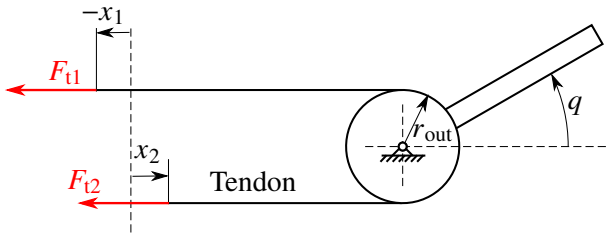

Figure 3.12 Mechanical model of the antagonistic tendon-driven robot joint

are

$$\boldsymbol{\tau}_{\text{a}} = \begin{pmatrix} F_{\text{t1}} & F_{\text{t2}} \end{pmatrix}^T, \boldsymbol{q}_{\text{a}} = \begin{pmatrix} x_1 & x_2 \end{pmatrix}^T, \boldsymbol{q} = q, \tag{3.65}$$

with F_{t1} and F_{t2} being the tendon force, and x_1 and x_2 being the translational deflection. The *extension function* of the joint is

$$\boldsymbol{h}(q) = \begin{pmatrix} l_1 - q r_{\text{out}} & l_1 + q r_{\text{out}}, \end{pmatrix} \tag{3.66}$$

with l_1 being a constant distance to the reference point and r_{out} the radius of the pulley. Based on (3.57), the tendon Jacobian follows to be

$$\boldsymbol{J}_{\text{t}}(q) = \begin{pmatrix} -1 & 1 \end{pmatrix} r_{\text{out}}. \tag{3.67}$$

The robot dynamics of the tendon-controlled 1-dof system can be derived by the Newton/Euler method as

$$M(q)\ddot{q} + C(q, \dot{q})\dot{q} + g(q) = \tag{3.68}$$

$$I_j \ddot{q} + M_{\text{j}} g l_{\text{CM}} \cos(q) = \boldsymbol{J}_{\text{t}}(q)\boldsymbol{\tau}_{\text{a}} + \tau_{\text{ext}}, \tag{3.69}$$

with M_j the joint mass, I_j the joint inertia, g being the scalar acceleration of the g vector and l_{CM} being the distance to the COM from the center of rotation.

Tendon Actuation – 2-Degrees Of Freedom

An exemplary tendon-driven 2-dof transmission mechanism is depicted in Fig. 3.13. Essentially, the mechanism is the logical straightforward extension of the 1-dof antagonistic joint from Fig. 3.12. The underlying idea is to use the minimum amount of individual tendons to control the 2-dof robot joint.

The mechanism may be classified as parallel 2-dof robot, categorized as the 3SPS-1RR structure [16], [17], where S stands for spherical, P for prismatic and R for rotational according to [249]. When practically considering the tendons as mass-less, the mechanism from Fig. 3.13 reduces to a serial kinematics system, consisting of a universal joint, which is described by the MDH-parameters in Tab. A.1 in the Appendix A.5.1.

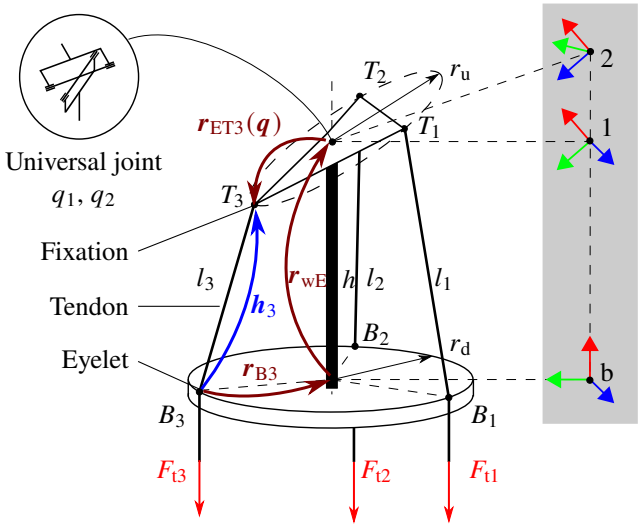

Figure 3.13 Kinematic 3SPS-1RR scheme of the tendon-driven wrist

The system variables are

$$\boldsymbol{\tau}_a = \begin{pmatrix} F_{t1} & F_{t2} & F_{t3} \end{pmatrix}^T, \boldsymbol{q}_a = \begin{pmatrix} l_1 & l_2 & l_3 \end{pmatrix}^T, \boldsymbol{q} = \begin{pmatrix} q_1 & q_2 \end{pmatrix}^T, \tag{3.70}$$

where $\boldsymbol{q}_w \widehat{=} \boldsymbol{q}$ denotes the joint coordinates of the robot. The wrist is driven by $k = 1..3$ tendons, which are fixed at T_k at the end effector and slide through the eyelets B_k, see Fig. 3.13. Both T_k and B_k are equally distributed on circles with radius r_u and r_d respectively. T_1 and B_1 lie on the same plane spanned by y and z of frame ${}^W\boldsymbol{T}_b$ and for $\boldsymbol{q} = \boldsymbol{0}$. Following [259], the extension function can be obtained by describing the tendon length $\boldsymbol{h}(\boldsymbol{q})$ from B_k to T_k for each tendon applying the Euclidean norm as

$$\boldsymbol{h}_1 = \boldsymbol{r}_{B1w} + \boldsymbol{r}_{wE} + \boldsymbol{r}_{ET1}(\boldsymbol{q}), \tag{3.71}$$

$$\boldsymbol{h}_2 = \boldsymbol{r}_{B2w} + \boldsymbol{r}_{wE} + \boldsymbol{r}_{ET2}(\boldsymbol{q}), \tag{3.72}$$

$$\boldsymbol{h}_3 = \boldsymbol{r}_{B3w} + \boldsymbol{r}_{wE} + \boldsymbol{r}_{ET3}(\boldsymbol{q}), \tag{3.73}$$

$$\boldsymbol{h}(\boldsymbol{q}) = \boldsymbol{h}_{wr}(\boldsymbol{q}) = \begin{pmatrix} \sqrt{h_{1,x}{}^2 + h_{1,y}{}^2 + h_{1,z}{}^2} \\ \sqrt{h_{2,x}{}^2 + h_{2,y}{}^2 + h_{2,z}{}^2} \\ \sqrt{h_{3,x}{}^2 + h_{3,y}{}^2 + h_{3,z}{}^2} \end{pmatrix}. \tag{3.74}$$

For clarity, Fig. 3.13 exemplifies the tendon geometry $\boldsymbol{h}_3$, which is calculated by $\boldsymbol{r}_{Bkw}$, $\boldsymbol{r}_{wE}$ and $\boldsymbol{r}_{ETk}(\boldsymbol{q})$. Here, $\boldsymbol{r}_{Bkw}$ is the vector from point B_k to the wrist base (b), $\boldsymbol{r}_{wE}$ is the vector from the wrist base to the end effector E, h is a height and $\boldsymbol{r}_{ETk}(\boldsymbol{q})$ is the vector from the end effector to the tendon fixation point T_k.

The proposed 3SPS-1RR structure is included in the design of a pneumatic robot and two prostheses in this thesis.

Hybrid Tendon/Non-Tendon Actuation - Prosthesis

The 2-dof mechanism from the previous section may be extended by a further two rotational dofs to a hybrid tendon/non-tendon-driven structure. More specifically, this configuration consists of two rotary actuators, followed by the 3SPS-1RR mechanism, see Fig. 3.14. According to (3.70), the variables of the hybrid system can be extended to

$$\boldsymbol{\tau}_\mathrm{a} = \begin{pmatrix} \tau_1 & \tau_2 & F_1 & F_2 & F_3 \end{pmatrix}^T, \boldsymbol{q}_\mathrm{a} = \begin{pmatrix} q_1, & q_2 & l_1 & l_2 & l_3 \end{pmatrix}^T, \boldsymbol{q} = \begin{pmatrix} q_1 & q_2 & q_3 & q_4 \end{pmatrix}^T. \tag{3.75}$$

The hybrid tendon kinematics may be obtained by extending (3.74) to

$$\boldsymbol{h}(\boldsymbol{q}) = \begin{pmatrix} q_1 \\ q_2 \\ \boldsymbol{h}_\mathrm{wr}(\boldsymbol{q}) \end{pmatrix} \tag{3.76}$$

and applying (3.57) to (3.63). Thus, the fully-fledged hybrid mechanism may be described in tendon and joint coordinates as depicted in Fig. 3.9. The full serial MDH kinematics is listed in Tab. A.2.

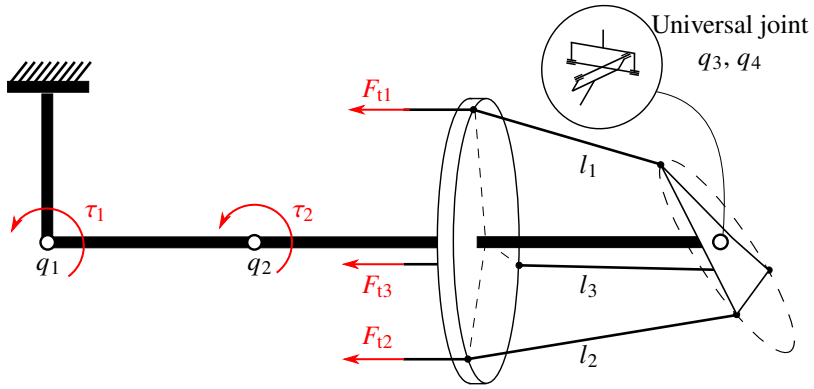

Figure 3.14 Kinematics and transmission scheme of the prosthesis with a 3SPS-1RR wrist

Hybrid Tendon/Non-Tendon Actuation - Exoprosthesis

The hybrid tendon/non-tendon-driven prosthesis from Fig. 3.14 is extended by an exoskeleton, carrying the prosthesis, see Fig. 3.15. More specifically, this configuration consists of three rotary actuators, where the first one is passive and joint 2 and 3 are driven remotely using Bowden-cables. This structure is followed by the prosthesis. According to (3.70), the variables of the hybrid system can be extended to

$$\boldsymbol{\tau}_\mathrm{a} = \begin{pmatrix} \tau_{\mathrm{a}2} & \tau_{\mathrm{a}3} & \tau_4 & \tau_5 & F_1 & F_2 & F_3 \end{pmatrix}^T, \tag{3.77}$$

$$\boldsymbol{q}_\mathrm{a} = \begin{pmatrix} q_{\mathrm{a}2} & q_{\mathrm{a}3} & q_4 & q_5 & l_1 & l_2 & l_3 \end{pmatrix}^T, \tag{3.78}$$

$$\boldsymbol{q} = \begin{pmatrix} q_1 & q_2 & q_3 & q_4 & q_5 & q_6 & q_7 \end{pmatrix}^T, \tag{3.79}$$

whereas q_1 is non-controllable. The hybrid tendon kinematics may be obtained by extending (3.74) to

$$\boldsymbol{h}(\boldsymbol{q}) = \begin{pmatrix} \frac{r_\mathrm{out}}{r_\mathrm{in}} q_2 \\ \frac{r_\mathrm{out}}{r_\mathrm{in}} q_3 \\ q_4 \\ q_5 \\ \boldsymbol{h}_\mathrm{wr}(\boldsymbol{q}) \end{pmatrix} \tag{3.80}$$

.

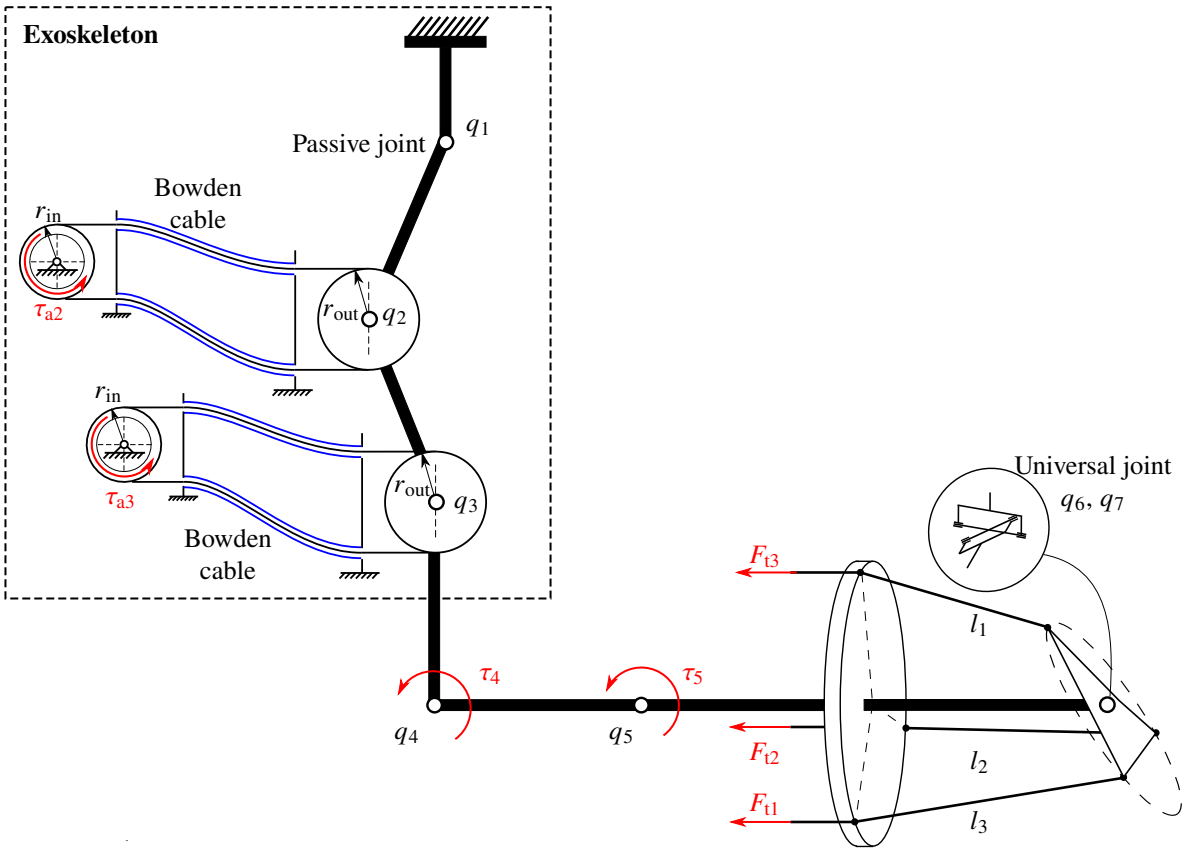

Figure 3.15 Kinematics and transmission scheme of the exoprosthesis with a 3SPS-1RR wrist

3.5 Summary

This chapter examined the mathematical approach for the modeling and control of serial and parallel[5] kinematic soft and tactile robots. On this basis, a modular *AAL+TAL*-structure was introduced, which allows for an adaption of the robot design, according to special design requirements, by varying the robot structural, actuation and control concept. Therefore, the robot may either be modeled as a fixed or floating-base system. The serial kinematic structure incorporated different complementary, state-of-the-art control approaches, such as a rigid body compensation, joint impedance controller and a momentum observer. With this control concept, a cascaded controller structure with underlying torque controllers could be constructed. Subsequently, a torque controlled system could be conceptually considered as an ideal torque source, allowing the application of alternative actuation principles under a single mechatronics framework. For achieving this goal, different force/torque controller variants for electromechanical and pneumatic actuators were debated. These ideas were denoted as *Actuator Abstraction Layer*. It was argued that also for the transmission methods between actuator and joint, a *Transmission Abstraction Layer* can be designed.

This framework builds the basis of the subsequent sim2real-guided design process. In order to show diverse use cases, and to obtain progress in other robotic domains, the framework is utilized for investigating muscle-like pneumatic robotic joint concepts (Chapter 4), wearable upper-limb prostheses (Chapter 5) and a wearable shoulder exoskeleton (Chapter 6).

[5]Parallel structures can be considered in the design as long as the parallel elements, apart from the central serial structure, are massless.

4 Part I ("Pneumatic Muscle-Like Actuators")

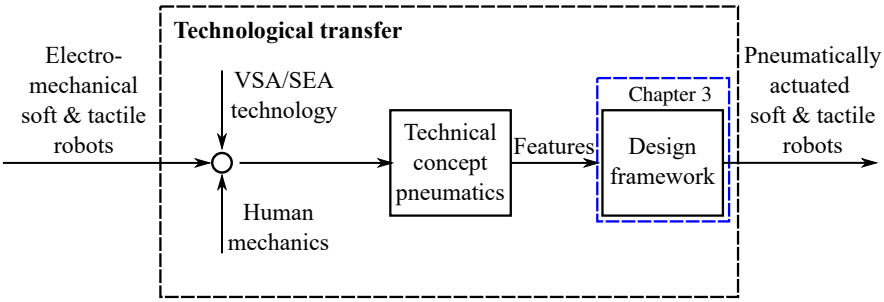

Figure 4.1 Development approach for the pneumatic robots

Soft and Tactile Pneumatics: To date, most pneumatic actuators were researched on actuator level or in a few experimental robot devices, see Sec 2.2. Recently, the company Festo SE & Co. KG introduced a commercially available robot with the capacity or potential for incorporating pneumatically actuated robot technology [125]. While FESTO did not disclose the technical details, its robot showed the potential functionality and performance for such underlying technology. Within the research community, however, pneumatic drives are sparsely used or considered as a common alternative to electromechanical actuation for soft and tactile robots. While mechatronics and control concepts were heavily elaborated for electromechanical drives, see Sec. 2.1, a similar attempt for pneumatic drives is currently still lacking. More specifically, a rigorous methodological transfer of mechatronics and control methods from electromechanical actuation to pneumatic actuation remains an open issue.

Approach: The approach of this work is to develop the basis for pneumatic technology for soft and tactile robots being inspired by human neuromechanics and utilizing state-of-the-art technology from VSAs and SEAs, see Fig. 4.1. For this, the design and synthesis framework from Sec. 3 uses a digital-twin-based development, and also incorporates the virtual modeling, control and design of the robot.

The development of tactile controllers and mechatronics for pneumatics starts with the investigation of 1-dof and 2-dof systems. For the 1-dof and 2-dof systems, novel tendon driven structures are investigated, which are driven by two or three tendons, respectively. For linearly-actuated pneumatic cylinders, a rotary joint with a bio-inspired, muscle-like actuator arrangement is designed. The proposed tendon-driven pneumatic structure shares many similarities with the human musculoskeletal systems in terms of i) backdrivability, ii) low friction, iii) remote actuation, iv) the ability for explosive motions, v) storage of energy and vi) impacts robustness.

For system development, commonly-used state-of-the-art controllers are applied, such as joint impedance control, force/torque control, momentum observation and unified-force impedance control. This provides a systematic transfer of control and mechatronics concepts to the field of pneumatics. Also, novel actuator-level controllers for leakage observation and compensation are presented. Finally, a 7-dof pneumatic robot simulation investigates the feasibility of a pneumatic soft and tactile robot for a common commercially available robot kinematics. It provides several possible application scenarios especially designed for pneumatic robot application. These are calculated based on a physically-correct robot simulation containing i) the rigid body model, ii) the simulation of seven pneumatic actuators, iii) the applicable pneumatic torque controllers and v) the joint-level impedance controller.

Contribution: The contributions of this chapter are

- the systematic transfer of mechatronics and control methods for pneumatic soft and tactile robot systems, including proposed kinematic structures,
- the design of biologically inspired drive-trains by using tendon-driven actuation and pneumatic muscle-like cylinders for 1-dof and 2-dof structures,
- the transfer of soft robotics control (i.e., joint impedance control, momentum observation, unified-force impedance control) for the proposed 1-dof, 2-dof and 7-dof structure, and
- a pneumatic-level disturbance observation and compensation approach for nonlinear sliding-mode force control.

The remainder of this chapter is dedicated to the following analysis. Section 4.1 presents the investigated systems. Sec. 4.2 examines actuator and joint-level control, and this evaluation also applies to multi-joint control under Sec. 4.3 . Finally, Sec. 4.4 summarizes key results and findings. This chapter was written based on [262], [14], [15], [16], [263].

4.1 Systems

The following pneumatic systems, are investigated in this section (see Fig. 4.2)

- 1-dof pneumatic antagonistic actuator,
- 2-dof pneumatic antagonistic actuator, and
- 7-dof pneumatic robot physical simulation.

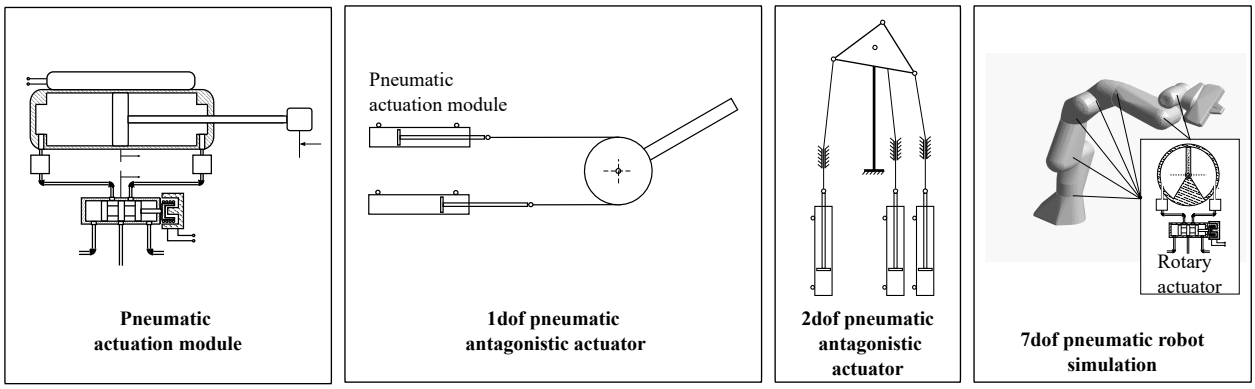

Figure 4.2 Overview of pneumatic systems analyzed in this work

1-dof Robot

Figure 4.3 depicts a 1-dof pneumatic robot joint, which is actuated by two pneumatic cylinders in an antagonistic tendon-driven, bio-inspired and muscle-like setup. The rigid body model of the robot joint is described in Sec. 3. The system is actuated by two force controlled pneumatic cylinders, for which model and force control are described in Sec. 3. The 1-dof actuator is designed to be robust against mechanical impacts. While buckling of rods is generally a problem in pneumatic cylinders, in this design, only pulling forces act on the pistons, and is therefore uncritical in case of high interaction forces. The 1-dof actuator is highly backdrivable. This is affected by the linear relation between pulley and piston, and further supported by the low friction cylinders. As a consequence, external joint torques can be fully absorbed by the pneumatic chambers when an external impact occurs.

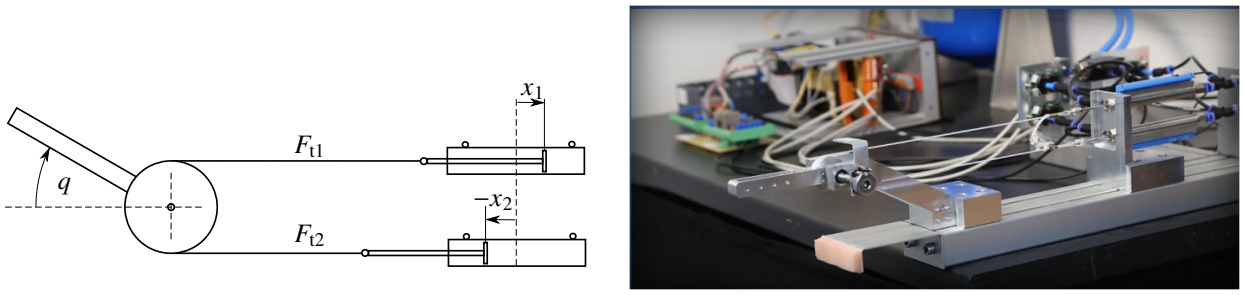

(a) Scheme **(b)** Testbed

Figure 4.3 Schematic and experimental testbed for the 1-dof pneumatic actuator

2-dof Robot

Fig. 4.4 depicts a 2-dof pneumatic robot joint. The mechanism is an extension of the prior actuator for two dimensions and is controlled by the minimum number of tendons. The consequence of this extension is a nonlinear kinematic relation between the actuator and the structure. The rigid body and transmission model of the 3SPS-1RR structure are shown in Sec 3.4.3. The mechanism in Fig. 4.4 shows a tendon-driven actuation by three pneumatic force-controlled cylinders. In this mechanism, the 2-dof mechanism is designed to be robust against impacts as only pulling forces are transmitted by the actuation.

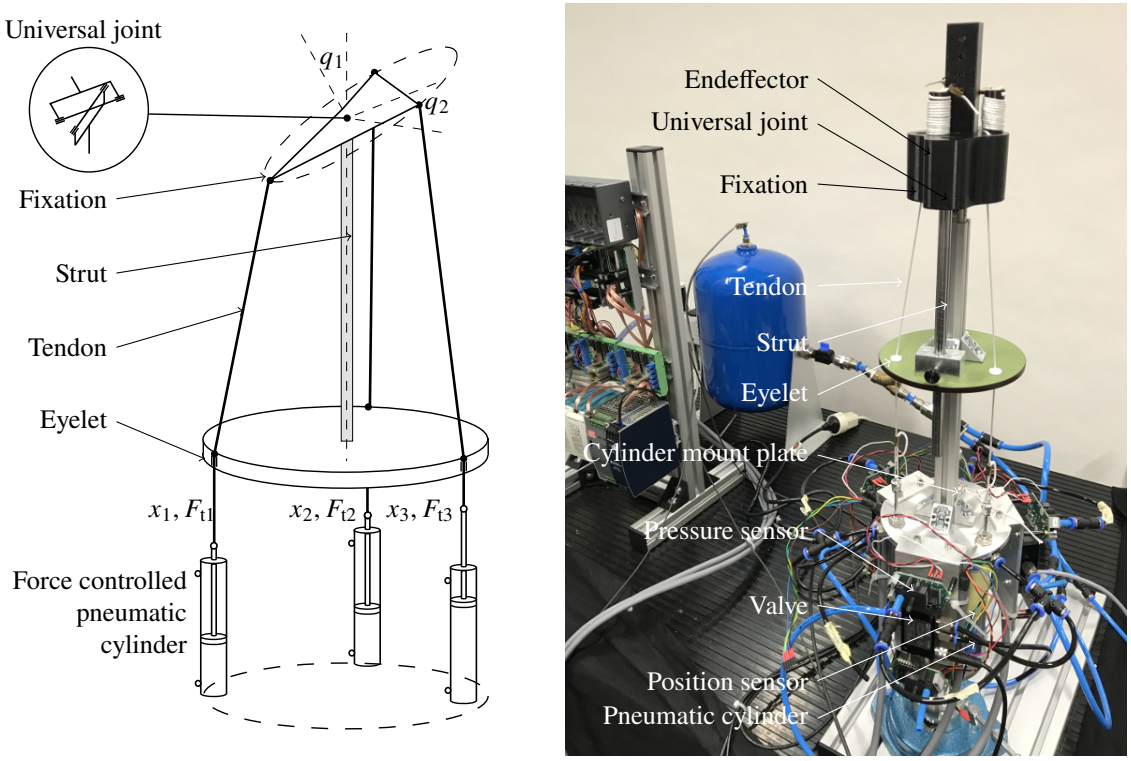

(a) 3SPS-1RR scheme **(b)** 3SPS-1RR testbed

Figure 4.4 Schematic and experimental testbed for the pneumatic wrist impedance controller

7-dof Robot Simulation

The final system of this work is a hypothetical 7-dof pneumatically actuated robot, see Fig. 4.5. The serial kinematic structure of the robot is based on the Franka Emika robot. Kinematic and dynamic parameters for the simulation are taken from [264]. The aim is to investigate the feasibility of a full 7-dof pneumatic robot and to analyze the robot performance when using pneumatic actuators. In contrast to the previous 1-dof

and 2-dof mechanisms, neither tendon-driven, nor linear cylinders were considered unsuitable for the given kinematic structure. Instead, double actuated rotary pneumatic actuators were used for the robot actuation, which are flanged to the robot joints. The framework from Sec. 3 enables straightforward modeling and control of the torque-controlled robot.

The actuators of the system are designed on the basis of the real Franka Emika robot [34]. Consequently, the pneumatic actuators are intended to provide the same maximum torque and joint limits as those of the Franka Emika robot [34]. For simplicity, only one actuator type was considered for all joints using the same proportional valve (Enfield technology LS-V05s), as used for the other simulations. The resulting hypothetical pneumatic actuator provides 79 Nm of torque, and has a radius and width of 6.4 cm. The valves may either be placed in the structure, or in the base of the robot. Neither a delay in the pipes between valves and cylinders, nor the weight of the valves was considered.

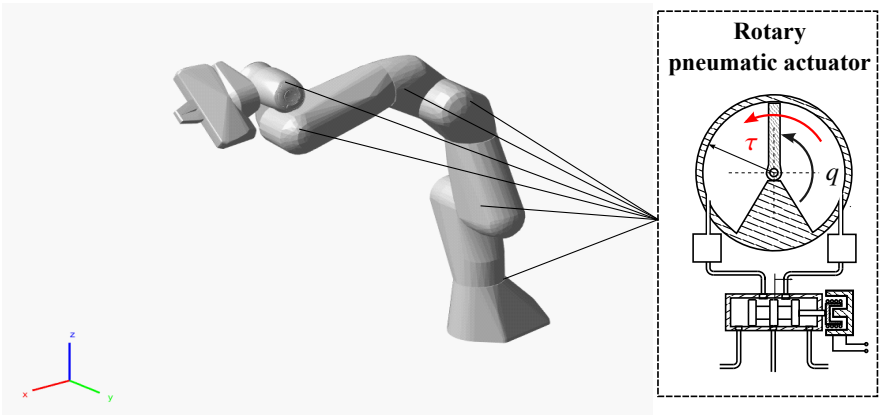

Figure 4.5 Simulation of a Franka Emika robot equipped with seven rotary torque controlled pneumatic actuators

4.2 Actuator and Joint Control

This section investigates actuator and joint control methods on the 1-dof actuator, see Fig. 4.3.

4.2.1 Joint Impedance Control

Figure 4.6 depicts the cascaded controller structure for the 1-dof antagonistic robot joint from Fig. 4.3. The system model is obtained by (3.69), with the tendon Jacobian $\boldsymbol{J}_\mathrm{t}(\boldsymbol{q})$ from (3.67). Pneumatic modeling and underlying force control are described in Sec. 3.3.3. The required mappings $\tau \rightarrow F$ and $x \rightarrow q$ (see Fig. 4.6) may be then obtained using (3.62) and (3.59). The joint impedance controller (3.37) with scalar entries is

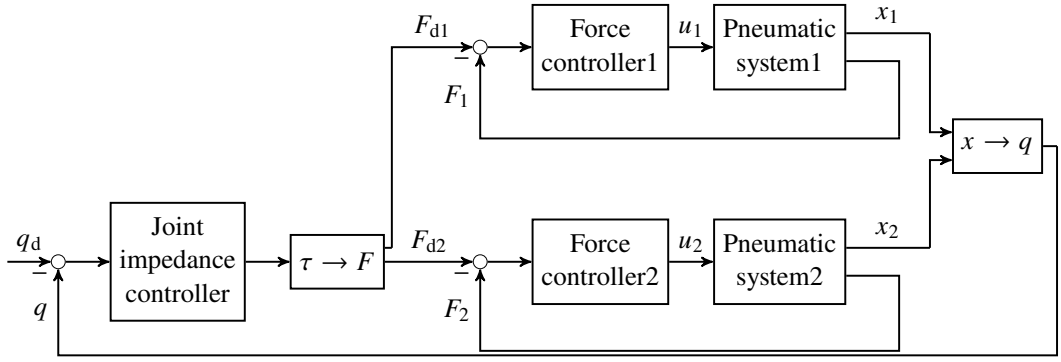

Figure 4.6 Signal flow diagram of impedance control for the tendon driven pneumatic system

applied to the system. The feed-forward control and the impedance controller are chosen to be

$$\tau_\mathrm{ff} = (I_j + 2l_\mathrm{CM}^2 M_\mathrm{p})\ddot{q}_\mathrm{d} + M_\mathrm{j} g l_\mathrm{CM} \cos(q) \tag{4.1}$$

$$\tau_\mathrm{d,imp} = K_\mathrm{imp}(q_\mathrm{d} - q) + D_\mathrm{imp}(\dot{q}_\mathrm{d} - \dot{q}) + \tau_\mathrm{ff} \tag{4.2}$$

for compensation inertia and gravity influences. The damping D_imp is adjusted by

$$D_\mathrm{imp} = 2D\sqrt{K_\mathrm{imp}(I_j + 2l_\mathrm{CM}^2 M_\mathrm{p})}, \tag{4.3}$$

enabling a unified damping adjustment by the damping factor D.

Joint Angle Motion

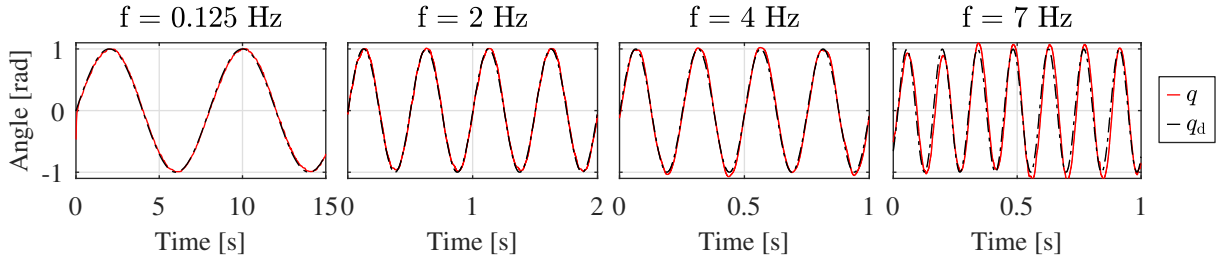

Figure 4.7 Experiment: position tracking of antagonistic impedance control

Figure 4.7 depicts the tracking performance for different sinusoidal signals. The desired joint angle q_d is achieved correctly for all frequencies 0.125, 2, 4, and 7 Hz. At 7 Hz, some noticeable deviation of q can be observed. The mean absolute errors are $\overline{|e|}_{0.125\mathrm{Hz}} = 1.2° \approx 0.021$ rad, $\overline{|e|}_{2\mathrm{Hz}} = 2.4° \approx 0.042$ rad, $\overline{|e|}_{4\mathrm{Hz}} = 1.6° \approx 0.028$ rad and $\overline{|e|}_{7\mathrm{Hz}} = 7.6° \approx 0.133$ rad. Consequently, high dynamics can be achieved by the 1-dof robotic actuator.

Stiffness Adjustment

An investigation of the static stiffness characteristics is shown in Fig. 4.8. The experiment was performed at $q_\mathrm{d} = 0$ rad. From this set point, the link is deflected in small angular steps up to $\pi/2$ for stiffness values ranging from 0.1 to 2.75 Nm/rad. The markers in Fig. 4.8 represent force measurements for specific deflections. The solid lines show the optimal levels of adjusted stiffness during the experiment. It can be observed that the expected torques are achieved correctly for smaller angular displacements. For increasing stiffnesses, earlier detachment from the ideal stiffness characteristic line can be observed. This detachment is caused by the particular choice of the pretension force in combination with a linear distribution of tension forces, which increases one tendon force while decreasing the other. When the lower tendon force reaches a predefined lower boundary, it saturates to prevent slacking. Furthermore, a maximum torque of about 0.55 Nm can be observed, which follows from supply pressure P_sup and cylinder piston areas A_1 and A_2. Finally, it can be stated that all defined stiffnesses are achieved correctly for angles lower than 0.1 rad.

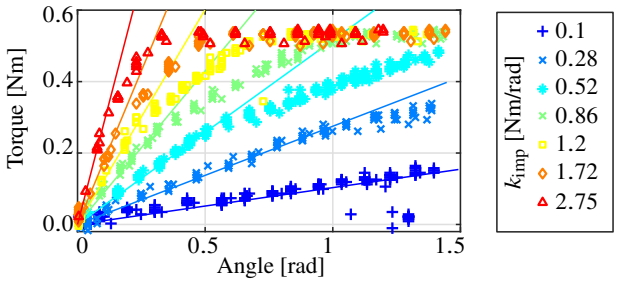

Figure 4.8 Experiment: Static torque-deflection characteristics of the impedance controlled finger

Damping Adjustment

The following section investigates adjustable damping. Based on the digital-twin-simulation, the damping adjustment is first analyzed by the simulation below, see Fig. 4.9, which shows the step response of the antagonistic impedance controlled system for a step change in q_d for three different damping ratios $D = 0.2$, $D = 0.7$ and $D = 1$ with underlying simulated force controllers. For validation purposes, the system response is compared to an ideal impedance behavior q_i (gray line in plot), which is characterized by the following transfer function

$$G(s) = \frac{\frac{K_\mathrm{imp}}{(I_j+2r^2M_\mathrm{p})}}{s^2 + 2D\sqrt{\frac{K_\mathrm{imp}}{(I_j+2r^2M_\mathrm{p})}}s + \frac{K_\mathrm{imp}}{(I_j+2r^2M_\mathrm{p})}}. \tag{4.4}$$

The results show that the system closely resembles the behavior of (4.4) on the basis of linear theory. As expected, slightly damped oscillations occur when reducing D. Minor differences can still be observed, which can be explained by the limited bandwidth of the controller.

Figure 4.10 depicts a system response test. Applying linear theory, the comparison reveals a similar system behavior. The experimental setup reflects the expectation for the chosen damping ratios. However, in comparison to simulation, the experimental system produces slightly larger overshoots. Due to a lower supply pressure of 3.5 bar, the required forces needed for deceleration are not achieved, leading to the observed overshoots.

Finally, the system response is also tested for varying damping factors when being deflected from the set-point by human interaction, see Fig. 4.11. The desired joint angle is set to $q_\mathrm{d} = 0$. One can see that the system is deflected for both damping parameters with the similar oscillations as observed in Fig. 4.10. After analyzing the impedance characteristics of the actuator, the next section focuses on impact robustness.

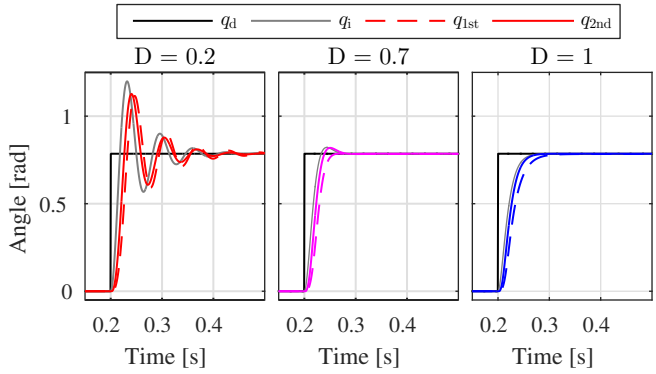

Figure 4.9 Digital twin simulation: Step responses of antagonistic impedance control for different damping ratios

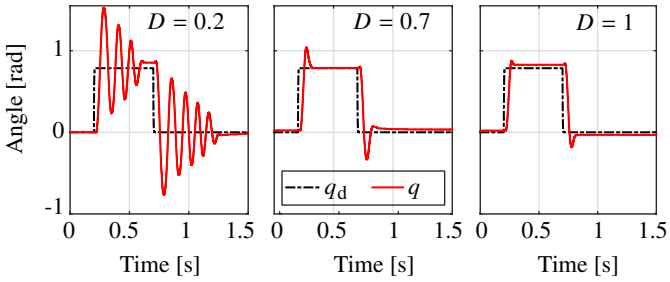

Figure 4.10 Experiment: System response of antagonistic impedance control for different damping ratios

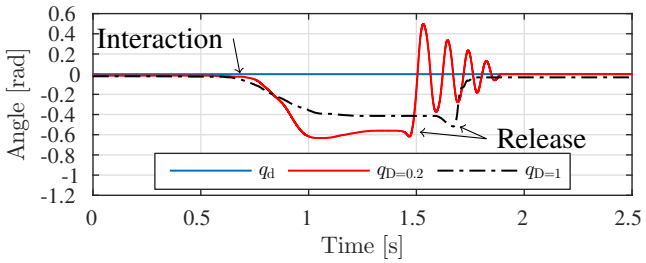

Figure 4.11 Experiment: Human interaction by application of an external force and system response for $D = 0.2$

Impact Robustness

The developed pneumatic actuator is designed to be robust against hard collision, as shown by the following experiment.

Fig. 4.12 (left) depicts a human lashing out for a strike on the actuator. Subsequently, the human is asked to hit the finger of the actuator with maximum force and speed. The measurement of this action can be seen in Fig. 4.12 (right). The upper row shows the deflection up to about 90 deg due to the impact. The lower row shows the desired and actual actuator forces of cylinder 1 of the system. F_{t1} follows F_d up to the maximum actuator force F_{max} within ≈ 0.01 s. F_{max} results from piston areas A_1 and A_2 and supply pressure P_{sup}. However, F_d increases to ≈ -50 N as demanded by the impedance controller. Consequently, when exceeding F_{max}, the impedance becomes nonlinear and is determined by the inherent compliance of the system. Once the finger returns, F_d comes in reach and the force control continues. This process takes ≈ 0.22 s for the system to settle, showing the high dynamics and impact robustness of the device.

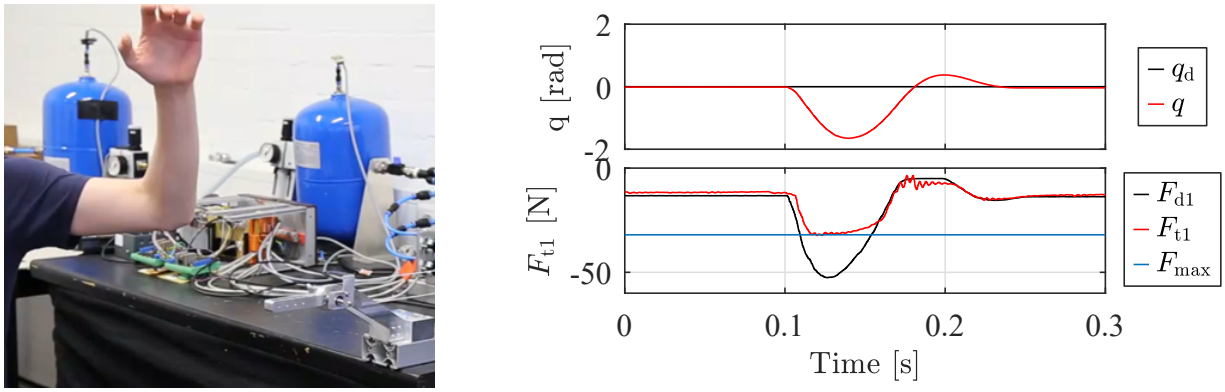

Figure 4.12 Impact handling: the proposed actuator can handle a collision in 80 ms.

4.2.2 Joint Disturbance Monitoring

Another important control element of a soft and tactile robots is the momentum observer [255] as described in Sec. 3.2.3. It allows for measuring external torques $\hat{\tau}_{\text{ext}}$ for models of type 3.31. For the 1-dof pneumatic actuator, the structure of the observer simplifies to

$$\hat{\tau}_{\text{ext}} = K_{\text{O}} \left(\int_0^T (\tau - g(q) - \hat{\tau}_{\text{ext}})\, dt - I\dot{q} \right), \tag{4.5}$$

with $g(q) = M_{\text{j}} l_{\text{CM}} \cos(q)$. τ is obtained from (3.58). While the joint disturbance observer is not further analyzed in this section, it contributes to the unified torque impedance controller as discussed in the following section.

4.2.3 Unified Force / Impedance Control

Tactile robots not only respond with desired impedances but also accurately regulate contact forces at the robot end effector. In principle, an impedance controller may be used to apply any demanded contact force: For this, the set-point $\boldsymbol{x}_{\text{d}}$ may be set underneath the contact surface, resulting in a desired force $\mathcal{F}_{\text{ext}}$ for a given stiffness $\boldsymbol{K}_{\text{imp}}$. A disadvantage of this approach is that the contact surface and properties must be known for achieving accurate force control. This is usually not the case for many robot applications. Another downside is a sudden contact loss. As the impedance controller stores potential energy when being deflected, a contact loss may lead to potentially harmful velocities. An alternative approach is to apply direct force control methods, as shown in [265] and [266].

The unification of force and impedance control was first introduced in [76] as well as the first safe contact-loss handling based on deflection monitoring. In this work, such method is directly applied to the antagonistically driven pneumatic robot joint from Fig. 4.3.

The main contributions of the present work are

- the application and validation of the momentum-based disturbance observer paradigm to pneumatic systems for estimating external torques without the need for acceleration measurements, and

- the application of unified torque and impedance control to pneumatically actuated robot joints.

Joint-Level Torque Control

A key component of the unified torque impedance controller is the extended joint torque controller. Contact joint torque control for the antagonistic pneumatic system is achieved by a PID controller

$$\tau_{\mathrm{d,trq}} = \alpha \left(K_{\mathrm{p}} e + K_{\mathrm{d}} \dot{e} + \int_{t_1}^{t} K_{\mathrm{i}} e \, d\sigma \right) \tag{4.6}$$

$$e = \tau_{\mathrm{d,f}} - \hat{\tau}_{\mathrm{ext}}, \tag{4.7}$$

with the controller parameters K_{p}, K_{i} and K_{d} for the proportional, integral and derivative part. $\tau_{\mathrm{d,f}}$ is the desired torque at joint level and $\hat{\tau}_{\mathrm{ext}}$ denotes an observed external torque from (4.5), which is used for the torque error e. The parameter $\alpha = [0, 1]$ enables the de-/activation of the controller. t_1 resets the integral part.

Passivity-Based Unified Torque/Impedance Controller

Based on (4.1) and (4.6), a preliminary unified torque/impedance control for the pneumatic joint can be constructed as

$$\tau_{\mathrm{d}}' = \tau_{\mathrm{d,trq}} + \tau_{\mathrm{d,imp}}. \tag{4.8}$$

However, passivity analysis outlined in the Appendix A.1.1 reveals that for the controller (4.8) passivity is violated. To resolve this issue, the controller design from [76] is adapted and an energy tank [267], [268] with the dynamics

$$\dot{x}_{\mathrm{t}} = \frac{\beta}{x_{\mathrm{t}}} (D_{\mathrm{imp}} \dot{q}^2 - \gamma \dot{q} \tau_{\mathrm{d,trq}}) + u_{\mathrm{t}} \tag{4.9}$$

state x_{t} and an input u_{t} is introduced. Additionally, the binary keys γ and β are defined as

$$\gamma = \begin{cases} 1, & \text{if } \dot{q}\tau_{\mathrm{d,trq}} < 0 \;\rightarrow \text{passivity not violated} \\ 0, & \text{if } \dot{q}\tau_{\mathrm{d,trq}} \geq 0 \;\rightarrow \text{passivity violated} \end{cases}$$

and

$$\beta = \begin{cases} 1, & T_{\mathrm{t}} < T_{\mathrm{u}} \\ 0, & \text{else} \end{cases}.$$

T_{u} defines an upper tank boundary referring to the tank energy

$$T_{\mathrm{t}} = \frac{1}{2} x_{\mathrm{t}}^2. \tag{4.10}$$

The connection between the tank and unified controller is established by a so-called Dirac structure

$$\begin{pmatrix} u_{\mathrm{c}} \\ u_{\mathrm{t}} \end{pmatrix} = \begin{bmatrix} 0 & \omega \\ -\omega & 0 \end{bmatrix} \begin{pmatrix} y_{\mathrm{c}} \\ y_{\mathrm{t}} \end{pmatrix}, \tag{4.11}$$

with the output port of the tank $y_{\mathrm{t}} = x_{\mathrm{t}}$, the input u_{c} and the output port of the controller $y_{\mathrm{c}} = \dot{q}$. The connection ω between controller and tank is defined by

$$\omega = \frac{\alpha}{x_{\mathrm{t}}} (1 - \gamma) \tau_{\mathrm{d,trq}}. \tag{4.12}$$

Another binary key α is introduced as

$$\alpha = \begin{cases} 1, & T_\mathrm{t} > T_\mathrm{l} \\ 0, & \text{else,} \end{cases} \tag{4.13}$$

with T_l being the lower boundary of the tank energy. The tank augmentation changes the control law (4.8) to

$$\Gamma = \gamma \tau_{\mathrm{d,trq}} + \omega x_\mathrm{t} \tag{4.14}$$

$$\tau_\mathrm{d} = -K_\mathrm{imp}\tilde{q} - D_\mathrm{imp}\dot{q} + \hat{g}(q) + \Gamma. \tag{4.15}$$

The passivity analysis of this controller is done in Appendix A.1.1.

Controller Shaping Function

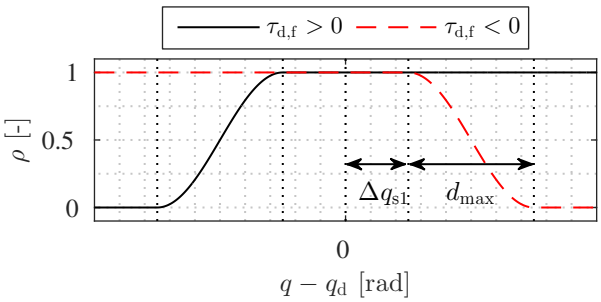

Figure 4.13 Shaping function for contact-loss handling

For handling unexpected contact losses, a shaping function ρ is introduced, which provides a smooth transition between torque and impedance control [76]. The definition of Γ is changed to

$$\Gamma' = \Gamma\rho, \tag{4.16}$$

where ρ is defined as

$$\rho = \begin{cases} 1 & \tau_\mathrm{d} q^* \geq 0 \\ \frac{1}{2}\left(1 + \cos\left(\pi \frac{q^*}{d_\mathrm{max}}\right)\right) & \tau_\mathrm{d} q^* < 0 \wedge \\ & |q^*| > 0 \wedge |q^*| < d_\mathrm{max} \\ 0 & \text{else,} \end{cases} \tag{4.17}$$

where $q^* = \tilde{q} - \Delta q_\mathrm{s}$ and $\Delta q_\mathrm{s} = \mathrm{sign}(\tau_\mathrm{d})\Delta q_{\mathrm{s1}}$. The parameter d_max adjusts the width of the transition range. The parameter Δq_{s1} denotes a robustness region, see Fig. 4.13. Finally, Fig. 4.14 shows the complete schematics of the controller.

Joint-Level Torque Control

Figure 4.15 shows the torque tracking performance in simulation and experiment for sinusoidal and step signals. With this, the experimental results are also compared to the results from the digital-twin simulation. After establishing contact, torque control is assessed under (4.15). To prevent slacking, the actuator provides a theoretical maximum torque of $\tau_\mathrm{max} = 0.52$ Nm, considering a maximum actuator force of $F_{ti,\mathrm{max}} = 34$ N (based on 6 bar) and a minimum actuator force of $F_{ti,\mathrm{min}} = 5$ N of the opposite actuator.

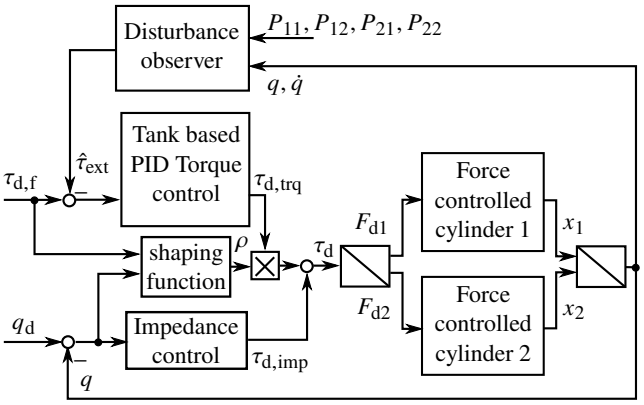

Figure 4.14 Torque/impedance control for a pneumatic antagonistic joint

The left two columns of Fig. 4.15 show the torque tracking results for sinusoidal signals of 2 Hz with different offsets. The offset of the desired torque is increased until a loss in performance can be observed. Simulations and experiments show accurate phase-less tracking for all offsets.

The right two columns show a step function tracking for different offsets. Both simulation and experimental results show an overshoot of ≈ 0.05 Nm. Presumably, the experimental noise originates from noise of the pressure sensors in combination with a high momentum observer gain. The latter was chosen as a compromise between filtering and dynamics. In the simulation and the experiment ≈ 23 % below τ_{max}, a decreasing control performance can be observed. The pressure potential between cylinder chamber and tank is likely too low to provide a sufficient mass flow. As a consequence, both the simulation and the experiment provide very similar results.

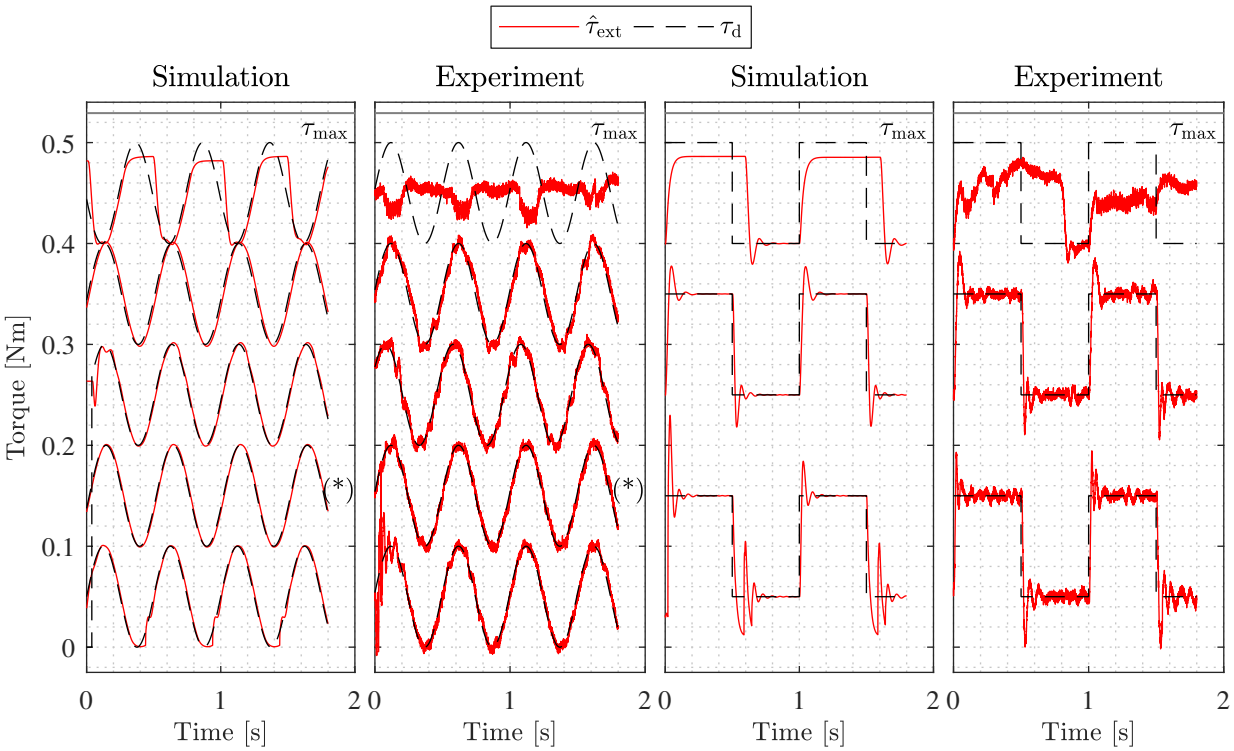

Figure 4.15 Digital twin and experimental results for torque tracking of sinusoidal and step functions with different contact offsets

Unified Torque Impedance Control

For the evaluation of the unified impedance controller, an experiment is designed to provide contact and non-contact situations for the pneumatic robot joint, see Fig. 4.16. The idea of the experiment is to first allow for the free motion of the finger, and then block the way with a slider to affect a controller transition to torque control. When the finger performs torque control in contact, the slider is pulled out of the way. This experiment is investigated both in simulation and experiments, see Fig. 4.17. The investigation is divided into intervals (a)-(e). For the analysis, the desired trajectory q_{d2} is introduced. q_{d2} is connected in series with q_{d}, and q_{d2} performs a repetitive motion (see Fig. 4.17, blue line). For tracking, it yields $q_{\mathrm{d}} = q_{\mathrm{d2}}$ depending on the current state of the state machine q_{d2} is detached from q_{d}.

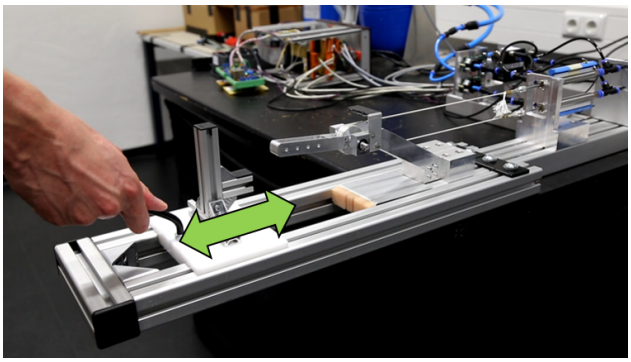

Figure 4.16 Contact experiments with a slider providing contact/non-contact situations

The following experimental protocol describes the states and transitions of the state machine:

- **Position tracking** (a), (b), (c): the controller fulfills tracking $q_{\mathrm{d}} = q_{\mathrm{d2}}$ with pure impedance control at predefined stiffness K_{imp} and damping D_{imp}.
- **Recognize contact** (c) $\rightarrow$ (d) : A contact is recognized at time t_0 if the external torque $\hat{\tau}_{\mathrm{ext}}$ has been exceeded a predefined threshold $\hat{\tau}_{\mathrm{t}}$ for a certain time period Δt. It yields $q_{\mathrm{d}} = q_{\mathrm{d2}}$.
- **Activate PID torque control** (d): the parameter α of (4.6) is set to 1 to activate PID torque control. Furthermore, the integral part of the controller is reset by setting $t_1 = t_0$. Subsequently, the next state is ascertained.
- **Fade q_{d} to contact point** (d): To avoid fast and unwanted initial motions in case of contact loss, caused by the impedance controller, the set point of the impedance control is set close to the contact point q_{co}, as $q_{\mathrm{d}} = q_{\mathrm{co}} - \epsilon$. q_{co} is the measured position at t_0. ϵ is a small angle to ensure contact until the PID torque controller has reached the desired torque $\tau_{\mathrm{d,f}}$. A possible fading function

$$q_{\mathrm{d}} = (q_{\mathrm{co}} - \epsilon - q_{\mathrm{d},t0}) f(t) + q_{\mathrm{d},t0} \tag{4.18}$$

$$f(t) = \left(1 - e^{-\lambda(t-t_0)}\right)^3 \tag{4.19}$$

  is applied to obtain a continuous transition to the new set point. $q_{\mathrm{d},t0}$ is the desired angle at the time of contact recognition. λ affects the widths of the fading zone. q_{d} remains at this position until the end of (e). Consequently, the torque controller performs its desired control operation while being in contact.

- **Recognize contact loss** (d) $\rightarrow$ (e): in case of sudden contact loss, the link accelerates in the same direction as the force applied to the surface of the obstacle. As a consequence, q passes the intervals Δq_{s1} and d_{max} of the shaping function ρ, see Fig. 4.13. The further q travels along d_{max}, the lower the value that ρ becomes. Since ρ is multiplied with the torque controller (4.14) in (4.16), the contribution of the torque control is continuously decreased. If ρ has reached zero, the contact loss is recognized and the system transits to the next state.

- **Deactivate Proportional Integral Derivative (PID) torque control** (d) → (e): Since it was ensured in the previous state that the torque control faded out continuously, switching off the torque control by setting $\alpha = 0$ does not affect the system behavior anymore. This will be analyzed in Fig. 4.18.
- **Hold position** (e): the system holds the position to show the contact loss handling.
- **After time** (e) → (a): a smooth transition is used to align q_d and q_d2 again.

Figure 4.17 shows both the simulation and the experimental results of the experimental protocol. Clearly, the behavior of the experimental protocol can be accurately reproduced both in simulation and experiment.

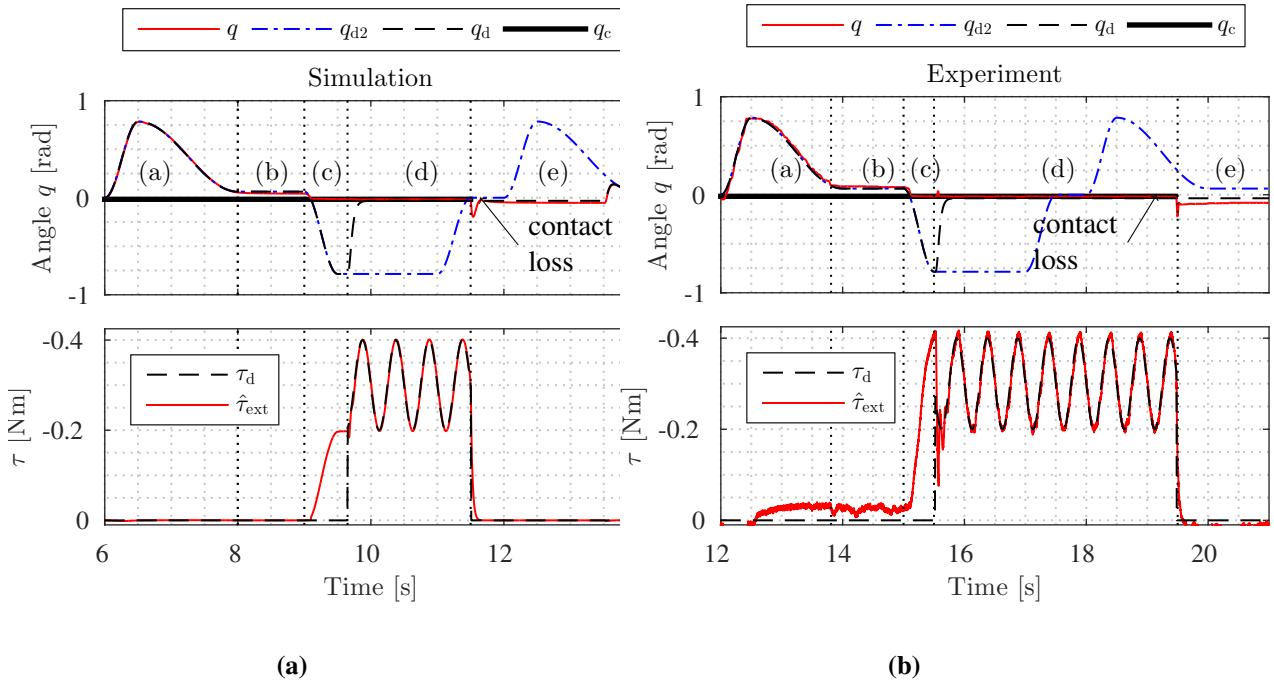

(a) **(b)**

Figure 4.17 Position tracking with a contact/non-contact situation under unified torque/impedance controller comparing the simulation and the experimental device

Figure 4.18 investigates the contact loss between $t = 19.45$ s and $t = 19.55$ s of Fig. 4.17b in more detail. The maximum angular deflection amounts to -0.062 rad or $-3.56°$, respectively. 70 ms after contact loss occurs, the system reaches a resting position. The difference to the desired angle q_d may be explained by friction. The upper row of Fig. 4.17b shows the result of the shaping function ρ. It is evident that the shaping function decays smoothly to zero before the torque control is switched off.

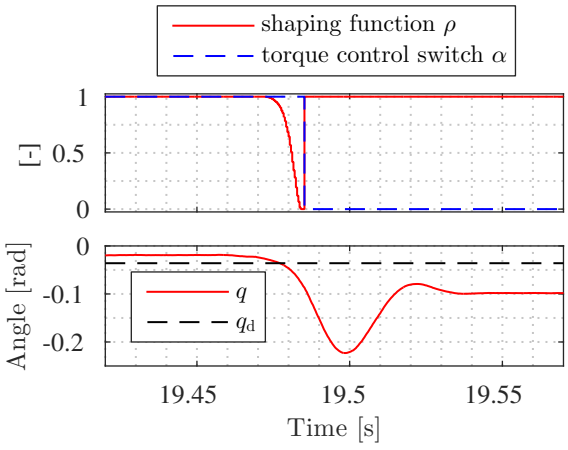

Figure 4.18 Enlarged section of Fig. 4.17b clearly visualizing the contact loss

In this section, it was shown that the new concept of unified torque impedance controller can be successfully applied to the pneumatic robot joint. The next section proposes and evaluates novel pneumatic actuator-level methods such as a pneumatic disturbance observer and a compensated sliding mode force controller.

4.2.4 Leakage Observation

On the pneumatic level, the piston force can be controlled by state-of-the-art sliding-mode controllers. However, disturbances such as leakages remain a significant limitation for performance. For this reason, a novel pneumatic disturbance observer is introduced in this section, which is designed pursuant to the well-known momentum observer concept known from soft and tactile robotics [33], see Tab 4.1. This new observer allows for measuring disturbances in a pneumatic chamber, which can be transformed to leakages when combining the observer results of two pneumatic chambers, respectively. Consequently, an observer-based leakage estimation and measurement becomes possible. In addition, a controller structure is proposed to equip the sliding mode force controller in Sec. 3.3.3 with the output of the observer. This further improves the performance, robustness and accuracy of the force controller – even in the case of extreme system parameter changes, such as lost pipes.

Table 4.1 Comparison between mechanical momentum observer from [265] and this work. Mechanical terms: Momentum $\boldsymbol{p}$. Measured units $\square$, estimated units $\hat{\square}$.

Mechanical momentum observer [33]	Approach: $\dot{\hat{\boldsymbol{\tau}}}_{\text{ext}} = K_{\text{o}} \left(\dot{\hat{\boldsymbol{p}}} - \dot{\boldsymbol{p}} \right)$ Assumption: $\dot{\hat{\boldsymbol{\tau}}}_{\text{ext}} = \boldsymbol{0}$ Observer: $\hat{\boldsymbol{\tau}}_{\text{ext}} = \ldots$ $= K_{\text{o}} \left(\int_0^T \left[\boldsymbol{\tau} - \boldsymbol{\beta}(\dot{\boldsymbol{q}}, \boldsymbol{q}) - \hat{\boldsymbol{\tau}}_{\text{ext}} \right] \mathrm{d}t - \dot{\boldsymbol{M}}(\boldsymbol{q}) \dot{\boldsymbol{q}} \right)$ $\boldsymbol{\beta}(\dot{\boldsymbol{q}}, \boldsymbol{q}) = \boldsymbol{C}(\boldsymbol{q}, \boldsymbol{q}) + \boldsymbol{g}(\boldsymbol{q}) + \dot{\boldsymbol{M}}(\boldsymbol{q}) \dot{\boldsymbol{q}}$
Pneumatic observer (this work)	Approach: $\dot{\hat{z}} = K_{\text{o}} \left(\dot{\hat{P}} - \dot{P} \right)$ Assumption: $\dot{\hat{z}} = 0$ ... see Sec. 4.2.4 ... Observer: $\hat{z} = K_{\text{o}} \left(\int_0^T \left(\dot{\hat{P}} - \hat{z} \right) \mathrm{d}t - P \right)$ $\dot{\hat{P}} = \frac{R \sqrt{T_{\text{atm}}}}{V(x)} \sum_i^n \alpha_i \dot{m}_{\text{in}} - \alpha \frac{P}{V(x)} \dot{V}(x)$

Consequently, this method can also be used for detecting system parameter changes, and if used as a disturbance compensator in the controller, to improve performance, robustness and accuracy.

Disturbance Model

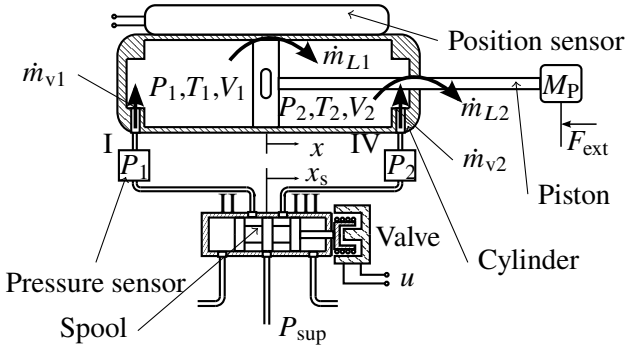

Figure 4.19 Architecture of the considered pneumatic system with leakage

An updated model of the disturbed system is proposed below. In contrast to the chamber description in (3.48), the model is now rewritten[1] as

$$\dot{P} = \dot{\tilde{P}} - z, \tag{4.20}$$

with

$$\dot{\tilde{P}} = \frac{R\sqrt{T_{\text{atm}}}}{V(x)} \overbrace{(\alpha_{\text{in}}\dot{m}_{\text{in}} - \alpha_{\text{ex}}\dot{m}_{\text{out}})}^{\dot{m}_{\text{v}}} - \alpha_{\text{mt}} \frac{P}{V(x)} \dot{V}(x) \tag{4.21}$$

being the ideal chamber model. Furthermore, z is the disturbance and $\dot{m}_{\text{v}}$ is the combined in- and outflow of the respective valve.

Now, leakages $\dot{m}_{\text{L1}}$ and $\dot{m}_{\text{L2}}$ are introduced, see Fig. 4.19, which are incorporated into the model by (4.21), (4.20). These scalar chamber equations can be stacked to a double chamber system

$$\begin{pmatrix} z_1 \\ z_2 \end{pmatrix} = \begin{pmatrix} \frac{R\sqrt{T_{\text{atm}}}}{V_1(x)} & 0 \\ -\frac{R\sqrt{T_{\text{atm}}}}{V_2(x)} & \frac{R\sqrt{T_{\text{atm}}}}{V_2(x)} \end{pmatrix} \begin{pmatrix} \dot{m}_{\text{L1}} \\ \dot{m}_{\text{L2}} \end{pmatrix}. \tag{4.22}$$

With this, the effect of all mass flows $\dot{m}_{\text{v}i}$, $\dot{m}_{\text{L}i}$ and volume changes $V(x)$ is summed up on $\dot{P}$ in (4.20). For this, $\dot{m}_{\text{L1}}$ and $\dot{m}_{\text{L2}}$ are calculated by using the flow model (3.49) (as used for the valve) but with a constant, significantly smaller leakage area $A_{\text{m},X} \hat{=} A_{\text{m,L}i} \ll A_{\max}$ than that of the valve aperture.

Consequently, equation (4.22) computes the disturbances z_1 and z_2 (e.g., in Pa/s) based on the actual leakages, $\dot{m}_{\text{L1}}$ and $\dot{m}_{\text{L2}}$ (e.g., in g/s). In particular, equation (4.22) takes into considerate the lossless forward and backward transformation between $\dot{m}_{\text{L}}$ and z.

Observer Design

In the following analysis shows that the observer resembles the dynamics of a first order Linear Time Invariant (LTI) system with first order dynamics.

First, let us define the residual dynamics [269], [270] of the observer and the disturbance model to be

$$\dot{\hat{z}} = k_{\text{o}} \left(\dot{\hat{P}} - \dot{P} \right), \dot{\hat{z}} = 0, \tag{4.23}$$

with the observer gain k_{o}, see also Tab. 4.1. Estimated entries are indicated by $\hat{\square}$. $\hat{\dot{P}}$ denotes the estimated chamber pressure

$$\hat{\dot{P}} = \dot{\tilde{P}} - \hat{z}, \tag{4.24}$$

which is composed of the ideal chamber dynamics $\tilde{P}$ from (4.21) and the estimated disturbance $\hat{z}$. When inserting equations (4.20) and (4.24) into (4.23), it follows that

$$\hat{z} = k_{\text{o}} \int_0^T \left(\dot{\tilde{P}} - \hat{z} \right) \text{dt} - \underbrace{k_o \int_0^T \left(\dot{\tilde{P}} - z \right) \text{dt}}_{Y}. \tag{4.25}$$

The expression Y in (4.25) can be substituted by the actual chamber pressure P after applying an integration of (4.20) over time. Consequently, the final observer form becomes

$$\hat{z} = k_{\text{o}} \int_0^T \left(\dot{\tilde{P}} - \hat{z} \right) \text{dt} - k_{\text{o}} P, \tag{4.26}$$

[1] A negative sign for z is used as it is necessary for derivation of the disturbance observer and the signs in (4.29).

or in more detail

$$\hat{z} = k_\mathrm{o} \int_0^T \left(\frac{R\sqrt{T_\mathrm{atm}}}{V(x)} \left(\alpha_\mathrm{in}\dot{m}_\mathrm{in} - \alpha_\mathrm{out}\dot{m}_\mathrm{out}\right) - \alpha \frac{P}{V(x)}\dot{V}(x) - \hat{z} \right) \mathrm{dt} - k_\mathrm{o} P, \tag{4.27}$$

when inserting the nonlinear pneumatics model[2] from (4.21).

The observer dynamics between actual and estimated error z and $\hat{z}$ can be analyzed by following the approach from [270]. From (4.25), it follows that

$$\hat{z} = -k_\mathrm{o}\frac{1}{s}\hat{z} + k_o\frac{1}{s}z, \tag{4.28}$$

when applying a Laplace transformation, with s being the complex variable, and canceling out $\dot{\hat{P}}$. Obviously, (4.28) can be written as

$$\hat{z} = \frac{k_\mathrm{o}}{s + k_\mathrm{o}} z, \tag{4.29}$$

which is a stable first order LTI low-pass filter or PT1 system. The cancellation of $\dot{\hat{P}}$ in (4.28) also shows that the observer is not affected by external forces or friction.

Leakage Estimation

The simulations and experiments below investigate the ability of the observer structure for estimating disturbances and leakages. In particular, two observers are required to estimate the leakage in a double actuated cylinder.

The simulation in Figure 4.20a shows the observer response for two disturbance step inputs z_1 and z_2 (row four). In this experiment, no leakage model is used. The system is driven in open loop control mode via a sinusoidal voltage u (row 1). As a result, a complex pressure evolution in both chambers can be observed (row 2). At $t = 0.25$ s and $t = 0.3$ s, two step signals of z_1, z_2 until $t = 0.5$ s and $t = 0.55$ s are applied. Both disturbances are estimated correctly with the expected dynamics (4.29) at high precision (row 4). Also, the estimation quality is not affected by the varying force F (row 3) that is present at the piston.

Fig. 4.20b shows a simulation with the leakage plant model (4.22), (4.20) and a leakage estimation of the observer. The system runs in open loop control mode via two stepwise voltages. It can be observed that the chamber pressures rise for non-zero voltages. When the voltage is 0 % and the pressures are higher than the atmospheric pressure, a declining behavior can be recognized in the pressure (second row), which is affected by the two leakages. Investigating the observer leakage estimation, it can be seen that the disturbance is estimated correctly within the expected observer dynamics (third row). Additionally, $\hat{z}_1$ and $\hat{z}_2$ can be transferred to $\hat{\dot{m}}_{L1}$ and $\hat{\dot{m}}_{L2}$ via (4.22), see the last row of the figure.

The experiment, depicted in Fig. 4.21, explores the capabilities of the observer to estimate leakages in SI units under isolated conditions (without inflowing valve mass flows). Referring to Fig. 4.19, entrance II is blocked with a plug. As chamber 2 is filled with air by activating the valve voltage, only leakage affects the pressure evolution of chamber 1. An observer gain of $k_\mathrm{o} = 50$ is used. It can be noted that the sign of $\dot{m}_\mathrm{L1}$ changes according to the sign of $P_1 - P_2$. A maximum leakage of < 0.1 g/s can be observed. Due to the small magnitude of the flow (< 0.1g/s), the validation with external measuring devices, such as flow sensors, is difficult. Instead, $\dot{m}_\mathrm{valid} = \dot{m}_\mathrm{in}$ is calculated based on (4.21) by differentiating low pass filtering P_1 numerically ($\omega_c = 25$ 1/s) and setting $\alpha_\mathrm{mt} = 1$. Very similar results obtained by this validation step validate the observer calculation.

[2] The other dependencies (3.49)-(3.51) are omitted for a better readability.

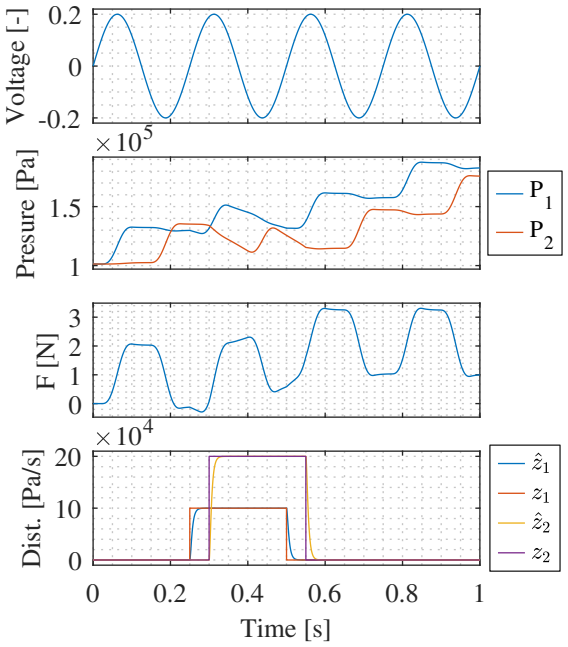

(a) Disturbance observers estimates for complex input voltages and pressure signals.

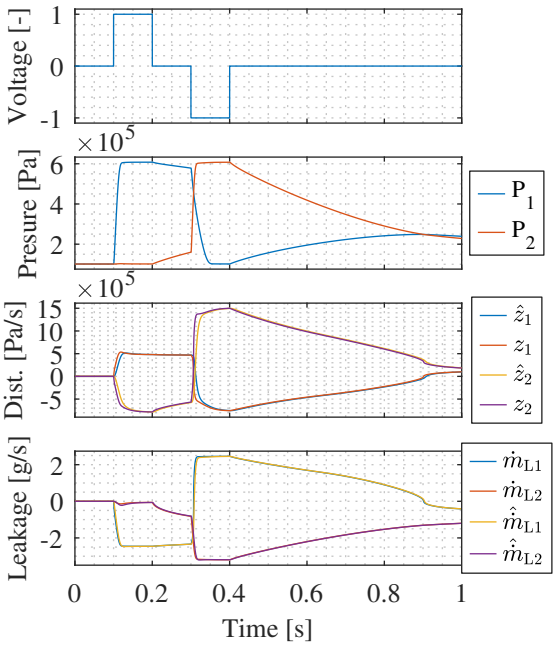

(b) Disturbance observers estimates independent leakage flows $\hat{z}_1$ and $\hat{z}_2$.

Figure 4.20 Open-loop pressure disturbance simulation

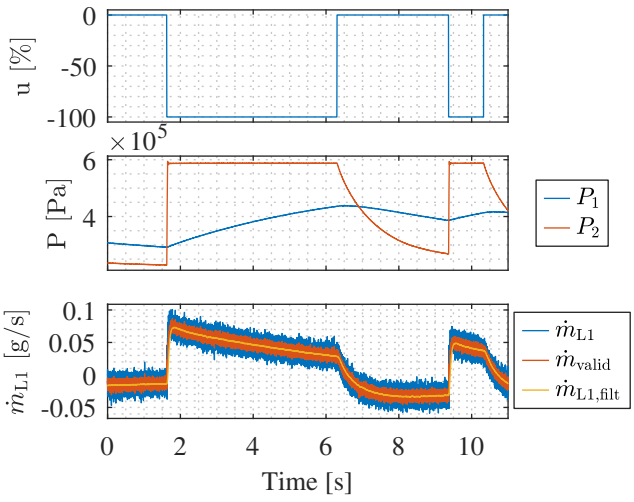

Figure 4.21 Experiment: Leakage observer for a single chamber, port II at Fig. 4.19 is blocked.

4.2.5 Leakage Compensated Force Control

Figure 4.22 investigates the observer extended sliding mode force control, as depicted below. In particular, Fig. 4.22 shows how the observer (4.27) can handle disturbances in closed loop control together with the sliding mode force controller (3.55). The controller is derived according to the *reduced order* controller from [81], but with z_1 and z_2 implemented in the approach.

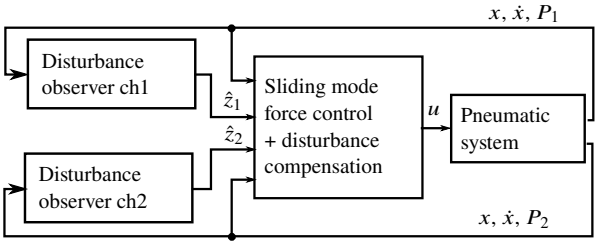

Figure 4.22 Sliding mode force control with disturbance compensation for chamber 1 (ch1) and chamber 2 (ch2)

The simulation in Fig. 4.23a shows how leakage influences the observer extended controller. Here, the leakage model of (4.22), (4.20) is used in plant modeling. The observer compensation is active, however, when switched off between $t = 0.3$ s and $t = 0.7$ s. When the disturbance observer is active, it can be observed that the force is accurately tracked . If the observers are switched off and the estimated leakages $\hat{z}_1$ and $\hat{z}_2$ drop to zero, the desired force cannot be tracked accurately anymore. When the disturbance observers are active, the controller returns again to its original performance.

The experiment, with the results shown below in Fig. 4.23b, is done according to the simulation in Fig. 4.23a. In contrast to the latter, the origin of disturbances may be unmatched model parameters or leakages. Prior to the experiment, the control gains were reduced until the sliding mode controller was not able to track the desired force anymore (i.e., the observer was switched off). Figure 4.23b shows the control performance of the observer-extended sliding mode controller, see Fig. 4.22. Clearly, the controller is able to track the desired force, however, if the observers are switched off, between $t = 2$ s and $t = 4.5$ s), the tracking performance decreases significantly, as shown in the simulation.

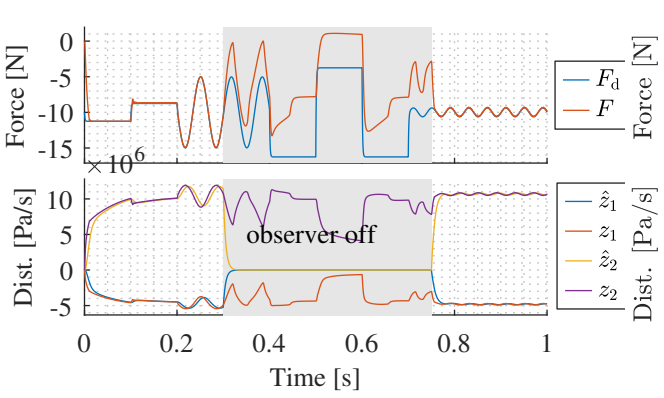

(a) Simulation with a leakage compensation

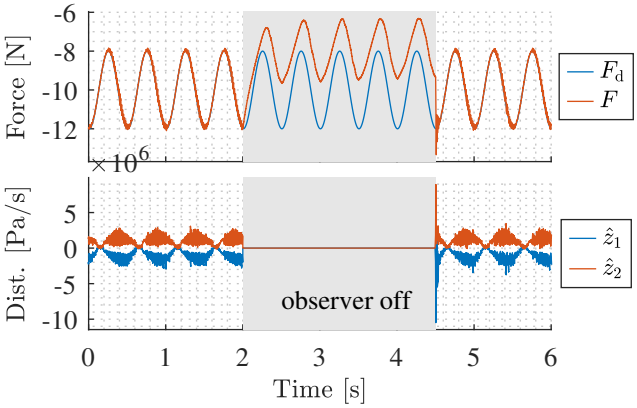

(b) Experimental lekage compensation

Figure 4.23 Sliding mode force controller with disturbance compensation

4.3 Multi Joint Control

After analyzing the aforementioned pneumatic 1-dof system with actuator- and joint-level, multi joint structures are investigated in the following section.

4.3.1 2-dof Wrist

Figure 4.24 depicts the cascaded controller structure for the 2-dof antagonistic robot joint from Fig. 4.4. In analogy to the 1-dof system, the system model is obtained by MDH-parameters following the approach from Sec. 3. The transmission is based on the tendon Jacobian $\boldsymbol{J}_\mathrm{t}(\boldsymbol{q})$ by deriving the extension function $\boldsymbol{h}(\boldsymbol{q})$ from (3.74). According to the 1-dof system, the 2-dof joint is actuated by force controlled pneumatic cylinders for which both pneumatic modeling and force control are described in Sec. 3.3.3. The control scheme from Fig. 4.24 shows the specific tendon mappings as conceptually introduced in Fig. 3.7.

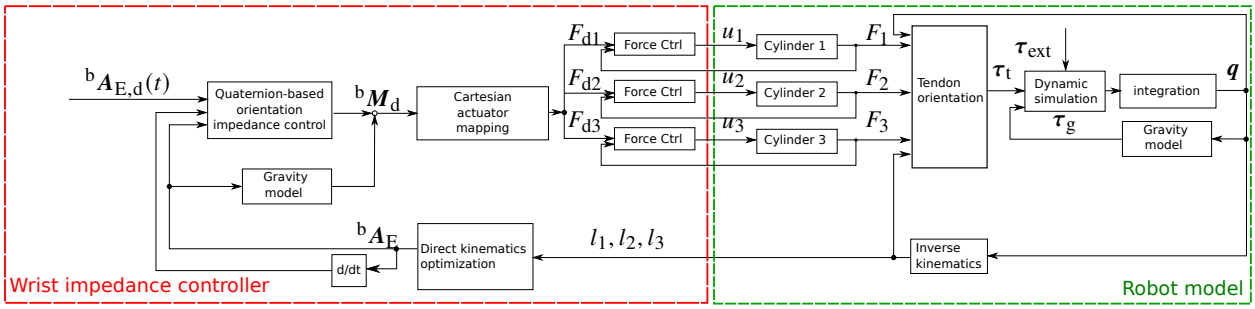

Figure 4.24 Control and simulation model for the 2-dof pneumatically controlled 3SPS-1RR robot

This system is controlled by a quaternion-based Cartesian-level impedance controller, see Fig. 4.24, and derives from the concept in [250] and elaborated accordingly for the pneumatic systems. Furthermore, the desired and current orientation of the end effector are represented by the quaternions $\mathfrak{Q}_\mathrm{d} = \boldsymbol{f}\left({}^\mathrm{b}\boldsymbol{A}_{2,\mathrm{d}}\right)$ and $\mathfrak{Q}_\mathrm{e} = \boldsymbol{g}\left({}^\mathrm{b}\boldsymbol{A}_2(\boldsymbol{q})\right) \in \mathbb{R}^{1\times 4}$. The actual orientation ${}^\mathrm{b}\boldsymbol{A}_2(\boldsymbol{q})$ is obtained by the kinematics model (3.30) and the joint angles by the optimization (3.61). The respective orientation error of the controller is expressed by

$$\mathfrak{Q}_\mathrm{de} = \mathfrak{Q}_\mathrm{e}^{-1}\mathfrak{Q}_\mathrm{d} = \begin{pmatrix}\bar{\rho} & \bar{\boldsymbol{\eta}}\end{pmatrix}, \tag{4.30}$$

consisting of a scalar and vector part $\bar{\rho} \in \mathbb{R}^{1\times 1}$ and $\bar{\boldsymbol{\eta}} \in \mathbb{R}^{1\times 3}$, respectively. It yields $\mathfrak{Q}^{-1} = \frac{-\bar{\mathfrak{Q}}}{\|\mathfrak{Q}\|_2}$, which is the inverse of a quaternion using its adjoint $\bar{\mathfrak{Q}}$. The desired torque ${}^\mathrm{b}\boldsymbol{M}_\mathrm{d}$ in Cartesian coordinates of b is obtained by the impedance control law

$${}^\mathrm{b}\boldsymbol{M}_\mathrm{d} = \boldsymbol{K}_\mathrm{p}({}^\mathrm{b}\boldsymbol{A}_2\bar{\boldsymbol{\eta}}) + \boldsymbol{D}_\mathrm{p}(\boldsymbol{\omega} - \boldsymbol{\omega}_\mathrm{d}) + {}^\mathrm{b}\boldsymbol{\tau}_\mathrm{g}, \tag{4.31}$$

with ${}^\mathrm{b}\boldsymbol{M}_\mathrm{g}$ being the gravitational vector expressed in base coordinates. This may be modeled as

$${}^\mathrm{b}\boldsymbol{M}_\mathrm{g} = {}^\mathrm{b}\boldsymbol{A}_2\,{}^2\boldsymbol{r}_\mathrm{com} \times (m_j\,{}^\mathrm{b}\boldsymbol{g}), \tag{4.32}$$

where ${}^2\boldsymbol{r}_\mathrm{com}$ is the COM, m_j is the mass and ${}^\mathrm{b}\boldsymbol{g}$ is the gravity vector. The desired moment is mapped to joint coordinates by

$$\boldsymbol{\tau}_\mathrm{d} = \boldsymbol{J}^T(\boldsymbol{q})\begin{pmatrix}\boldsymbol{0}_{3\times 1} \\ {}^\mathrm{b}\boldsymbol{M}_\mathrm{d}\end{pmatrix} \tag{4.33}$$

and to tendon forces by (3.63). $\boldsymbol{K}_\mathrm{p}$ and $\boldsymbol{D}_\mathrm{p} \in \mathbb{R}^{3\times 1}$ are the positive impedance gain vectors for adjusting rotational stiffness and damping. The task stiffness is $K_\mathrm{task} = \frac{\tau_\mathrm{ext}}{\epsilon} \approx \frac{1}{2}K_{\mathrm{p},i}$ for small angular deflections ϵ around the set-point $\mathfrak{Q}_\mathrm{d}$. For larger angles, the stiffness scales according to the nonlinearities of $\boldsymbol{K}_\mathrm{p}({}^0\boldsymbol{A}_\mathrm{E}\bar{\boldsymbol{\eta}})$ in (4.31). $\boldsymbol{\omega}_\mathrm{d}$ denotes the desired wrist angular velocity. $\boldsymbol{\omega}$ may be obtained by numerical differentiation.

Joint Angle Motion

The joint angle tracking capability of the system is investigated both in simulation and experiment, see Fig. 4.25. The desired trajectory consists of a 5th-order polynomial with duration of $t = 0.3$ s per motion interval. Arbitrary combinations of 0 deg, ±45 deg are set to q_1 and q_2. The results show that the angular

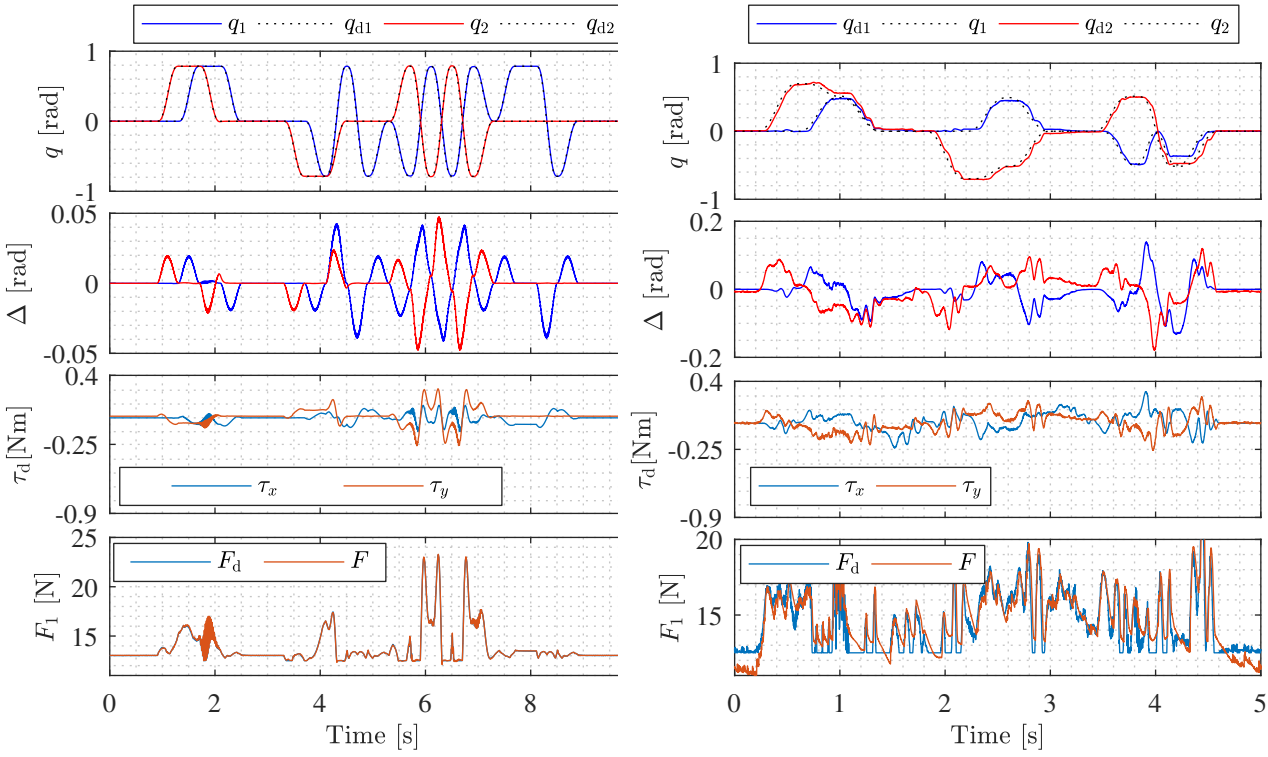

(a) Simulation **(b)** Experiment

Figure 4.25 Orientation tracking for simulation and experimental device

position of the wrist is tracked correctly with a maximum control error ≤ 0.05 rad ≈ 3 deg for the simulation and ≤ 0.1 rad ≈ 6 deg for the experiment, see row 2 of (a) and(b). Furthermore, it reveals that the desired moment are very similar in magnitude for simulation and experiment, see row 3, underlying the quality of simulation. The last row shows the underlying force control of the robot on the first cylinder. Again, simulation and experiment are in good agreement. Still, in simulation shorter response times of the force controller are observed, while in the experiment, higher control errors can be observed, which presumably occur due to unmodeled effects.

Gravity Compensation

The gravity compensation controller is tested by mounting a 200 g payload to the end effector, see Fig. 4.26. One can see that the weight is compensated by the robot in arbitrary configurations with no noticeable drift.

External Contact and Impact Robustness

The response of the wrist in a human robot interaction scenario can be found in Fig. 4.27. The system is commanded to regulate a desired angle of $q_1 = 0$ and $q_2 = 0$. It is deflected from its set point by manual interaction and then released (left column). The trends of $\boldsymbol{\tau}_d$ and $F_{d,1}$ follow the trend of the deflection. As the system is relieved, all control states stabilize after $t = 0.4$ s. The right column shows the system behavior under the same conditions for an impact, see Fig. 4.27. The results appear to align with those of the previous experiment. The system stabilizes itself $t = 0.3$ s after the impact.

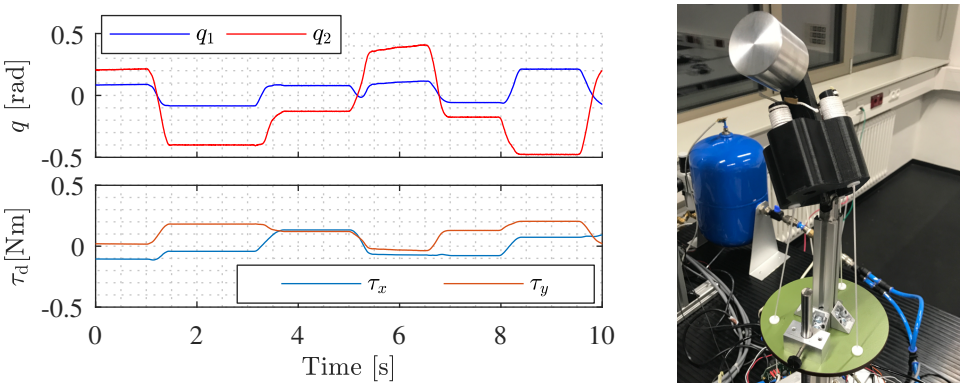

(a) Exeperimental data

(b) Experimental setup

Figure 4.26 Gravity compensation experiment

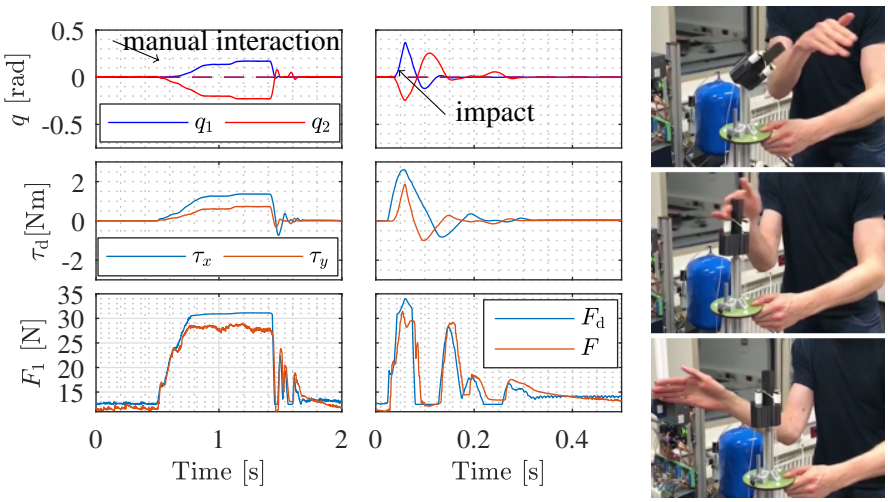

(a) Experimental data of deflection and collision experiment

(b) Photo sequence of the collision experiment

Figure 4.27 Deflection and collision experiment

4.3.2 7-dof System Simulation

Finally, the simulation below examines the 7-dof pneumatic robot with the kinematics and rigid body dynamics of the Franka Emika robot. With this, the feasibility of pneumatic actuation for soft and tactile robots is investigated for a full robot. The simulations aim for presenting strengths, weaknesses, performance and possible application scenarios. This severs the analysis of the strength, weaknesses, performance and possible application scenarios of potential future systems.

Position Tracking

Two position tracking scenarios are investigated by the following figures. Figure 4.29 shows sinusoidal joint position tracking, with the robot depicted above. Row 1 depicts accurate joint position following with underlying joint torque control in row 2 and 3. Additionally, joint velocity, input voltage and chamber pressures are shown for the fourth joint in row 4, 5 and 6. The utilized stiffness is $K_{\text{imp3}} = 60\,\text{Nm/rad}$, which was close to the highest working parameter set of the simulation. The last row depicts the Cartesian error for three different joint stiffness values $K_{\text{imp1}} = 10\,\text{Nm/rad}$, $K_{\text{imp2}} = 40\,\text{Nm/rad}$, $K_{\text{imp3}} = 60\,\text{Nm/rad}$. Additionally, the stiffness $K_{\text{imp3,id}} = K_{\text{imp3}}$ instigates the Cartesian error by assuming $\boldsymbol{\tau} = \boldsymbol{\tau}_{\text{d}}$. The control error in Cartesian space, see row 6, increases with lower stiffness values of K_{imp}, ranging from $\approx 2\,\text{cm}$ to

$\approx 6\,\text{cm}$. As a comparison, the ideal actuator assumption does not lead to a remaining error $K_{\text{imp3,id}}$. This means that the pneumatic actuator has a negative effect on the position accuracy.

Figure 4.31 shows a maximum speed test. The robot is commanded to follow a straight line in vertical direction. The trajectory from row 1, with the respective acceleration from row 2, is applied to the robot. Cartesian control is performed by an inverse kinematic solver, which provides suitable joint angles for the Cartesian trajectory. Maximum Cartesian velocities of $1.5\,\text{m/s}$ and acceleration of $3\,\text{m/s}^2$ are achieved, as depicted in row 2. Additionally, actuator information of the deflection angle in row 3, actuator speeds in row 4, actuator voltage in row 5, actuator torque control in row 6, and chamber pressures are provided in row 7, showing i) the accuracy in position, velocity and acceleration and actuator torque control and ii) the evidence for the underlying pneumatic behavior.

Collision Behavior

Collision behavior of the simulated 7-dof system is investigated in Fig. 4.29 and Fig. 4.31. The former shows the results of a ball drop test for three different joint stiffness values of $K_{\text{imp}} = \{5\,\text{Nm/rad}, 30\,\text{Nm/rad}, 60\,\text{Nm/rad}\}$, respectively. An animation of the experiment is depicted in the figure above. The ball has a weight of 3 kg and is dropped from a height of 20 cm above the end effector. The underlying collision model can be found in the Appendix A.1.2. Row 1 of the figure depicts the absolute external force being $\approx 200\,\text{N}$ for all stiffness values. Row 2 shows the joint deflection of joint 4 for all different stiffnesses. Clearly, deflection increases with lower joint stiffnesses. The joint torque control shows that the slope of the torque control is limited, possibly as the valves provide limited in- and outflow. Furthermore, the maximum simulated torque of $\approx 50\,\text{Nm}$ is lower than the maximum torque of the actuator. However, bearings and structure are not considered. Also, no joint limit collisions occur, which means that the impact energy can be fully absorbed by the controlled air chambers. Finally, the momentum observer is investigated in row 4. The impact torque can be accurately estimated based on the pressure sensors.

Figure 4.31 investigates an intended collision with an obstacle, such as a table, for two different stiffness valves, leading to $\approx 300\,\text{N}$ contact force. For both stiffness parameters, the torque controllers and the momentum observer can handle the impact. The good momentum observer performance in the presence of noise in the pressure sensors (10 % full scale) is depicted in Fig. 4.36.

The final experiment, shown in Fig. 4.37, analyses the possible accuracy for a very shallow contact. For this, it is expected that the robot is equipped with low friction cylinders (as already used with the other pneumatic robot joints). Consequently, the joint torque measurement is expected to be of high quality. For this, a small ball (300 g) is dropped onto the robot. Due to the combination of the small mass and the short contact time, the observer output hardly rises up to 20 N. Note that the actual peak reaches $\approx 60\,\text{N}$.

These simulations reveal that the the 7-dof pneumatic robot achieves a high speed, impact robustness and high precision when using the momentum observeration. The following section concludes this chapter.

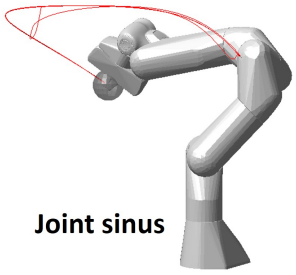

Figure 4.28 Trajectory tracking

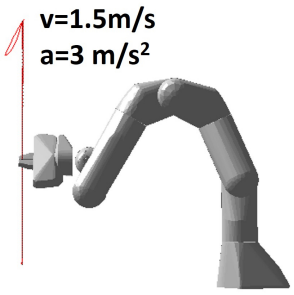

Figure 4.30 Fast vertical motion

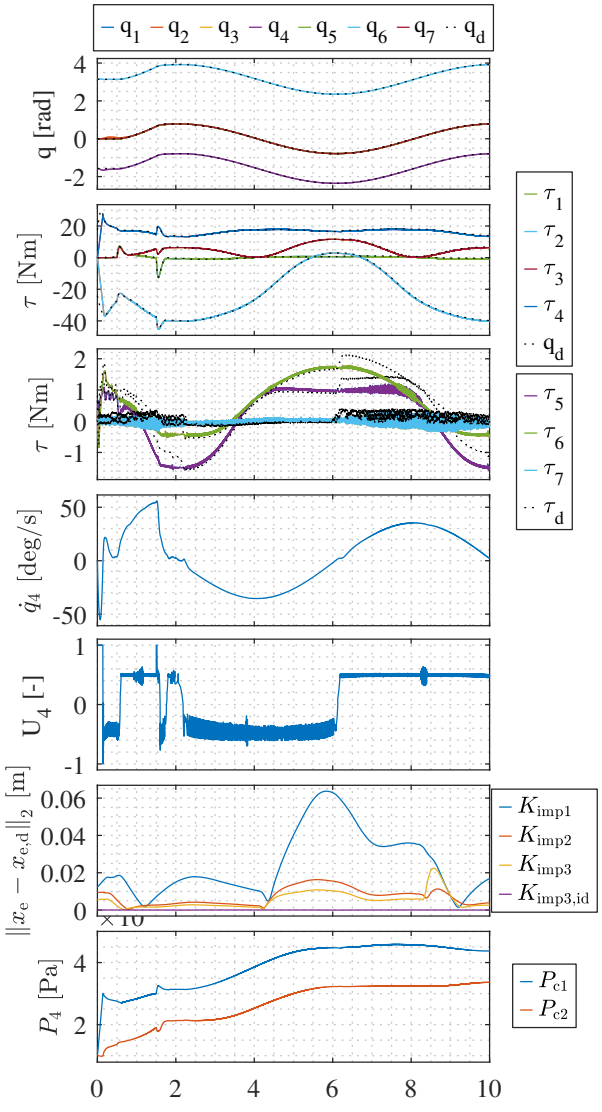

Figure 4.29 Cartesian position error for simulating different joint stiffnesses

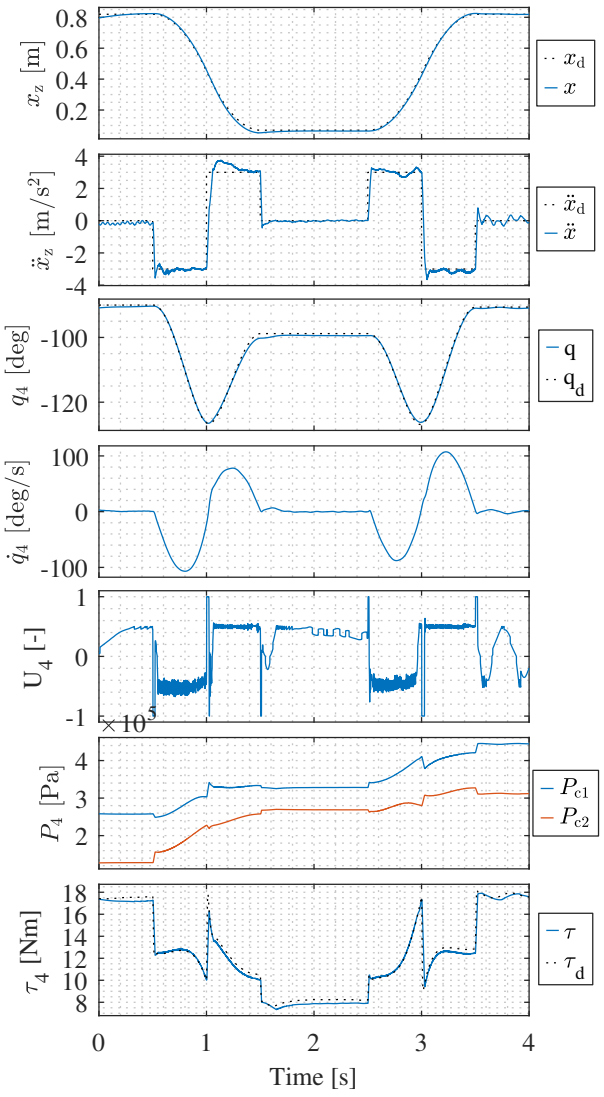

Figure 4.31 Simulating fast vertical motion tracking

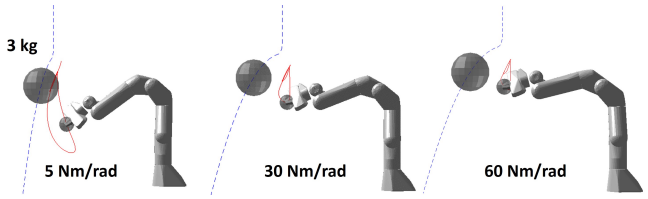

Figure 4.32 Ball drop for different joint stiffnesses

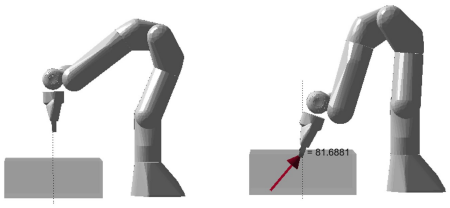

Figure 4.34 Table collision for different joint stiffnesses

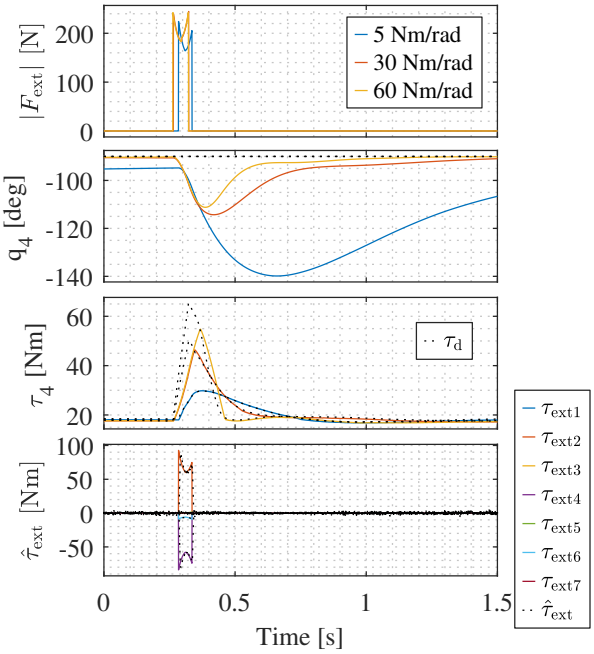

Figure 4.33 Data of the ball drop simulation

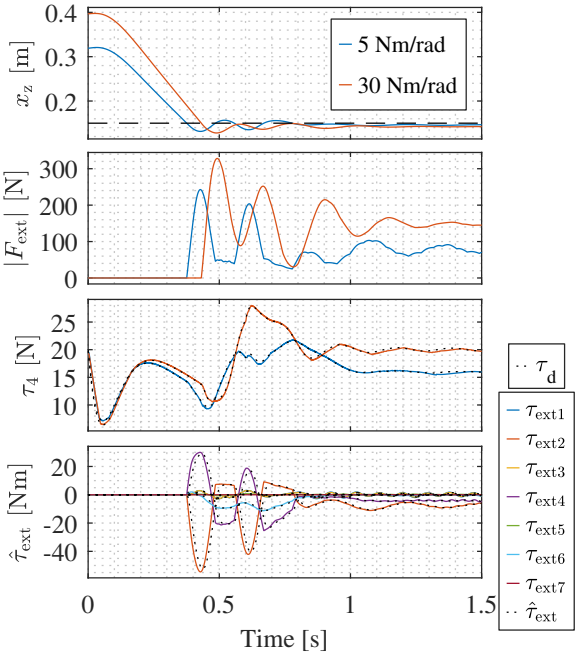

Figure 4.35 Data of the table collision simulation

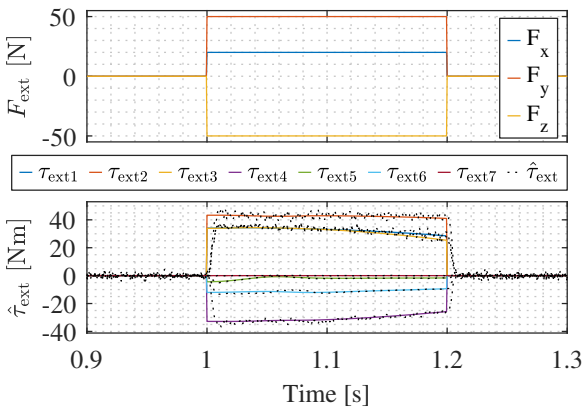

Figure 4.36 External force step evaluated by the observer

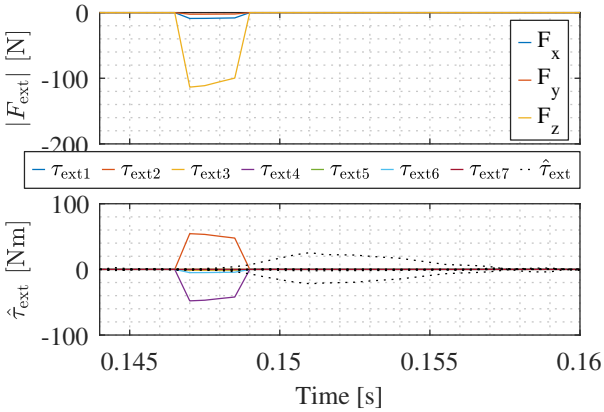

Figure 4.37 Ball drop test with small ball

4.4 Summary

This chapter utilized the modeling and control framework from Chapter 3 for a systematic transfer of technologies from soft and tactile robots to pneumatics. The following contributions were made

- a systematic transfer of mechatronics and control methods from soft and tactile robots to pneumatics, exemplarily researched for the proposed 1-dof, 2-dof and 7-dof kinematic structures,
- a biologically inspired concept for 1-dof and 2-dof robot joints by proposing a tendon-driven, muscle-like actuation concept using force-controlled pneumatic cylinders,
- model-based controllers for joint impedance, joint torque, gravity compensation, unified torque/impedance, contact loss, and external joint torque,
- observers for external joint torque and pneumatic-level disturbances such as leakages, including a compensation scheme for sliding-mode force control by using the output of the pneumatic-level disturbance observer applied to pneumatic robots, and
- a feasibility simulation of a 7-dof pneumatic lightweight robot with soft control methods, illustrating future application scenarios of the pneumatic actuation technology.

These advances were achieved by a digital-twin-based simulation approach using the framework from Chapter 3. This allowed for systematic development of model and controllers, such that the feasibility of the systems could be validated in simulation before the devices were realized. Both simulation and control confirmed the fast achievable actuator velocities (Fig. 4.7, Fig. 4.11, Fig. 4.31), fast response (Fig. 4.18), accurate torque control (Fig. 4.15), backdrivability (Fig. 4.27) and impact robustness (Fig. 4.12, Fig. 4.33, Fig. 4.35) of the pneumatically actuated robots. In this regard, the accurate torque control benefits from the low friction cylinder, which is also expected to be a key enabler for precise momentum observer results. In contrast, negative aspects were also observed, such as low precision (Fig. 4.29) and low stiffness (Fig. 4.8, Fig. 4.29) in contrast to electromechanical systems in the simulation and experiment. While not all controller combinations and test scenarios are applied to every system, the evaluated experiments are a significant step for a successful transfer of soft and tactile robotic methods to pneumatic systems.

5 Part II (The "Artificial Neuromuscular Prosthesis")

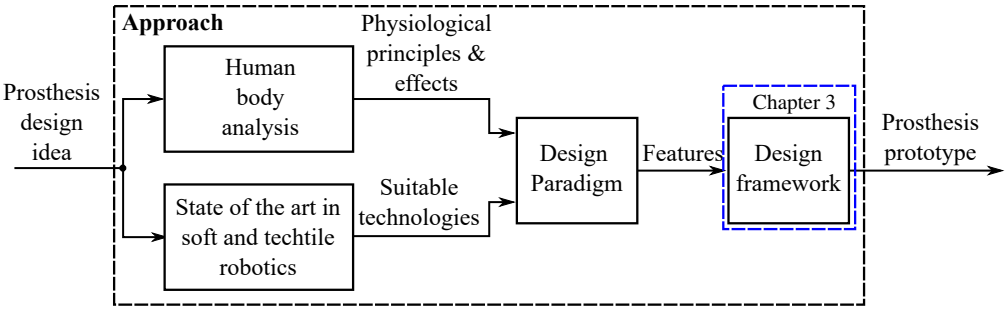

Figure 5.1 Development approach for the upper limb prosthesis

This chapter utilizes the framework from Chapter 3 for developing a novel upper limb prosthesis. Upper limb prostheses are wearable robotic devices, which are attached to the human body, aiming to render the natural functionality of a lost limb as close as possible at maximum robustness. As prostheses should reflect certain properties of human body parts (e.g., in terms of weight, dimensions and appearance), the integration of technical features and the realization of human performance is a significant challenge, and often a trade-off, in the mechatronics design.

Related Work Following the state of the art, remarkable high-tech prostheses have been developed, which achieved human-like size, weight [146, 149, 161], torque and kinematics[149], see Chapter 2. Still very rare in transhumeral prostheses are a full 4-dof human-like kinematics from elbow to wrist, joint torque sensing, as well as active compliance control[1].

Paradigm This work proposes a holistic human-centered development paradigm as the next step for developing the next generation of upper-limb prostheses. The goal of this approach is to design mechanical structures, sensors, actuators, controllers and device intelligence in a systematic manner and based on core functionalities of human neuromechanics. With such a paradigm, the resulting technology choices and specific design details are not the result of a trail-and-error process, or a combination of proven existing technologies, but rather the consequence of a superordinated design and synthesis process with minimal numbers of iteration. The underlying hypothesis is that a human-inspired technical solution, developed by this appraoch, would also provide more human-like behavior.

The importance for a novel paradigm may be better understood when looking at the human: the neuromuscular system stands out for its unmatched actuation in terms of high degrees of freedom, high-torque, low friction and backdrivability. It provides numerous unconscious kinesthetic processes such as gravitiy compensation and impedance adjustment, giving the human a feeling of body and contact awareness. For a prosthesis user, all aforementioned natural functionalities are lost in case of an amputation. Thus, the goal is a prosthesis that symbiotically integrates within the human body and resembles the natural functionality of the human-neuromuscular system as close as technologically possible.

[1] Reported by only one system in [149]

Approach In this work, a prosthesis is proposed, which recreates these natural features such as *body awareness*, *contact awareness*, *human-like kinematics* and *human-like contact response*, which are further described in Sec. 5.2. In this case, *contact awareness* may be understood as an artificial sense of touch using proprioceptive sensor information. An exterioceptive sense of touch, i.e., an artificial skin, was not yet considered for the ANP due to many unsolved challenges of the technology. Insights from human motor control are integrated with the technology from soft, tactile and humanoid robotics, aiming for a human-inspired mechatronic prosthesis design, see Fig. 5.1. This mechatronics concept is obtained by identifying working principles of the human motor control system and by developing a corresponding technological solution for upper limb prosthetics.

Mechatronic Device The resulting device is the Artificial neuromuscular prosthesis (ANP) mimicking the human neuromuscular system in terms of body awareness, contact awareness, contact-response and kinematics. Key features of the ANP mechatronics are i) torque controlled robot joints, ii) a 4-dof kinematics from elbow to wrist and iii) an IMU, which measures the orientation of the device for internal real-time-capable models. Based on that, the Artificial Neuromuscular controller is introduced, consisting of a floating base dynamics, an extended momentum observer and a joint-level impedance controller.

These conceptual advances are accompanied by novel mechatronic development approaches, ensuring additional features in a powerful human-size prosthesis. A gapless mathematical formualtion of the controlled prosthesis, called sim2real-guided design, provides a detailed understanding of the prosthetic device and is used for controller design, dimensioning and choice of components. Consequently, the prosthesis can be adapted exactly to specified loads. Further advances in mechatronics are obtained by a remote tendon actuation of the prosthesis wrist. Especially, the wrist is challenging in the mechatronics design due to the three intersecting rotational axes. While conventional solutions are already hard to be integrated, the use of remote actuation and sensing allows to fit torque controlled wrist joints within the human-like design space. The prosthesis is developed in two prototypes, called prototype I and II, where the later one forms the Artificial Neuromuscular Prosthesis (ANP).

The chapter is structured as follows. Section 5.1 deals with the analysis of the human body. Section 5.2 explains the design paradigm and Sec. 5.3 examines the design process of the prosthesis. The mechatronic prototypes, including control methods are described in Sec. 5.5. The validation of the approach can be found in Sec. 5.6. Finally, the chapter is concluded under Sec. 5.7. The chapter was written based on [17], [19].

5.1 Human Neuromechanics Analysis

Before describing the prosthesis development approach, key aspects of human biomechanics are elaborated that serve several design choices as inspiration.

Elbow-Wrist Biomechanics: The human arm is generally characterized as having 3-dofs in the wrist (F/E, R/U, P/S) and 1-dof in the elbow (F/E). Human muscles are able to generate relatively high joint torques given their size and weight, which poses one of the main challenges to mechatronic prosthesis design. Specifically, the static force-to-weight ratio of the human arm is around 4:1 vs. 1:1 for robotic systems [271]. Human male joint torques from elbow-to-wrist are 40 Nm for the elbow (F/E), 9 Nm for wrist (P/S), 15 Nm for wrist R/U and 11 Nm for P/S [272]. Average maximum speeds of typical human motion (F/E, R/U, and P/S) are 144 deg/s for elbow (F/E), 156 deg/s for wrist (P/S), 108 deg/s for wrist (R/U) and 80 deg/s for (P/S)[2]. The lower arm constitutes up to an estimated 2 % of the human body weight and has a length that is nearly 16 % of the human height [276]. Thus, the ideal transhumeral prosthesis weight and length should be approximately < 2 kg and 25-30 cm for an adult male, while still achieving human-level joint torques.

[2]This is the average velocity of all tasks and subjects from human arm data published in [273, 274, 275].

Motor Control: The human motor control system is characterized by relatively precise movement independent of both body orientation with respect to gravity [277] and visual perception [278, 279]. Humans are also able to perceive and to respond to contact forces, regardless of where along the body the contact occurs. They can distinguish contacts by comparing expected and measured signals [280]. Furthermore, human limbs exhibit accurate compliant behavior during physical interaction with the environment. In fact, the muscle impedance can be modulated; a skill, which is used by humans for learning new motor tasks and compensating for uncertainties [281, 279].

Neuromechanics: The musculoskeletal system is tendon-driven with very low friction and inertia [282, 283], which corresponds to high-performance backdrivability in mechanical terms. A multi-modal sensory system provides a wide range of information about the external world and the state of the body, even without considering the sense of vision, see Fig. 5.3 (left). Muscle spindles and the Golgi tendon apparatus, which are integrated into the muscle fibers and tendons, respectively, provide sensory feedback on muscle length, speed of stretching, and proprioceptive force. A wide variety of tactile sensors in the skin provide detailed information about contact points, pressure, and texture. The vestibular system senses body orientation relative to gravity.

In the Central Nervous System (CNS), the cerebellum, the primary motor cortex, and the spinal cord, are mainly responsible for complex motor control and learning, including adaptation to novel dynamics [284]. It is believed that this is achieved by learning an internal (inverse) dynamics model of the self and of the environment, which may be referred to as a “body image" [285, 286], see Fig. 5.3 (left). Thus, the human does not rely on reactive feedback control only, but is able to deliver predictive feedforward motor commands [287]. Internal models are also used to detect contacts based on proprioceptive sensory information by comparing the expectation from the internal model with the measured signal [280]. Furthermore, human motor control can be described as a form of impedance control [288, 281]. After describing the properties of the human body, a corresponding artificial prosthesis with the aforementioned features shall be derived.

5.2 Design Paradigm

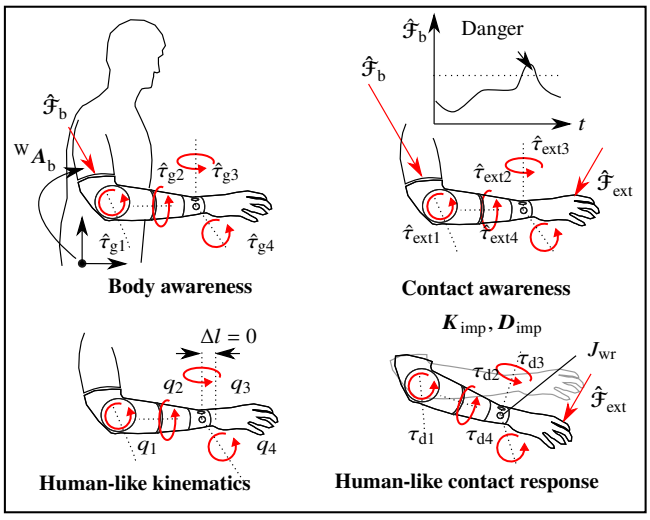

Figure 5.2 Main Features of the Artificial Neuromuscular Prosthesis (ANP)

In this chapter, a novel prosthesis paradigm is introduced that is systematically inspired by the fundamental design and control properties of the human neuromuscular system. In particular, the paradigm renders the following four key properties of the human body, namely *body awareness*, *contact awareness*, *human-like kinematics* and *human-like contact response*, see Fig. 5.2. *Contact awareness* may be understood as an artificial sense of touch using proprioceptive sensor information. An exterioceptive sense of touch, i.e., an artificial skin, is not yet considered due to many unsolved challenges in the basic technology. As the

proposed prosthesis renders these aforementioned features, it is denoted Artificial Neuromuscular Prosthesis (ANP).

Its human-inspired design paradigm is grounded in sensors, actuators and controllers with direct biological correspondence to the human body, see Fig. 5.3.

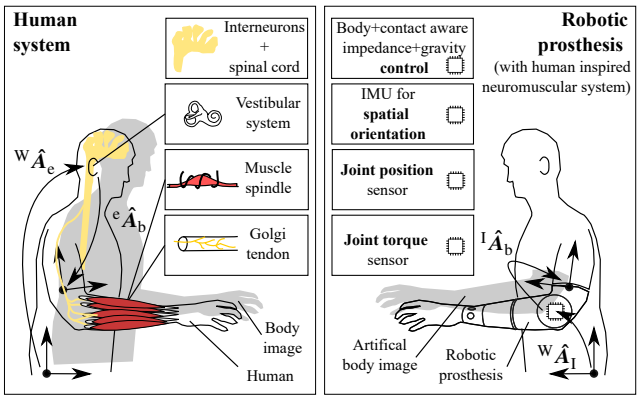

Figure 5.3 Correspondences between human body and artificial prosthesis

It also builds on the concept of the body image [285, 286], which is mathematically speaking, the kinematic and dynamic model that the human has of him/herself, see Fig. 5.3. For the ANP, an artificial body image is proposed, which transfers this concept to the prosthetics field[3]. While the human can determine the body orientation ${}^{\mathrm{W}}\hat{\boldsymbol{A}}_{\mathrm{e}}$ over the spinal cord and limb kinematics ${}^{\mathrm{e}}\hat{\boldsymbol{A}}_{\mathrm{b}}$, the location of the ANP in space can be obtained by the IMU orientation measurement using ${}^{\mathrm{W}}\hat{\boldsymbol{A}}_{\mathrm{I}}$. The device orientation is then used for computing internal models.

Figure 5.4 depicts the state of the art in human motor control (left) and the corresponding mechatronic solution for the ANP with human-inspired sensing, actuation and control methods (right).

In this work, the term *body awareness* is used to refer to the ability of the device to create an artificial body image of the prosthesis kinematics and dynamics as part of the hybrid human/prosthesis body. For this, the joint position $\boldsymbol{q}$ and the base orientation ${}^{\mathrm{W}}\hat{\boldsymbol{A}}_{\mathrm{b}}(\boldsymbol{\varphi}_{\mathrm{b}})$ are measured to compute model-based estimated forces and moments $\boldsymbol{u} = (\hat{\boldsymbol{\tau}}_{\mathrm{g}}, \hat{\mathcal{F}}_{\mathrm{b}})^T$, which act on the prosthesis for the contact-free case. Here, $\hat{\boldsymbol{\tau}}_{\mathrm{g}}(\boldsymbol{\varphi}_{\mathrm{b}})$ denotes the estimated model of gravity torque, and $\hat{\mathcal{F}}_{\mathrm{b}}(\boldsymbol{\varphi}_{\mathrm{b}})$ denotes the estimated base wrench. Similar to the human, *body awareness* is used to adjust the right joint torque $\hat{\boldsymbol{\tau}}_{\mathrm{g}}(\boldsymbol{\varphi}_{\mathrm{b}})$ for holding the joints $\boldsymbol{q}$ in position, regardless of the prosthesis base orientation ${}^{\mathrm{W}}\boldsymbol{A}_{\mathrm{b}}(\boldsymbol{\varphi}_{\mathrm{b}})$, and without using position feedback control. *Body awareness* is extended to *contact awareness* by estimating the external wrench $\hat{\mathcal{F}}_{\mathrm{ext}}$ and its effect on the joint torques and the prosthesis base wrench, expressed by $\boldsymbol{u}^* = (\hat{\boldsymbol{\tau}}_{\mathrm{g}} + \hat{\boldsymbol{\tau}}_{\mathrm{ext}}, \hat{\mathcal{F}}_{\mathrm{b}}(\hat{\mathcal{F}}_{\mathrm{ext}}), \hat{\mathcal{F}}_{\mathrm{ext}})^T$.

Based on these features, the device is equipped with an actively controlled *human-like contact response* in the sense that the device is able to adjust its joint impedance from 0 Nm/rad up to $\approx$ 90 Nm/rad. While conventional high-geared robot joints are hardly backdrivable, backdrivability of the human muscles is emulated by using torque controlled robot joints (as reported in [28]) and exploiting their ability to render arbitrary desired joint torques $\boldsymbol{\tau}_{\mathrm{d}} = \boldsymbol{f}(\boldsymbol{q}, \boldsymbol{q}_{\mathrm{d}}, \boldsymbol{\varphi}_{\mathrm{b}})$. Finally, the prosthesis is equipped with a 4-dof *human-like kinematics* from elbow to wrist, rendering elbow (F/E) and wrist motion (F/E, R/U, and P/S).

As a consequence, the prosthesis is able to behave similar to a human limb in terms of i) *body awareness*, ii) *contact awareness*, iii) *human-like contact response* and iv) *human-like kinematics*, see Fig. 5.2.

[3] In the following, the body image is denoted as *body awareness* and *contact awareness* for the contact-free and contact case.

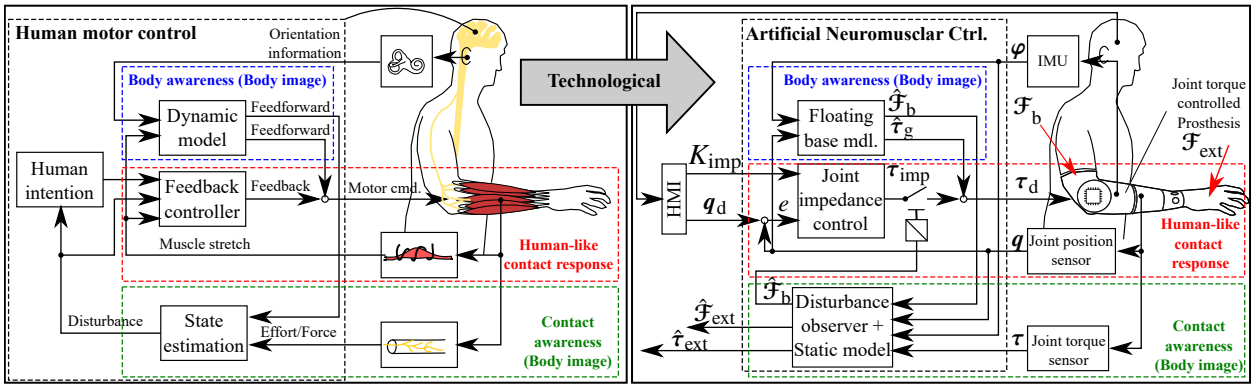

Figure 5.4 Mechatronics concept of the ANP derived from human biomechanics and control concepts. The left image is a modified version from [289] and was extended accordingly.

5.3 Design Process

The design paradigm from Sec. 5.2 introduces new human-inspired features, and specifies the specific choice of actuators, sensors and controllers. However, such a paradigm clearly increases complexity and makes the design and integration of a wearable devices even more challenging for most mechanical solutions. For this reason, a novel approach is required to enable the implementation of these features in a prosthesis with human-like size and weight.

- The first enabler is the use of soft and tactile robotics technology. It allows for
  - precise joint torque and joint/Cartesian position control,
  - complex algorithms to render arbitrary artificial intelligence features,
  - minimized mechatronics to mimic the fineness of human limbs.
- The second enabler is a sim2real-guided development process. With an increasing number of features, the implementation of any additional feature becomes more and more challenging. For this reason, the prosthesis is developed in a simulation-driven design process, using the framework from Chapter 3, and exploiting the capabilities of the mechatronics, and tailoring the mechatronic components exactly to the demanded operating conditions. So, only the minimum required space/weight is utilized, revealing resources for more advanced mechatronic features, such as joint torque sensors. In addition, the digital twin simulation also allows for faster kinematics, actuation, sensing and control iterations, helping in designing an advanced robotic prosthesis.

Sim2real-Guided Design The sim2real-guided design process is shown in Fig. 5.5, where the specific steps of the development process, including the flow of information, are depicted. Based on the initial concept idea from Fig. 5.2-Fig. 5.4, the requirements of the prosthesis, i.e., functional requirements (F), technical requirements (T) and specification (S) are derived. Then, a conceptual approach of the system is elaborated, which includes the kinematic, transmission, sensor and actuation concept. Based on that, a model and control approach is developed and implemented in numerical simulation. This time-domain simulation plays a key role in the sim2real-guided design process, as it provides information about the feasibility of the control concept and about loads acting on components and structure. More specifically, test scenarios are defined, which translate the requirements F, T, S into input trajectories, parameter sets, interactions and test metrics M for simulation and experiment. The simulation is considered successful if all conditions, referred to as *Condition1*, are fulfilled for the full stack of test scenarios, see Fig. 5.5. For this, the full Artificial Neuromuscular Controller, see Fig. 5.4, needs to work together with the plant model in the simulation.

The simulated controller should use the same interface, i.e., actuator commands and sensor readings, as in the experiments. This is important as the ANP is a hybrid tenon/non-tendon driven system. While

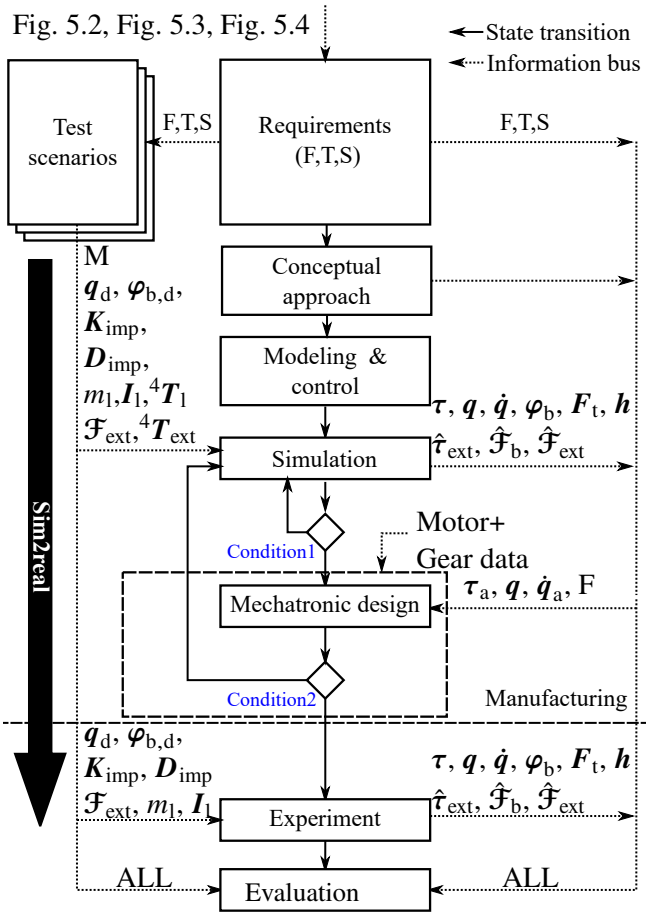

Figure 5.5 Single iteration ANP sim2real guided design process

joints 1 and 2 have to be controlled in joint-space, joints 3 and 4 are controlled in tendon-space. Non-measurable information shall be calculated mathematically, if possible, via mappings, numerical solvers or observers. For that, actuator coordinates, such as angles $\boldsymbol{q}_a$ and torques $\boldsymbol{\tau}_a$, shall be transformed to joint coordinates by $\{\boldsymbol{q}_a, \boldsymbol{\tau}_a\} \rightarrow \{\boldsymbol{q}, \boldsymbol{\tau}_J\}$ and vice versa. The use of the same controller module for simulations and experiments is an approach for dealing with system complexity by early fault elimination, module testing and fast experimental control implementation. In the next step, the mechatronics design is elaborated. This process includes the choice of suitable components, in particular, gears and motors, which provide sufficient performance to realize all simulated values of $\boldsymbol{q}_a, \boldsymbol{\tau}_a$ in the smallest possible design. For this, $\boldsymbol{q}_a, \boldsymbol{\tau}_a$ are compared to motor and gear data, which are provided by component manufacturers. After the component choice, the prosthesis geometry is designed, validated and manufactured. The detailed mechatronic design decision tree, denoted as *Condition2*, is explained in Appendix A.2.1. Finally, the prosthesis is systematically evaluated experimentally. In the following, the specific requirements F, T, S are defined, based on which the ANP was developed.

5.4 Requirements

Functional Requirements (F) - Mechanics:

A transhumeral prosthesis with 3-dof wrist, without a hand is to be developed (F_1). In addition, a modular hand shall be attachable at the wrist (F_2). The prosthesis needs to be wearable by both healthy subjects and individuals with a transhumeral amputation. For healthy subjects, the device shall be attached at the center of the upper arm (humerus) via 3D-printed components and Velcro fasteners (for testing reasons). For users with a transhumeral amputation, the device should be worn by a stump interface in future versions (F_3).

Functional Requirements (F) - Control:

The device shall provide 4-dof motion control from elbow to wrist, which shall be realized by an active compliance controller, controlling force/torque and motion (F_4). More specifically, the prosthesis shall be capable of reproducing everyday real human motion data as close as possible (F_5). The joints of the prosthesis should imitate human muscles in the sense of contact response, joint stiffness and backdrivability (F_6). In gravity compensation, guidance of the device solely via interaction forces shall be possible (F_7). The device shall be equipped with a mechanical body image/body awareness including the floating-base kinematics and robot dynamics of the device. This should include the awareness of joint torques and base reaction forces/moments at the prosthesis attachment affected by gravity and orientation (F_8). By this, the ANP should be able to compensate its own weight during arbitrary operation (F_9). The device is to be equipped with a contact recognition estimating the magnitude of the wrench distal from the wrist (F_{10}). With this, the device is enabled to calculate the effect of the contact wrench on the prosthesis base and the residual limb by providing base forces and moments (F_{11}). In addition, the device shall be equipped with a protective control mechanism to a safe mode (e.g., to gravity compensation) if contacts induce too large base moments (F_{12}). Reaching, grasping and placing objects of Activities Of Daily Life (ADL) shall be possible (F_{13}).

Technical Requirements (T)

These functional requirements are further specified by the following technical requirements. The human-like contact response shall be realized by joint torque controlled robot joints (T_1). This mimics the backdrivability of human muscles if the desired torque is set to zero. Otherwise, they render arbitrary desired torques as provided by an impedance controller or a gravity compensation. For that, the robot joints need to be equipped with a torque sensor to provide appropriate measurement to the torque controller (T_2 to realize F_6). Additionally, the prosthesis shall be equipped with floating-base gravity compensation, essential for providing the body awareness (T_3 to provide F_8, F_9). Consequently, the prosthesis requires at least one IMU, which must be implemented in the control cycle in order to provide spatial orientation measurement to the floating-base gravity compensation (T_4). An active compliance controller shall be realized by joint impedance control (T_5 to provide F_6, F_4). The underlying algorithm of the contact awareness shall be a generalized floating-base momentum observer, enabling the measurement of external joint torques (T_6 to provide F_{10}, F_{11}, F_{12}). In the following section, the technical solutions are introduced. Futhermore, specifications S are listed in Tab. A.6 and Tab. A.7 in the Appendix.

5.5 Solution

Two prosthesis prototypes I and II were developed in this thesis, focusing on realizing the concepts from Sec. 5.2 and the requirements from Sec. 5.4. As prototype I was developed under specific restrictions, not all requirements could be fulfilled within this device generation, see Fig. 5.6. Nonetheless, soft and tactile robotic capabilities could already be shown for the mechatronics concept of prototype I. Subsequently, prototype II was developed based on the same mechatronics concept as prototype I, however, with a redesigned mechatronics and more advanced control algorithms, then fulfilling the full set of requirements, see Fig. 5.6. The following section describes,the mechanical design of the prototypes and the control algorithms.

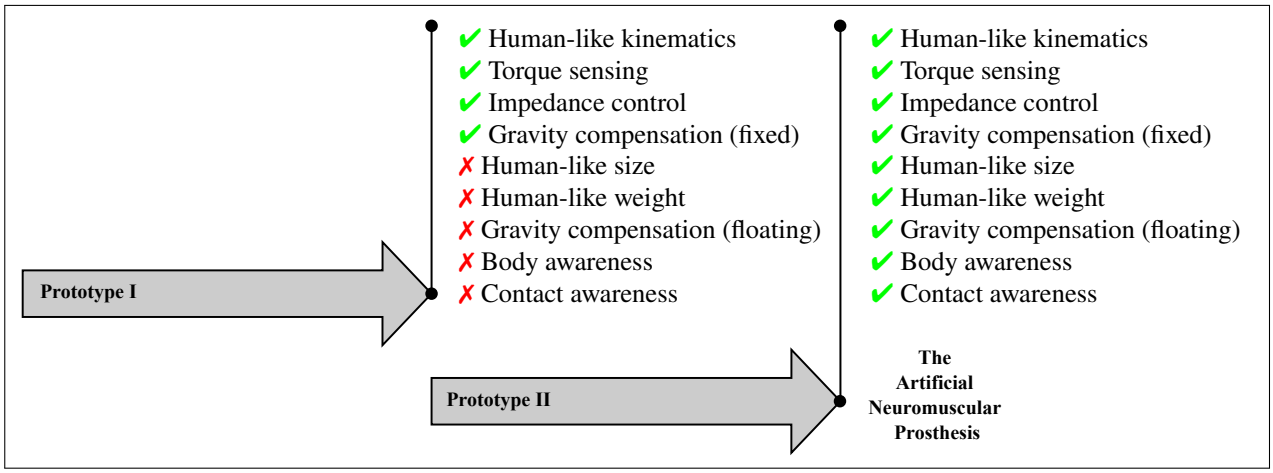

Figure 5.6 Development stages of prototype I and II

5.5.1 Prototype I

Prototype I was developed in direct continuation of the prosthesis µlimb [12], where the prosthesis µlimb provides two degrees of freedom (i.e., elbow and forearm). The device also provides torque and impedance control. Due to the still considerable high weight and large dimensions, in comparison to a human arm, µlimb was not yet designed to be worn by a human. Instead, the device may be operated in two scenarios i) by being mounted at a robot end effector of a lightweight robot, being the initial test system for an *exoprosthesis*, or ii) by being placed in table top mode.

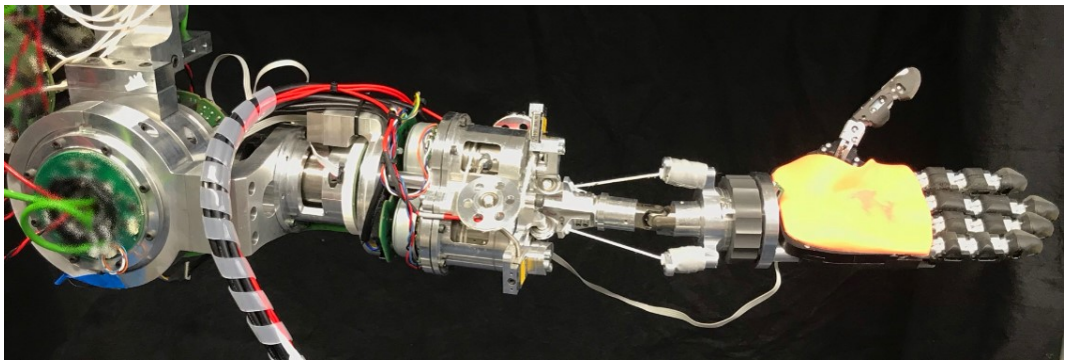

Figure 5.7 Mechatronic solution of prototype I with the modular hand (Softhand Pro 2)

Goals This first iteration was built with available mechatronics components from a cooperation partner. This way the author was able to first complete a high performance iteration of the ANP. Some of the essential design goals from Sec. 5.2 and Sec. 5.4 could already be implemented in prototype I. The main goal of prototype I was to develop a design solution for an active torque-controlled human-like 4-dof kinematics, including a 3-dof wrist, realized at about the same weight and dimensions as µlimb. For this, a wrist solution had to be developed to fit into the available design space of µlimb. Similar to µlimb, prototype I was designed as a stationary prosthesis and was not yet wearable.

Integration Philosophy In prototype I, the focus of improvement was mainly on the forearm and the wrist module, with the help of the following integration philosophy: i) Develop specialized and custom-made mechatronic actuator modules instead of off-the-shelf robotic ones to adapt to the available design space. ii) Integrate multiple functionalities within a single mechanical component. With this, the mechanical part may get more complex but the number of parts and attachment elements (also threads, screws and consequently weight and size) are reduced. In this respect, the increased complexity in part geometries

exploits capabilities of state-of-the-art CNC machines. iii) Consider complex three dimensional component placement techniques, and tendon routings to fulfill the requirements. iv) Use remote actuation (such as tendon-driven designs) to solve the wrist integration and torque sensor integration problem.

System Description The implementation of prototype I is depicted in Fig. 5.7, with CAD drawings depicted in Fig. 5.8a and Fig. 5.8b showing the dimensions and coordinate frames used for the modeling and control. The system consists of an elbow joint (1-dof), a forearm joint (1-dof) and a wrist module (2-dof). A modular hand may be attached to the system, which is the Softhand Pro 2 [290]. The system is controlled in real-time at 1 kHz using the EtherCat protocol with an EtherCat master running Matlab/Simulink 2017b.

Forearm and Elbow Elbow and forearm joints are depicted in Fig. 5.8a and Fig. 5.8c. The elbow of the system consists of a torque-controlled, proprietary joint. The forearm joint is depicted in Fig. 5.8c, and is custom made i) to decrease the required design space of the module in contrast to µlimb, and ii) to obtain further design space for the wrist module.

Wrist The wrist consists of a *kinematics module*, realizing a 3S$\bar{\text{P}}$S-1RR parallel kinematics, as described in Sec. 3.4.3. There is also a *drive-train module* containing actuators and sensors, see Fig. 5.8d. The wrist kinematics was already utilized in Sec. 4.3.1 using pneumatic cylinders. In the following, the principle of the electromechanical wrist is described. Each of the three *tendons* and drive-trains are equally distributed point-symmetrically along the longitudinal axis of the wrist by 120 degree. Each of the three *tendons* enter an *eyelet* being transmitted by three *pulleys* (green), arranged in three dimensional space, to the driving *spool*, see Fig. 5.8d. The tendon force F_t is measured by a *tendon force sensor* via the resulting senor force F_s based on an isosceles triangle (see Fig. 5.8d) with angle α as

$$F_\text{t} = \frac{F_\text{s}}{2\cos(\alpha/2)}. \tag{5.1}$$

The sensor is placed as close to the *Eyelet* as possible to reduce the influence of friction on the measurement. The *Spool* is driven by a BLDC motor (*BLDC*) and a *harmonic gear* with a transmission ration of $i_\text{g} = 50$. The components of the *harmonic gear* consist of: a wave generator (*WG*), a circular spline (*CS*) and a flex spline (*FS*), which are used in the configuration *driving*, *driven*, *fixed*, respectively. The flex spline is attached to the housing by the flex spline connector (*FPC*). The *FPC* limits the minimum radius[4] of the *Spool* r_s, as it goes through its hollow shaft. A *BLDC* drives the system. The motor rotation is measured by a magnetic *Position sensor*. The wrist does not have any angular joint position sensors. Instead, the motor position and the kinematics model are used for calculating $\boldsymbol{q}$ in real-time. The tendon was optimized for a long endurance, especially against wear. It consists of a Dyneema rope with a thickness of 2.5 mm and maximum load of 580 daN. All custom made components were made of aluminum EN-AW-7075 by Computerized Numerical Control (CNC). Heavily stressed parts were optimized using Finite Element Analysis (FEA). The weight of the wrist mechanics is 1.75 kg, its length is 228.6 mm, and its diameter lies between 96 – 133.6 mm. Motor torque and current control are provided by the proprietary custom-made electronics.

[4] A smaller radius is beneficial for a higher output torque and thus maximum tendon force.

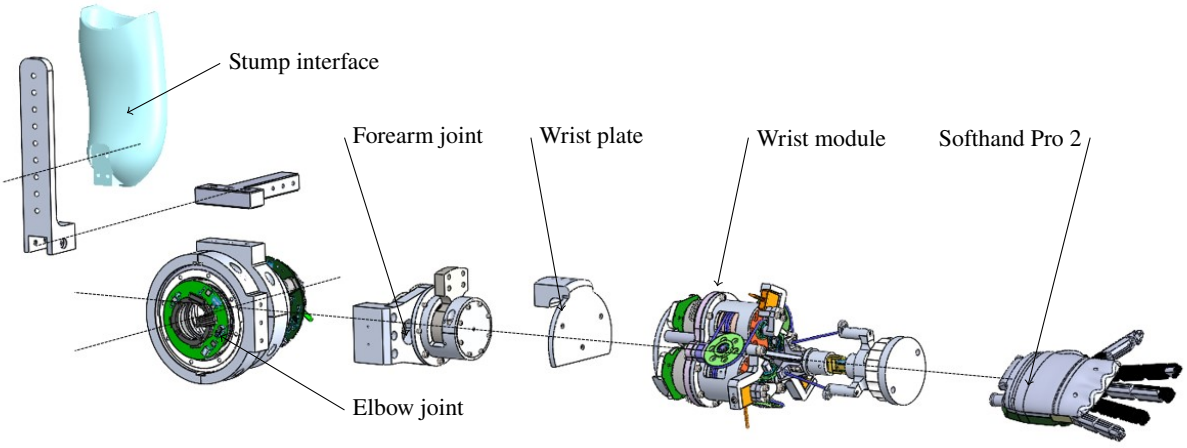

(a) ANP exploded view. Alternative modular hands [291] are also compatible with the ANP.

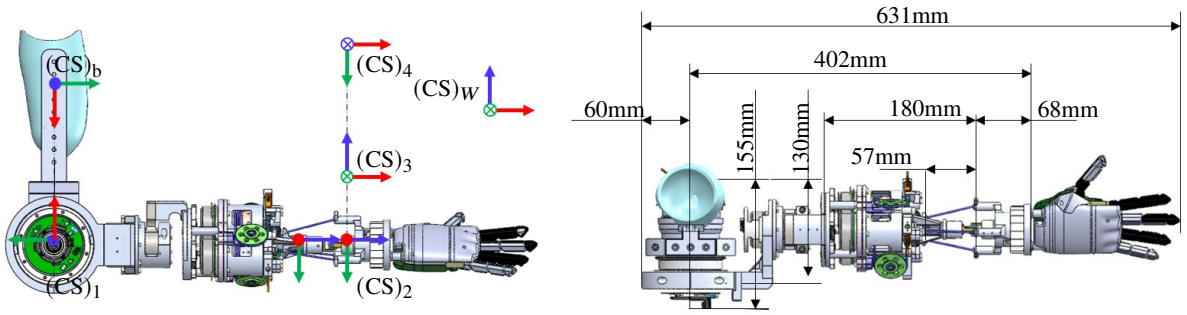

(b) Side and top view of the ANP with dimensions and coordinate frames.

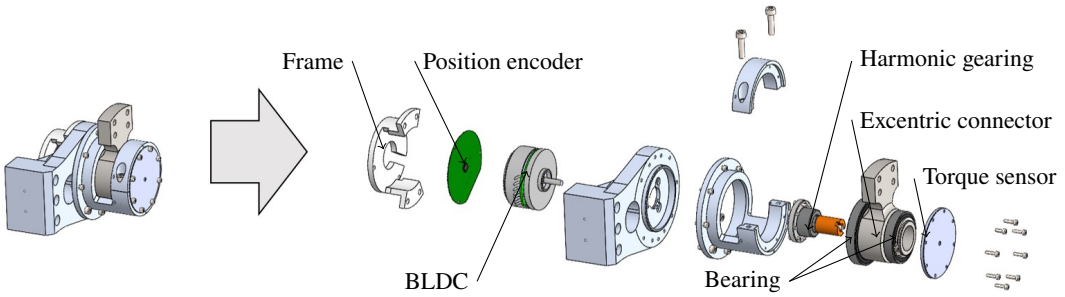

(c) Forearm joint exploded view

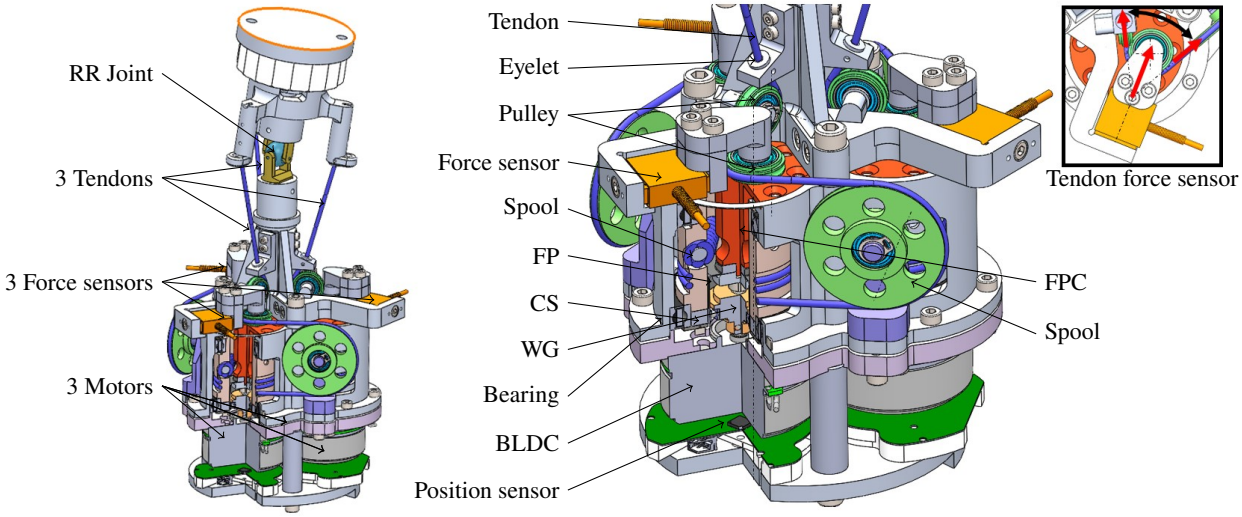

(d) Wrist module with sliced view

Figure 5.8 Design solution of Prototype I

5.5.2 Prototype II - The ANP

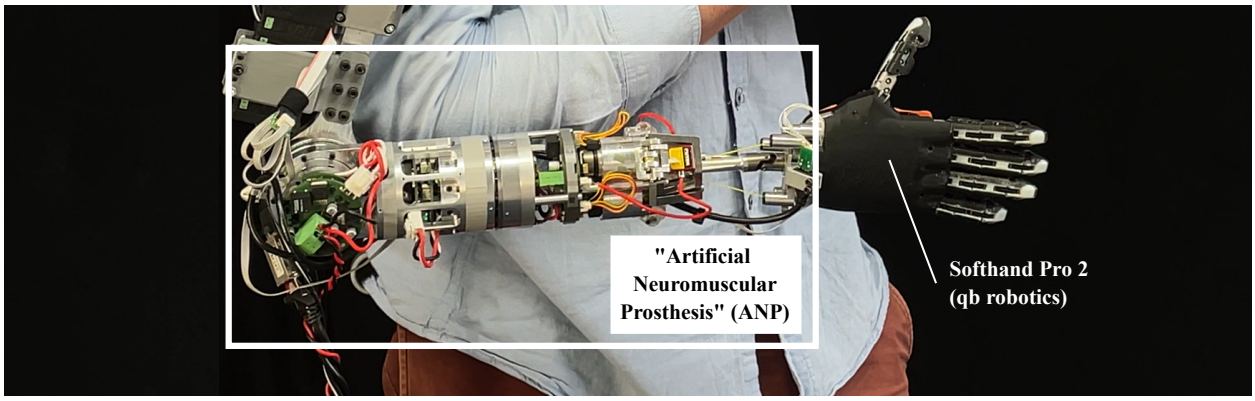

Figure 5.9 Mechatronic solution of prototype II (ANP) with the modular hand Softhand Pro 2

In the following, the mechatronics of the prototype II, also denoted as ANP, is proposed, see Fig. 5.9. The ANP continues the work of prosthesis I aiming to provide all requirements as described in Sec. 5.2.

Goal The aim of the ANP is to develop a wearable device with human-like size and human-like weight, based on the same mechatronic approach of prosthesis I, i.e., elbow and forearm actuation with a two dof tendon-driven 3SPS-1RR wrist, fulfilling all concepts and requirements from Sec. 5.2 and Sec. 5.4. The ANP should provide the necessary hardware, i.e, sensors and actuators, for running the artificial neuromuscular controller see Fig. 5.4.

Integration Philosophy For the ANP, the dimensions (diameter < 50 mm, length < 50 mm) and weight (< 2 kg) are significantly reduced. For the ANP, new specialized components are chosen, based on the design process from Sec. 5.3. Foremost, a new generation of i) custom-made, miniaturized, torque-controlled robot elbow and forearm joints are designed for the ANP such that also more lightweight attachment mechanisms could be designed suitable for prosthesis requirements. Also, the elbow and the forearm joint share the same design to maximize development resources.

The drive-train of the wrist of the ANP is also redesigned, as the wrist design approach from prototype I required excessive space, e.g., via the high number of pulleys, complex routings and excentric force sensor placements. Finally, the motor electronics are integrated into the prosthesis and a hollow shaft design is applied to ensure clean cable routing.

System Description The ANP consists of four active degrees of freedom as elbow (1-dof), forearm rotation (1-dof), wrist (2-dof) and additionally a modular 1-dof hand Softhand Pro 2 [290]. Figure 5.10a depicts an exploded view of the system. It consists of a robotic *elbow joint* and a *forearm joint* (of the same size and type). Both are interconnected by a *rigid structure* and followed by the *wrist module*. Figure 5.10b provides an overview of the system, its dimensions and coordinate frames.

Electronics In contrast to Prototype I, the electronics of the ANP is integrated within the structure. The software and electronics architecture are depicted in Fig. 5.10f. A control PC (x86) runs the high-level control routines on an Ubuntu 16.04 hard real-time system with Matlab/Simulink (MathWorks, MA, USA) at 1 kHz. The control PC, which is the EtherCat Master, communicates with the actuators (EtherCat Slaves) in real-time. Elbow, forearm and wrist run with individual, custom made Printed Circuit Board (PCBs) and control software[5]. These provide PI-field oriented current control in a cascade with a P torque controller at 8kHz. IMU measurements are provided by the elbow and forearm electronics over the EtherCat protocol in real-time, as well.

[5]These were not developed by the author.

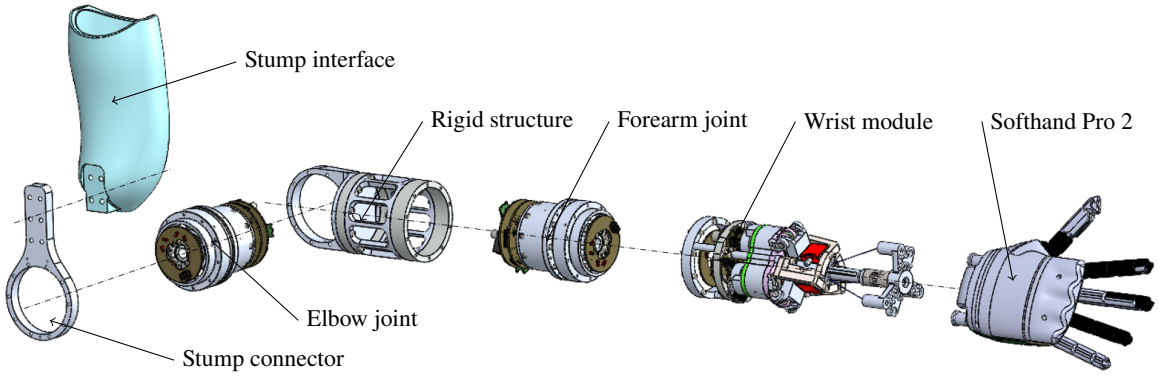

(a) ANP exploded view (Requirements F1, F2)

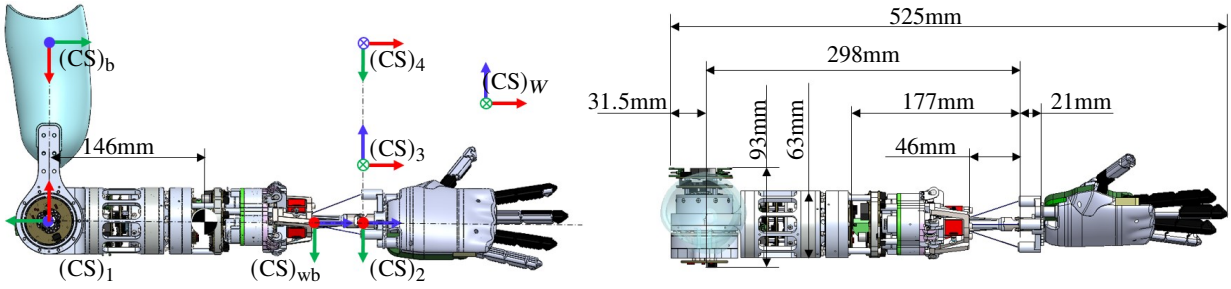

(b) Side and top view of the ANP with dimensions and coordinate frames (Requirements F1, F2)

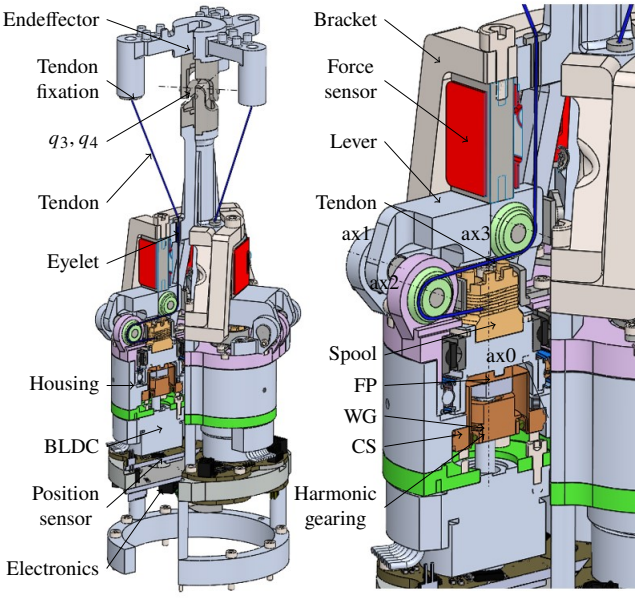

(c) Mechanical design of wrist and drive-train (Requirements F1, T2, T8)

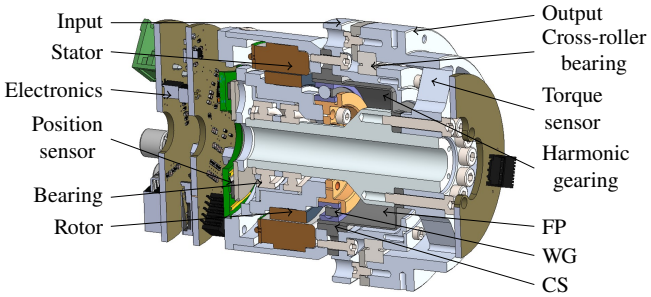

(d) Torque controlled robot actuator as used for joint 1 and 2 (Requirements T2)

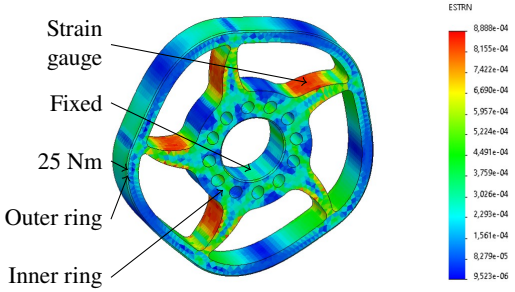

(e) FEA of the torque sensor under load (Requirements T2)

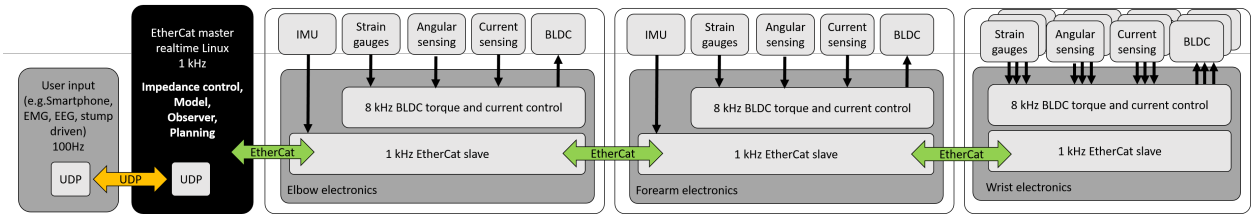

(f) High-level and low-level software and electronics architecture (Requirements T4, T7)

Figure 5.10 Design solution of prototype II (ANP)

Finally, all actuator dofs provide motor-side joint position and link-side joint torque measurements. The prosthesis desired joint motion $\boldsymbol{q}_\mathrm{d}, \dot{\boldsymbol{q}}_\mathrm{d}$ and joint stiffness K_i of the ANP can also be set via UDP at a clock cycle of 100 Hz. This allows control over a smartphone User Interface (UI) (for demonstration purpose), sEMG, EEG or other suitable HMIs in the future. The following paragraph explains the mechanical design of the ANP wrist and forearm/elbow in more detail.

Forearm and Elbow *Elbow joint* and *forearm joint* of the prosthesis are realized by the robotic actuator from Fig. 5.10d. The actuator is custom made with specifications from Tab. A.7. A suitable BLDC motor kit ($\tau_\mathrm{m,N} = 0.25$ Nm, $n_\mathrm{m,max} = 6000$ 1/min) and a harmonic gearing ($i_\mathrm{g} = 100$, $\tau_\mathrm{g,max} = 30$ Nm, $n_\mathrm{g,max} = 6000$ 1/min) is chosen by following the procedure from Fig. A.2 in the Appendix. Since the initial combination of the smallest gear and the smallest motor did not lead to a feasible mechanical design, then larger variants were chosen, which still could fit into the demanded forearm diameter, see Tab. A.6. As a consequence, the maximum torque of the joint $\tau_\mathrm{m,N} i_\mathrm{g} \approx 25$ Nm is larger than the maximum simulated actuator torque $\max(\tau_\mathrm{a}(t)) \approx 8$ Nm for lifting the simulated payload of 1.25 kg. The joint includes a custom made joint torque sensor, see Fig. 5.10e, which was designed by FEA. It consists of five spokes inspired by the design in [292, 293]. Four strain gauges were placed at the location of maximum positive and negative deflection (red color), caused by compression and bending, on the upper and lower side of each spoke. Brakes are deliberately left out from the design to save additional weight, though in the future it might become still required due to safety reasons.

Wrist Figure 5.10c depicts the mechanical design of the wrist based on the kinematics shown in Fig. 4.2. The advantage of such a design is the lightweight and space-saving joint design at the intersecting joints, as torque sensing, position sensing and actuation are placed remotely. In contrast to the wrist of prototype I, i) the number of pulleys are decreased, ii) the tendon routing is improved by a cage structure (to avoid slipping tendons), iii) the placement of the tendon force sensor is improved (to be less excentric), iv) the wrist size is significantly reduced and v) the weight of the ANP wrist is decreased to 25 % of the wrist of prototype I.

The wrist consists of three point symmetric actuator modules, each driving one of the three tendons, respectively, see Fig. 5.10c. As the tendons enter the *Eyelet*, they are guided via two *Pulleys* at ax2 and ax3 to the *Spool*, see Figure 5.10c. A *harmonic gear* ($i_\mathrm{g} = 100$, $\tau_\mathrm{g,max} = 1.4$ Nm, $n_\mathrm{g,max} = 10000$ 1/min, no-load starting torque $\tau_\mathrm{max} = 3$ mNm) drives the *Spool* ($r_\mathrm{s} = 3$ mm) and amplifies the motor torque of the BLDC (*BLDC*, $\tau_\mathrm{m,N} = 10$ mNm, $n_\mathrm{m,max} = 10000$ 1/min) lying on axis ax0. According to Fig. A.2 in Appendix, the smallest available gear variant with the highest gear ratio and the smallest motor available on the market was chosen. The wave generator (*WG*), circular spline (*CS*) and flex spline (*FP*) of the *harmonic gear* are used in the standard configuration *driving*, *fixed*, *driven*.

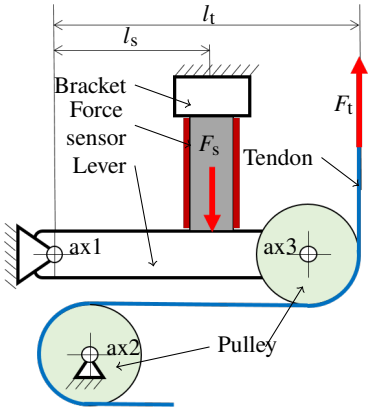

Figure 5.11 Lever mechanism for measuring the tendon force in the wrist module

The tendon force measurement is based on the novel mechanism shown in Fig. 5.11. A linear strain-gauge-based *Force sensor* ($F_\mathrm{s,max} = 440$ N) is located between a *Bracket* and a movable *Lever*. The tendon force F_t affects the resulting force $F_s = (l_\mathrm{t}/l_\mathrm{s})F_\mathrm{t}$ in the force sensor, where l_t and l_s are the distances from the

bearing axis ax1 to the force F_t and F_s, respectively. A magnetic *position sensor* measures the motor angle at the bottom of the *BLDC*, where low level *Electronics* for motor control and strain gauge amplification are also located. The tendons are made of 0.4 mm thick Dyneema and provide a break force of 330-360 N. A maximum tendon force of 170 N was measured.

5.5.3 Device Analysis

Fig. 5.12 compares all three generations, µlimb [12], prototype I and prototype II. µlimb and prototype I share similar size, with the latter having two additional degrees of freedom in the wrist. Specifically, the custom-made robotic forearm actuator of prototype I is significantly smaller with a length of 60 mm compared to µlimb. A further significant reduction in diameter and length can be seen when comparing µlimb and prototype I to prototype II. The table below lists the key features of the prostheses, showing the progress in the development.

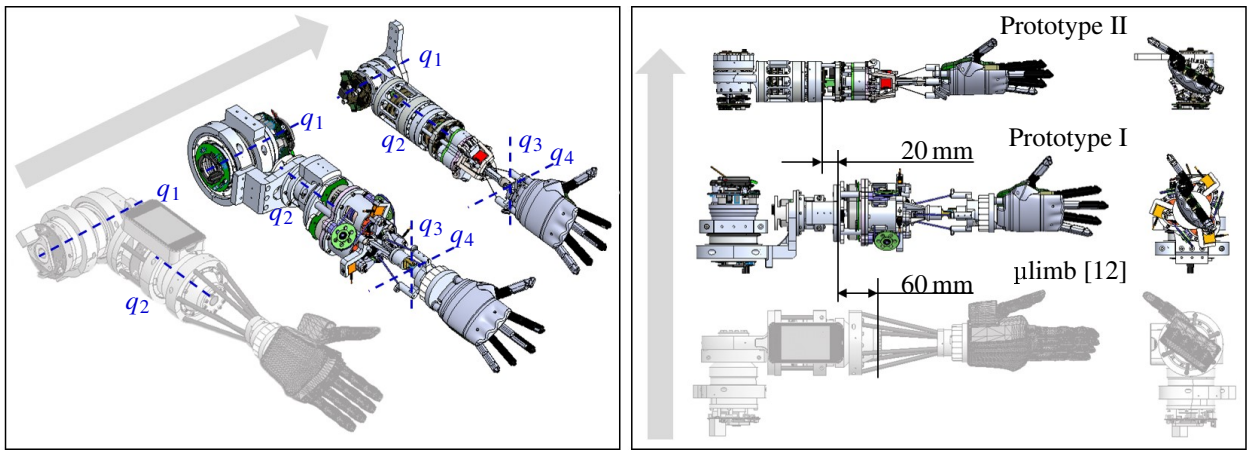

Figure 5.12 Device comparison and evolution of µlimb [12], prototype I and prototype II (ANP) in CAD software

Table 5.1 Comparison of µlimb [12], prototype I, prototype II (ANP)

	µlimb [12]	prototype I	prototype II (ANP)
Active dof (el-wr)	2	4	4
Weight [kg]	N.a	4-5	1.7 + hand
Payload [kg]	N.a.	2.5	1.25
Mechatronic approach	2x proprietary robot joints	3x custom robot joints + 1x proprietary robot joint	4x custom robot joints
Electronics	Internal	External	Internal
Sensing	Motor encoder, joint torque sensor	Motor encoder, joint torque sensor	Motor encoder, joint torque sensor , IMU
Number of actuators	2	5	5
Kinematics	RR	RR+3SPS-1RR	RR+3SPS-1RR

5.5.4 Modeling and Control

The prosthesis model is derived by the methods from Sec. 3, which is applicable to prototype I and II, as both systems share the same kinematics. The serial kinematics of the prosthesis model is described by MDH, see Tab. A.2 in the Appendix. These are used to derive fixed-/floating-base kinematic and dynamic models of the prosthesis, see Sec. 3.1. The hybrid tendon-/non-tendon actuation of the prostheses is described by

(3.56)-(3.63) using the approach (3.76) for the prosthesis. Actuator- and joint-level mappings, necessary for modeling and control, are depicted in Fig. 3.9.

Soft Robotics Control All prostheses are equipped with control methods from soft and tactile robotics. Prostheses prototype I and II are equipped with a fully fledged impedance controller (3.37), a floating-base gravity compensation (3.34) and a floating-base momentum observer (3.40). Together with the body and contact awareness, the Artificial Neuromuscular Controller is formed, see Fig 5.13.

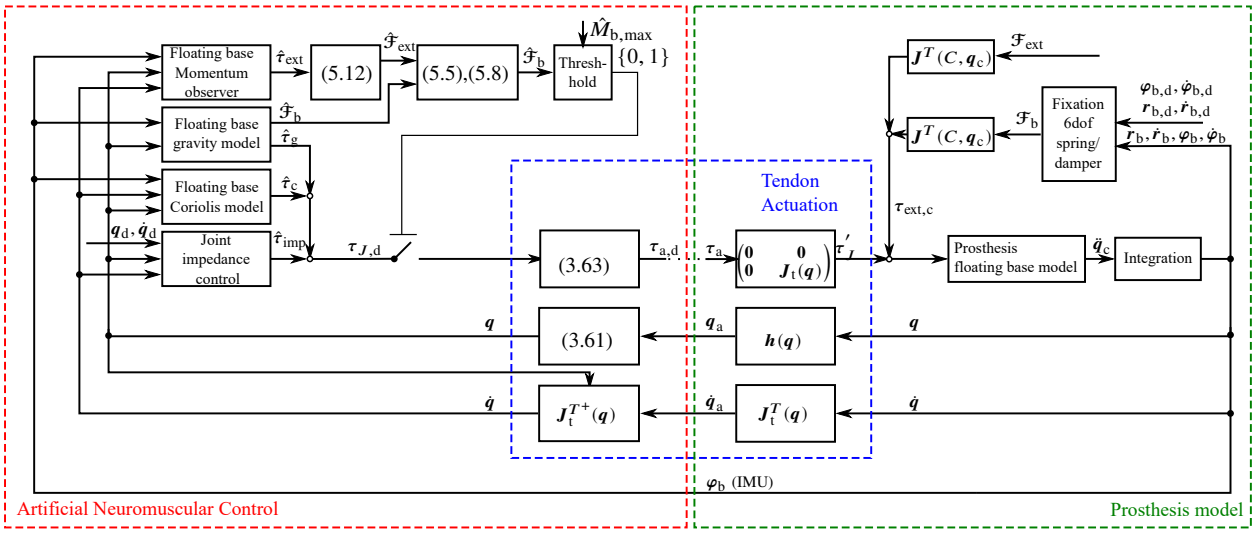

Figure 5.13 Model and control structure of the ANP

Body and Contact Awareness As described in Sec. 5.2, body and contact awareness simulate the human neuromuscular system in terms of proprioceptive sense of touch and body image. In the following, a quasi-static simplified model is derived, which is then used for computing the contact wrench ${}^{\mathrm{W}}\mathcal{F}_{\mathrm{b}}$ between the prosthesis and operator, and for computing external contacts ${}^{\mathrm{W}}\mathcal{F}_{\mathrm{ext}}$ between the prosthesis and environment based on proprioceptive measurements only. With this approach, only these two contact wrenches are considered, see Fig. 5.2.

In a first step, ${}^{\mathrm{W}}\boldsymbol{F}_{\mathrm{b}}$ and ${}^{\mathrm{W}}\boldsymbol{M}_{\mathrm{b}}$ are calculated, see Fig. 5.14. For the contact-free case, these can be derived by considering rows 1 to 6 from (3.20) and substituting (3.22) as

$$\cancel{\boldsymbol{M}_{\mathrm{b,b}}(\boldsymbol{q}_{\mathrm{c}})\begin{pmatrix}\ddot{\boldsymbol{r}}_{\mathrm{b}}\\ \ddot{\boldsymbol{\varphi}}_{\mathrm{b}}\end{pmatrix}} + \cancel{\boldsymbol{C}_{\mathrm{b}}(\boldsymbol{q}_{\mathrm{c}},\dot{\boldsymbol{q}}_{\mathrm{c}})\dot{\boldsymbol{q}}_{\mathrm{c}}} + \boldsymbol{g}_{\mathrm{b}}(\boldsymbol{q}_{\mathrm{c}}) = \begin{pmatrix}{}^{\mathrm{W}}\boldsymbol{F}_{\mathrm{b}}\\ {}^{\varphi}\boldsymbol{M}_{\mathrm{b}}\end{pmatrix} + \boldsymbol{P}_0\boldsymbol{J}^T(C,\boldsymbol{q}_{\mathrm{c}})\,{}^{\mathrm{W}}\mathcal{F}_{\mathrm{ext}}. \tag{5.2}$$

The transformation between moments in world coordinates and twisted coordinates is

$${}^{\varphi}\boldsymbol{M}_{\mathrm{ext}} = \boldsymbol{J}_{\omega}^{T}\,{}^{\mathrm{W}}\boldsymbol{M}_{\mathrm{ext}}, \tag{5.3}$$

with the twist matrix $\boldsymbol{J}_{\omega}$, which is defined by (3.11) in the Appendix. The matrix

$$\boldsymbol{P}_0 = \begin{pmatrix}\boldsymbol{I}_{6\times6} & \boldsymbol{0}_{6\times4}\end{pmatrix} \in \mathbb{R}^{6\times10} \tag{5.4}$$

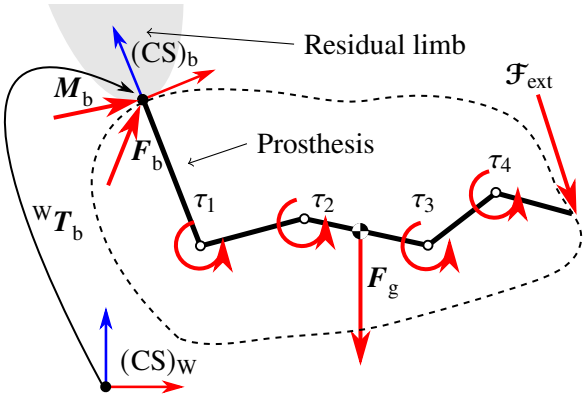

Figure 5.14 Approach for the wrench calculation between human and device

is sparse with binary entries to adapt the dimension of the Jacobian to only affect the base. Slow dynamics is assumed in this work for the sake of simplicity. Specifically, the time derivatives $\ddot{\boldsymbol{r}}_b, \ddot{\boldsymbol{\varphi}}_b, \dot{\boldsymbol{r}}_b, \dot{\boldsymbol{\varphi}}_b$ are considered to be zero, leading to the quasi-static model

$$\begin{pmatrix} {}^W\boldsymbol{F}_b \\ {}^{\varphi}\boldsymbol{M}_b \end{pmatrix} = \boldsymbol{g}_b(\boldsymbol{q}_c) - \boldsymbol{P}_0 \boldsymbol{J}^T(C, \boldsymbol{q}_c)\, {}^W\mathcal{F}_{ext}. \tag{5.5}$$

The contact wrench ${}^W\mathcal{F}_{ext}$ can then be estimated (for an arbitrary single contact point) via

$$\begin{aligned} {}^W\hat{\mathcal{F}}_{ext} &= \left(\boldsymbol{J}(C, \boldsymbol{q}_c)\boldsymbol{J}^T(C, \boldsymbol{q}_c)\right)^{-1} \boldsymbol{J}(C, \boldsymbol{q}_c)\hat{\boldsymbol{\tau}}_{ext} && (5.6) \\ &= \boldsymbol{J}_C^{\#}(\boldsymbol{q})\hat{\boldsymbol{\tau}}_{ext}. && (5.7) \end{aligned}$$

More advanced concepts for force contact point estimations may also be used [294]. Finally, the reaction wrench is expressed in the base frame coordinates (in correspondence to a sensor) via

$$\begin{pmatrix} {}^b\boldsymbol{F}_b \\ {}^b\boldsymbol{M}_b \end{pmatrix} = \begin{pmatrix} {}^b\boldsymbol{A}_W\, {}^W\boldsymbol{F}_b \\ {}^b\boldsymbol{A}_W \left(\boldsymbol{J}_\omega^T\right)^{-1} {}^{\varphi}\boldsymbol{M}_b \end{pmatrix}. \tag{5.8}$$

Practical remarks Equation (5.7) calculates a wrench with respect to an arbitrary point C. However, C has to be chosen carefully in order to allow a general usage of ${}^W\hat{\mathcal{F}}_{ext}$. Furthermore, not all components of ${}^W\hat{\mathcal{F}}_{ext}$ in any configuration of $\boldsymbol{q}_c$ and C may be computable due to singular configurations and numerical reasons. For instance, if the contact point C is chosen to be in the wrist (Fig. 5.10b, (CS_4)) for $\boldsymbol{q} = (0,0,0,0)^T$), forces along the longitudinal axis of the prosthesis (${}^W\boldsymbol{e}_x$) do not have any effect on the joint torque and result in singular configurations. Furthermore, radial forces parallel to the ground (${}^W\boldsymbol{e}_y$) do not have any affect on the joint torques, also distorting the results. Consequently, a contact point could be chosen as ${}^4\boldsymbol{r}_C = (k_c, 0, 0)^T$ with $k_c \neq 0$, and on a practical device as $k_c = 12\,\text{cm}$. Further model assumptions for the prosthesis are described below.

In order to obtain the most stable results for the specific prosthesis kinematics and for showcasing the best practical use for the device, the extended wrench is assumed to take the form

$${}^W\hat{\mathcal{F}}_{ext} = \begin{pmatrix} 0 & 0 & {}^W\hat{F}_{ext,z} & 0 & 0 & 0 \end{pmatrix}^T, \tag{5.9}$$

which considers the scalar contact force ${}^{\mathrm{W}}\hat{F}_{\mathrm{ext,z}}$ to be parallel to the gravity vector. The assumption is not mandatory and others may work as well. The equations

$$\boldsymbol{J}^{*}(C, \boldsymbol{q}_{\mathrm{c}}) = \boldsymbol{P}_1 \boldsymbol{J}(C, \boldsymbol{q}_{\mathrm{c}}) \boldsymbol{P}_2^{T} \tag{5.10}$$

$$\hat{\boldsymbol{\tau}}_{\mathrm{ext}}^{*} = \boldsymbol{P}_2 \hat{\boldsymbol{\tau}}_{\mathrm{ext,c}}, \tag{5.11}$$

represent any possible model assumption and are used for selecting submatrices of $\boldsymbol{J}(C, \boldsymbol{q}_{\mathrm{c}})$ and rows of $\hat{\boldsymbol{\tau}}_{\mathrm{ext}}$. $\boldsymbol{P}_1$ is a selector matrix for the rows of $\boldsymbol{J}(C, \boldsymbol{q}_{\mathrm{c}})$, corresponding to the components of ${}^{\mathrm{W}}\hat{\mathcal{F}}_{\mathrm{ext}}$. $\boldsymbol{P}_2$ is a selector matrix for the columns of $\boldsymbol{J}(C, \boldsymbol{q}_{\mathrm{c}})$, determining, which sensor information of $\hat{\boldsymbol{\tau}}_{\mathrm{ext,c}} = \left(\boldsymbol{F}_{\mathrm{b}}^{T}, \boldsymbol{M}_{\mathrm{b}}^{T}, \boldsymbol{\tau}_{\mathrm{ext}}\right)^{T}$ is used. The selector matrices in this case are chosen to be $\boldsymbol{P}_1 = (0, 0, 1, 0, 0, 0)$ and $\boldsymbol{P}_2 = (\boldsymbol{0}_{4\times 6}, \boldsymbol{I}_{4\times 4})$. Finally, the estimated wrench is

$${}^{\mathrm{W}}\hat{F}_{\mathrm{ext,z}} = \boldsymbol{J}^{*}(C, \boldsymbol{q}_{\mathrm{c}})^{\#} \hat{\boldsymbol{\tau}}_{\mathrm{ext}}^{*}. \tag{5.12}$$

The aforementioned limitations can be partly overcome by running multiple variants of (5.11) in parallel. For instance, forces in the direction $({}^{\mathrm{W}}\boldsymbol{e}_{\mathrm{y}})$ might be detected by using only τ_3. Another solution might be an algorithm that analyses the structure for singularities in real-time for any given configuration of $\boldsymbol{q}_{\mathrm{c}}$. It then chooses the components of $\hat{\boldsymbol{\tau}}_{\mathrm{ext}}$ and ${}^{\mathrm{W}}\hat{\mathcal{F}}_{\mathrm{ext}}$ (by $\boldsymbol{P}_1$ and $\boldsymbol{P}_2$), which do not lead to numerical instabilities. Another solution would be the implementation of suitable force/torque sensors along the structure or even a full tactile skin, but other difficulties and challenges may arise therefrom. After proposing the control concepts of the ANP, the next section focuses on the validation of the control concepts.

5.6 Control and Skill Validation

The following experiments validate the design paradigm from Sec. 5.2 and the technical features from Sec. 5.4 for prototype I and II, showing typical human-like behaviors such as *body awareness*, *contact awareness*, *human-like kinematics* and *human-like contact response* on the prosthetic devices, according to Fig. 5.2. The validation of technical features focuses on testing the underlying controllers, namely torque control, joint impedance control, floating-base gravity compensation, and disturbance observation.

In the following section, first the basic mechatronic functionality of the prostheses, such as tendon actuation and control, active compliance and gravity compensation, are examined. Thereafter, the more advanced controller features such as body awareness and contact awareness are investigated. Finally, the principle grasping capabilities of prototype II are shown by a human-in-the-loop experiment.

5.6.1 Tendon Actuation and Control

Figure 5.15 shows sinusoidal impedance control for prototype I, applied with and without the maximum tested payload of 2.5 kg, depicted in the left and the right column. The first row of the plot shows working joint impedance control when applying a sinusoidal joint motion to the joints. The second row shows the underlying desired and actual joint torques at the wrist axes. It can be noted that even though the torque is controlled in tendon space (row 3) via the tendon force controller and (3.58)-(3.63), the joint torque is accurately controlled in joint space (row 2) .The maximum joint torques are ≈ 3 Nm and maximum tendon forces are ≈ 180 N occur. It can be noted that a position error of up to 10 deg can occur in q_2 in the payload experiment. This is most likely affected by the control error in the force controller of F_{t1} due to difficulties with controlling high forces.

Figure 5.16 repeats a similar experiment with prototype II, where the impedance control, torque control and tendon force control appear to work properly. For prototype II, a maximum payload of 1.25 kg was tested. A high pitch signal in τ_1 can be observed, which is caused by an unknown effect of the custom-made robot joint. This effect induces vibrations, which however are not noticeable in the position signal q_1. In addition, the system shows the full 4-dof motion control.

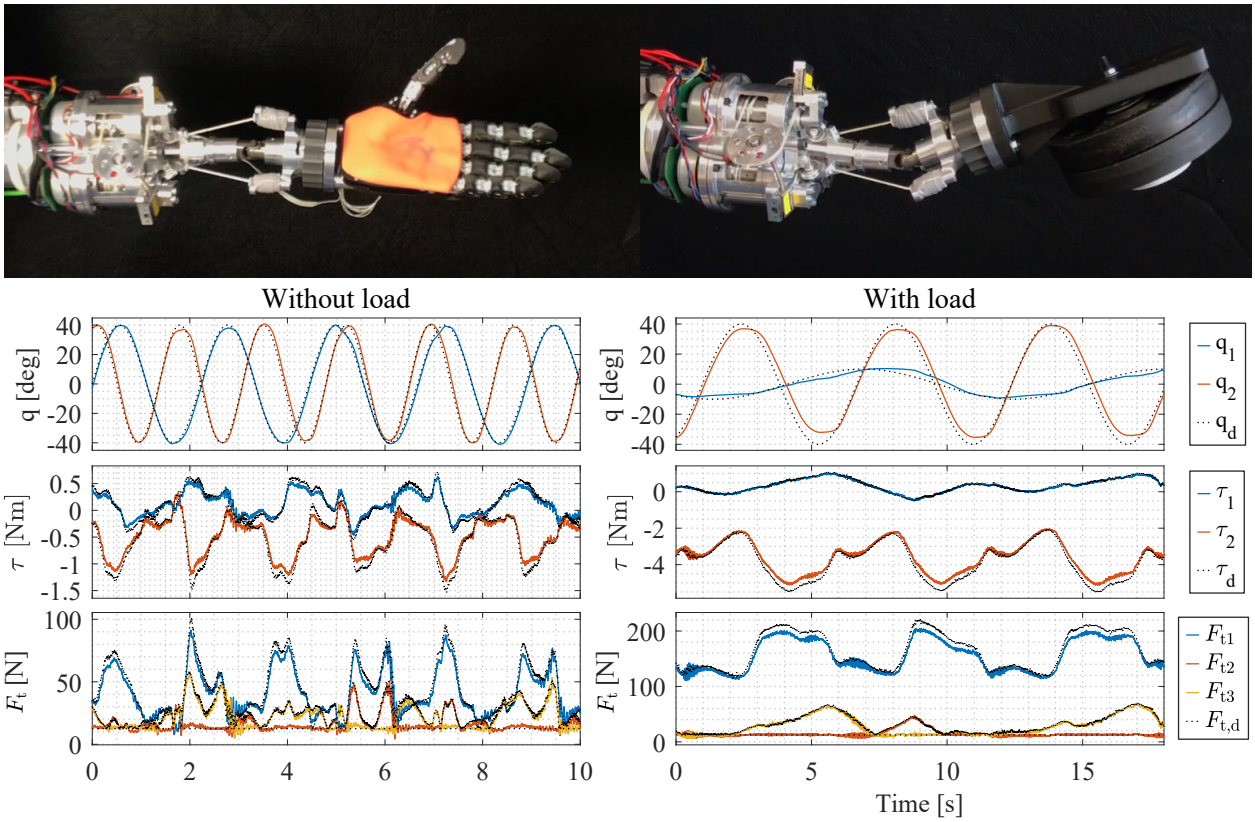

Figure 5.15 Sinusoidal joint tracking without and with payload of prototype I

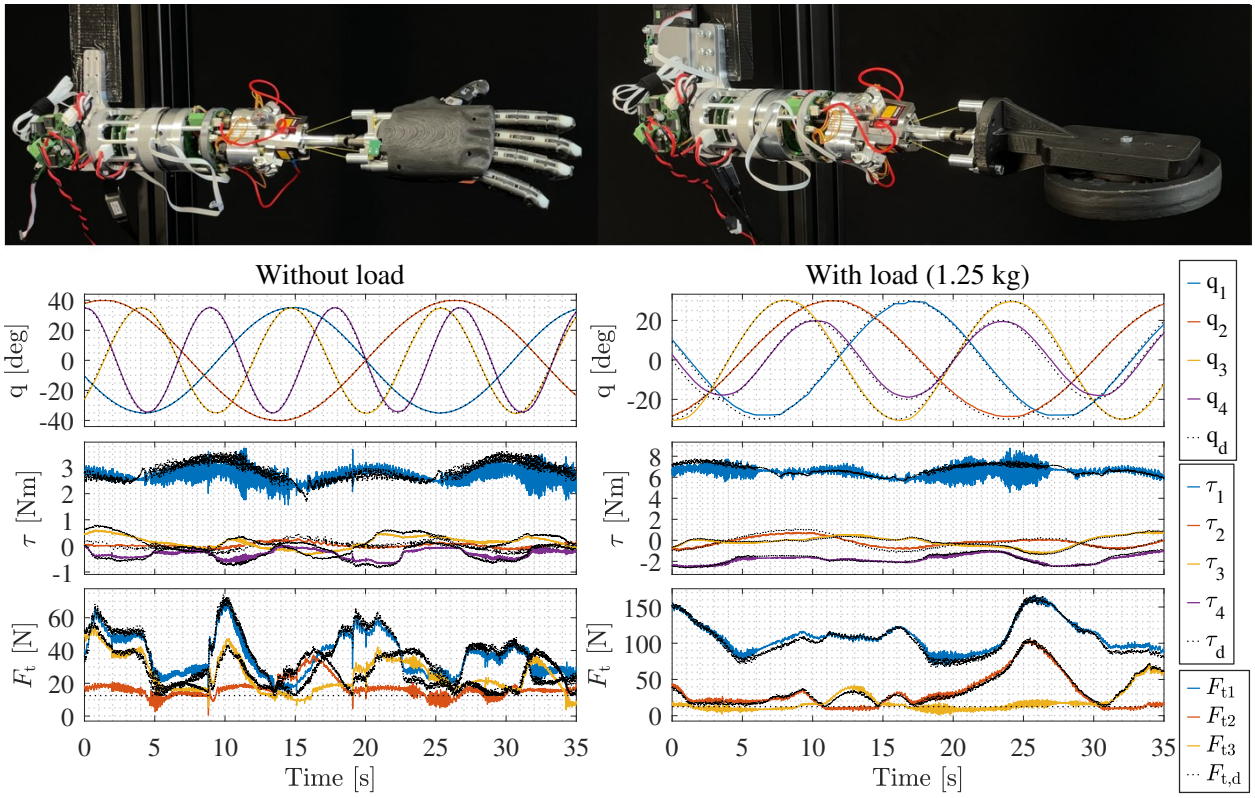

Figure 5.16 Sinusoidal joint tracking without and with payload of prototype II (ANP)

5.6.2 Active Compliance

A handshake recording between the wrist of prosthesis I and a human is depicted in Fig. 5.17a. The experiment shows that joint angles of up to 20 deg (row 1), motor speeds of up to 5000 1/min (74% of maximum motor speed, row 2) and forces of up to 62 N (row 3) can occur, while the maximum torque does not exceed 1 Nm (not depicted in the figure).

Figure 5.17b depicts joint stiffness for prototype II. In the experiment, a human applies a force at the hand palm in vertical direction while the stiffness is varied from $\boldsymbol{K}_{\text{imp},1}$ to $\boldsymbol{K}_{\text{imp},2}$. The stiffness parameter in this experiment is $\boldsymbol{K}_{\text{imp},1} = \text{diag}\{(15, 5, 5, 5)\}\text{Nm/rad}$ and $\boldsymbol{K}_{\text{imp},2} = 6\boldsymbol{K}_{\text{imp},1}$. The figure shows that higher deflections for $\boldsymbol{K}_{\text{imp},1}$ than for $\boldsymbol{K}_{\text{imp},2}$ can occur.

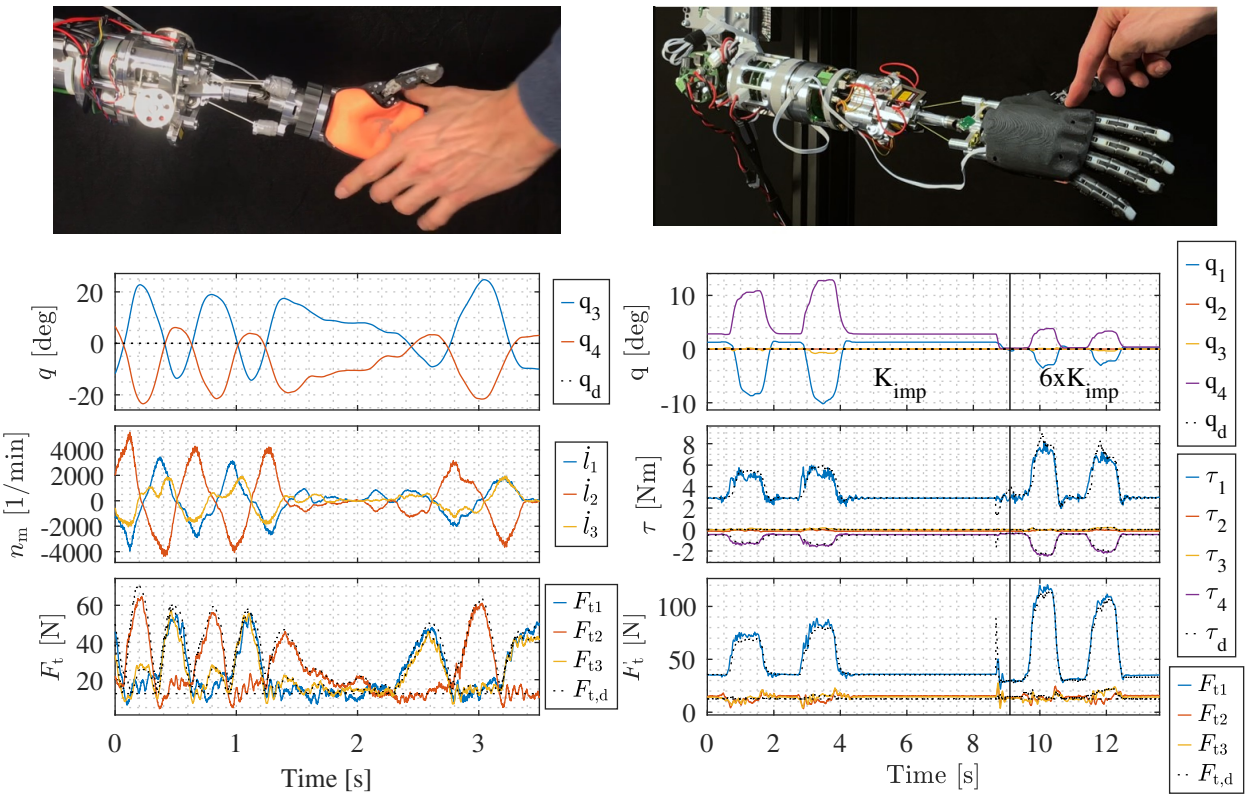

(a) Handshake experiment with prototype I

(b) Stiffness variation experiment with prototype II

Figure 5.17 Active compliance of prototype I and II

5.6.3 Gravity Compensation

Figure 5.18 illustrates a gravity compensation experiment with row one, showing the joint position, and row two and three showing the joint torques. The gray areas in the figure denote intervals in which a human changes the joint position by a contact wrench $\hat{\mathcal{F}}_{\text{ext}}$ of the ANP via interaction forces. With this experiment, both the active backdrivability and the gravity compensation are showcased. It can be seen that the system maintains its position in all white intervals, where no contact occurs, which can be explained by the underlying joint torque controller and the active gravity models. It can be seen that the set-point of the joint torque controller changes depending on the kinematic and gravitational model of the prosthesis. In the following section, the body awareness is tested for the ANP.

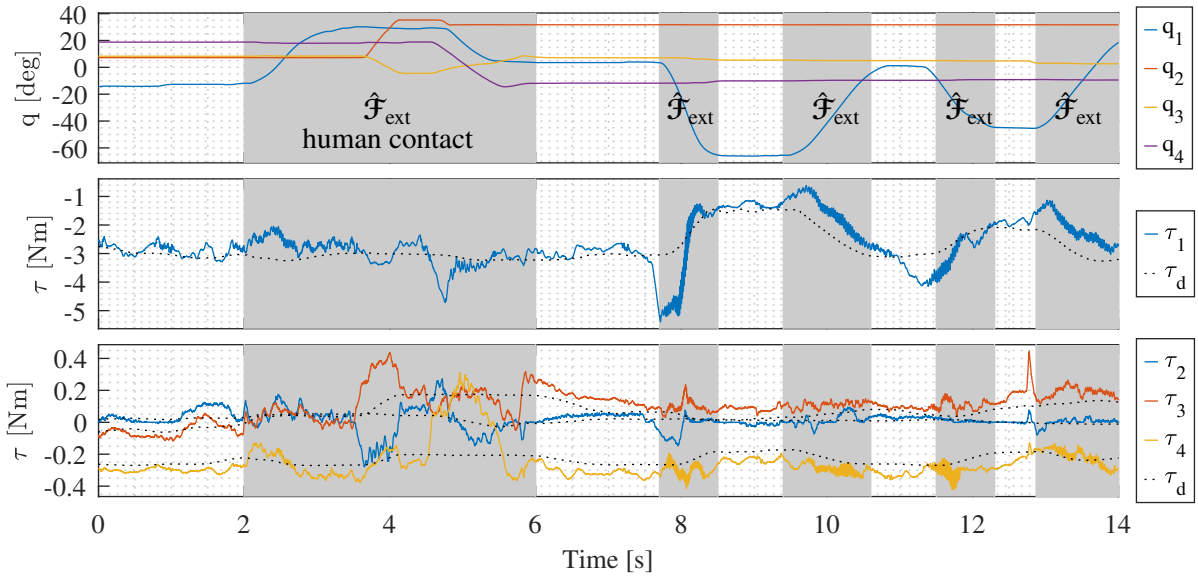

Figure 5.18 Gravity compensation of prototype II (ANP)

5.6.4 Body Awareness

The body awareness is demonstrated by a human interacting with the ANP, see Fig. 5.19. In this context, the active backdrivability of the torque controlled actuators is also shown. During the experiment, only the floating-base gravity compensation $\boldsymbol{\tau}_\mathrm{d} = \hat{\boldsymbol{\tau}}_\mathrm{g}(\boldsymbol{q}, \boldsymbol{\varphi}_\mathrm{b})$, see (3.34), and the underlying joint torque controllers are active. The first row shows the human tilting the base of the prosthesis, noticeably in the variation of $\boldsymbol{\varphi}_\mathrm{b}$. Additionally, the prosthesis joints are moved by an interaction wrench $\hat{\mathcal{F}}_\mathrm{ext}$ in the gray areas of the figure. Column three shows that $\dot{\boldsymbol{q}} \approx \mathbf{0}$ for the contact-free case, even though $\boldsymbol{q}$ and $\boldsymbol{\varphi}_\mathrm{b}$ are varied and $\boldsymbol{q}$ is not actively controlled via e.g, joint position control. Still, $\boldsymbol{q}$ can be changed by an interaction wrench $\hat{\mathcal{F}}_\mathrm{ext}$, making the system backdrivable by active control. The reason for this behavior can be understood by looking at $\hat{\boldsymbol{\tau}}_\mathrm{g}(\boldsymbol{q}, \boldsymbol{\varphi}_\mathrm{b})$ in row four and five. Row six shows the output of the momentum observer $\hat{\boldsymbol{\tau}}_\mathrm{ext}$, which contains the same floating-base model. $\hat{\boldsymbol{\tau}}_\mathrm{ext}$ remains essentially constant despite the change in $\boldsymbol{q}$ and $\boldsymbol{\varphi}_\mathrm{b}$, which shows the goodness of the applied floating-base model. However, an error of about $0.4\,\mathrm{Nm} > \hat{e}_{\tau,\mathrm{max}} = 0.1\,\mathrm{Nm}$ can still be observed in $\hat{\tau}_{\mathrm{ext}1}$ being larger than the admissible error $\hat{e}_{\tau,\mathrm{max}}$, which indicates a static model inaccuracy above the admissible error[6]. The goodness of the backdrivability is quantified by looking at row seven, showing the exchanged energy between human and device. At $t = 5\,\mathrm{s}$ the exchanged energy is $0.4\,\mathrm{J}$ for deflecting the joints by $\Delta q_1 \approx 20\,\mathrm{deg}$ and $\Delta q_3 \approx 20\,\mathrm{deg}$. In comparison, an impedance controlled system with a stiffness of $10\,\mathrm{Nm/rad}$ would have stored a maximal energy of $E_\mathrm{imp} = 2 \times 0.5 \times 10 \times (20 \times \pi/180)^2 = 1.22\,\mathrm{J}$. The last two rows show the model-based base wrenches, which change in dependency of $\boldsymbol{\varphi}_\mathrm{b}$, see Fig. 5.19. The black dashed line shows the pure gravity model, while the colored lines are equipped with the estimation from (5.5), (5.8) and (5.12) using the momentum observer $\hat{\boldsymbol{\tau}}_\mathrm{ext}$. Thus, the system from the figure is also equipped with a drift-free contact awareness, here applied in the contact-free case. As contact and body awareness are almost equal (black and colored lines), a correct model estimation is obtained.

Figure 5.20 shows a visualization of the body image as used for the floating-base kinematics and dynamics model. The figure also shows the output for the floating-base model in N and Nm at the joint axes, the base wrench and the external wrench. Also, it appears that the kinematics model generally conforms to the associated experimental photos. The floating-base kinematics model depends on motor encoder measurements and IMU data. The proprietary IMU provides a full rotation matrix.

[6] It will be shown in Fig. 5.21 that this error is comparably small in a contact situation.

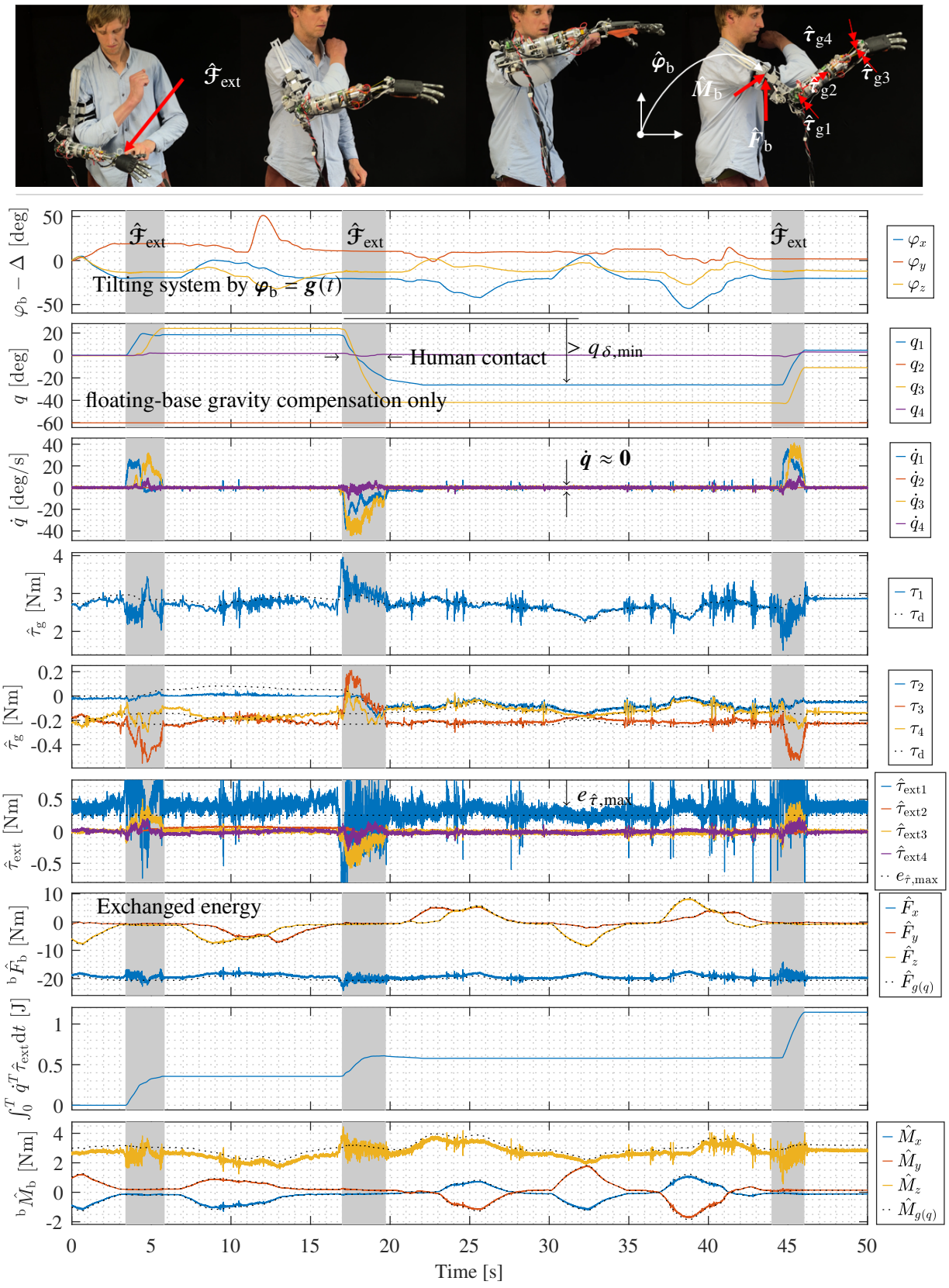

Figure 5.19 Investigation of body awareness and human-like contact response

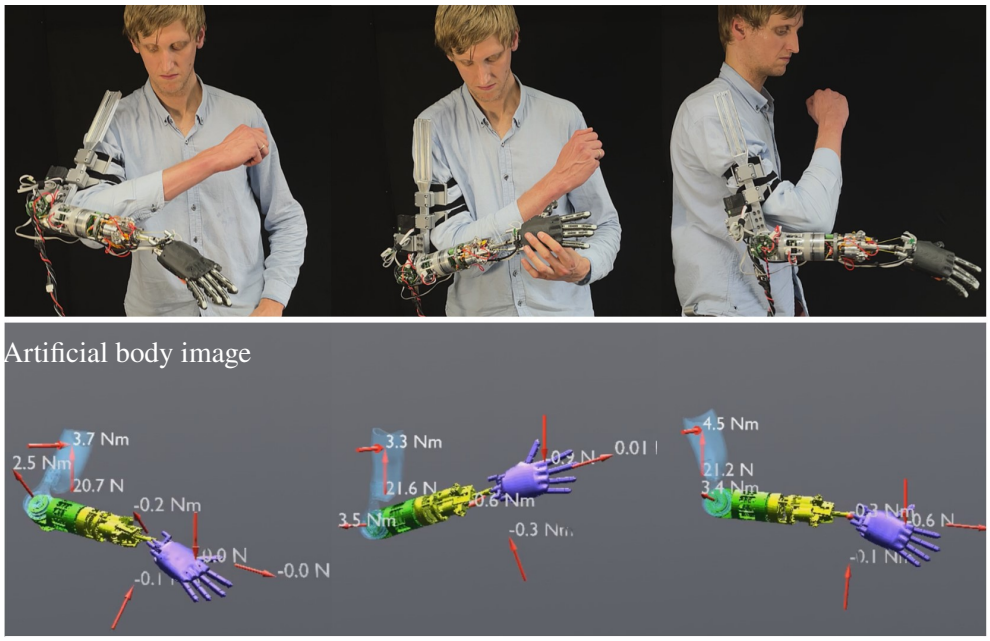

Figure 5.20 Visualization of the real-time-capable artificial body image as used for the floating-base model

5.6.5 Contact Awareness

Contact awareness of the ANP is used to estimate the contact force ${}^{\mathrm{W}}\boldsymbol{F}_{\mathrm{ext}}$ by a human, see Fig. 5.21. Two amplitudes of $\hat{\boldsymbol{\tau}}_{\mathrm{ext}} \approx 5\,\mathrm{Nm}$ can be observed in column two, which are due to the contact. The observer torque $\hat{\boldsymbol{\tau}}_{\mathrm{ext}}$ is utilized for estimating the external force ${}^{\mathrm{W}}\boldsymbol{F}_{\mathrm{ext}}$ in row one by (5.7). Based on this, the effect on ${}^{\mathrm{b}}\boldsymbol{F}_{\mathrm{b}}$ and ${}^{\mathrm{b}}\boldsymbol{M}_{\mathrm{b}}$ is calculated by (5.8). Therefore, the contact force detection and the estimation of base forces in the contact case can be confirmed as properly functioning.

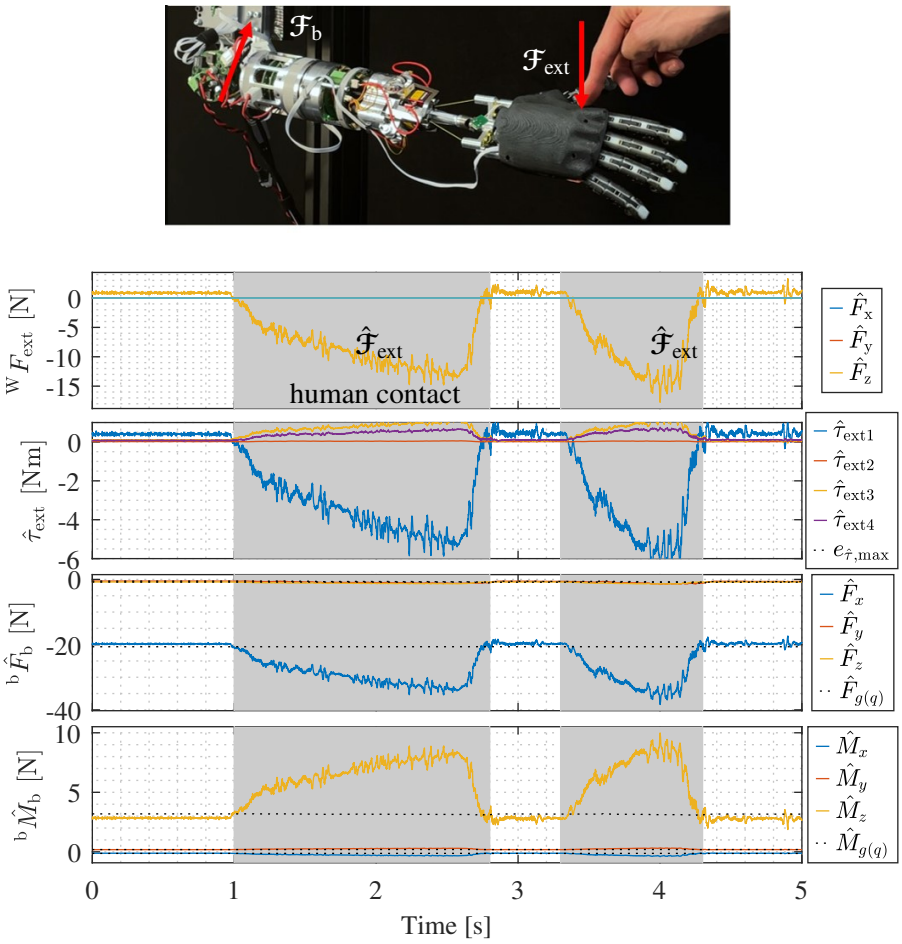

Figure 5.21 Investigation of the contact awareness via an external interaction force

Finally, contact awareness is used for monitoring the stress induced in the prosthesis base and for reacting with a protective control mode switch, see Fig 5.22. In the first experiment, see Fig. 5.22a, the prostheses are programmed to move from $q_1 = 0$ to $q_1 = -\pi/2$. Due to obstacle presence, a collision occurs. The methods for body and contact awareness are used to calculate $\boldsymbol{M}_{\mathrm{b}}$. $\boldsymbol{M}_{\mathrm{b}}$ increases up to 11 Nm, which may be harmful for a prosthesis user. The experiment is repeated with activated collision detection and reaction, see Fig. 5.22b. After the prosthesis collides with the surface, the base moment ${}^{\mathrm{b}}\boldsymbol{M}_{\mathrm{b}}$ exceeds the given threshold $r_{\mathrm{th}} = 4\,\mathrm{Nm}$. As a consequence, a control switch from joint impedance control to a safe gravity compensation is initiated. The base wrench reduces to ${}^{\mathrm{b}}\boldsymbol{M}_{\mathrm{b}} \approx 3\,\mathrm{Nm}$, corresponding to the initial gravity moment only.

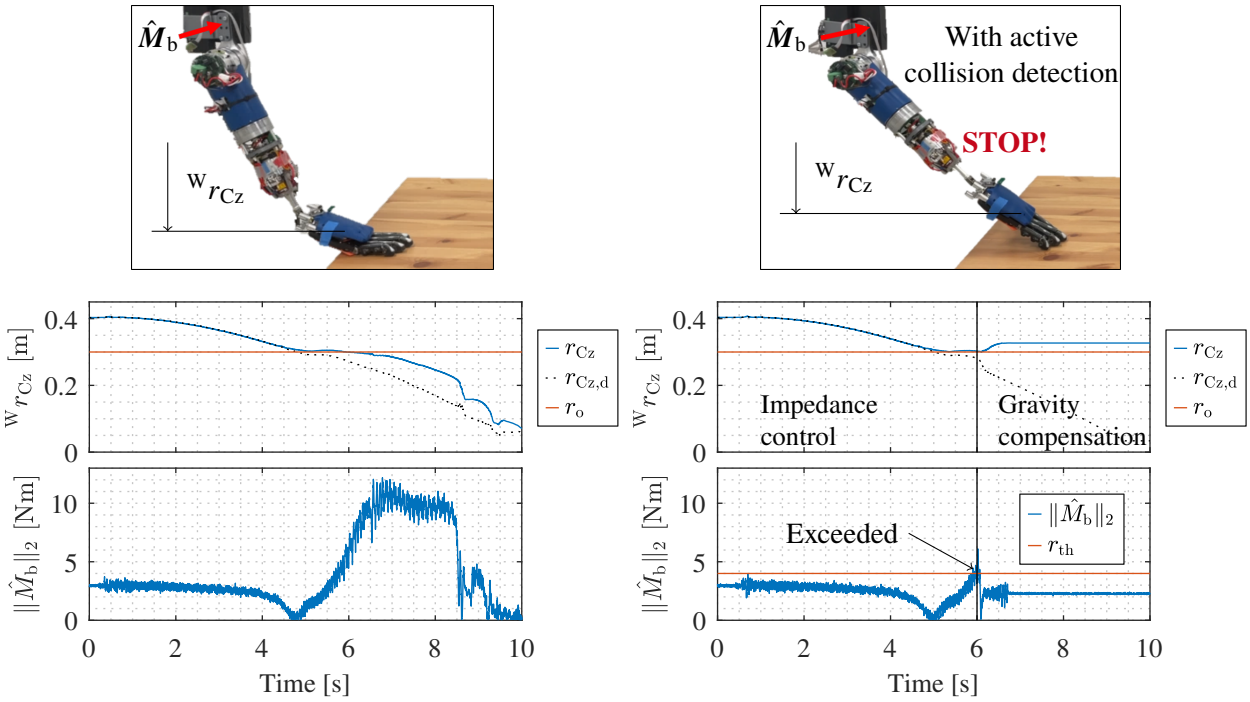

(a) ANP collides without collision reaction

(b) Experiment: ANP collides with collision reaction

Figure 5.22 Contact response strategies comparing pure compliance control and contact awareness

5.6.6 Grasping

Smartphone Interface

The overall grasping human-commanded capabilities of prototype II (ANP) are validated by two human-in-the-loop experiments. Furthermore, the functionality of the the novel 4-dof kinematics is investigated, particularly how such a kinematics fulfills a chosen set of daily grasping tasks. The prosthesis is controlled by the user via a Graphical User Interface (GUI) on a smartphone, see Fig. 5.23.

The experimental procedure is as follows: Four different objects of daily use are placed on a table, specifically, i) a can of tomatoes (250g), ii)a can of tuna (125g), iii) a bottle of water (500g) and iv) a glass (300g). The prosthesis operator is then asked to place the objects at different locations using the smartphone interface. The objects must not be in contact with other body parts and the contralateral hand must not be used to support the prosthesis. The task is to move all objects from the top of the table to the middle level of the shelf, and then to move all objects from the middle level of the shelf back to the top level of the shelf. By varying placement levels and objects, the operator needs to use all available dof of the prosthesis. Figure 5.24 depicts 12 different grasping cases of the experiment showing the grasping capabilities for different situations. The rows depict the experiments with varying objects (i.e., i) tomato can, ii) tuna can, iii) water bottle and iv) glass). The columns show the different locations (i.e., i) table top, ii) middle level of the shelf and iii) upper level of the shelf). The figure also shows the wide variety of configurations, which exploit the 4-dof human-like kinematics. Experimental data for a chosen grasping task is depicted in Fig. 5.25, showing the measurement of $\boldsymbol{\varphi}_b$, $\boldsymbol{q}$ and the hand, and the intervals of the grasping process.

Kinesthetic Guidance

A final grasping experiment is depicted in Fig. 5.26, where the hand of the prosthesis is guided to the object via interaction forces in floating-base gravity compensation. This is in lieu of using the impedance controller and the smartphone GUI. The related data depicts the guidance, control switch and grasping for this control mode.

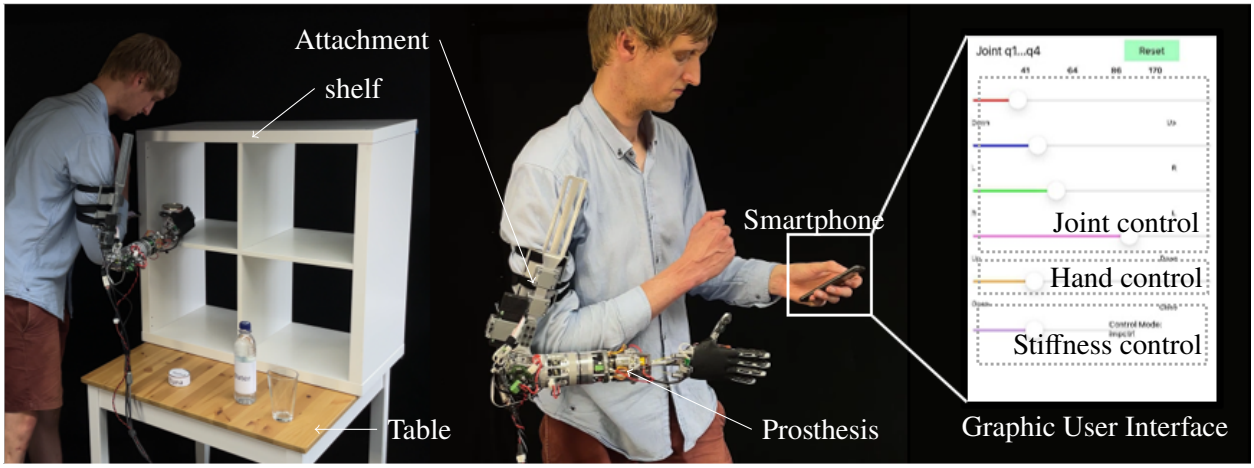

Figure 5.23 Experimental setup including the ANP attached to an unimpaired user.

Figure 5.24 Grasping validation for differ grasping poses using the Softhand Pro 2

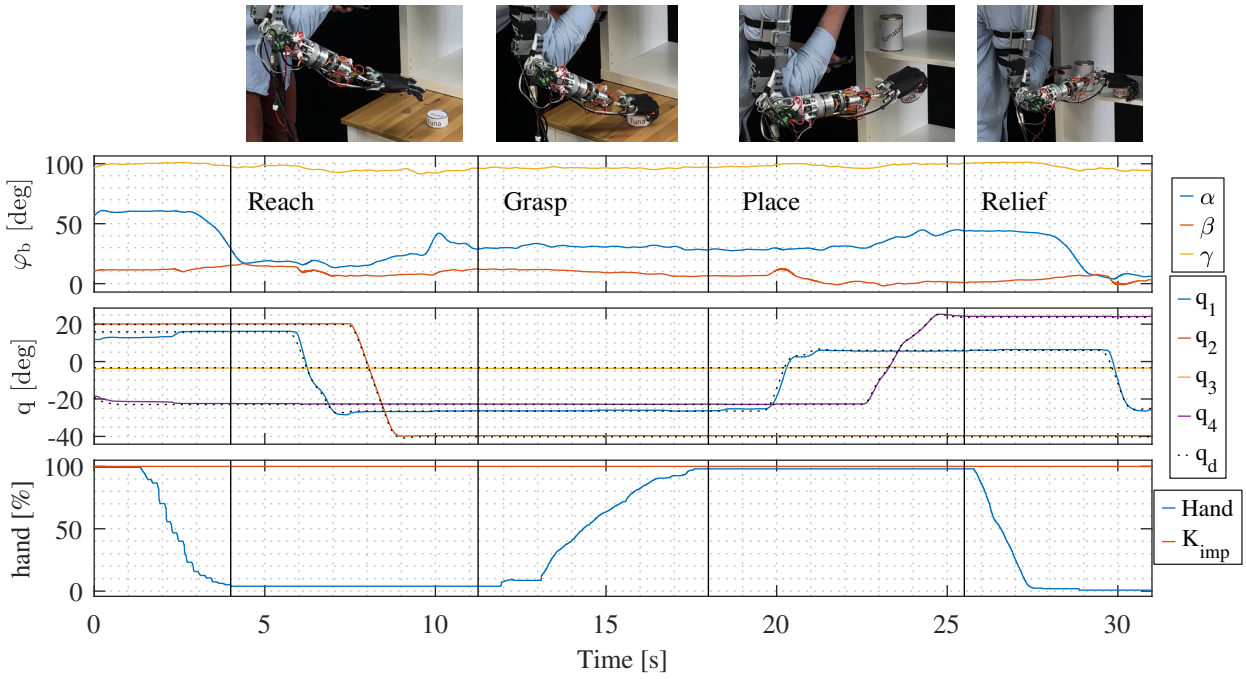

Figure 5.25 Smartphone-controlled grasping process of prototype II (ANP)

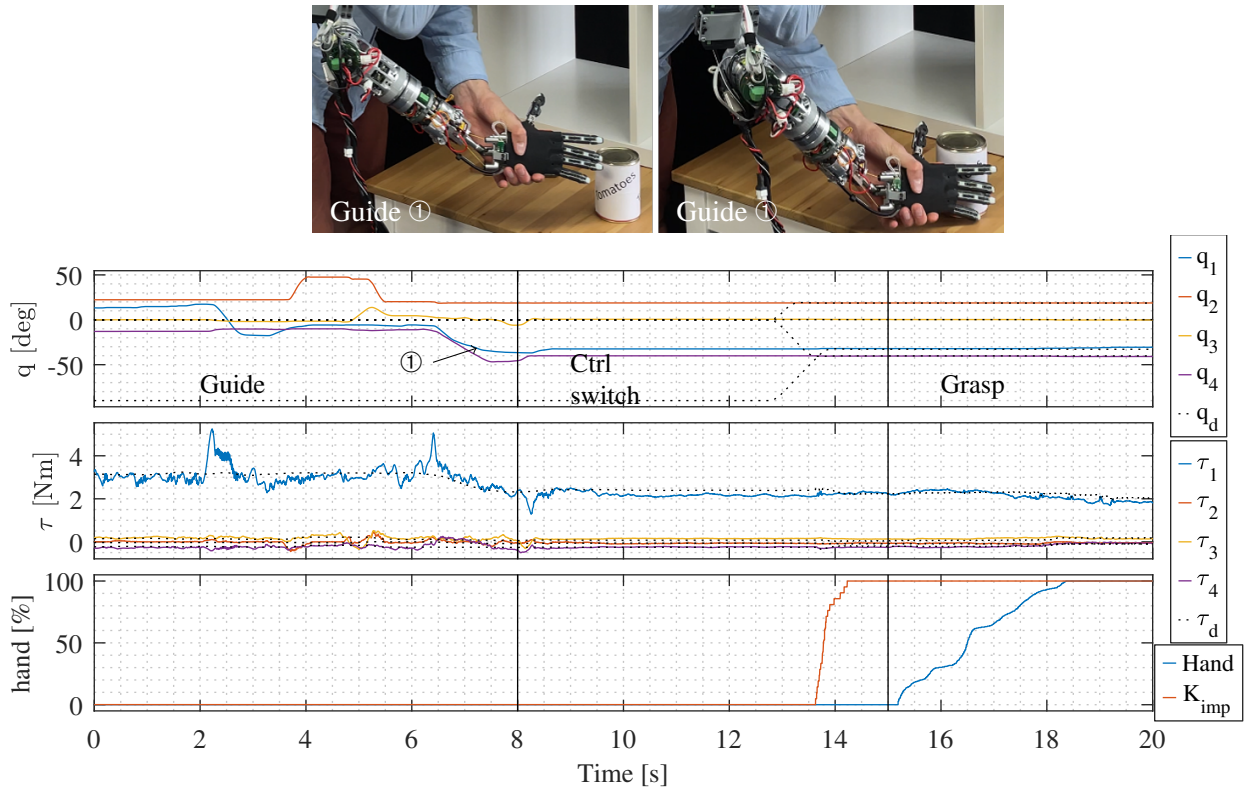

Figure 5.26 Grasping by kinesthetic guidance using the floating-base gravity compensation

5.7 Summary

This chapter utilized the modeling and control framework from Chapter 3 for extending the state of the art in upper limb prosthetics. The main contributions are

1. a human-inspired design pardigm for actuators, sensors, controllers and device intelligence implementation in upper-limb prosthetics,
2. the methods and technology transfer from soft and tactile robotics, including modeling, control and mechatronics, to upper limb prosthetics,
3. a sim2real-guided digital twin development approach to handle a complex from-scratch robotic prosthesis development,
4. the first prosthesis, which is able to imitate the human neuromuscular system in terms of *body awareness*, *contact awareness*, *human-like contact response* and *human-like kinematics*.
5. the Artificial Neuromuscular Prosthesis (ANP) system, with 4-dof human-like kinematics, fully fledged joint torque control, impedance control, floating-base model compensation and momentum observeration with contact detection monitoring algorithm at human-like size and weight of 1.7 kg.

These advances were achieved by an analysis of the human body and the state of the art in soft and tactile robotics. Based on these, the novel prosthesis paradigm was elaborated, which i) allowed for a corresponding human-inspired actuator, sensor and device intelligence design principle ii) and allowed for generating human-like behavior. Requirements for functional, technical features and specification were also defined. This includes the proposal for applying a detailed technical concept for an upper-limb prosthesis to replicate key functionalities of the human neuromuscular system. The challenging complexity of the development was addressed by a sim2real-guided design process. For this, a digital twin simulation of the prosthesis was constructed for the design of the controllers, device intelligence, load simulation, the design of geometries and the choice of sensors and actuators. Two prosthesis mechatronic solutions, prototype I and prototype II (ANP), were proposed for fulfilling the aforementioned requirements and concepts. A tendon-driven wrist, consisting of a hybrid tendon-/non-tendon-driven structure with parallel 3SPS-1RR kinematics, was developed. This allowed for i) fitting the wrist kinematics inside the dimensions of a human arm, and for ii) implementing joint torque sensing. During the development of the kinematics model and controller, the framework from Chapter 3 was extensively utilized.

While prototype I was developed for a first paradigm validation, prototype II was designed to incorporate all key features, specifications and requirements, with a from-scratch, lightweight, wearable design. Finally, control and skills of the devices were shown in experiments to validate control features, such as impedance control, torque control, and floating-base gravity compensation. In addition, the more conceptual features such as *body awareness*, *contact awareness*, *human-like contact response* were also successfully validated. Finally, the human-controlled and kinesthetically-guided grasping capabilities of the prosthesis could be confirmed with an unimpaired user.

Next steps in such development should focus on testing the developed prosthesis with impaired users. For a subsequent clinical analysis, however, another device iteration is likely required to incorporate necessary battery and computation into the device.

6 Part III (The "Exoprosthesis")

Applying the prosthesis technology from the previous chapter, this chapter introduces a novel method for the attachment of upper-limb prostheses to the human body. This is realized by a shoulder exoskeleton. Being inspired by a first concept of a robotic prosthesis attachment [12] and the patent [13], various technologies from tactile robotics (Sec. 2.1), prosthetics (Sec. 2.3), exoskeletons (Sec. 2.4) and passive sockets (Sec. 6.1) are combined to develop a technical concept of an active robotic socket, see Fig. 6.1. These features are then realized by the control framework from Chapter 3, providing a toolbox of structures and transmission models and related controllers. Based on the mathematical description, a new device, denoted *exoprosthesis*, is developed. The belonging investigation includes a multi-body simulation for analyzing the feasibility and the reaction loads of such an *exoprosthesis* device.

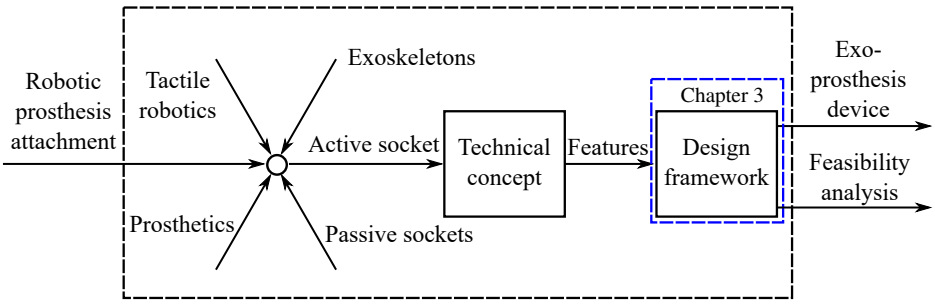

Figure 6.1 Development approach for the upper limb prosthesis

The *exoprosthesis* may be classified as a wearable robot. The design goals are somewhat different from the lightweight robots. Most notably, a wearable robot requires special consideration to attachment wrenches, COM and inertia to ensure ergonomic comfort for the user. The mathematical framework from Chapter 3 is utilized for the mechatronics development and the ergonomic analysis (in terms of COM and interaction wrenches).

State-of-the-art upper limb prostheses are commonly attached to the human residual limb by a passive socket, which comes along with several challenges. Reaction wrenches occur in the attachment point between the prosthesis and residual limb, which may be harmful for the human. This wrench may be visualized by a straightforward experiment, see Fig 6.2.

According to the state of the art, a prosthesis may either be attached to the human by a socket or a more recent method called Osseo Integration (OI). While OI requires surgical intervention, an attachment via a prosthesis socket is reported to be unpleasant for the prosthesis user [295]. In this work, a third option is introduced. An active tactile robotic socket carries the prosthesis, offloads the residual limb and allows a tactile guidance via small interaction forces at the same time. The feasibility of this concept is verified by a tactile and wearable shoulder exoskeleton, called an *exoprosthesis* when combined with a prosthesis. A first

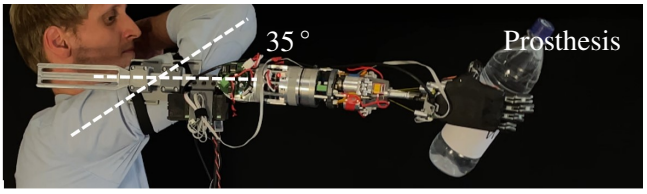

Figure 6.2 Problem: High reaction stress and deflection in the prosthesis attachment affected by gravity

mechatronics prototype, two floating-base controllers and an analysis of the loads acting on the user body is provided.

The contributions of this chapter include

- The first hardware realization of a wearable *exoprosthesis* consisting of shoulder exoskeleton and transhumeral prosthesis;
- The first body-aware prosthesis socket controller, which includes a floating-base gravity compensation and joint impedance control to compensate for trunk rotation, realized by a *monolithic* and *modular* control approach;
- A simulation-based and experimental comparison of residual limb and pelvis loads between a traditional prosthesis and the *exoprosthesis*;
- A full feasibility test of the *exoprosthesis* for a set of real-wold grasping tasks.

The chapter is structured as follows. Section 6.1 presents common solutions and challenges in passive sockets. Section 6.2 introduces and explains the novel active socket paradigm. The chapter was written based on [18].

6.1 Passive Socket

While significant advancements were made in prosthesis design and functionality over the past decades, the socket remains a source of safety risks, considerable discomfort and a major reason for prosthesis rejection [295, 296, 297]. This is especially true for individuals with proximal amputations. The socket provides the interface between the rigid prosthesis and the amputee's soft tissue. It is responsible for stability and load transmission to the device [298]. The mechanical stresses generated at the stump interface include compression, adhesion, and shear stress combined with poor ventilation and sweating. This inherently leads to soft tissue irritation, often resulting in skin wounds and pain [299, 300]. This problem has been approached from the perspective of various disciplines. For example, Osseo Integration (OI) is a surgical alternative to a prosthetic socket that is currently under investigation. For OI, the prosthesis is directly anchored to the bone via an implant that exits through an opening in the stump [301, 300]. This invasive method poses a number of risks, including superficial and deep infection [301]. However, it has found positive feedback from test subjects [302], indicating that there is indeed a strong need for alternatives. In particular, less invasive, however more comprehensive prosthesis options are also explored, as they may have the potential to increase the usage safety and decrease the rejection of upper limb prostheses at the same time. The following section introduces the active prosthetic socket.

6.2 Active Socket

While state-of-the-art prostheses are generally attached to the residual limb of the user by a passive socket, see Fig. 6.3 (left), an unnecessarily large reaction wrench $\mathcal{F}_{\mathrm{R}}$ often occurs. This wrench is not only unpleasant but also potentially harmful to the prosthesis user. This problem shall be addressed by an active socket, which carries the prosthesis by an actively controlled gravity compensated exoskeleton, reducing the size of the wrench $\mathcal{F}_{\mathrm{R}}$ and enabling direct guidance of the prosthesis via minimized interaction forces, see Fig. 6.3 (right). Consequently, the device targets for increased user comfort when wearing the upper-limb prosthetic device, measured by the interaction wrench $\mathcal{F}_{\mathrm{R}}$.

6.2.1 Technical Concept

The *exoprosthesis* prototype was developed based on the functional requirements summarized in Fig. 6.4 (left). Based on these requirements, technical features of the first generation prototype were elaborated, see

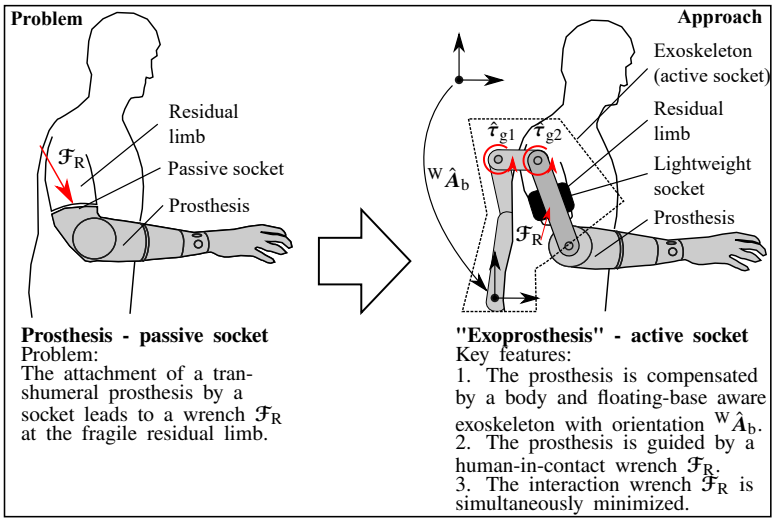

Figure 6.3 Concept: Description of the *exoprosthesis* concept

Fig. 6.4 (right). In order to better understand the design approach, key points of this approach are highlighted below.

The prosthesis is carried by the exoskeleton such that the residual limb can guide the system by small interaction forces $\mathcal{F}_R$. In case of a one-sided amputation, the exoskeleton and prosthesis are unsymmetrical with respect to the sagittal plane of the human. The prosthesis system is prone to provide an excentric COM, and consequently, provides an unpleasantness or even unergonomic user experience. With the aim of finding a better ergonomic solution, the following requirements are defined. The moment $\boldsymbol{M}_{\mathrm{pv,z}}$ at the pelvis needs to be zero and the forces $\boldsymbol{F}_{\mathrm{pv,z}}$ at the pelvis should be minimized. This is achieved by i) a passive actuation in the first shoulder joint, ii) a remote placement of the actuators on the contralateral side of the human body and iii) Bowden cables, which transmit the torque from the actuators to the exoskeleton joints, see Fig. 6.4 (right). The mechatronics concept includes torque controlled actuators and an IMU to measure the spatial orientation of the device. Consequently, the exoskeleton utilizes mechatronics and control methods common to soft and tactile robots. This device utilizes the torque controlled actuators as AAL and the Bowden-cables driven mechanism from Fig. 3.11 as TAL. The transmission scheme of the whole exoprosthesis may be found in Fig. 3.15.

The following section evaluates the mechatronic solution of this first generation prototype in detail – particularly, the design of the prototype, the human-in-the-loop model for analyzing the multi-body-structure, and the control methods of the exoskeleton.

6.2.2 Exoskeleton Prototype

The resulting design of the wearable *exoprosthesis*, including the front and back view, is depicted in Fig. 6.5. The device consists of a three degrees of freedom shoulder exoskeleton with one passive (q_1) and two actively controlled joints (q_2 and q_3). The exoskeleton mimics the human shoulder kinematics with three intersecting axes approximately coinciding with the glenohumeral joint of the shoulder. An additional passive slider a is implemented in the attachment of the residual limb to address kinematic mismatches between the human shoulder and the exoskeleton, see Fig. 6.5. The *upper arm* of the exoskeleton connects to the human *residual limb* via a *mechanical interface*. This connects the human to the device using a 3d printed *Shell* and *Velcro fasteners*, see Fig. 6.6.

Figure 6.6 depicts an exploded view, showing how the components *Arc0*, *Arc1*, *Arc2*, *spring* and *upper arm* of the exoskeleton are assembled. For typical every day motions/orientations, joint q_1 of the exoskeleton was designed to be passive in order to reduce weight, as gravity has a rather low effect on the joint, see Fig. 6.5. A magnet encoder measures the joint position of q_1. *Bowden cables* transmit power between *robotic actuators* and the exoskeleton joint q_2 and joint q_3. A downside of the *Bowden cables* is that a disturbing

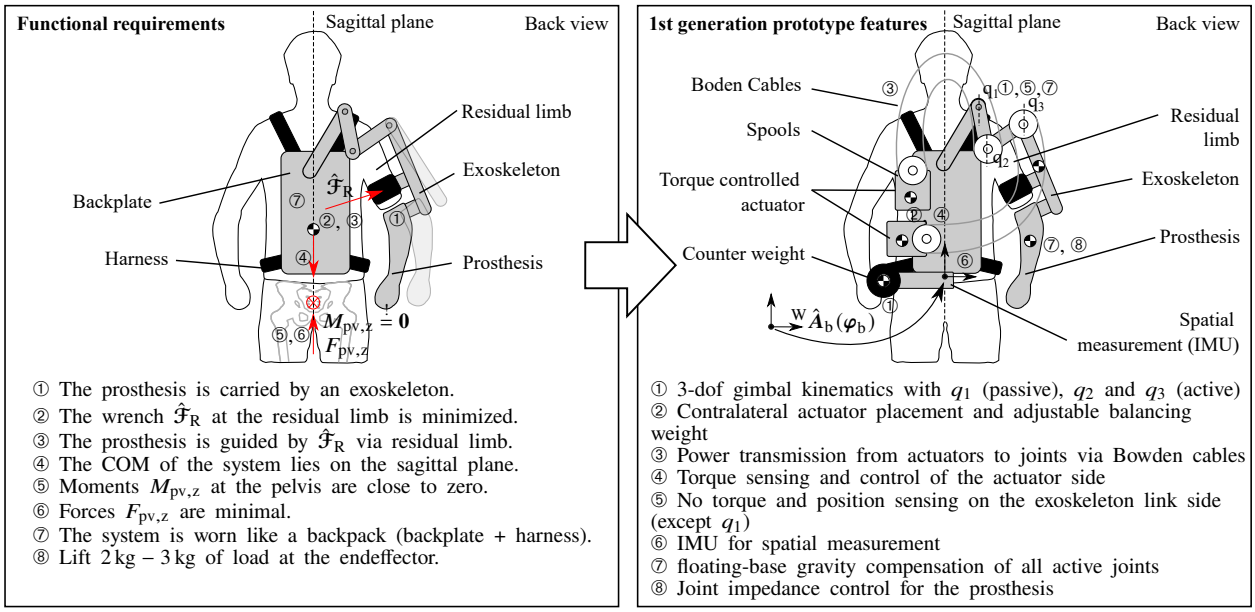

Figure 6.4 Functional requirements and features of the 1st generation prototype *exoprosthesis* ExoPro Gen I

torque on the passive joint q_1 is induced, as *Bowden cables* have an inherent compliance. This problem is addressed by a lightweight 3d printed mechanical torsion centering *spring*, which counteracts the inherent stiffness of the *Bowden cables*, see Fig. 6.6. The exoskeleton can be adjusted in all relevant directions to be suited for individual body dimensions, see Fig. 6.5. The arc elements were designed to be non-adjustable to avoid weakening of the structure. The system is built up on a *backplate*. Consequently, the device can be worn similar to a backpack. A *counter weight* with an adjustable *slider* helps to manually fine tune the COM. Figure A.4 in the Appendix shows how the COM could be successfully placed on the sagittal plane. The *prosthesis*, modularly attached to the exoskeleton, is described in Chapter 5.

The mechanical realization of the drive-train is depicted in Fig. 6.7. The system consists of a *driving spool* that is driven by a *robotic actuator*, and a *driven spool* that transmits the torque to the exoskeleton joint. Both spools are interconnected by two *Bowden cables* using belt-like kinematics. The *Bowden cable* consists of an outer pipe and an inner *steel wire*.

A custom made *robotic actuator* drives the system. While one side is attached to a *fixation*, the other side is connected to the *driving spool*. It contains a custom made, strain gauge based torque sensor (based on a design with 5 spokes, see Fig. 6.7, similar to [244]), a harmonic gearing ($i = 120$), a brushless dc motor ($\tau_m = 500$ mNm), a magnetic motor-side position sensor and custom made electronics. The electronics[1] include custom developed current and torque controllers.

It is apparent that torque sensing and torque control are located at the *robotic actuator* while the output torque is required for the exoskeleton joint *ax2*. Thus, *Bowden cables* are utilized for transmitting torques for measurement and actuation. This design choice was made intentionally, despite the friction produced by the *Bowden cables*. It constitutes the trade off between friction or higher complexity and weight/inertia that would be created by torque sensing directly at the exoskeleton joints. Another striking benefit of the Bowden cables are their ability to bypass complex kinematic structures, i.e., the exoskeleton shoulder kinematics in this case. The system is powered at 24 V and controlled by a real-time computer running a Linux real-time kernel together with Matlab/Simulink and the EtherCat protocol at 1 kHz. In the following section, the *exoprosthesis* is further analyzed via a multi-body simulation.

[1] Not developed by the author.

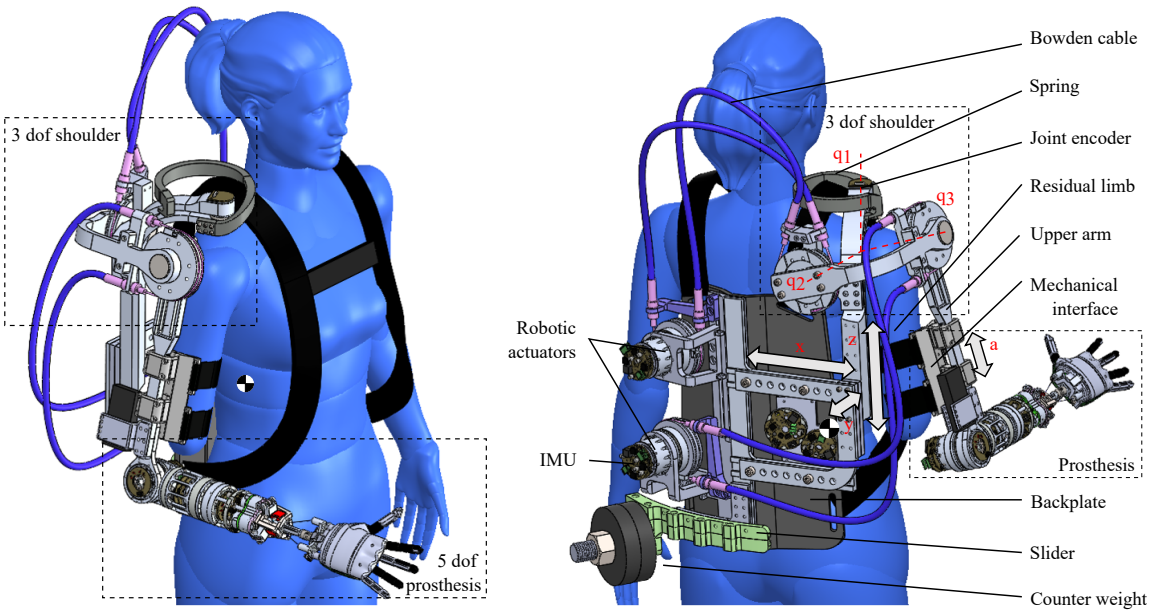

Figure 6.5 Front and back view of the *exoprosthesis* prototype ExoPro Gen I consisting of an exoskeleton and a prosthesis. The human model is taken from [303]

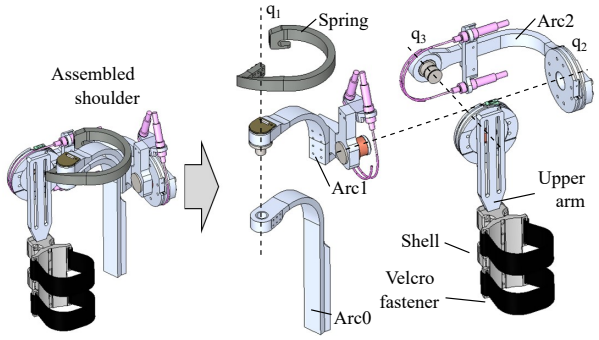

Figure 6.6 Exploded view of the shoulder module of the *exoprosthesis*

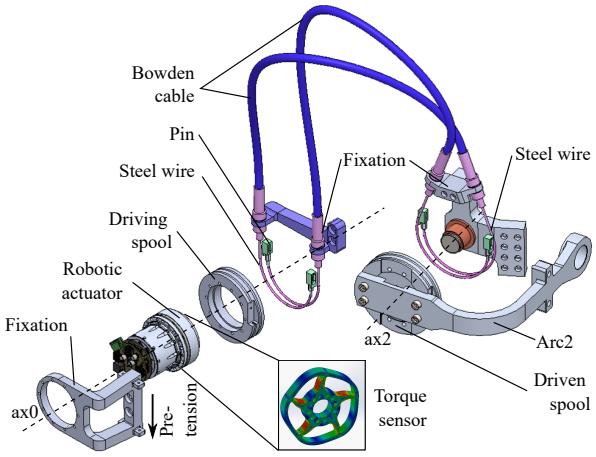

Figure 6.7 Exploded view of the upper actuation unit, which is located on the Backplate

6.2.3 Exo-Human-In-The-Loop Model

The exoskeleton of this work is built based on serial kinematics floating-base sub systems. With the foundation of a floating-base model from Sec. 3.1, the sub systems are introduced. This work incorporates four different serial kinematic systems, i) *exoprosthesis*, ii) *exoskeleton*, iii) *human* and iv) *prosthesis*, which are derived utilizing (3.1) to (3.22). The kinematic properties of the systems are based on MDH parameters [248], see Tab. A.4 in the Appendix. From here on, the nomenclature from Sec. 3.1 is subsequently applied $\square_{\square} \widehat{=} \square_{\square \mathrm{X}}$ (e.g., ${}^{\mathrm{W}}\boldsymbol{t}_{\mathrm{b}} \widehat{=} {}^{\mathrm{W}}\boldsymbol{t}_{\mathrm{be}}$).

Now, a floating-base multi-body plant model of the *exoprosthesis* with human attachment is assembled, see Fig. 6.8 (left). For this, the model of *exoprosthesis* with subscripts (e) and (h) from Tab. A.4 with human attachment are analogous to (3.20)[2] as

$$\begin{pmatrix} \boldsymbol{M}_{\mathrm{e}} & \boldsymbol{0} \\ \boldsymbol{0} & \boldsymbol{M}_{\mathrm{h}} \end{pmatrix} \begin{pmatrix} \ddot{\boldsymbol{q}}_{\mathrm{ce}} \\ \ddot{\boldsymbol{q}}_{\mathrm{ch}} \end{pmatrix} + \begin{pmatrix} \boldsymbol{C}_{\mathrm{e}} & \boldsymbol{0} \\ \boldsymbol{0} & \boldsymbol{C}_{\mathrm{h}} \end{pmatrix} \begin{pmatrix} \dot{\boldsymbol{q}}_{\mathrm{ce}} \\ \dot{\boldsymbol{q}}_{\mathrm{ch}} \end{pmatrix} + \begin{pmatrix} \boldsymbol{g}_{\mathrm{e}} \\ \boldsymbol{g}_{\mathrm{h}} \end{pmatrix} = \begin{pmatrix} \boldsymbol{\tau}_{\mathrm{e}} + \boldsymbol{\tau}_{\mathrm{ext,e}} \\ \boldsymbol{\tau}_{\mathrm{h}} + \boldsymbol{\tau}_{\mathrm{ext,h}} \end{pmatrix}. \tag{6.1}$$

[2] The dependency of $\boldsymbol{q}_{\mathrm{ce}}$ and $\boldsymbol{q}_{\mathrm{ch}}$ is omitted for better readability.

Up to this point, the systems from (6.1) are still decoupled.

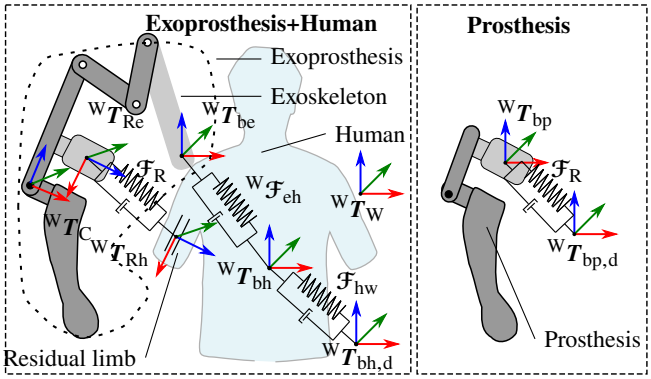

Figure 6.8 Comparison of models "Exoprosthesis+Human" and "Prosthesis" depicting spring-damper systems for mutual attachment associated coordinate frames

Figure 6.8 (left) depicts how the coupling between human and *exoprosthesis* are modeled as spatial spring-damper systems, corresponding to wrenches ${}^{\mathrm{W}}\mathcal{F}_{\mathrm{R}}$, ${}^{\mathrm{W}}\mathcal{F}_{\mathrm{eh}}$ and ${}^{\mathrm{W}}\mathcal{F}_{\mathrm{hw}}$. Here, the subscript (R) denotes the wrench at the residual limb, (eh) the wrench between exoskeleton and human and (hw) the wrench between human and world. These are projected to generalized forces $\boldsymbol{\tau}_{\mathrm{ext,e}}$, $\boldsymbol{\tau}_{\mathrm{ext,h}}$ as

$$\begin{pmatrix}\boldsymbol{\tau}_{\mathrm{ext,e}}\\ \boldsymbol{\tau}_{\mathrm{ext,h}}\end{pmatrix} = \dots$$
$$\begin{pmatrix}\mathbf{0} & \boldsymbol{J}(\mathrm{be},\boldsymbol{q}_{\mathrm{ce}})^T & \boldsymbol{J}(\mathrm{Re},\boldsymbol{q}_{\mathrm{ce}})^T\\ -\boldsymbol{J}(\mathrm{bh},\boldsymbol{q}_{\mathrm{ch}})^T & -\boldsymbol{J}(\mathrm{bh},\boldsymbol{q}_{\mathrm{ch}})^T & -\boldsymbol{J}(\mathrm{Rh},\boldsymbol{q}_{\mathrm{ch}})^T\end{pmatrix}\begin{pmatrix}{}^{\mathrm{W}}\mathcal{F}_{\mathrm{hw}}\\ {}^{\mathrm{W}}\mathcal{F}_{\mathrm{eh}}\\ {}^{\mathrm{W}}\mathcal{F}_{\mathrm{R}}\end{pmatrix}. \tag{6.2}$$

The wrench ${}^{\mathrm{W}}\mathcal{F}_{\mathrm{R}}$ acts between the coordinate frames ${}^{\mathrm{W}}\boldsymbol{T}_{\mathrm{Re}}$ and ${}^{\mathrm{W}}\boldsymbol{T}_{\mathrm{Rh}}$, the wrench ${}^{\mathrm{W}}\mathcal{F}_{\mathrm{eh}}$ between ${}^{\mathrm{W}}\boldsymbol{T}_{\mathrm{be}}$ and ${}^{\mathrm{W}}\boldsymbol{T}_{\mathrm{bh}}$, and the wrench ${}^{\mathrm{W}}\mathcal{F}_{\mathrm{hw}}$ between ${}^{\mathrm{W}}\boldsymbol{T}_{\mathrm{bh}}$ and ${}^{\mathrm{W}}\boldsymbol{T}_{\mathrm{bh,d}}$. Here, ${}^{\mathrm{W}}\boldsymbol{T}_{\mathrm{Re}}$ and ${}^{\mathrm{W}}\boldsymbol{T}_{\mathrm{Rh}}$ are the coordinate frames at the residual limb for exoskeleton and human side. ${}^{\mathrm{W}}\boldsymbol{T}_{\mathrm{be}}$ and ${}^{\mathrm{W}}\boldsymbol{T}_{\mathrm{bh}}$ are the base frames for exoskeleton and human, respectively. ${}^{\mathrm{W}}\boldsymbol{T}_{\mathrm{bh,d}}$ is the desired human base frame.

The floating-base Jacobians $\boldsymbol{J}(\mathrm{be},\boldsymbol{q}_{\mathrm{ce}})$, $\boldsymbol{J}(\mathrm{bh},\boldsymbol{q}_{\mathrm{ch}})$, $\boldsymbol{J}(\mathrm{Rh},\boldsymbol{q}_{\mathrm{ce}})$ and $\boldsymbol{J}(\mathrm{Re},\boldsymbol{q}_{\mathrm{ch}})$ in (6.2) are based on the transformation matrices ${}^{\mathrm{W}}\boldsymbol{T}_{\mathrm{be}}$ and ${}^{\mathrm{W}}\boldsymbol{T}_{\mathrm{bh}}$ from (3.3), the approach (3.9) and

$${}^{\mathrm{W}}\boldsymbol{T}_{\mathrm{Rh}} = {}^{\mathrm{W}}\boldsymbol{T}_{\mathrm{bh}}\,{}^{\mathrm{bh}}\boldsymbol{T}_{\mathrm{3h}}(\boldsymbol{q}_{\mathrm{ch}})\,{}^{\mathrm{3h}}\boldsymbol{T}_{\mathrm{Rh}} \tag{6.3}$$
$${}^{\mathrm{W}}\boldsymbol{T}_{\mathrm{Re}} = {}^{\mathrm{W}}\boldsymbol{T}_{\mathrm{be}}\,{}^{\mathrm{be}}\boldsymbol{T}_{\mathrm{3e}}(\boldsymbol{q}_{\mathrm{ce}})\,{}^{\mathrm{3e}}\boldsymbol{T}_{\mathrm{Re}}. \tag{6.4}$$

The transformation matrices ${}^{\mathrm{3e}}\boldsymbol{T}_{\mathrm{Re}}$ and ${}^{\mathrm{3h}}\boldsymbol{T}_{\mathrm{Rh}}$, expressed in frame 3 of the exoskeleton and human, locate the contact frame for both systems at the residual limb, respectively. It yields ${}^{\mathrm{3h}}\boldsymbol{T}_{\mathrm{Rh}} = {}^{\mathrm{3e}}\boldsymbol{T}_{\mathrm{Re}} = {}^{3}\boldsymbol{T}_{\mathrm{R}}$ with

$${}^{3}\boldsymbol{T}_{\mathrm{R}} = \begin{pmatrix}1 & 0 & 0 & a_4/2\\ 0 & 1 & 0 & 0\\ 0 & 0 & 1 & 0\\ 0 & 0 & 0 & 1\end{pmatrix}, \tag{6.5}$$

where a_4 is an MDH parameter, see Tab. A.3 in the Appendix. ${}^{\mathrm{bh}}\boldsymbol{T}_{\mathrm{3h}}$ and ${}^{\mathrm{be}}\boldsymbol{T}_{\mathrm{3e}}$ are derived from the serial kinematics, using the MDH parameters, as listed in Tab. A.4 and Tab. A.3 in the Appendix. Given all transformation matrices, the particular Jacobians can be derived by (3.10) accordingly.

The detailed spring-damper systems for ${}^{\mathrm{W}}\mathcal{F}_{\mathrm{R}}$,${}^{\mathrm{W}}\mathcal{F}_{\mathrm{eh}}$ and ${}^{\mathrm{W}}\mathcal{F}_{\mathrm{hw}}$ connecting the sub-systems are described in Sec. A.3.1 in the Appendix. The prosthesis and human are modeled as serial kinematics and designed accordingly, using Tab. A.3 and Tab. A.4 in Appendix. In the following section, two suitable controllers for the *exoprosthesis* are proposed, which allow for directly guiding the exoskeleton via interaction forces.

6.3 Active Socket Control

Two *exoprosthesis* controller variants, namely the *monolithic* and *modular* prosthesis socket control, are proposed, see Fig. 6.9. These variants enable a guidance of the prosthesis socket by gentle interaction forces at the residual limb, while the prosthesis is controlled by a joint impedance controller. The basic

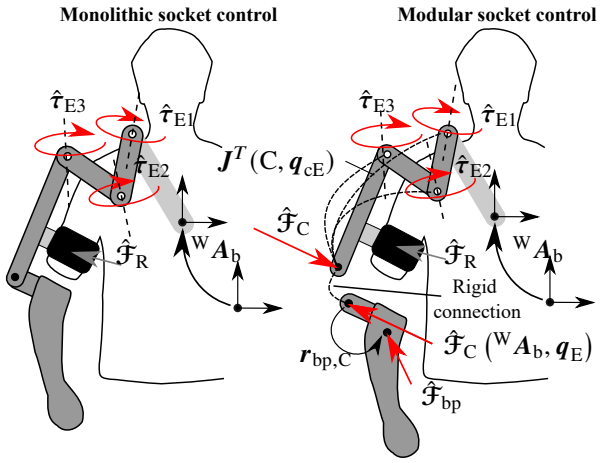

Figure 6.9 *Monolithic* and *modular* prosthesis socket control concept of the *exoprosthesis*. Note, that it yields $(\hat{\tau}_{e1}, \hat{\tau}_{e2}, \hat{\tau}_{e3})^T \widehat{=} (\hat{\tau}_{E1}, \hat{\tau}_{E2}, \hat{\tau}_{E3})^T$.

idea underlying the *monolithic* controller is to consider the *exoprosthesis* as a single 7-dof floating-base serial kinematic system for which a suitable gravity compensation is derived. The basic idea of the *modular* controller is to consider the exoskeleton as 3-dof stand-alone system. For this, a floating-base gravity compensation is derived, however, the prosthesis is interacting with the exoskeleton via the wrench $\hat{\mathcal{F}}_C$, see Fig. 6.9 (right). For this approach, a prosthesis floating-base model is required[3], providing the base wrench $\hat{\mathcal{F}}_{bp}$, which can be transformed to $\hat{\mathcal{F}}_C$. In turn, the prosthesis model requires information about the exoskeleton configuration ${}^W A_b$ and q_E in order to provide the correct prosthesis joint torque that considers the orientation of the entire structure. The overall control scheme of both variants is depicted in Fig. 6.10. In the following, the control algorithms for the particular mechanical systems are introduced, based on key findings under Chapter 3.

For the following detailed description of the *monolithic* and *modular* control approach in Sec. 6.3.1 and Sec. 6.3.2, please consider the introduced indices from Sec. 6.2.3.

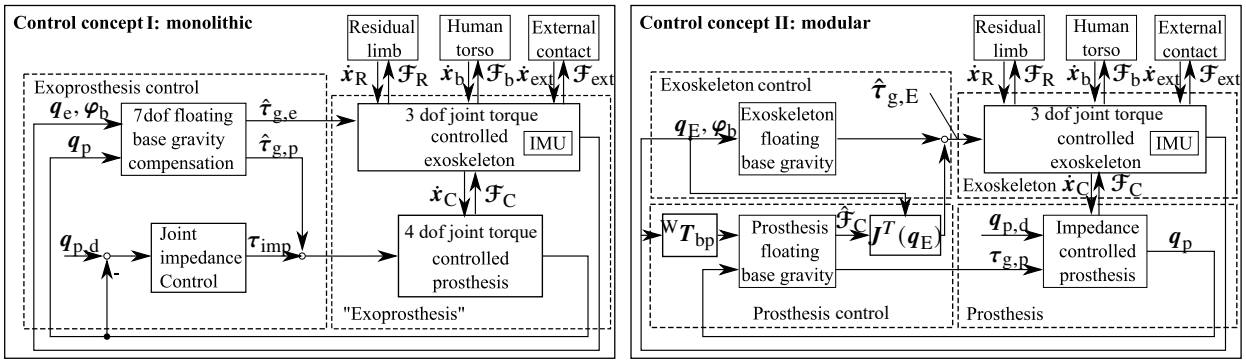

Figure 6.10 Control schemes for the *exoprosthesis* ExoPro Gen I, see Sec. 6.3

[3] Alternatively, a 6-dof force/torque sensor could be used between prosthesis base and exoskeleton to directly measure $\hat{\mathcal{F}}_C$.

6.3.1 Monolithic

The robot compensation dynamics (without inertia effects) of the 7-dof floating-base kinematics is described by

$$\boldsymbol{\tau}_{\mathrm{mc,e}} = \hat{\boldsymbol{C}}_{\mathrm{je}}(\boldsymbol{q}_{\mathrm{ce}}, \dot{\boldsymbol{q}}_{\mathrm{ce}})\dot{\boldsymbol{q}}_{\mathrm{ce}} + \hat{\boldsymbol{g}}_{\mathrm{je}}(\boldsymbol{q}_{\mathrm{ce}}), \tag{6.6}$$

based on (3.34), which includes gravity and Coriolis compensation for all joints of the *exoprosthesis*. Equation (6.6) utilizes block matrices for Coriolis and gravity from the robot dynamics with subscript (e). The weight of the human limb is not considered in the dynamics model. In contrast to a fixed-base model, (6.6) was derived based on $\boldsymbol{q}_{\mathrm{ce}}$, which considers the base orientation ${}^{\mathrm{W}}\boldsymbol{\varphi}_{\mathrm{be}}$. This model is then applied to the joint torques

$$\boldsymbol{\tau}_{\mathrm{e}} = \boldsymbol{\tau}_{\mathrm{mc,e}} + \begin{pmatrix} \boldsymbol{0}_{3\times 1} \\ \boldsymbol{\tau}_{\mathrm{imp,p}} \end{pmatrix}, \tag{6.7}$$

where τ_{e1} is the first element of $\boldsymbol{\tau}_{\mathrm{e}}$, which is not actuated.

At this point, the system is gravity compensated in the active joints. Consequently, the residual limb is able to intuitively guide the system via direct kinesthetic interaction forces. The prosthesis joints $q_4 - q_7$ are controlled by the joint impedance controller (3.37).

6.3.2 Modular

The exoskeleton compensator is modeled by its floating-base model[4] (subscript E) as

$$\boldsymbol{\tau}_{\mathrm{E}} = \hat{\boldsymbol{C}}_{\mathrm{jE}}(\boldsymbol{q}_{\mathrm{cE}}, \dot{\boldsymbol{q}}_{\mathrm{cE}})\dot{\boldsymbol{q}}_{\mathrm{cE}} + \hat{\boldsymbol{g}}_{\mathrm{jE}}(\boldsymbol{q}_{\mathrm{cE}}) + \hat{\boldsymbol{\tau}}_{\mathrm{ext,E}} \in \mathbb{R}^{3\times 1}, \tag{6.8}$$

based on (3.34), which provides gravity and Coriolis compensation for the subsystem. Additionally, the effect of the prosthesis on the exoskeleton model is described by the estimated model-based torques

$$\hat{\boldsymbol{\tau}}_{\mathrm{ext,E}} = \boldsymbol{J}^T(\mathrm{C}, \boldsymbol{q}_{\mathrm{cE}})\,{}^{\mathrm{W}}\hat{\boldsymbol{\mathcal{F}}}_{\mathrm{C}} \in \mathbb{R}^{3\times 1}, \tag{6.9}$$

utilizing a Jacobian $\boldsymbol{J}(\mathrm{C}, \boldsymbol{q}_{\mathrm{cE}})$, which is referred to coordinate frame ${}^{\mathrm{W}}\boldsymbol{T}_{\mathrm{C}}$. Before obtaining the interaction wrench ${}^{\mathrm{W}}\hat{\boldsymbol{\mathcal{F}}}_{\mathrm{C}}$ between the prosthesis and the exoskeleton, the base wrench compensator of the prosthesis

$${}^{\mathrm{W}}\hat{\boldsymbol{\mathcal{F}}}^{*}_{\mathrm{bp}} = \hat{\boldsymbol{C}}_{\mathrm{bp}}(\boldsymbol{q}_{\mathrm{cp}}, \dot{\boldsymbol{q}}_{\mathrm{cp}})\dot{\boldsymbol{q}}_{\mathrm{cp}} + \hat{\boldsymbol{g}}_{\mathrm{bp}}(\boldsymbol{q}_{\mathrm{bp}}) \in \mathbb{R}^{6\times 1} \tag{6.10}$$

needs to be calculated. The model uses the subscript (p) (see Tab. A.4) and the submatrices for the base from (3.21) and for the base reaction wrench (b). As the moment ${}^{\mathrm{W}}\hat{\boldsymbol{M}}^{*}_{\mathrm{bp}}$ of ${}^{\mathrm{W}}\hat{\boldsymbol{\mathcal{F}}}^{*}_{\mathrm{bp}}$ is twisted by RPY coordinates, the wrench is transformed to Cartesian coordinates via

$${}^{\mathrm{W}}\hat{\boldsymbol{\mathcal{F}}}_{\mathrm{bp}} = \begin{pmatrix} {}^{\mathrm{W}}\hat{\boldsymbol{F}}^{*}_{\mathrm{bp}} \\ \boldsymbol{J}_{\omega}\,{}^{\mathrm{W}}\hat{\boldsymbol{M}}^{*}_{\mathrm{bp}} \end{pmatrix} \tag{6.11}$$

with the twisted matrix $\boldsymbol{J}_{\omega} \in \mathbb{R}^{3\times 3}$ from (3.11). The wrench ${}^{\mathrm{W}}\hat{\boldsymbol{\mathcal{F}}}_{\mathrm{C}}$ is then calculated by a shift along ${}^{\mathrm{W}}\boldsymbol{r}_{\mathrm{bp,C}}$ by

$${}^{\mathrm{W}}\hat{\boldsymbol{\mathcal{F}}}_{\mathrm{C}} = \begin{pmatrix} {}^{\mathrm{W}}\hat{\boldsymbol{F}}_{\mathrm{bp}} \\ {}^{\mathrm{W}}\hat{\boldsymbol{M}}_{\mathrm{bp}} \end{pmatrix} + \begin{pmatrix} \boldsymbol{0}_{3\times 1} \\ {}^{\mathrm{W}}\boldsymbol{r}_{\mathrm{bp,C}} \times {}^{\mathrm{W}}\hat{\boldsymbol{F}}_{\mathrm{bp}} \end{pmatrix}. \tag{6.12}$$

The vector ${}^{\mathrm{W}}\boldsymbol{r}_{\mathrm{bp,C}}$ is obtained from the translational differences between ${}^{\mathrm{W}}\boldsymbol{T}_{\mathrm{C}}$ and ${}^{\mathrm{W}}\boldsymbol{T}_{\mathrm{bp}}$, see Fig. 6.9.

[4] Note, that here $\hat{\boldsymbol{\tau}}_{\mathrm{ext,E}}$ is not the external torque calculated by a momentum observer. Rather, it is the model-based torque computed by (6.9)-(6.12).

Finally, the prosthesis controller becomes

$$\boldsymbol{\tau}_{\mathrm{p}} = \boldsymbol{\tau}_{\mathrm{imp,p}} + \hat{\boldsymbol{C}}_{\mathrm{jp}}(\boldsymbol{q}_{\mathrm{cp}}, \dot{\boldsymbol{q}}_{\mathrm{cp}})\dot{\boldsymbol{q}}_{\mathrm{cp}} + \hat{\boldsymbol{g}}_{\mathrm{jp}}(\boldsymbol{q}_{\mathrm{cp}}), \tag{6.13}$$

using $\boldsymbol{\tau}_{\mathrm{imp,p}}$ from (3.37), where $\hat{\boldsymbol{C}}_{\mathrm{jp}}(\boldsymbol{q}_{\mathrm{cp}}, \dot{\boldsymbol{q}}_{\mathrm{cp}})$ and $\hat{\boldsymbol{g}}_{\mathrm{jp}}(\boldsymbol{q}_{\mathrm{cp}})$ are Coriolis and gravity vector compensators for the prosthesis.

For simplicity, the human limb is assumed to be driven by a PD-type joint impedance controller using a high joint stiffness in simulation. In the following section, the concept is evaluated in simulations and experiments.

6.4 Control and Skill Validation

In the following, the *exoprosthesis* is validated, covering the high-level skills and the underlying controllers. In the experiments, only the *monolithic* controller variant is used.

6.4.1 Active Socket Control

The following experiment aims for validating the main functionality of the *exoprosthesis*: the guidance of the device by direct interaction forces $\mathcal{F}_{\mathrm{R}}$ on the residual limb and the simultaneous control of the prosthesis joints.

Figure 6.12 depicts a human guidance experiment, using the floating-base gravity compensation in the exoskeleton joints (row 1), with sinusoidal tracking in the prosthesis joints (row 2). The *exoprosthesis* is attached to a fixed strut in an upright position. The underlying torque controlled joints of the gravity compensated shoulder are shown in row 3. It can be seen that the torques change in accordance to joint motion of q_2 and q_3 (row 1) to compensate for the right gravity torque and to keep the exoskeleton in place, see ① (row 3). The torques of the impedance controlled prosthesis are depicted in row 4. A similar experiment, with a human guiding the prosthesis by his upper arm when wearing the device, is depicted in the photo sequence in Fig. 6.11.

Figure 6.13 aims for validating the floating-base control of the *exoprosthesis* under a varying device orientation and showing its function. The system is tilted multiple times by ≈ 30 deg in the intervals *Move base* (row 1). Note that no motion in the joints occurs due to the floating-base gravity compensation. As a consequence of the base orientation change, the underlying torques in the exoskeleton adapt accordingly (row 3), see ① and ②. In interval *Move stump*, the exoskeleton is moved intentionally via human interaction forces. This results in a higher model-based joint torque τ_4 in the last interval (row 4), see ③. Clearly, actual and desired torques accord with one another. The photo sequence in Fig. 6.14 demonstrates the same experiment with a human wearing the device. The human tilts his body and shifts the prosthesis joints via interaction forces. However, the joints of the *exoprosthesis* remain essentially constant due to the underlying gravity compensation.

6.4.2 Grasping

The performance of picking and placing objects in common daily activities is a key criterion for transhumeral prostheses [304]. First grasping experiments with the *exoprosthesis* prototype are performed with an expert user. The prosthesis is equipped with the Softhand pro 2 [290]. The experiments are done in accordance to those from Fig. 5.23, where the prosthesis was tested. Specifically, the human is given the task to utilize the *exoprosthesis* as a tool for solving a set of tasks. For this purpose, the following non standardized pick and place test was developed.

Figure 6.15 depicts the experimental setup (left) and the HMI of the 5-dof prosthesis (right). The operator of the *exoprosthesis* uses his right arm to guide the *exoprosthesis* kinesthetically and his left arm to hold the smartphone for operating the prosthesis by a GUI. The GUI of the smartphone allows the operator to individually control the dof of prosthesis and hand via virtual sliders on the smartphone. These slider values are directly mapped to the respective joints using the User Datagram Protocol (UDP).

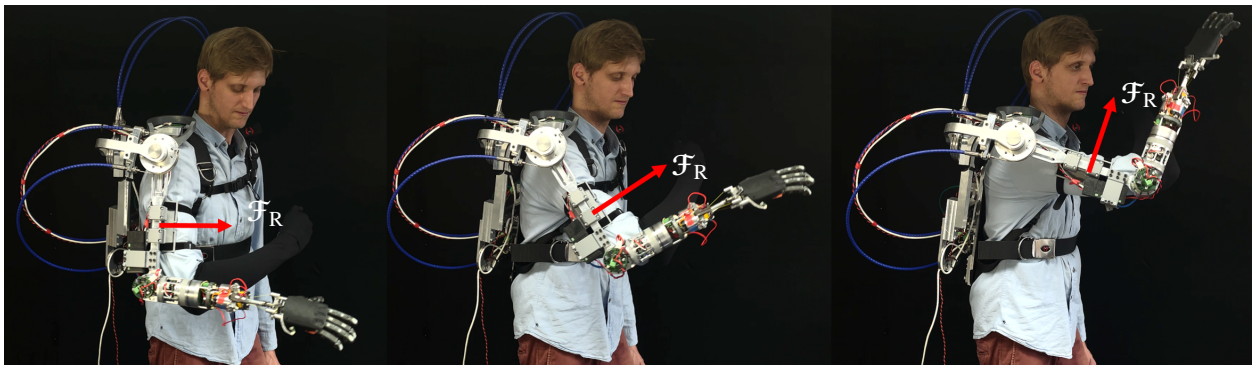

Figure 6.11 An expert user guides the *exoprosthesis* ExoPro Gen I with his upper arm through kinesthetic interaction forces, see Fig. 6.12

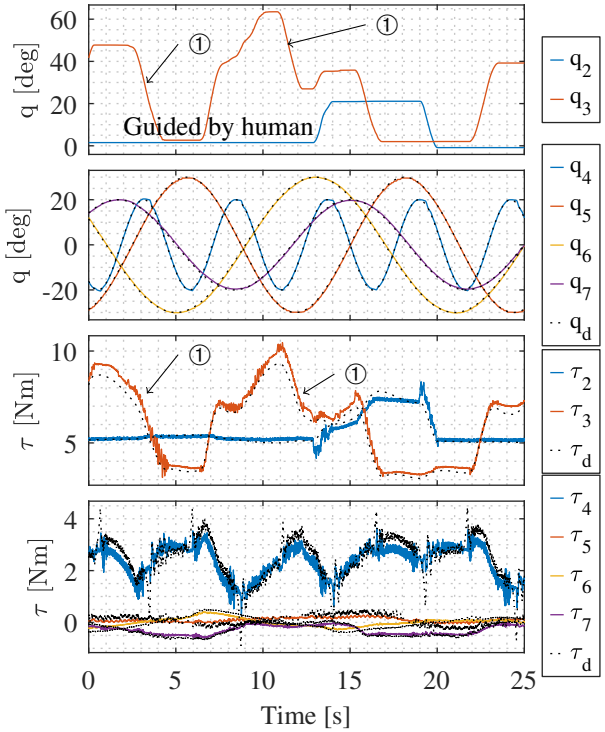

Figure 6.12 Sinusoidal tracking of the prosthesis joints while the shoulder joints are guided via human interaction forces, see Fig. 6.11.

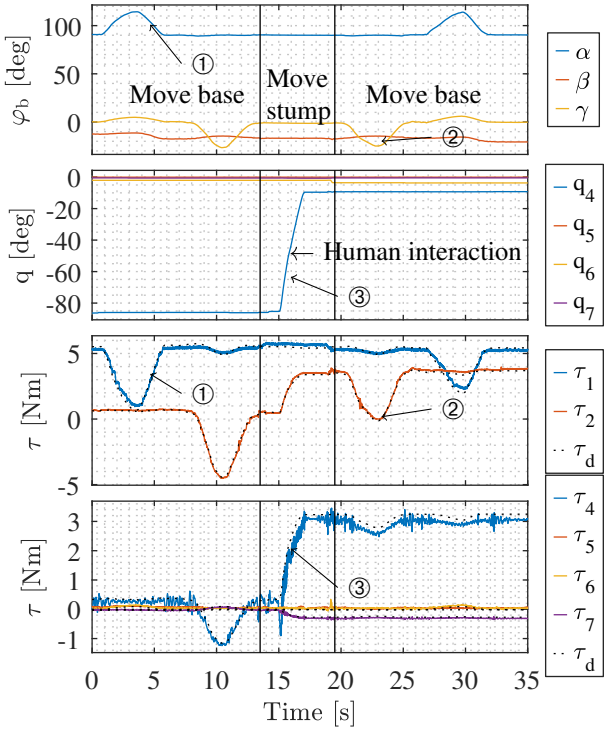

Figure 6.13 The *exoprosthesis* is tilted around x- and y-axes with activated floating-base gravity compensation, see Fig. 6.14.

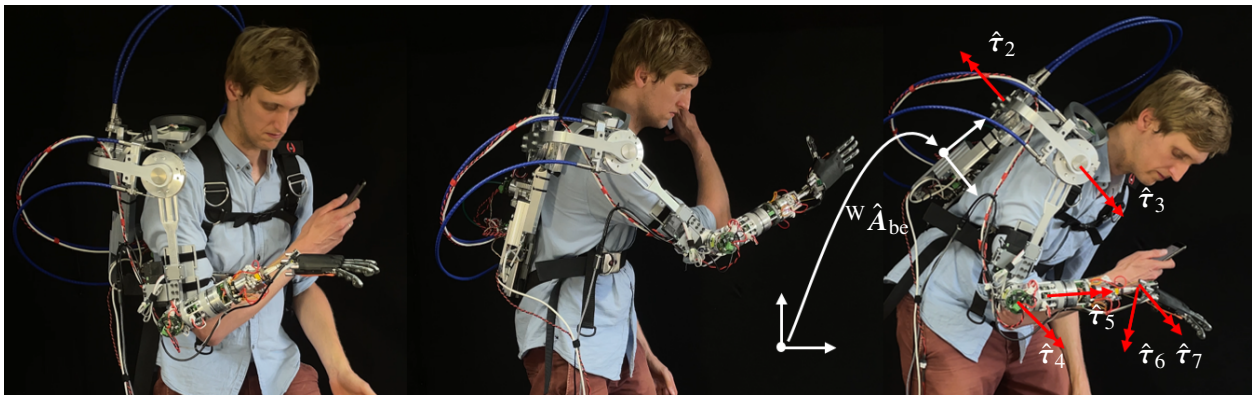

Figure 6.14 The human tilts his torso, varies the position of the prosthesis joints and the exoskeleton base orientation. Result: the *exoprosthesis* joints remain in position due to the underlying floating-base gravity compensation. See also the data of a similar experiment in Fig. 6.13. See underlying animation in Fig. 6.17.

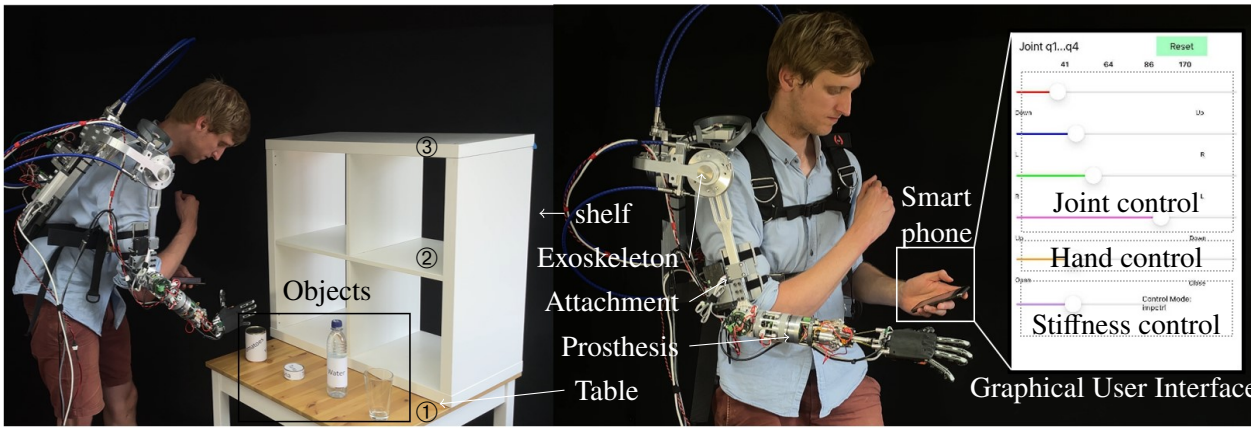

Figure 6.15 Experimental setup to validate the grasping capabilities of the *exoprosthesis* ExoPro Gen I (left). User machine interface of the prosthesis (right).

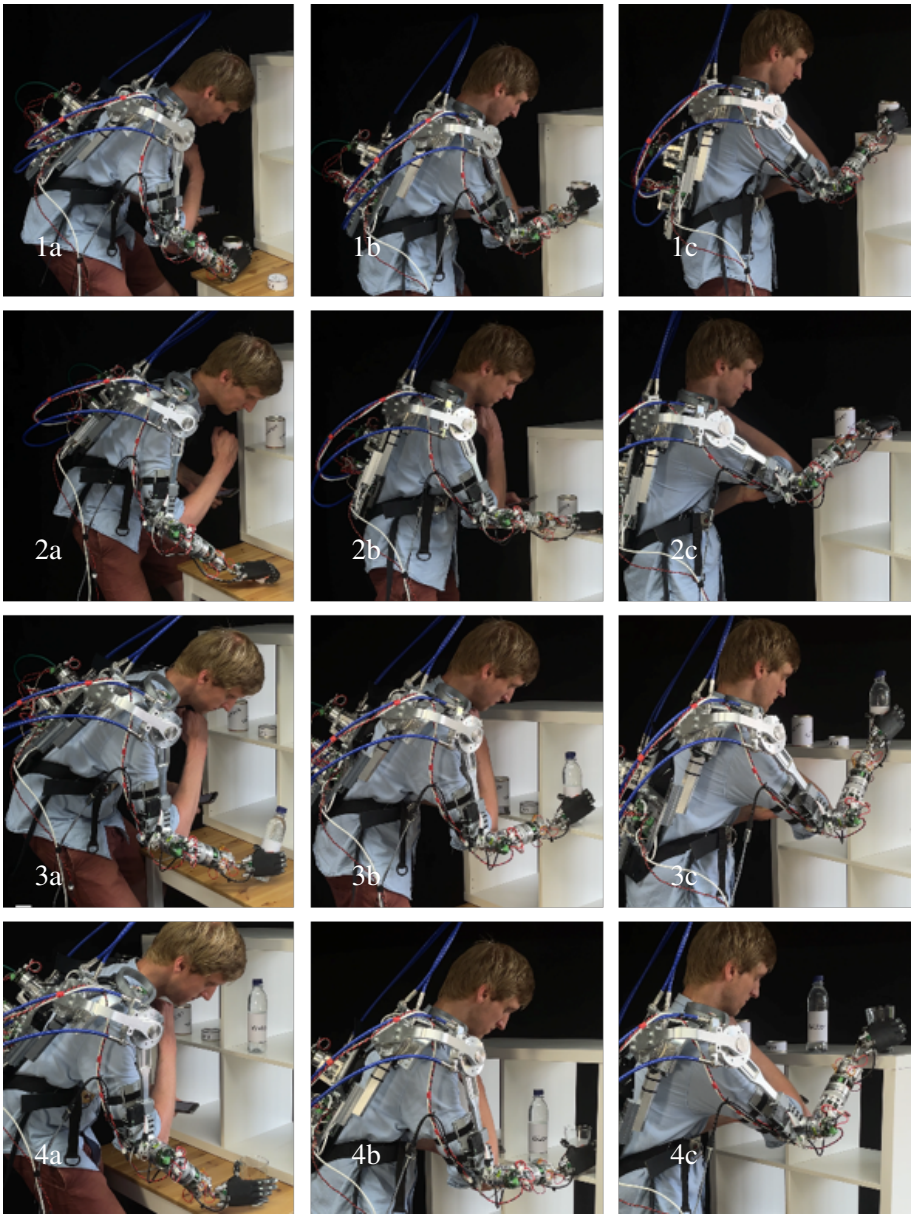

Figure 6.16 Validation of grasping capabilities for differ grasping poses. The objects to be grasped are a can of tomatoes (500 g), a can of tuna (125 g), a bottle of water (500 g), and a glass (100 g).

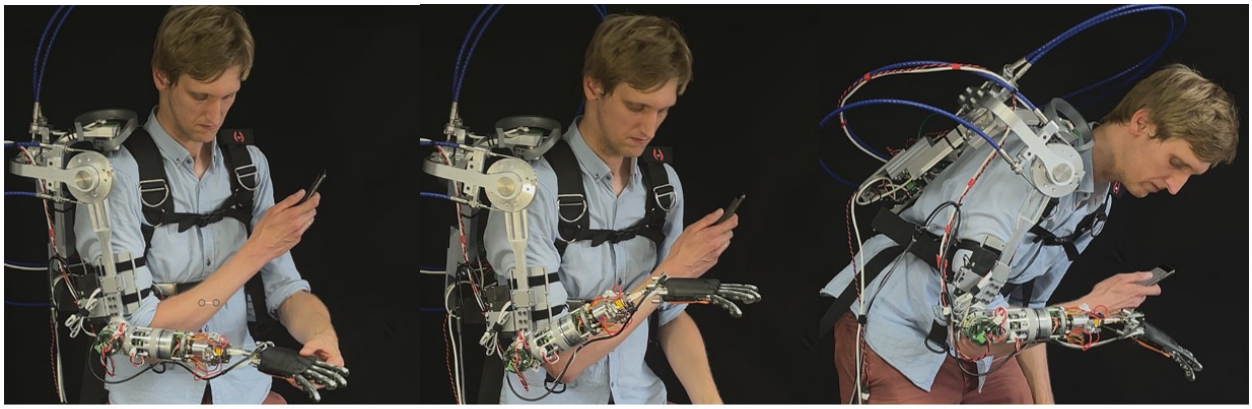

Floating base visualization

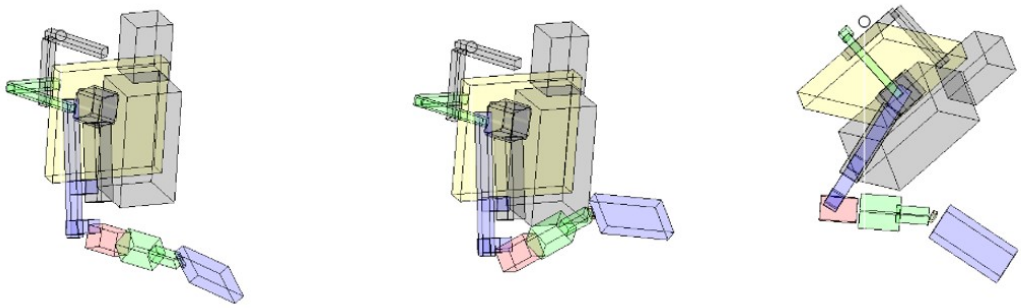

Figure 6.17 Floating base visualization of the real-time-capable model, compare Fig. 5.20

The experimental setup is depicted in Fig. 6.15 (left). It consists of a table and shelf, which is placed on top of the table surface. In total, the experiment provides three levels ①,②,③, which were constructed for the sake of picking and placing objects. Four types of objects are used in the experiment: i) a can of tomatoes, ii) a can of tuna, iii) a bottle of water and iv) an empty glass.

Experimental procedure: The user wearing the *exoprosthesis* stands in front of the table. The user is asked to pick up each object and place it on the next upper level of the shelf. Once all objects are placed on a certain level, all objects are picked up and placed on the next upper level. The experiment was designed in such a way that the user is encouraged to use as many degrees of freedom of the device as possible. During the experiment, the healthy arm must not be used to interact with the experimental setup or the prosthesis.

Figure 6.16 depicts the key moments of the experiment, arranged in a matrix. The rows depict the different objects and the columns depict the levels of placement, respectively. All objects could be grasped and placed successfully. Furthermore, it is noted that the shoulder flexion and extension angle q_3 is actively used for picking and placing the objects.

6.4.3 Reaction Wrench Analysis

Up to now, the basic functionality of the *exoprosthesis* was validated. It was shown that the device can be guided via interaction forces, while the prosthesis perform an arbitrary joint controller action. In this context, a closer look was given to the underlying floating-base controller, providing the right joint torque regardless the body orientation. Furthermore, the grasping capabilities of the device were successfully shown by human-in-the-loop experiments.

However so far, the analysis of the interaction wrenches between human body and device is missing. Based on the initial concepts from Fig. 6.3 and Fig. 6.4, the goal is to minimize the interaction wrench and the pelvis moment, which should ideally be zero. In the following, both the wrench at the residual limb and the pelvis are analyzed in more detail.

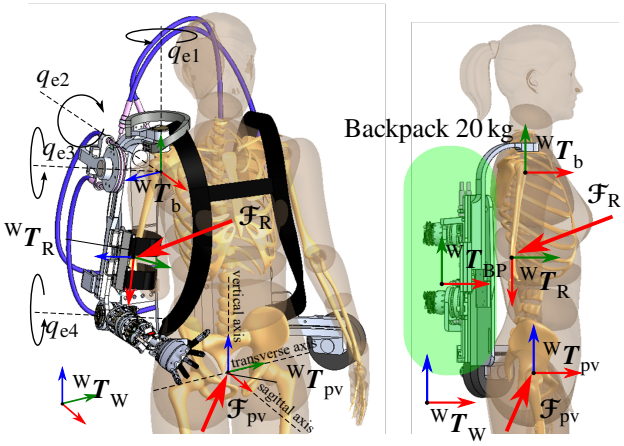

Figure 6.18 Coordinate frames, joint axes and wrenches of the exoprosthesis with human anatomy. The human model is taken from [303]

Simulation

The following simulation investigates the wrenches of interest

$$\mathcal{F}_{R} = \left(\boldsymbol{F}_{R}^{T}\ \boldsymbol{M}_{R}^{T}\right)^{T}, \mathcal{F}_{pv} = \left(\boldsymbol{F}_{pv}^{T}\ \boldsymbol{M}_{pv}^{T}\right)^{T}, \tag{6.14}$$

at residual limb ${}^{W}\boldsymbol{T}_{R}$ and pelvis ${}^{W}\boldsymbol{T}_{pv}$ for a chosen motion, see Fig. 6.19. Figure 6.18 helps in understanding the evaluation, where the device is depicted in its zero position $\boldsymbol{q}_{e} = (0,0,0,0,0,0,0)^{T}$.The wrenches $\mathcal{F}_{R}$ and $\mathcal{F}_{pv}$ are calculated based on the spring-damper systems from Fig. 6.8, which were tuned such that the stiffness is maximized and oscillations are minimized. While $\mathcal{F}_{R}$ can be directly obtained, $\mathcal{F}_{pv}$ is calculated based on $\mathcal{F}_{eh}$ for the *exoprosthesis* and based on $\mathcal{F}_{R}$ for the prosthesis, and then shifted to the pelvis frame, see Sec. A.3.2 in Appendix. The spatial spring damper systems measure the contact wrenches between the systems. For all forces and moments, the 2-norm is considered. The simulation is performed with an idealized actuator level torque controller $\boldsymbol{\tau} = \boldsymbol{\tau}_{d}$.

The simulation compares the two plant models *exoprosthesis*+human Fig. 6.8 (left) to the prosthesis only Fig. 6.8 (right) by applying the same motion to the systems. The simulation procedure is as follows:

1. The experiment is first performed with human and *exoprosthesis*, see Fig. 6.8 (left). This model corresponds to (6.1)-(6.5). The human shoulder drives the exoskeleton via $\boldsymbol{q}_{h,d}$ using a PD controller. The pose of the torso (${}^{W}\boldsymbol{A}_{bh,d}$ and ${}^{W}\boldsymbol{t}_{bh,d}$) and the joint position of the prosthesis $\boldsymbol{q}_{p,d}$ are controlled by respective controllers as well. The motion of the residual limb ${}^{W}\boldsymbol{T}_{Rh}(t)$ and $\boldsymbol{q}_{p,d}(t)$ are stored.

2. The experiment is repeated for the prosthesis Fig. 6.8 (right). The trajectory from the attachment ${}^{W}\boldsymbol{T}_{bp}(t) = {}^{W}\boldsymbol{T}_{Rh}(t)$ and the prosthesis joints $\boldsymbol{q}_{p,d}(t)$ motion from 1) are then applied to the prosthesis.

In the simulation (see Fig. 6.19), the human model lifts the prosthesis by a flexion of the shoulder joint by 90 deg ①. The upper and lower arm are aligned, and the elbow joint is straight ②. The arm is parallel to the body at the beginning of the experiment. Row 3 and 4 of Fig. 6.19 show the 2-norm of forces and moments of $\mathcal{F}_{R}$. Clearly, both forces and moments at ${}^{W}\boldsymbol{T}_{Rh}$ are much lower for the exoskeleton in comparison to a directly attached prosthesis, see ③, with maximum values of 5 N and 0 Nm compared to 20.6 N, 5.4 Nm. In fact, the interaction wrench is zero for the static case for the *exoprosthesis* due to the control bandwidth limits. The remaining forces of the *exoprosthesis* are likely caused by uncompensated acceleration and deceleration. Row 2 shows that the gravity compensation generates $\approx$ 10 Nm of supporting torque in the third joint explaining why ${}^{W}\boldsymbol{F}_{R}$ and ${}^{W}\boldsymbol{M}_{R}$ are close to zero for the static cases, e.g., $t = 6.5$ s. The last row depicts the pelvis wrenches, see Fig. 6.18. The moment ${}^{W}M_{ex}$ affected by the *exoprosthesis* is close to zero ($\approx$ 1 Nm at ④), and is in fact even lower than the moment caused by the prosthesis alone. Indeed, ${}^{W}M_{ex}$

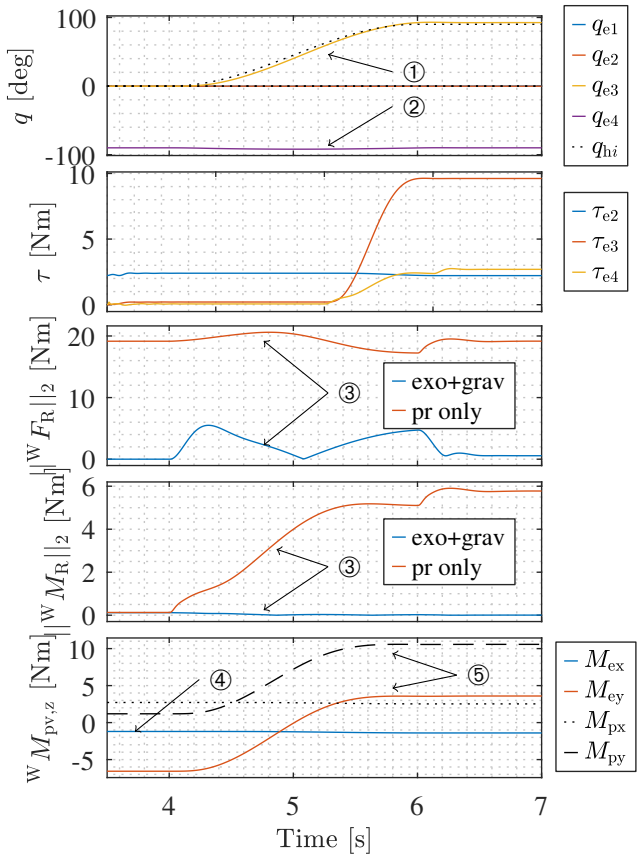

Figure 6.19 Simulation: the residual limb performs a shoulder extension for two cases prosthesis and *exoprosthesis* using the floating-base gravity compensation. The *exoprosthesis* reduces the wrench $\mathcal{F}_{R}$ significantly compared to a conventional prosthesis attachment.

can be adjusted to any value by shifting the counter weight or by adding more weight (1.25 kg – 2.5 kg)[5]. Consequently, almost no moment along the sagittal axis acts on the body. The moment along the transverse axis is ≈ -6 Nm for the exoskeleton. As a comparison, a backpack with 15 kg and a lever arm from the pelvis of 20 cm produces about −40 Nm. Consequently, comparably low moments act on the transverse axis. When the arm is lifted, higher pelvis moments can be observed, which are lower for the exoskeleton than for the prosthesis, see ⑤. Forces acting on the pelvis were omitted as these were constant to the greatest extent. These corresponded to the gravity forces of the entire system (e.g., ${}^{W}F_{pv,z} \approx (14.4\,\text{kg} + 2.5\,\text{kg}) \cdot 9.81\,\text{m/s}^2$).

Experiment

Figure 6.20 compares the *exoprosthesis* and the prosthesis in a payload lifting experiment, referring to the initial problem statement depicted in Fig. 6.2. For both devices, a shoulder extension by ≈ 90 deg is performed to lift a bottle filled with one liter of water. The gravity models within the controller were updated according to the known properties of the load. Before the experiment, Velcro fasteners attached the upper limb of the user with the same level of tension to the two devices. Note that a much higher deflection angle (of 35 °) for the prosthesis than for the exoskeleton (of 15 °) is observed in the attachment, indicating higher stress in the prosthesis attachment location. This observation is also in accordance with the simulation results from Fig. 6.19 in which much higher wrenches for the prosthesis attachment than for the *exoprosthesis* were observed. Related experimental data of the exoskeleton joints are depicted at the bottom of Fig. 6.20. It can be seen that the shoulder exoskeleton supports the human shoulder by ≈ 18 Nm in joint q_3, see ①.

[5]The model of the *exoprosthesis* is based on CAD data. In the CAD software, the counter weight was shifted virtually until the COM of the entire system was aligned with the sagittal plane of the human.

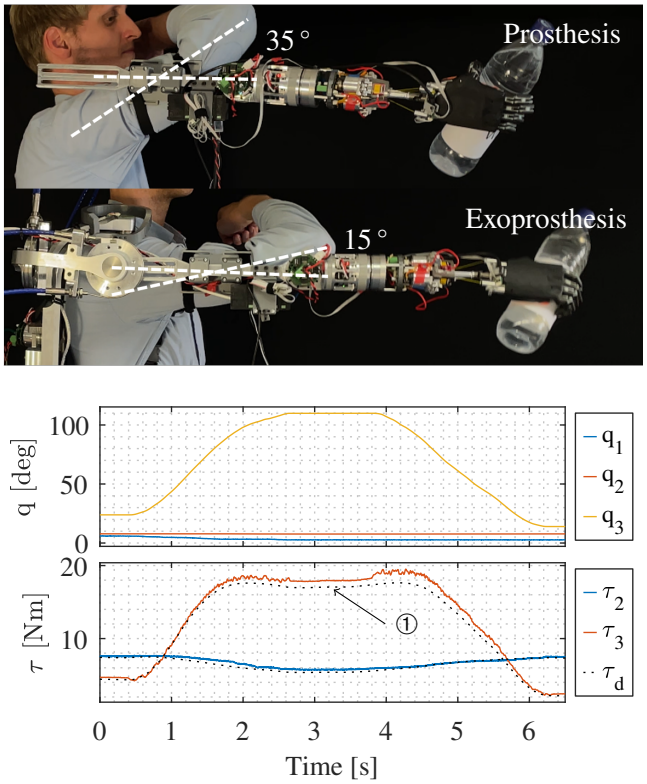

Figure 6.20 A payload (1 l bottle) is lifted by the user comparing prosthesis and exoprosthesis with exoskeleton data.

A final load experiment investigates the difference in reaction wrench at ${}^{\mathrm{W}}\boldsymbol{T}_{\mathrm{R}}$ for the *exoprosthesis* (left) and the prosthesis (right), using a robot (Franka Emika Robot, Franka Emika GmbH, Germany), see Fig. 6.21. The robot was used for following a prerecorded trajectory for both systems, respectively. The robot controller of the manufacturer allows for accurately measuring the end effector wrench $\mathcal{F}_{\mathrm{R}}$ [34]. In this experimental realization of the simulation from Fig. 6.8, the robot is attached to the upper arm of the exoprosthesis by a 3d printed part. The experiment follows the following procedure:

1. Before the experiment, the *exoprosthesis* is attached to the robot, see Fig. 6.21 (left). A trajectory is recorded through kinesthetic teaching, intending to cover a large range of the joint space. With this, it is ensured that the kinematic constraints of the exoskeleton are respected in the recorded trajectory. The prosthesis holds its position via joint impedance control.

2. The recorded robot trajectory is applied to the *exoprosthesis* and the contact wrench $\mathcal{F}_{\mathrm{R}}$ is measured.

3. The connection at the shoulder is detached and the exoskeleton is moved out of the place, see Fig. 6.21 (right). The trajectory is applied to the prosthesis and the contact wrench $\mathcal{F}_{\mathrm{R}}$ is measured again.

Figure 6.21 depicts the recorded data. The first row of Fig. 6.21 shows the robot joints with two experimental repetitions, respectively. The second and third row display the 2-norm of force and moment, respectively. The red line corresponds to the prosthesis (carried by the robot) and the blue line corresponds to the *exoprosthesis* (guided by the robot). The black dotted lines depict the repetition of the same experiment. The data confirms that much lower forces and moments for the *exoprosthesis* are measured than for the conventional prosthesis attachment, see ①. For certain angles, the moment of the prosthesis decrease ② and are almost equal to the *exoprosthesis*. Presumably, the prosthesis is tilted in such a way that the prosthesis COM lies under the robot end effector and the prosthesis acts with a lower moment on the robot end effector.

Finally, the experiment shows that the reaction forces are reduced by 70 % and moments are reduced by 50 % for the chosen dynamic trajectory. For $t = 0\,\mathrm{s}$, it can also be observed that the wrench for the exoskeleton is close to zero, i.e., the exoskeleton completely cancels the interaction wrench $\mathcal{F}_{\mathrm{R}}$ for the static

case. This observation accords with prior simulations and experiments. Overall, the experiment confirmed that the *exoprosthesis* can successfully compensate the contact wrench $\mathcal{F}_{\mathrm{R}}$.

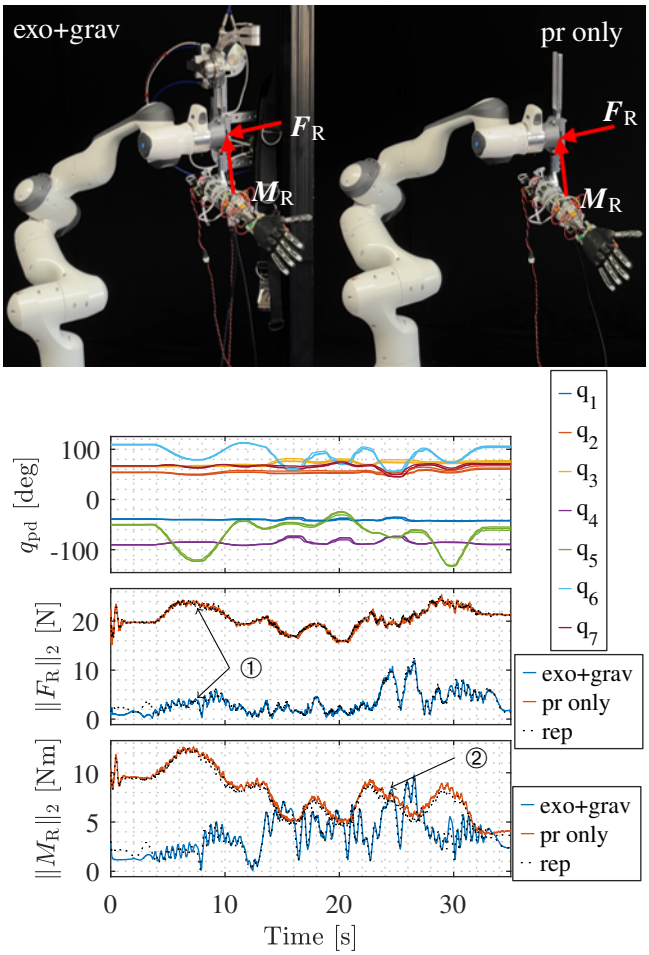

Figure 6.21 Robot follows a prerecorded trajectory with *exoprosthesis* and prosthesis attached.

6.4.4 Other Applications: Teleoperation

A modified version of the exoskeleton from Fig. 6.5 was also used as a bilateral tactile control device for controlling a service robot by teleoperation, see Fig. 6.23.

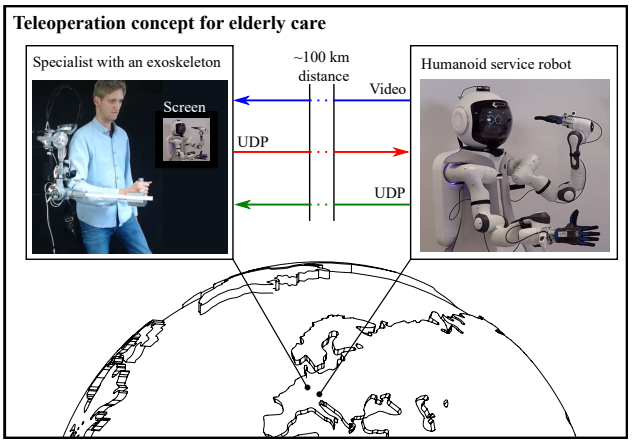

Figure 6.22 Teleoperation of GARMI robot through exoskeleton

The future use-case is a remote control of the service robot GARMI [305] by a medical specialist wearing the exoskeleton, see Fig. 6.22. The specialist controls the joints of the service robot and receives suitable force-feedback. By this, multiple application scenarios such as virtual physiotherapy or medical examination over the Internet become possible.

The *exoprosthesis* from Fig. 6.5 was mechanically and electrically modified. For this, the transhumeral prosthesis is detached and replaced by a specially-designed torque-controlled robotic actuator. A mechanical extension and a handle are attached to enable guidance of the exoskeleton. The exoskeleton is supposed to follow the same motion as the operator arm.

Two simple controllers couple exoskeleton and service robot. The service robot runs the following torque-level controller

$$\boldsymbol{\tau}_{\mathrm{R,d}} = \boldsymbol{K}\left(\boldsymbol{q}_{\mathrm{E}}^{*} - \boldsymbol{q}_{\mathrm{R0}}\right) + \hat{\boldsymbol{g}}(\boldsymbol{q}_{\mathrm{R}}), \tag{6.15}$$

where $\boldsymbol{q}_{\mathrm{E}}^{*} = \boldsymbol{q}_{\mathrm{E}} - \boldsymbol{q}_{\mathrm{E,0}}$ is the joint position of the exoskeleton, shifted along $\boldsymbol{q}_{\mathrm{E,0}}$. $\boldsymbol{\tau}_{\mathrm{R,d}}$ and $\hat{\boldsymbol{g}}(\boldsymbol{q}_{\mathrm{R}})$ are the desired torque and the gravity model of the service robot, and $\boldsymbol{q}_{\mathrm{R0}}$ is its zero position. $\boldsymbol{K}$ is a gain matrix, which is also used for assigning the joints of the two different robots. The exoskeleton runs the controller

$$\hat{\boldsymbol{\tau}}_{\mathrm{E,d}} = \boldsymbol{P}\hat{\boldsymbol{\tau}}_{\mathrm{R,ext}} + \hat{\boldsymbol{g}}(\boldsymbol{q}_{\mathrm{E}}), \tag{6.16}$$

where $\hat{\boldsymbol{\tau}}_{\mathrm{E,d}}$ is the desired torque of the exoskeleton, $\boldsymbol{P}$ is a distribution matrix for joint assignment between the two systems, $\hat{\boldsymbol{g}}(\boldsymbol{q}_{\mathrm{E}})$ is the exoskeleton gravity model, and $\hat{\boldsymbol{\tau}}_{\mathrm{R,ext}}$ is the output of the service robot's momentum observer (sent to the exoskeleton). Both systems are connected via a university-reserved network and communicate over UDP .

Figure 6.23 shows an experiment with a human operator controlling the joints of the robot using the exoskeleton, and showing a stable, accurate and responsive joint position for following the service robot in this teleoperation scenario. Figure 6.24 shows the teleoperation with force-feedback over the internet at $\approx$ 100 km distance. While the first row depicts the joint angle of the robot, the second row depicts the external joint torques measured by the robot and transmitted to the exoskeleton over internet. Finally, the tactile exoskeleton can also be utilized in alternative applications showing the generalizability of the design.

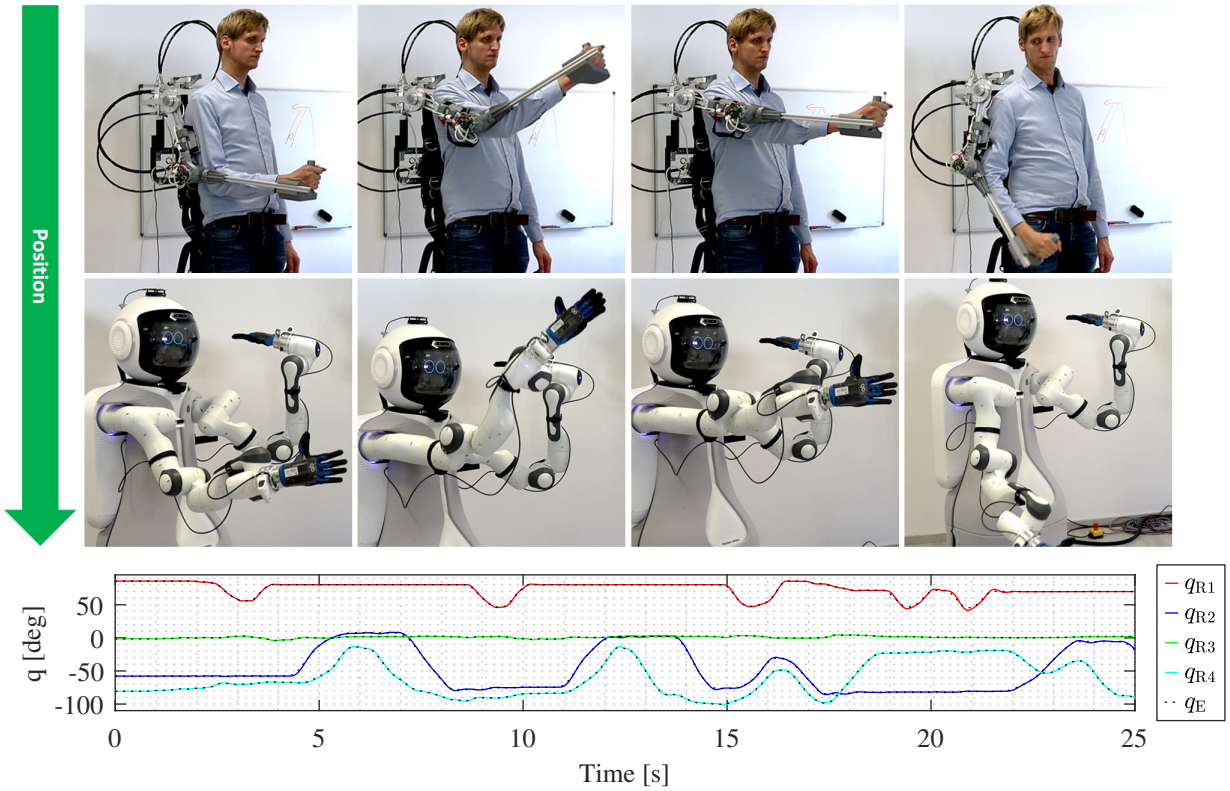

Figure 6.23 Robot angular tracking by exoskeleton via teleportation

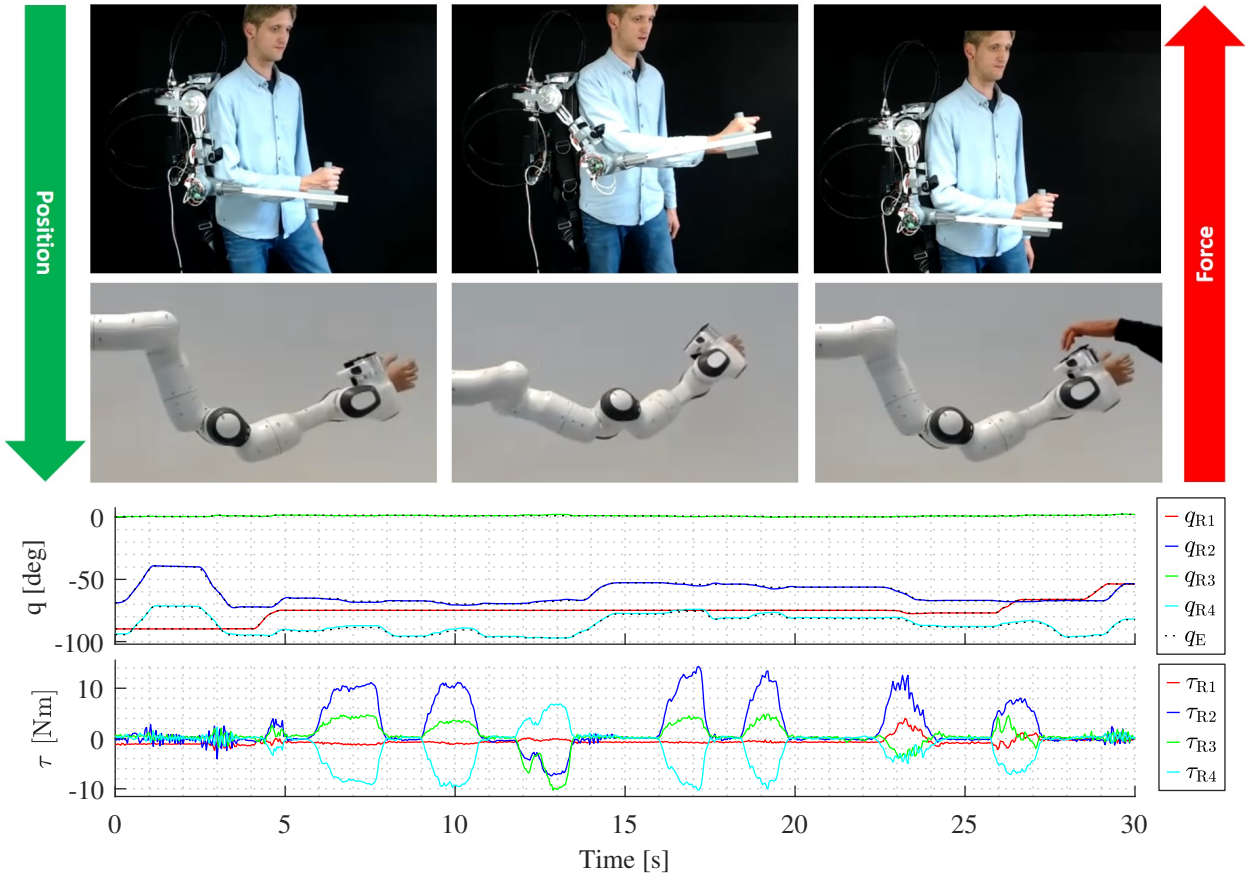

Figure 6.24 Robot force feedback via teleportation between Garmisch-Partenkirchen and Munich over internet

6.5 Summary

This chapter utilized the modeling and control framework from Chapter 3 as a tool for extending the state of the art in attachment methods for upper-limb prosthetics. Commonly, prostheses are attached via passive sockets or Osseo Integration (OI). These methods still suffer from several drawbacks for the prosthesis user, also pointing out a significant safety risk. In this work, a new solution was investigated by using a shoulder exoskeleton for active load compensation as conceptualized in prior works [12]. The exoskeleton carries the prosthesis for the user and offloads the stump via a floating-base gravity compensation. Consequently, the wearing comfort at the residual limb is expected to be more convenient and safer than conventional attachment methods. As the mechatronics of the exoskeleton utilizes tactile control, the residual limb of the prosthesis user can guide the system via direct interaction forces. This seamless and quite natural control method of the device requires no learning of complex abstract human machine interfaces. Overall, the following contributions were made.

1. The first design of a wearable *exoprosthesis* prototype was developed for laboratory-level experiments,
2. A mechatronic solution was proposed for a tactile, single-sided shoulder exoskeleton rebalancing the COM by contralateral actuator placements and Bowden cables,
3. Two prosthesis socket control schemes were introduced for the tactile robotic exoskeleton based on i) joint torque control and ii) a floating-base gravity compensation,
4. A feasibility analysis of the *exoprosthesis* was completed via multi-body simulation, controller tests and human-in-the-loop grasping experiments.

These advances are achieved by the following approach. A RRR gimbal-like shoulder exoskeleton in combination with the slider mechanism a is proposed. A mathematical human-in-the-loop multi-body model of the *exoprosthesis* allows for a simulation-based controller design such that monolithic and modular controllers could be proposed and analyzed. Both the model and the control were derived using the toolbox from Chapter 3. Even though both the monolithic and the modular controller are numerically equal, the modular controller allows for exchanging attached prostheses models without the need for regenerating the entire mathematical model of the system. The *exoprosthesis* prototype is validated by stationary controller experiments of the active socket and grasping human-in-the-loop tests. Finally, a reaction wrench analysis at pelvis and residual limb validates the *exoprosthesis* concept: i) The residual limb allows guiding the prosthesis socket by small interaction forces, ii) the floating-base gravity compensation maintains the *exoprosthesis* position, regardless the human body orientation, iii) the device is successfully used as a tool in grasping experiments, and iv) the wrench at the residual limb is reduced with respect to a conventional prosthesis attachment, while the wrench at the pelvis is comparable, i.e., to a backpack.

With this work, a significant step towards a wearable *exoprosthesis* was completed, and some fundamental research questions could be clarified. Future work should focus on a further miniaturization of the mechanical design, such that the concept becomes useful for real prosthetic users. In future prototypes, the structure should be minimized in terms of size and weight. Once these problems are solved, clinical trials should be performed.

7 Conclusion

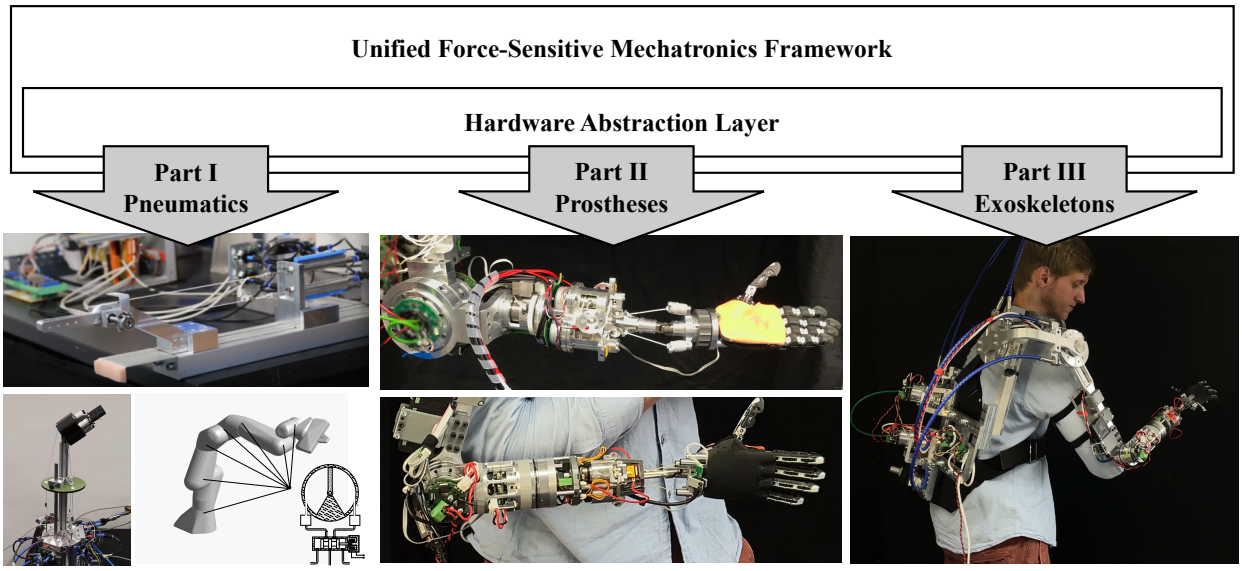

Figure 7.1 Systems developed by the mechatronic design synthesis framework proposed in this thesis

Soft and tactile robots have revolutionized the robotics field over the last 15 years. In this thesis, a complete design framework for soft and tactile robotic systems was introduced, which can be used for developing both stationary and wearable devices. Two limitations of state-of-the-art soft and tactile robotic systems inspired this work, namely that

- the drive-train of electromechanical soft and tactile robots is prone to hard collisions, which may damage the torque sensor or the gear, and
- the structural design of the robot, with actuators flanged at the rotary axes, might not be suitable for wearable robot designs, such as exoskeletons and prostheses.

The hypothesis of this thesis was that these problems can be addressed by altering the mechatronics design, more specifically, the actuation and the transmission elements of the robot. For these reasons, this thesis proposed a simulation-guided and digital-twin-based development framework by which soft- and tactile robotic systems can be designed, controlled and optimized, before the robot is built. Key concepts of this design are i) state-of-the-art robot modeling and controller approaches, ii) *Actuator Abstraction Layer*s and iii) *Transmission Abstraction Layers*, allowing the investigation of various robot types by generally applying the same approach. The framework also includes the subsequent mechanical design of the robot, utilizing the results from the physics simulation to perform kinematics, load and stress simulations for the sake of optimizing the mechatronics design. The kinematic, dynamic and controller simulation, as well as the computer aided design then form the *unified mechatronics design framework*. To the best of the author's knowledge, this is the first work following this approach for the design and control of soft and tactile robots. The expected impact of the framework is a simplified digital-twin-based robot development, which evolves in shorter development times and/or more complex and specialized robotic systems.

The framework was then utilized for making further research progress in other robot domains such as pneumatically-actuated robots, upper-limb prostheses and exoskeletons. By this, the ability of the framework to generalize and to predict robot systems with different actuation and transmission technologies could

be empirically confirmed. The works of this thesis were published in peer-reviewed and highly respected international conferences and journals such as *RA-L*, *ICRA*, *T-RO* and *IJRR*.

Pneumatics Pneumatic actuators were researched in this thesis, as these actuators were considered as an alternative actuation concept to electromechanical actuators for soft and tactile robots. Due to the inherent compliance and backdrivability, they have unique properties in contact response, collision robustness and speed, in contrast to electromechanical actuation. The goal of this work was to perform fundamental research by transferring the technology from soft and tactile robotics (established in electromechanical systems) to pneumatically actuated robots, by developing novel mechatronics and control algorithms. In this context, alternative mechatronic design approaches for torque-controlled pneumatic actuators were also proposed, without using strain-gauge-based sensors.

The pneumatic technology was researched on novel bio-inspired muscle-like and tendon-driven robot joints, and finally on a 7-dof pneumatic robot simulation. The specific contribution of this work was to show that joint torques, joint impedances and contact losses can be successfully controlled by the proposed methods for pneumatically driven robots. Also, disturbant joint torques and disturbant actuator pressure variations (such as leakages) could be successfully observed by suitable observer structures. Consequently, full knowledge and control over the pneumatic actuator could be gained. The 7-dof robot simulation provided the first step of a digital-twin-based development towards a real 7-dof pneumatic robot. Simulations and experiments on the pneumatic actuators revealed the strength in inherent compliance, impact robustness and high speed, but also weaknesses in a low stiffness, thereby limiting possible application scenarios.

While the integration of the technology is still challenging, the 7-dof robot simulation provided a path of how to design a pneumatic robot, with a higher number of dof. The pneumatic technology may be used in highly dynamic industrial environments, where functionality such as catching and throwing is demanded. Also, autonomously learning robots, with contact interaction, could benefit from a pneumatic actuation, as the non-optimal learning parameters do not damage the robot structure. Furthermore, due to their inherent compliance, pneumatic actuators are also a perfect actuator technology for human-robot interaction. In addition, the experiments and simulations demonstrated the ability for highly precise proprioceptive disturbance measurements – particularly when considering low friction cylinders.

Prostheses The main goal of the prosthesis research was to provide more human-like features for upper-limb prostheses. For this ambitious goal, a novel upper limb prosthesis design and synthesis approach was established. Specifically, i) a novel *development approach* for upper-limb prostheses, ii) additional human-like and human-inspired *prostheses features*, iii) the systematic transfer of soft and tactile robotic methods to upper-limb prosthetics[1] and iv) the specific *mechatronic solution* for the Artificial Neuromuscular Prosthesis (ANP) were achieved.

- *Development approach*: A human-inspired mechatronics concept was then derived, which included sensors, actuators and controllers in correspondence to the human body, realized by the state-of-the-art technology from soft and tactile robotics. A simulation-guided, digital-twin-based development was performed, which utilized the framework of this thesis. These methods provided the foundation for developing a complex robotic prototype from scratch, with a minimum number of prototypes. This kind of development approach has never before been shown for upper-limb prostheses to the best of the author's knowledge.
- *Prostheses features*: The human-inspired prostheses features are derived from the aforementioned human-inspired *development approach*. In particular, the developed prosthesis could imitate the

[1] Though, there is one prosthesis [149] claiming the use of torque and impedance control. However, neither a mathematical formulation of the controller nor an experimental analysis could be found.

human neuromuscular system in terms of body awareness, ii) contact awareness, iii) human-like contact response and iv) human-like kinematics. This thesis is the first work aimed at applying key features of the human neuromuscular system to an artificial prosthetic device.

- *Mechatronic solution*: The foregoing features required a specialized mechatronic solution to be developed. The resulting device, the ANP, is characterized by i) a 4-dof human-like elbow-to-wrist kinematics, ii) torque-controlled robot joints and iii) an inertial measurement unit (IMU) for real-time orientation measurements. Custom-made robotic joints, wrist modules and torque sensors were developed to match the special requirements of the device. The ANP is equipped with the human-inspired Artificial Neuromuscular Controller, which consists of a joint impedance controller, a real-time-capable floating-base rigid-body model and a floating-base momentum observer. All of these features were provided at a small size and a weight of 1.7 kg.

  Consequently, the features of the ANP, especially at this size and weight, are unique in prosthetic research.

The feasibility of the ANP concept was validated in simulation, experiments and human-in-the-loop test. The ANP will be further utilized in the subsequent project A.ID, focusing on a clinical investigation of the prosthetic device and the development of novel human machine interfaces.

Exoskeletons The exoskeleton of this thesis was researched as an alternative attachment method for upper-limb prostheses. While passive attachment devices are commonly utilized for connecting a prosthesis to the human body, these come along with several disadvantages, as discussed in this thesis. For these reasons, a third option was proposed by using a robotic active socket. In this thesis, the active socket was realized by a wearable tactile shoulder exoskeleton, which carries the prosthesis for the user. The combination of the prosthesis and the exoskeleton is commonly known as an *exoprosthesis*, as investigated in prior works. However, the feasibility of the concept has remained an open question. In particular, a wearable prototype has not been realized to date. These open questions were investigated by the development of the first wearable *exoprosthesis* prototype and concluded by subsequent feasibility analysis.

The first generation prototype of the *exoprosthesis* was designed to

- minimize the potentially harmful wrench between prosthesis and residual limb,
- guide the prosthesis socket intuitively via small interaction forces (simply by moving the residual limb),
- simplify the lifting of prosthesis and external loads, and
- provide a reasonable wearing comfort for lab experiments, measured by the wrench at the pelvis.

The mechatronics and control of the *exoprosthesis* were based on the concept from soft and tactile robots of providing tactility and body awareness to the device. Due to the single-sided application to the human body, a special design solution was developed to shift the center of mass close to the sagittal plane of the human body.

The thesis focused on the validation of these control concepts and on the feasibility test of the *exoprosthesis* concept in both simulation and experiment.

The author believes that the novel concept of an active socket is a helpful device for near-future upper limb prostheses, constituting a first step in terms of the control concept and mechatronics prototype of this paradigm shift. Although the wearable device is still too heavy for pilot experiments, or a use outside the lab, fundamental research questions around the feasibility of the concept were resolved in this thesis.

Future Work Future work on the unified mechatronics framework should include additional structures and controllers to simulate a larger choice of test scenarios. While the framework up to now consists of modular components, which are manually combined by the developer, future work should also focus on an automated or semi-automated robot design pipeline.

Future work on pneumatic actuators should focus on developing a full 7-dof pneumatic tactile robotic system, actuated either by rotary cylinders or tendon-actuated linear cylinders. The proposed application scenarios of pneumatic robots, such as catching, throwing, autonomous learning and highly tactile torque sensing should be further investigated.

Future work on prostheses should focus on advancing concepts and mechatronics of the ANP. The overall concept of an Artificial Neuromuscular System should be maintained and extended by further human-inspired features. In general, the human archetype served as a perfect guideline for a meaningful prosthetic development. It is expected that further human-inspired and theory-based mechatronic features will significantly advance prosthesis technology. The mechatronics development of the prosthesis should focus on a further integration, especially, of the battery and the central computation unit (CPU). This may be achieved by exploiting more synergies in the electronic design and by using less powerful joints for the elbow and forearm.

Future work on the *exoprosthesis* should focus on i) minimizing the mechatronics of the device, and ii) introducing novel control methods. While the current device was designed for lifting approximately 3 kg, the demands could be lowered such that smaller mechatronic components can be chosen. Also, the shoulder kinematics and transmission elements (Bowden Cables) could be reconsidered to obtain a smaller device. For the shoulder kinematics, alternative mechanisms could be evaluated to cover a larger range of human shoulder motions. The performance of the transmission elements regarding friction and force/torque measurements should be improved. A possible approach would be a complex spool or pulley kinematics, compensating the exoskeleton kinematics, in order to also improve the friction of the design. If this is achieved, the torque signal should also be improved, without requiring additional torque sensors in the joints. Joint torque sensors are not recommended for a single-sided, wearable design. In particular, these would require additional space and weight, and could complicate COM-related problems. In addition, the material for the exoskeleton structure should be reconsidered, e.g., by choosing carbon-fiber-based solutions. However, such an approach should be accompanied by suitable FEA tools. Also, all contact points between the human and the device should be equipped with 6-dof-force-torque sensors to allow for an improved contact estimation. A fully 3-dof actuated shoulder would finally enhance the ability for further model-based control approaches.

In summary, this thesis sets forth a significant step for the structured design of soft and tactile robots based on the most relevant transmission, actuation and control technologies. This is done by introducing a unified design and synthesis framework for a digital twin-based robot design, development and verification. The approach was validated by the successful development of pneumatic robots, upper-limb prostheses and exoskeletons of varying complexity both in simulations and experiments.

A Appendix

A.1 Pneumatics

A.1.1 Passivity Analysis of the 1-dof System

Preliminary Controller

For the stability analysis of the controller, a passivity-based approach is used, which is defined as follows:

Theorem (Passivity)
Considering the state space model of a standard nonlinear system $\dot{x} = f_{ss}(x, u)$ with output $y = h_{ss}(x, u) \in \mathbb{R}^p$ and $x(0) = x_0 \in \mathbb{R}$, passivity holds if there exists a positive semidefinite function such that:

$$S(x(\kappa)) - S(x_0) \leq \int_0^\kappa \boldsymbol{y}^T(t)\boldsymbol{u}(t)dt \tag{A.1}$$

for all input signals $u : [0, \kappa] \rightarrow \mathbb{R}^p$, initial states $x_0 \in \mathbb{R}^n$ and $\kappa \in \mathbb{R}_+$. Several passive sub-systems can be combined as one single passive system via feedback or parallel interconnections.

In the following it is shown that the passivity of controller (4.8) is not guaranteed. Similar to [76] this problem is solved by inserting a virtual tank to preserve passivity.

Passivity of the proposed unified torque/impedance control (4.8) w.r.t. $[\dot{q}, -\tau_\mathrm{d}']$ can be examined by considering the power ports τ_d' and $\dot{q}$ of the system as

$$\begin{aligned} -\dot{q}\tau_\mathrm{d}' &= -\dot{q}\big(- k_\mathrm{imp}\tilde{q} - d_\mathrm{imp}\dot{q} + \hat{g}(q) + \tau_\mathrm{d,trq}\big) \\ &= \dot{S}_I + d_\mathrm{imp}\dot{q}^2 - \dot{q}\tau_\mathrm{d,trq} \\ &\geq \dot{S}_I - \dot{q}\tau_\mathrm{d,trq}, \end{aligned} \tag{A.2}$$

where

$$\tilde{q} = q - q_\mathrm{d} \tag{A.3}$$

is the displacement from the impedance set-point and

$$S_\mathrm{I} = \frac{1}{2}k_\mathrm{imp}\tilde{q}^2 - V_{\hat{g}}(q) \tag{A.4}$$

is the storage function of the impedance controller. The relation between $V_{\hat{g}}(q)$ and $\hat{g}(q)$ is defined as

$$\hat{g}(q) = \frac{\partial V_{\hat{g}}(q)}{\partial q}. \tag{A.5}$$

From (A.2) it can be seen that passivity is potentially violated since $\dot{q}\tau_\mathrm{d,trq}$ is not necessarily negative.

Passivity New Controller

Now, the passivity of the unified impedance controller including tank is examined. The new overall storage function is $S_\mathrm{u} = S_\mathrm{I} + T_\mathrm{t}$. Hence, considering (4.11) for the case of $T_\mathrm{t} < T_\mathrm{u}$ leads to

$$
\begin{aligned}
\dot{S}_{\mathrm{u}} &= \dot{q} k_{\mathrm{imp}} \tilde{q} - \dot{V}_{\hat{g}}(q) + \dot{x}_{\mathrm{t}} x_{\mathrm{t}} \\
&= \dot{q} k_{\mathrm{imp}} \tilde{q} - \dot{V}_{\hat{g}}(q) + \left(\frac{1}{x_{\mathrm{t}}} \left(d_{\mathrm{imp}} \dot{q}^2 - \gamma \dot{q} \tau_{\mathrm{d,trq}} \right) - \omega y_{\mathrm{c}} \right) x_{\mathrm{t}} \\
&= \dot{q} k_{\mathrm{imp}} \tilde{q} - \dot{V}_{\hat{g}}(q) + d_{\mathrm{imp}} \dot{q}^2 - \gamma \dot{q} \tau_{\mathrm{d,trq}} - \omega \dot{q} x_{\mathrm{t}} \\
&= \dot{q} \left[k_{\mathrm{imp}} \tilde{q} - \hat{g}(q) + d_{\mathrm{imp}} \dot{q} - \gamma \tau_{\mathrm{d,trq}} - \alpha(1-\gamma) \tau_{\mathrm{d,trq}} \right] \qquad \text{(A.6)} \\
&\leq -\dot{q} \tau_{\mathrm{d}}, \qquad \text{(A.7)}
\end{aligned}
$$

are obtained, which not only guarantee the passivity of the unified impedance torque controller w.r.t. $[\dot{q}, -\tau_{\mathrm{d}}]$, but also makes it a lossless system.

It should be mentioned that for $\beta = 0$ the passivity condition still holds, although the system would not be lossless anymore. In case of $\alpha = 0$ there are two situations. If $\gamma = 1$, the system would be passive and lossless, with $\gamma = 0$, the torque controller would be deactivated to guarantee the passivity. Hence, in order to avoid this unwanted situation and keeping α to be always 1, the tank should have sufficient initial energy [76].

In [306] a force controlled pneumatic actuator with linear feedback is shown to be passive. For a sliding mode controlled pneumatic actuator, as used in this paper, the passivity analysis and possibly necessary modifications are left for future work. Assuming a passive force controlled pneumatic actuator the overall system is passive, see Fig. A.1.

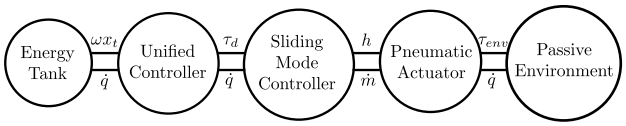

Figure A.1 Port-based representation of the antagonistic pneumatically actuated system

A.1.2 Franka Emika Robot

Rotary Pneumatic Actuator

The pressure dynamics and valve model are described by (4.20), (3.49), (3.49) and (3.50). The only difference in modeling between the linear pneumatic cylinders exists for the volume and the torque, see Fig. 4.5

Volume The volume of the rotary actuator is calculated by the volume integral

$$
V = \int \int \int_V dV \mathrel{\widehat{=}} \int_0^b \int_0^{q^*} \int_{r_{\mathrm{ri}}}^{r_{\mathrm{ro}}} r \mathrm{d}r \mathrm{d}\varphi \mathrm{d}z \qquad \text{(A.8)}
$$

$$
V = q^* \frac{b}{2} \left(r_{\mathrm{ro}}^2 - r_{\mathrm{ri}}^2 \right) \qquad \text{(A.9)}
$$

with b being the width of the actuator, r_{ro} the outer Radius, r_{ri} the inner radius. q^* consists of $q^* = q - q_0$ where q is the describing coordinate and q_0 is constant angle, which maps between robot and actuator coordinates. The final volume becomes

$$
V = V_{0i\mathrm{r}} \pm A_{\mathrm{eq}}(q - q_0) \qquad \text{(A.10)}
$$

with

$$
A_{\mathrm{eq}} = \frac{b}{2} \left(r_{\mathrm{ro}}^2 - r_{\mathrm{ri}}^2 \right), \qquad \text{(A.11)}
$$

which is required for (4.20). Additionally, for $q = 0$ a volume V_{0ir} is present, see (A.10).

Torque The output torque of the actuator can be found by integration. When considering the differential output

$$\mathrm{d}\tau = F\mathrm{d}s. \tag{A.12}$$

Due to the pressure difference ΔP between chamber 1 and 2, this can be further expressed as

$$\mathrm{d}\tau = \Delta PA\mathrm{d}s = \Delta Pbs\mathrm{d}s \tag{A.13}$$

with $F = \Delta PA$ and $A = bs$. Integration leads to

$$\tau = \Delta Pb \int_{r_{\mathrm{ri}}}^{r_{\mathrm{ro}}} s\mathrm{d}s = \Delta Pb \left[\frac{s^2}{2}\right]_{r_{\mathrm{ri}}}^{r_{\mathrm{ro}}} \tag{A.14}$$

$$= (P_2 - P_1)\frac{b}{2}({r_{\mathrm{ro}}}^2 - {r_{\mathrm{ri}}}^2). \tag{A.15}$$

Finally, with (A.11) it follows that

$$\tau_{\mathrm{a}} = A_{\mathrm{eq}}\left(P_2 - P_1\right). \tag{A.16}$$

Collision Modeling

In the simulation, a collision between the robot and i) moving and ii) residing object is investigated, respectively. First, a collision with a sphere and then with a table top is discussed.

Two Spheres The developed model is designed to simulate a collision between the robot and a ball, which is thrown against or falls on top of the robot. This behavior is modeled by two spheres as follows:

- Sphere 0 is attached to the robot end effector, expressed via ${}^{\mathrm{W}}\boldsymbol{r}_{\mathrm{s0}} = {}^{\mathrm{W}}\boldsymbol{r}_{\mathrm{E}}$, with ${}^{\mathrm{W}}\boldsymbol{r}_{\mathrm{s0}}$ being the position and $\boldsymbol{r}_{\mathrm{E}}$ the position of the robot end effector.
- Sphere 1 can move in space freely and is described by the vector ${}^{\mathrm{W}}\boldsymbol{r}_{\mathrm{s1}}$, which represents the position of sphere 1 in space.

Sphere 0 and Sphere 1 have a radius of r_{s} and R_{s}. A collision between the two sphere is described by position depending contact forces. The distance between the spheres is

$${}^{\mathrm{W}}\Delta r_{\mathrm{s}} = \left\| {}^{\mathrm{W}}\boldsymbol{r}_{\mathrm{s1}} - {}^{\mathrm{W}}\boldsymbol{r}_{\mathrm{s0}} \right\|_2 \tag{A.17}$$

and the orientation of the collision force

$$\boldsymbol{e} = \frac{\Delta r_{\mathrm{s}}}{\left\| \boldsymbol{t}_{\mathrm{r1}} - \boldsymbol{t}_{\mathrm{s0}} \right\|_2}. \tag{A.18}$$

A case distinction

$$\alpha = \begin{cases} 1 & \text{if } \Delta r_{\mathrm{s}} \leq r_{\mathrm{s}} + R_{\mathrm{s}} \\ 0 & \text{else} \end{cases} \tag{A.19}$$

checks if a collision occurs. The scalar collision force is obtained based on a spring-damper model

$$F(\alpha, \beta) = \alpha K \Delta r_{\mathrm{s}} + \alpha\beta D \Delta \dot{r}_{\mathrm{s}} \tag{A.20}$$

with spring and damper constant K and D, taking into account the penetration depth Δr_s. Additionally, a damping term is active when a penetration occurs and the spheres are approaching. This is tested by

$$\beta = \begin{cases} 1 & \text{if } \Delta \dot{r}_\mathrm{s} \leq 1 \\ 0 & \text{else} \end{cases}. \tag{A.21}$$

Based on (A.18) and (A.20), the contact force ${}^\mathrm{W}\boldsymbol{F}_\mathrm{c}$, acting between robot and spheres is

$${}^\mathrm{W}\boldsymbol{F}_\mathrm{c} = F(\alpha, \beta)\,{}^\mathrm{W}\boldsymbol{e}. \tag{A.22}$$

Based on the Jacobian of the contact point $\boldsymbol{J}_{B0}^T(\boldsymbol{q})$, the effect on the robot joints is calculated by

$$\boldsymbol{\tau}_\mathrm{ext} = \boldsymbol{J}_{B0}^T(\boldsymbol{q})\,{}^\mathrm{W}\boldsymbol{F}_\mathrm{c}. \tag{A.23}$$

The dynamics of Sphere 1 is modeled by the differential equation

$${}^\mathrm{W}\ddot{\boldsymbol{r}}_\mathrm{s1} m_\mathrm{s1} = -m_\mathrm{s1}\,{}^\mathrm{W}\boldsymbol{g} - {}^\mathrm{W}\boldsymbol{F}_\mathrm{ext}, \tag{A.24}$$

$$\tag{A.25}$$

with m_s1 being the sphere mass and ${}^\mathrm{W}\boldsymbol{g}$ the gravitational acceleration. The models neglect friction in contact, rotational spin and the mass of Sphere 0.

Table Collision The collision model between table and robot end effector consists of components, namely the collision in z-direction and the adhesive friction. First, the distances in z-direction is evaluated by

$$\Delta r_T = \| {}^\mathrm{W} r_\mathrm{Ez} - t_\mathrm{box,z} \|_2, \tag{A.26}$$

where $t_\mathrm{box,z}$ is the height of the collision surface, represented as a box. The equivalent case distinctions

$$\alpha_T = \begin{cases} 1 & \text{if } \Delta \boldsymbol{r}_T \\ 0 & \text{else} \end{cases}, \quad \beta_T = \begin{cases} 1 & \text{if } \Delta \dot{r}_\mathrm{T} \leq 1 \\ 0 & \text{else} \end{cases}. \tag{A.27}$$

lead to

$$F_\mathrm{Tz} = \alpha_T K \Delta r_\mathrm{T} + \alpha_T \beta_T D \Delta \dot{r}_\mathrm{T}. \tag{A.28}$$

Second, adhesive friction is modeled by another spring with constant K_x and K_y for x- and y-direction. Once α_T has switched to 1, K_x and K_y are permanently switched on an the vector ${}^\mathrm{W}\boldsymbol{r}_\mathrm{Ex}^*$ of the first penetration is stored. This model does not take into account contact loss but is assumed to be sufficient.

$$\boldsymbol{F}_\mathrm{ext} = \begin{pmatrix} K_\mathrm{x} \left({}^\mathrm{W} r_\mathrm{Ex} - {}^\mathrm{W} r_\mathrm{Ex}^* \right) \\ K_\mathrm{y} \left({}^\mathrm{W} r_\mathrm{Ey} - {}^\mathrm{W} r_\mathrm{Ey}^* \right) \\ F_\mathrm{Tz} \end{pmatrix} \tag{A.29}$$

A.2 Prosthesis

A.2.1 Design Process

The mechatronic design follows the flow chart of Fig. A.2, which focuses on choosing motor and strain wave gearbox to realize a high torque-to-weight-ratio prosthesis actuator unit[1] with the help of simulation data of joint-side actuator angles, speeds and torques q_a, $\dot{q}_\mathrm{a}$, τ_a. The process starts with the choice of the smallest possible gear variant[2] in terms of outer dimensions. For this, the largest possible gear ratio i_g is

[1] A similar process was elaborated for the sensor choices but are in principle redundant to the gearbox and actuator choice.

[2] The logic behind the choice of the next component is hidden for a simpler description.

chosen as this is a common design choice to achieve a high torque-to-weight-ratio. For the selected gear, the maximum torque $\tau_{g,max}$ of the gear is determined and compared to the maximum torque of all simulations $\max(\tau_a(t))$. If this test is successful, the smallest possible BLDC motor is chosen. It is then checked, whether the motor, with the given gear combination i_g, can fulfill the maximum demanded torque from simulation $\max(\tau_a(t))\, S_1$, where $S_1 \approx 1.3$ is a chosen safety factor. Furthermore, it is checked whether the maximum speed of motor and gear $n_{m,max}$, $n_{g,max}$ are exceeded by the maximum simulated motor speed from simulation data $n_{sim,max} = \max\left(\frac{\dot{q}_a i_g 60}{2\pi}\right)$. If one of the conditions is not successful, another component is chosen. If all variants are checked, however, no feasible combination can be found, the process is aborted and the requirements are reevaluated. In such a case, the demanded external loads need to be maintained but the maximum demanded speed is reduced up to lower boundary $\dot{q}_{min}$. If then no feasible solution was found, the external loads are reduced. For a successful component choice, a structural design is elaborated and the feasibility of the design is checked (i.e., assembly, stress analysis by FEA, etc.). If this is finally successful, the device is assembled. The aforementioned process can be applied to any electromechanical geared actuator of the prosthesis, regardless the respective kinematics, as it is applied on actuator-level.

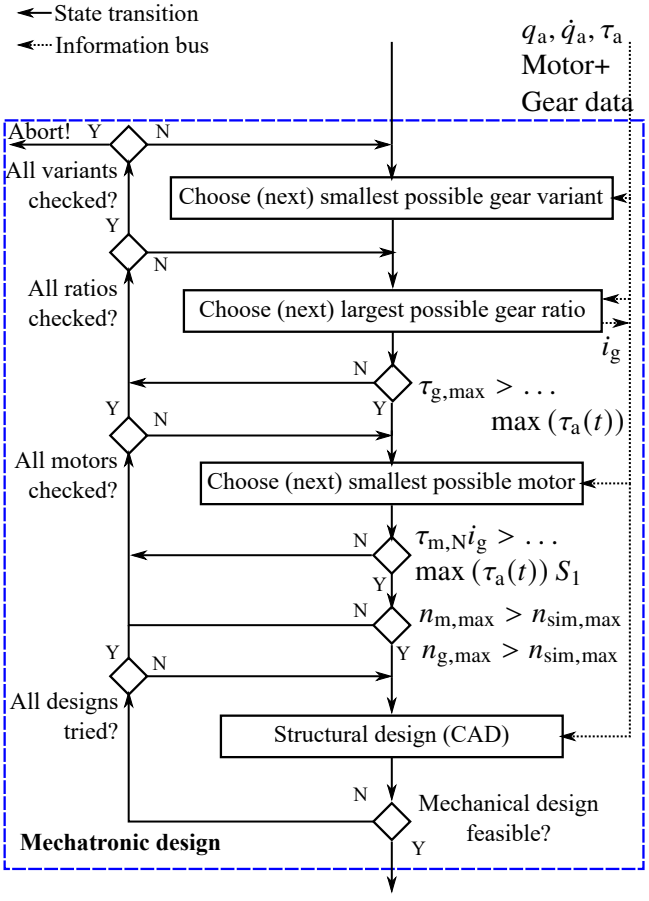

Figure A.2 Mechatronic design of subsystem from Fig. 5.5

A.3 Exoskeleton

A.3.1 Interconnection Wrenches

Wrench $\mathcal{F}_{\mathrm{hw}}$

The wrench $\mathcal{F}_{\mathrm{hw}}$ keeps the base of the human torso at a desired pose, see Fig. 6.8. Its translational part is

$$\boldsymbol{F}_{\mathrm{hw}} = \boldsymbol{K}_{\mathrm{x}} \left({}^{\mathrm{W}}\boldsymbol{t}_{\mathrm{bh,d}} - {}^{\mathrm{W}}\boldsymbol{t}_{\mathrm{bh}} \right) + \boldsymbol{D}_{\mathrm{x}} \left({}^{\mathrm{W}}\dot{\boldsymbol{t}}_{\mathrm{bh,d}} - {}^{\mathrm{W}}\dot{\boldsymbol{t}}_{\mathrm{bh}} \right), \tag{A.30}$$

with ${}^{\mathrm{W}}\boldsymbol{t}_{\mathrm{bh,d}}$ being a desired base translation of the system and $\boldsymbol{K}_{\mathrm{x}}$ and $\boldsymbol{D}_{\mathrm{x}}$ being diagonal stiffness and damping matrices, respectively.

The torsional behavior is modeled by an adapted Euler-angles orientation spring [250]. This requires an actual and a desired orientation of the human base ${}^{\mathrm{W}}\boldsymbol{A}_{\mathrm{bh}}$ and ${}^{\mathrm{W}}\boldsymbol{A}_{\mathrm{bh,d}}$ in order to calculate the mutual orientation matrix

$${}^{\mathrm{bh}}\boldsymbol{A}_{\mathrm{bh,d}} = \left({}^{\mathrm{W}}\boldsymbol{A}_{\mathrm{bh}} \right)^{T} {}^{\mathrm{W}}\boldsymbol{A}_{\mathrm{bh,d}}. \tag{A.31}$$

Adapted Euler angles

$$\boldsymbol{\varphi}_{\mathrm{x1}} = \boldsymbol{\alpha}_{\mathrm{RPY}}({}^{\mathrm{bh}}\boldsymbol{A}_{\mathrm{bh,d}}) \tag{A.32}$$

may be interpreted as suitable control error. The stiffness matrix $\boldsymbol{K}_{\mathrm{pr}}$ multiplied with $\boldsymbol{\varphi}_{\mathrm{x1}}$ provides a moment in a twisted Frame, which is transformed to the local frame $(\mathrm{CS})_{\mathrm{bh}}$ using $\boldsymbol{J}_{\omega}$ from (3.11) as transformation matrix. The result is then transformed to world coordinates $(\mathrm{CS})_{\mathrm{W}}$ using ${}^{\mathrm{W}}\boldsymbol{A}_{\mathrm{bh}}$. The final spring-damper system becomes

$$\boldsymbol{M}_{\mathrm{hw}} = \underbrace{{}^{\mathrm{W}}\boldsymbol{A}_{\mathrm{bh}} \boldsymbol{\Omega}_{\mathrm{RPY}}^{T} \left(\boldsymbol{\varphi}_{\mathrm{x1}} \right) \boldsymbol{K}_{\mathrm{pr}}}_{=: \boldsymbol{K}_{\varphi}\left({}^{\mathrm{W}}\boldsymbol{A}_{\mathrm{bh,d}}, {}^{\mathrm{W}}\boldsymbol{A}_{\mathrm{bh}} \right)} \boldsymbol{\varphi}_{\mathrm{x1}} + \boldsymbol{D}_{\varphi} \left({}^{\mathrm{W}}\boldsymbol{\omega}_{\mathrm{bh,d}} - {}^{\mathrm{W}}\boldsymbol{\omega}_{\mathrm{bh}} \right), \tag{A.33}$$

with $\boldsymbol{D}_{\varphi}$ being a diagonal damping matrix. In the following, the spring behavior from (A.33) is denoted $\boldsymbol{K}_{\varphi}\left({}^{\mathrm{W}}\boldsymbol{A}_{\mathrm{bh,d}}, {}^{\mathrm{W}}\boldsymbol{A}_{\mathrm{bh}} \right)$.

Wrench $\mathcal{F}_{\mathrm{eh}}$

The wrench $\mathcal{F}_{\mathrm{eh}}$ models the attachment of the *exoprosthesis* to the human model as the human wears the system as a backpack, see Fig. 6.8. Translational and rotational spring-damper systems are

$$\boldsymbol{F}_{\mathrm{eh}} = \boldsymbol{K}_{\mathrm{x}} \left({}^{\mathrm{W}}\boldsymbol{t}_{\mathrm{bh}} - {}^{\mathrm{W}}\boldsymbol{t}_{\mathrm{be}} \right) + \boldsymbol{D}_{\mathrm{x}} \left({}^{\mathrm{W}}\dot{\boldsymbol{t}}_{\mathrm{bh}} - {}^{\mathrm{W}}\dot{\boldsymbol{t}}_{\mathrm{be}} \right), \tag{A.34}$$

$$\boldsymbol{M}_{\mathrm{eh}} = \boldsymbol{K}_{\varphi} \left({}^{\mathrm{W}}\boldsymbol{A}_{\mathrm{bh}}, {}^{\mathrm{W}}\boldsymbol{A}_{\mathrm{be}} \right) \boldsymbol{\varphi}_{\mathrm{x2}} + \boldsymbol{D}_{\varphi} \left({}^{\mathrm{W}}\boldsymbol{\omega}_{\mathrm{bh}} - {}^{\mathrm{W}}\boldsymbol{\omega}_{\mathrm{be}} \right). \tag{A.35}$$

The only difference to (A.30) and (A.33) is that desired position and orientation ${}^{\mathrm{W}}\boldsymbol{t}_{\mathrm{bh,d}}$ and ${}^{\mathrm{W}}\boldsymbol{A}_{\mathrm{bh,d}}$, are substituted by the base position and orientation ${}^{\mathrm{W}}\boldsymbol{t}_{\mathrm{be}}$ and ${}^{\mathrm{W}}\boldsymbol{A}_{\mathrm{be}}$ of the opposite body.

Wrench $\mathcal{F}_\mathrm{R}$

The wrench $\mathcal{F}_\mathrm{R}$ models the upper limb attachment of the *exoprosthesis* to the residual limb of the human model at ${}^\mathrm{W}\boldsymbol{T}_\mathrm{Rh}$ and ${}^\mathrm{W}\boldsymbol{T}_\mathrm{Re}$. In contrast to the prior spring-damper systems, only three of the 6-dof are actively controlled (to reduce numerical tension). The translational part is

$$\boldsymbol{F}'_\mathrm{R} = \boldsymbol{K}_\mathrm{x}\boldsymbol{e} + \boldsymbol{D}_\mathrm{x}\dot{\boldsymbol{e}} \tag{A.36}$$

$$\boldsymbol{F}_\mathrm{R} = {}^\mathrm{W}\boldsymbol{A}_\mathrm{Re}\boldsymbol{P}_1{}^\mathrm{Re}\boldsymbol{A}_\mathrm{W}\boldsymbol{F}'_\mathrm{R}, \tag{A.37}$$

where $\boldsymbol{e}$ denotes the translation error as defined below. $\boldsymbol{F}'_\mathrm{R}$ is defined in the coordinates of $(\mathrm{CS})_\mathrm{W}$ and is transformed to $(\mathrm{CS})_\mathrm{Re}$ via the orientation matrix ${}^\mathrm{Re}\boldsymbol{A}_\mathrm{W}$ from (6.4). The multiplication with $\boldsymbol{P}_1 = \mathrm{diag}\begin{bmatrix}0 & 1 & 1\end{bmatrix}$ ensures that no forces along the x-direction of system ${}^\mathrm{W}\boldsymbol{T}_\mathrm{Re}$ are applied. The result is then transformed back to $(\mathrm{CS})_\mathrm{W}$ by ${}^\mathrm{W}\boldsymbol{A}_\mathrm{Re}$. Finally, the control error and its derivative are defined as

$$\boldsymbol{e} = {}^\mathrm{W}\boldsymbol{t}_\mathrm{Rh} - {}^\mathrm{W}\boldsymbol{t}_\mathrm{Re}, \tag{A.38}$$

$$\dot{\boldsymbol{e}} = \boldsymbol{P}_2\left(\boldsymbol{J}_\mathrm{Rh}(\boldsymbol{q}_\mathrm{h})\dot{\boldsymbol{q}}_\mathrm{Rh} - \boldsymbol{J}_\mathrm{Re}(\boldsymbol{q}_\mathrm{e})\dot{\boldsymbol{q}}_\mathrm{Re}\right). \tag{A.39}$$

While ${}^\mathrm{W}\boldsymbol{t}_\mathrm{Rh}$ and ${}^\mathrm{W}\boldsymbol{t}_\mathrm{Re}$ are obtained from (6.3) and (6.4), the derivative $\dot{\boldsymbol{e}}$ is calculated based on (3.7) by utilizing the corresponding Jacobian matrices. $\boldsymbol{P}_2 = \mathrm{diag}\begin{pmatrix}\boldsymbol{I}_{3\times3} & \boldsymbol{0}_{3\times3}\end{pmatrix}$ maps the translational part of the Jacobians.

The structure of the torsional spring-damper system

$$\begin{aligned}\boldsymbol{M}'_\mathrm{R} &= \boldsymbol{K}_\varphi\left({}^\mathrm{W}\boldsymbol{A}_\mathrm{Rh}, {}^\mathrm{W}\boldsymbol{A}_\mathrm{Re}\right)\boldsymbol{\varphi}_{\mathrm{x}3}\ldots + \boldsymbol{D}_\varphi\left({}^\mathrm{W}\boldsymbol{\omega}_\mathrm{Rh} - {}^\mathrm{W}\boldsymbol{\omega}_\mathrm{Re}\right)\\ \boldsymbol{M}_\mathrm{R} &= {}^\mathrm{W}\boldsymbol{A}_\mathrm{Re}\boldsymbol{P}_3{}^\mathrm{Re}\boldsymbol{A}_\mathrm{W}\boldsymbol{M}'_{\mathrm{S}3}\end{aligned} \tag{A.40}$$

is the same as (A.35) but utilizes the orientation matrices ${}^\mathrm{W}\boldsymbol{A}_\mathrm{Rh}$ and ${}^\mathrm{W}\boldsymbol{A}_\mathrm{Re}$ of the human and the exoprosthesis upper arm, respectively. $\boldsymbol{P}_3 = \mathrm{diag}\begin{pmatrix}1 & 0 & 0\end{pmatrix}$ ensures that the local rotation around the x-axis in frame ${}^\mathrm{W}\boldsymbol{T}_\mathrm{Re}$ is controlled. The error of the angular velocity

$${}^\mathrm{W}\boldsymbol{\omega}_\mathrm{Rh} - {}^\mathrm{W}\boldsymbol{\omega}_\mathrm{Re} = \boldsymbol{P}_4\left(\boldsymbol{J}_\mathrm{Re}(\boldsymbol{q}_\mathrm{h})\dot{\boldsymbol{q}}_\mathrm{Rh} - \boldsymbol{J}_\mathrm{Re}(\boldsymbol{q}_\mathrm{e})\dot{\boldsymbol{q}}_\mathrm{Re}\right) \tag{A.41}$$

of frames ${}^\mathrm{W}\boldsymbol{T}_\mathrm{Rh}$ and ${}^\mathrm{W}\boldsymbol{T}_\mathrm{Re}$ is calculated by the same concept of (A.39) but here the sub-matrix $\boldsymbol{P}_4 = \mathrm{diag}\begin{pmatrix}\boldsymbol{0}_{3\times3} & \boldsymbol{I}_{3\times3}\end{pmatrix}$ affects the orientation.

A.3.2 Pelvis Wrench

As the floating-base systems provide base reaction forces ${}^\mathrm{W}\boldsymbol{F}_\mathrm{pv}$ and ${}^\mathrm{W}\boldsymbol{M}_\mathrm{pv}$, the wrench may be calculated at any point. Here, the pelvis wrench is of special interest. Consequently, the reaction forces and moments at the pelvis may be computed by a quasi-static approach as

$$\begin{pmatrix}{}^\mathrm{W}\boldsymbol{F}_\mathrm{pv}\\ {}^\mathrm{W}\boldsymbol{M}_\mathrm{pv}\end{pmatrix} = \begin{pmatrix}{}^\mathrm{W}\boldsymbol{F}_\mathrm{b}\\ -{}^\mathrm{W}\boldsymbol{M}_\mathrm{b} - {}^\mathrm{W}\boldsymbol{r}_\mathrm{bpv}\times{}^\mathrm{W}\boldsymbol{F}_\mathrm{b}\end{pmatrix}, \tag{A.42}$$

where the location of the pelvis can be obtained from

$${}^\mathrm{W}\boldsymbol{T}_\mathrm{pv} = {}^\mathrm{W}\boldsymbol{T}_\mathrm{b}{}^\mathrm{b}\boldsymbol{T}_\mathrm{pv} \tag{A.43}$$

with

$${}^\mathrm{b}\boldsymbol{T}_\mathrm{pv} = \begin{pmatrix}\boldsymbol{I}_{3\times3} & {}^\mathrm{W}\boldsymbol{r}_\mathrm{bpv}\\ \boldsymbol{0} & 1\end{pmatrix}. \tag{A.44}$$

Here, ${}^{\mathrm{W}}\boldsymbol{r}_{\mathrm{bpv}}$ is a constant distance from the floating-base to the pelvis. The wrench may also be expressed in local coordinates (similar to a sensor) by

$$\begin{pmatrix} {}^{\mathrm{pv}}\boldsymbol{F}_{\mathrm{pv}} \\ {}^{\mathrm{pv}}\boldsymbol{M}_{\mathrm{pv}} \end{pmatrix} = \begin{pmatrix} {}^{\mathrm{pv}}\boldsymbol{A}_{\mathrm{W}} & \mathbf{0} \\ \mathbf{0} & {}^{\mathrm{pv}}\boldsymbol{A}_{\mathrm{W}} \end{pmatrix} \begin{pmatrix} {}^{\mathrm{W}}\boldsymbol{F}_{\mathrm{pv}} \\ {}^{\mathrm{W}}\boldsymbol{M}_{\mathrm{pv}} \end{pmatrix}. \tag{A.45}$$

A.4 Images

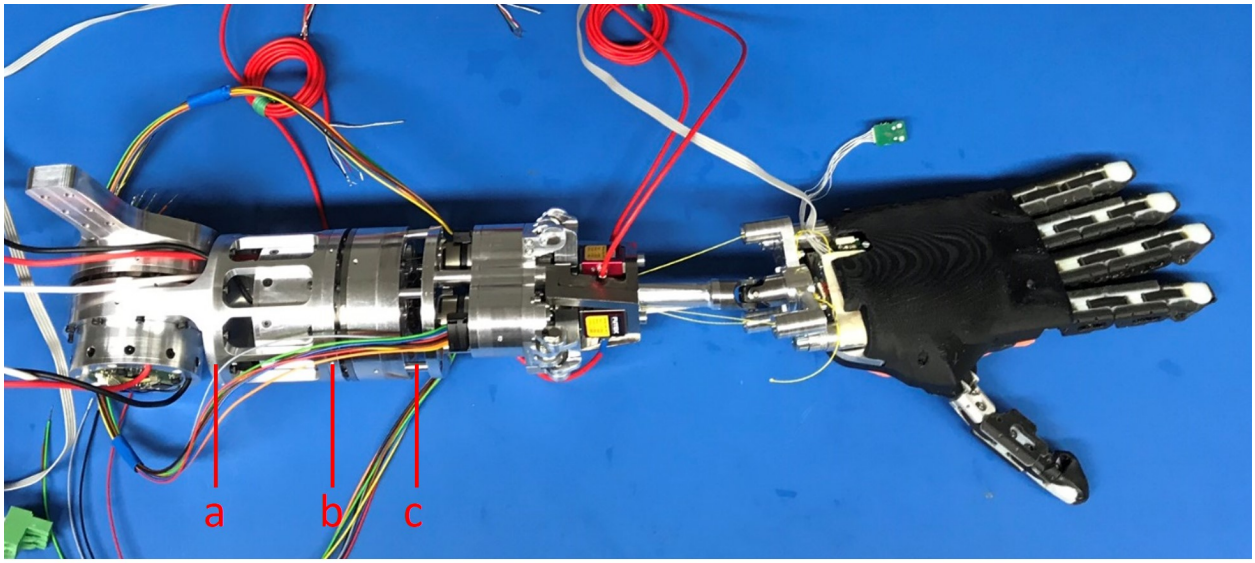

Figure A.3 Shorter version of the Prototype II (ANP) in an early development stage without extension elements at (a), (b), (c), which are required for the current electronics prototype.

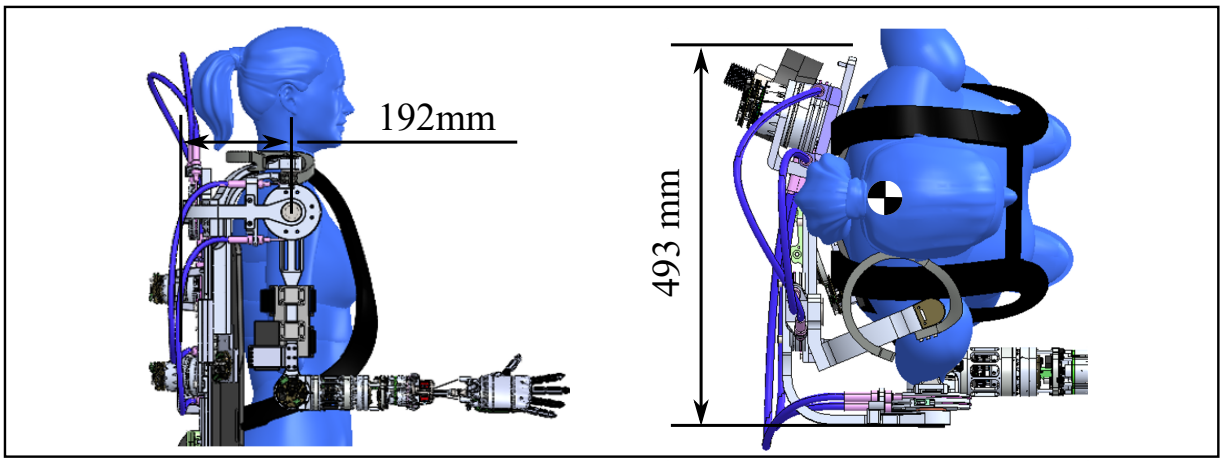

Figure A.4 Top, side view and dimensions of the *exoprosthesis*

A.5 Tables

A.5.1 Kinematics

Table A.1 MDH-Parameters of the 3SPS-1RR wrist for ${}^{\mathrm{b}}\boldsymbol{T}_j$

i	α_i [rad]	a_i [m]	d_i [m]	θ_i [rad]
1	0	h	0	q_j
2	$-\frac{\pi}{2}$	0	0	q_j

Table A.2 MDH-Parameters of prosthesis I and II to derive coordinate frames ${}^{\mathrm{b}}\boldsymbol{T}_j$

i	α_i [rad]	a_i [m]	d_i [m]	θ_i [rad]
1	0	a_1	d_1	$q_1 + \pi$
2	$\frac{\pi}{2}$	a_2	d_2	$q_2 + \frac{\pi}{2}$
3	$\frac{\pi}{2}$	0	0	$q_3 + \frac{\pi}{2}$
4	$-\frac{\pi}{2}$	0	0	q_4

Table A.3 MDH-Parameters for *exoprosthesis* $i = 1..7$, exoskeleton $i = 1..3$, human $i = 1..3$ and prosthesis $i = 4..7$

i	α_i [rad]	a_i [m]	d_i [m]	θ_i [rad]
1	$-\frac{\pi}{2}$	0	0	$q_1 + \frac{\pi}{2}$
2	$-\frac{\pi}{2}$	0	0	$q_2 + \frac{\pi}{2}$
3	$-\frac{\pi}{2}$	0	0	q_3
4	0	3.31e-01	0.0	$q_4 + \pi$
5	$\frac{\pi}{2}$	0.0	2.57e-01	$q_5 + \frac{\pi}{2}$
6	$\frac{\pi}{2}$	0	0	$q_6 + \frac{\pi}{2}$
7	$-\frac{\pi}{2}$	0	0	q_7

Table A.4 Generalized coordinates of the floating-base systems exoskeleton, prosthesis, *exoprosthesis* and human

	Generalized coordinates	Rows of Tab. A.3
Exoskeleton	$\boldsymbol{q}_{\mathrm{cE}} = \left({}^{\mathrm{W}}\boldsymbol{t}_{\mathrm{bE}}^T \quad {}^{\mathrm{W}}\boldsymbol{\varphi}_{\mathrm{bE}}^T \quad \boldsymbol{q}_{\mathrm{E}}^T\right)^T$	1 . . . 3
Prosthesis	$\boldsymbol{q}_{\mathrm{cp}} = \left({}^{\mathrm{W}}\boldsymbol{t}_{\mathrm{bp}}^T \quad {}^{\mathrm{W}}\boldsymbol{\varphi}_{\mathrm{bp}}^T \quad \boldsymbol{q}_{\mathrm{p}}^T\right)^T$	4 . . . 7
Exoprosthesis	$\boldsymbol{q}_{\mathrm{ce}} = \left({}^{\mathrm{W}}\boldsymbol{t}_{\mathrm{be}}^T \quad {}^{\mathrm{W}}\boldsymbol{\varphi}_{\mathrm{be}}^T \quad \boldsymbol{q}_{\mathrm{e}}^T\right)^T$	1 . . . 7
Human	$\boldsymbol{q}_{\mathrm{ch}} = \left({}^{\mathrm{W}}\boldsymbol{t}_{\mathrm{bh}}^T \quad {}^{\mathrm{W}}\boldsymbol{\varphi}_{\mathrm{bh}}^T \quad \boldsymbol{q}_{\mathrm{h}}^T\right)^T$	1 . . . 3

A.5.2 System Properties

Table A.5 Parameters of the pneumatic Franka Emika robot

Name	Variable	Value	Unit
Maximum joint torque	$\tau_{\max}$	79	Nm
Maximum joint angles	$q_{\max}$	±130	deg
Actuator outer radius	r_{ro}	6.4	cm
Actuator inner radius	r_{ri}	0.5	cm
Actuator width	b	6.4	cm
Volume at $q = 0$	V_0	0.236	l
Valve maximum area	$A_{\max}$	5	mm^2
Valve discharge coefficient	c_{f}	0.38	-
Valve bandwidth $q = 0$	f	666	Hz
Supply pressure	P_{sup}	7	bar

Table A.6 Size and weight specifications S of the prototype II (ANP)

		Unit
Total weight (without hand)	1.70	kg
Weight of hand (Softhand Pro 2) [290]	0.34	kg
Weight of forearm/elbow joint	0.5	kg
Weight of wrist module	0.4	kg
Payload	1.25	kg
Length (elbow-to-wrist)	350	mm
Forearm diameter	63	mm
Active dof (elbow to wrist)	4	-

Table A.7 Performance design specifications S of the prototype II (ANP)

i	1	2	3	4	Unit
$q_{\max,i}$	80	120	72	60	deg
$q_{\min,i}$	-100	-120	-72	-60	deg
$\dot{q}_{\max,i}$	360	360	60	60	deg/s
$\tau_{\max,i}$	30	15	3.5	3.5	Nm
$F_{\text{t,max},i}$	170	170	170	-	N

Bibliography

[1] A. Albu-Schäffer, O. Eiberger, M. Grebenstein, S. Haddadin, C. Ott, T. Wimböck, S. Wolf, and G. Hirzinger, "Soft robotics," *IEEE Robotics & Automation Magazine*, vol. 15, no. 3, pp. 20–30, 2008.

[2] J. F. Broenink, Y. Ni, and M. A. Groothuis, "On model-driven design of robot software using co-simulation," in *Proceedings of SIMPAR 2010 workshops international conference on simulation, modeling, and programming for autonomous robots*, pp. 659–668, 2010.

[3] L. Zhou and J. F. Broenik, "Co-simulation design towards cyber-physical robotic applications," 2017.

[4] W. A. Mattingly, D.-j. Chang, R. Paris, N. Smith, J. Blevins, and M. Ouyang, "Robot design using unity for computer games and robotic simulations," in *2012 17th International Conference on Computer Games (CGAMES)*, pp. 56–59, 2012.

[5] J. M. McCarthy, "Mechanism synthesis theory and the design of robots," in *Proceedings 2000 ICRA. Millennium Conference. IEEE International Conference on Robotics and Automation. Symposia Proceedings (Cat. No. 00CH37065)*, vol. 1, pp. 55–60, IEEE, 2000.

[6] G. S. Hornby, H. Lipson, and J. B. Pollack, "Generative representations for the automated design of modular physical robots," *IEEE transactions on Robotics and Automation*, vol. 19, no. 4, pp. 703–719, 2003.

[7] J.-P. Merlet, "Optimal design of robots," in *Robotics: Science and systems*, 2005.

[8] K. Chen, J. Bankston, J. H. Panchal, and D. Schaefer, "A framework for integrated design of mechatronic systems," *Collaborative Design and Planning for Digital Manufacturing*, pp. 37–70, 2009.

[9] A. Kellner, P. Hehenberger, L. Weingartner, and M. Friedl, "Design and use of system models in mechatronic system design," in *2015 IEEE International Symposium on Systems Engineering (ISSE)*, pp. 142–149, 2015.

[10] M. Martins da Silva, "Computer-aided integrated design of mechatronic systems (geïntegreerd computer-ondersteund ontwerp voor mechatronische systemen)," 2009.

[11] A. Qamar, J. Wikander, and C. During, "A mechatronic design infrastructure integrating heterogeneous models," in *2011 IEEE International Conference on Mechatronics*, pp. 212–217, IEEE, 2011.

[12] J. Kühn, J. Ringwald, M. Schappler, L. Johannsmeier, and S. Haddadin, "Towards semi-autonomous and soft-robotics enabled upper-limb exoprosthetics: First concepts and robot-based emulation prototype," in *2019 International Conference on Robotics and Automation (ICRA)*, pp. 9180–9186, 2019.

[13] S. Haddadin, "U.S. Patent No. US20190117416A1," 2016. https://www.google.com/patents/US20190117416A1.

[14] A. Tödtheide, T. Lilge, and S. Haddadin, "Antagonistic impedance control for pneumatically actuated robot joints," *IEEE Robotics and Automation Letters*, vol. 1, pp. 161–168, Jan 2015.

[15] A. Tödtheide, E. Shahriari, and S. Haddadin, "Tank based unified torque/impedance control for a pneumatically actuated antagonistic robot joint," in *2017 IEEE International Conference on Robotics and Automation (ICRA)*, pp. 1255–1262, 2017.

[16] A. Tödtheide and S. Haddadin, "Cpa-wrist: Compliant pneumatic actuation for antagonistic tendon driven wrists," *IEEE Robotics and Automation Letters*, vol. 3, no. 4, pp. 3537–3544, 2018.

[17] A. Tödtheide, J. Kühn, E. P. Fortunić, and S. Haddadin, "An integrated, force-sensitive, impedance controlled, tendon-driven wrist: Design, modeling, and control," in *2020 IEEE-RAS 20th International Conference on Humanoid Robots (Humanoids)*, pp. 25–32, 2021.

[18] A. Tödtheide, E. Pozo Fortonić, J. Kühn, E. Jensen, and S. Haddadin, "A wearable force-sensitive and body-aware exoprosthesis for a transhumeral prosthesis socket," *IEEE Transactions on Robotics*, 2023.

[19] A. Tödtheide, E. Pozo Fortonić, J. Kühn, E. Jensen, and S. Haddadin, "A transhumeral prosthesis with an artificial neuromuscular system: Sim2real-guided design, modeling and control," *The International Journal of Robotics Research*, 2023.

[20] A. Tödtheide, X. Chen, H. Sadeghian, A. Naceri, and S. Haddadin, "A tactile exoskeleton for teleoperation: An application in elderly care robotics," *IEEE International Conference on Robotics and Automation (ICRA) 2023*, 2022.

[21] A. Albu-Schäffer, S. Haddadin, C. Ott, A. Stemmer, T. Wimböck, and G. Hirzinger, "The DLR lightweight robot: design and control concepts for robots in human environments," vol. 34, no. 5, pp. 376–385.

[22] G. Hirzinger, N. Sporer, A. Albu-Schäffer, M. Hahnle, R. Krenn, A. Pascucci, and M. Schedl, "DLR 's torque-controlled light weight robot iii-are we reaching the technological limits now?," in *Proceedings 2002 IEEE International Conference on Robotics and Automation (Cat. No. 02CH37292)*, vol. 2, pp. 1710–1716, IEEE, 2002.

[23] A. Albu-Schäffer, O. Eiberger, M. Fuchs, M. Grebenstein, S. Haddadin, C. Ott, A. Stemmer, T. Wimböck, S. Wolf, C. Borst, and G. Hirzinger, "Anthropomorphic soft robotics – from torque control to variable intrinsic compliance," in *Robotics Research* (C. Pradalier, R. Siegwart, and G. Hirzinger, eds.), (Berlin, Heidelberg), pp. 185–207, Springer Berlin Heidelberg, 2011.

[24] A. Albu-Schäffer, C. Ott, and G. Hirzinger, "A unified passivity-based control framework for position, torque and impedance control of flexible joint robots," *The international journal of robotics research*, vol. 26, no. 1, pp. 23–39, 2007.

[25] A. Bicchi and G. Tonietti, "Fast and" soft-arm" tactics - robot arm design," *IEEE Robotics & Automation Magazine*, vol. 11, no. 2, pp. 22–33, 2004.

[26] S. Haddadin, A. Albu-Schäffer, and G. Hirzinger, "Requirements for safe robots: Measurements, analysis and new insights," *The International Journal of Robotics Research*, vol. 28, no. 11-12, pp. 1507–1527, 2009.

[27] S. Haddadin, *Towards safe robots: approaching Asimov's 1st law*, vol. 90. Springer, 2013.

[28] C. Ott, *Cartesian impedance control of redundant and flexible-joint robots*. Springer, 2008.

[29] Y.-J. Kim, "Design of low inertia manipulator with high stiffness and strength using tension amplifying mechanisms," in *2015 IEEE/RSJ International Conference on Intelligent Robots and Systems (IROS)*, pp. 5850–5856, IEEE, 2015.

[30] A. De Santis, B. Siciliano, A. De Luca, and A. Bicchi, "An atlas of physical human–robot interaction," *Mechanism and Machine Theory*, vol. 43, no. 3, pp. 253–270, 2008.

[31] M. Zinn, O. Khatib, B. Roth, and J. K. Salisbury, "Playing it safe [human-friendly robots]," *IEEE Robotics & Automation Magazine*, vol. 11, no. 2, pp. 12–21, 2004.

[32] C.-h. Wu and R. P. Paul, "Manipulator compliance based on joint torque control," in *1980 19th IEEE Conference on Decision and Control including the Symposium on Adaptive Processes*, pp. 88–94, 1980.

[33] S. Haddadin, A. De Luca, and A. Albu-Schäffer, "Robot collisions: A survey on detection, isolation, and identification," *IEEE Transactions on Robotics*, vol. 33, no. 6, pp. 1292–1312, 2017.

[34] S. Haddadin, S. Parusel, L. Johannsmeier, S. Golz, S. Gabl, F. Walch, M. Sabaghian, C. Jaehne, L. Hausperger, and S. Haddadin, "The franka emika robot: A reference platform for robotics research and education," *IEEE Robotics & Automation Magazine*, pp. 2–20, 2022.

[35] S. Haddadin, T. Laue, U. Frese, S. Wolf, A. Albu-Schäffer, and G. Hirzinger, "Kick it with elasticity: Safety and performance in human–robot soccer," *Robotics and Autonomous Systems*, vol. 57, no. 8, pp. 761–775, 2009. Humanoid Soccer Robots.

[36] M. Zinn, O. Khatib, B. Roth, and J. K. Salisbury, "Towards a human-centered intrinsically safe robotic manipulator," in *IARPIEEE/RAS joint workshop on technical challenges for dependable robots in human environments, Toulouse, France*, Citeseer, 2002.

[37] G. Palli and S. Pirozzi, "An optical torque sensor for robotic applications," *International Journal of Optomechatronics*, vol. 7, no. 4, pp. 263–282, 2013.

[38] G. Hirzinger and A. Albu-Schaeffer, "Light-weight robots," *Scholarpedia*, vol. 3, no. 4, p. 3889, 2008. revision #91430.

[39] S. Haddadin, A. Albu-Schäffer, A. De Luca, and G. Hirzinger, "Collision detection and reaction: A contribution to safe physical human-robot interaction," in *2008 IEEE/RSJ International Conference on Intelligent Robots and Systems*, pp. 3356–3363, 2008.

[40] W. T. Townsend and J. K. Salisbury, "Mechanical design for whole-arm manipulation," in *Robots and Biological Systems: Towards a New Bionics?*, pp. 153–164, Springer, 1993.

[41] T. Lens and O. Von Stryk, "Investigation of safety in human-robot-interaction for a series elastic, tendon-driven robot arm," in *2012 IEEE/RSJ International Conference on Intelligent Robots and Systems*, pp. 4309–4314, IEEE, 2012.

[42] M. Grebenstein, M. Chalon, W. Friedl, S. Haddadin, T. Wimböck, G. Hirzinger, and R. Siegwart, "The hand of the DLR hand arm system: Designed for interaction," *The International Journal of Robotics Research*, vol. 31, no. 13, pp. 1531–1555, 2012.

[43] S. C. Jacobsen, J. E. Wood, D. Knutti, and K. B. Biggers, "The UTAH/MIT dextrous hand: Work in progress," *The International Journal of Robotics Research*, vol. 3, no. 4, pp. 21–50, 1984.

[44] A. D. Deshpande, Z. Xu, M. J. V. Weghe, B. H. Brown, J. Ko, L. Y. Chang, D. D. Wilkinson, S. M. Bidic, and Y. Matsuoka, "Mechanisms of the anatomically correct testbed hand," *IEEE/ASME Transactions on mechatronics*, vol. 18, no. 1, pp. 238–250, 2011.

[45] Y.-J. Kim, Y. Lee, J. Kim, J.-W. Lee, K.-M. Park, K.-S. Roh, and J.-Y. Choi, "Roboray hand: A highly backdrivable robotic hand with sensorless contact force measurements," in *2014 IEEE International Conference on Robotics and Automation (ICRA)*, pp. 6712–6718, IEEE, 2014.

[46] T. Morita, H. Iwata, and S. Sugano, "Development of human symbiotic robot: Wendy," in *Proceedings 1999 IEEE International Conference on Robotics and Automation (Cat. No. 99CH36288C)*, vol. 4, pp. 3183–3188, IEEE, 1999.

[47] S. Haddadin, T. Laue, U. Frese, and G. Hirzinger, "Foul 2050: Thoughts on physical interaction in human-robot soccer," in *2007 IEEE/RSJ International Conference on Intelligent Robots and Systems*, pp. 3243–3250, IEEE, 2007.

[48] S. Haddadin, A. Albu-Schäffer, and G. Hirzinger, "Safety evaluation of physical human-robot interaction via crash-testing.," in *Robotics: Science and systems*, vol. 3, pp. 217–224, Citeseer, 2007.

[49] M. A. Peshkin, "Programmed compliance for error corrective assembly," *IEEE Transactions on Robotics and Automation*, vol. 6, no. 4, pp. 473–482, 1990.

[50] S. Haddadin, A. Albu-Schäffer, O. Eiberger, and G. Hirzinger, "New insights concerning intrinsic joint elasticity for safety," in *2010 IEEE/RSJ International Conference on Intelligent Robots and Systems*, pp. 2181–2187, IEEE, 2010.

[51] M. Grebenstein, *Approaching Human Performance: The Functionality-Driven Awiwi Robot Hand*, vol. 98. 01 2014.

[52] B. Vanderborght, A. Albu-Schaeffer, A. Bicchi, E. Burdet, D. Caldwell, R. Carloni, M. Catalano, O. Eiberger, W. Friedl, G. Ganesh, M. Garabini, M. Grebenstein, G. Grioli, S. Haddadin, H. Hoppner, A. Jafari, M. Laffranchi, D. Lefeber, F. Petit, S. Stramigioli, N. Tsagarakis, M. Van Damme, R. Van Ham, L. Visser, and S. Wolf, "Variable impedance actuators: A review," *Robotics and Autonomous Systems*, vol. 61, no. 12, pp. 1601–1614, 2013.

[53] Y. Yamada, Y. Hirasawa, S. Huang, Y. Umetani, and K. Suita, "Human-robot contact in the safeguarding space," *IEEE/ASME transactions on mechatronics*, vol. 2, no. 4, pp. 230–236, 1997.

[54] B. Vanderborght, B. Verrelst, R. Van Ham, M. Van Damme, D. Lefeber, B. M. Y. Duran, and P. Beyl, "Exploiting natural dynamics to reduce energy consumption by controlling the compliance of soft actuators," *The International Journal of Robotics Research*, vol. 25, no. 4, pp. 343–358, 2006.

[55] R. Van, T. Sugar, B. Vanderborght, K. Hollander, and D. Lefeber, "Compliant actuator designs. review of actuators with passive adjustable compliance/controllable stiffness for robotic applications," *IEEE Robotics Automation Magazine*, vol. 16, no. 3, pp. 81–94, 2009.

[56] N. Paine, S. Oh, and L. Sentis, "Design and control considerations for high-performance series elastic actuators," *IEEE/ASME Transactions on Mechatronics*, vol. 19, no. 3, pp. 1080–1091, 2013.

[57] S. Wolf, G. Grioli, O. Eiberger, W. Friedl, M. Grebenstein, H. Höppner, E. Burdet, D. G. Caldwell, R. Carloni, M. G. Catalano, D. Lefeber, S. Stramigioli, N. Tsagarakis, M. Van Damme, R. Van Ham, B. Vanderborght, L. C. Visser, A. Bicchi, and A. Albu-Schäffer, "Variable stiffness actuators: Review on design and components," *IEEE/ASME Transactions on Mechatronics*, vol. 21, no. 5, pp. 2418–2430, 2016.

[58] S. A. Migliore, E. A. Brown, and S. P. DeWeerth, "Biologically inspired joint stiffness control," in *Proceedings of the 2005 IEEE international conference on robotics and automation*, pp. 4508–4513, IEEE, 2005.

[59] K. Koganezawa, "Mechanical stiffness control for antagonistically driven joints," in *2005 IEEE/RSJ International Conference on Intelligent Robots and Systems*, pp. 1544–1551, IEEE, 2005.

[60] C. English and D. Russell, "Implementation of variable joint stiffness through antagonistic actuation using rolamite springs," *Mechanism and machine theory*, vol. 34, no. 1, pp. 27–40, 1999.

[61] F. Petit, A. Dietrich, and A. Albu-Schäffer, "Generalizing torque control concepts: Using well-established torque control methods on variable stiffness robots," vol. 22, no. 4, pp. 37–51.

[62] D. J. Braun, F. Petit, F. Huber, S. Haddadin, P. van der Smagt, A. Albu-Schäffer, and S. Vijayakumar, "Robots driven by compliant actuators: Optimal control under actuation constraints," *IEEE Transactions on Robotics*, vol. 29, no. 5, pp. 1085–1101, 2013.

[63] J. Nakanishi and S. Vijayakumar, "Exploiting passive dynamics with variable stiffness actuation in robot brachiation," in *Robotics: Science and systems*, vol. 8, p. 305, 2013.

[64] S. Haddadin, K. Krieger, M. Kunze, and A. Albu-Schäffer, "Exploiting potential energy storage for cyclic manipulation: An analysis for elastic dribbling with an anthropomorphic robot," in *2011 IEEE/RSJ International Conference on Intelligent Robots and Systems*, pp. 1789–1796, 2011.

[65] M. Grebenstein, A. Albu-Schäffer, T. Bahls, M. Chalon, O. Eiberger, W. Friedl, R. Gruber, S. Haddadin, U. Hagn, R. Haslinger, H. Höppner, S. Jörg, M. Nickl, A. Nothhelfer, F. Petit, J. Reill, N. Seitz, T. Wimböck, S. Wolf, T. Wüsthoff, and G. Hirzinger, "The DLR hand arm system," in *2011 IEEE International Conference on Robotics and Automation*, pp. 3175–3182, 2011.

[66] F. Petit, A. Dietrich, and A. Albu-Schäffer, "Generalizing torque control concepts: Using well-established torque control methods on variable stiffness robots," *IEEE Robotics & Automation Magazine*, vol. 22, no. 4, pp. 37–51, 2015.

[67] J. Lemburg, J. de Gea Fernández, M. Eich, D. Mronga, P. Kampmann, A. Vogt, A. Aggarwal, Y. Shi, and F. Kirchner, "Aila-design of an autonomous mobile dual-arm robot," in *2011 IEEE International Conference on Robotics and Automation*, pp. 5147–5153, IEEE, 2011.

[68] N. G. Tsagarakis, G. Metta, G. Sandini, D. Vernon, R. Beira, F. Becchi, L. Righetti, J. Santos-Victor, A. J. Ijspeert, M. C. Carrozza, and D. G. Caldwell, "icub: the design and realization of an open humanoid platform for cognitive and neuroscience research," *Advanced Robotics*, vol. 21, no. 10, pp. 1151–1175, 2007.

[69] D. E. Whitney, "Force feedback control of manipulator fine motions," 1977.

[70] J. Craig and M. Raibert, "A systematic method of hybrid position/force control of a manipulator," in *COMPSAC 79. Proceedings. Computer Software and The IEEE Computer Society's Third International Applications Conference, 1979.*, pp. 446–451, 1979.

[71] R. P. Paul, "Compliance and control," in *Proc. of the 1976 Joint Automatic Control Conference*, pp. 694–699, 1976.

[72] J. K. Salisbury, "Active stiffness control of a manipulator in cartesian coordinates," in *1980 19th IEEE conference on decision and control including the symposium on adaptive processes*, pp. 95–100, IEEE, 1980.

[73] N. Hogan, "Impedance control: An approach to manipulation," in *1984 American control conference*, pp. 304–313, IEEE, 1984.

[74] A. Albu-Schäffer, C. Ott, and G. Hirzinger, "A passivity based cartesian impedance controller for flexible joint robots-part ii: Full state feedback, impedance design and experiments," in *IEEE International Conference on Robotics and Automation, 2004. Proceedings. ICRA'04. 2004*, vol. 3, pp. 2666–2672, IEEE, 2004.

[75] L. Zollo, B. Siciliano, A. De Luca, E. Guglielmelli, and P. Dario, "Compliance control for an anthropomorphic robot with elastic joints: Theory and experiments," 2005.

[76] C. Schindlbeck and S. Haddadin, "Unified passivity-based cartesian force/impedance control for rigid and flexible joint robots via task-energy tanks," in *2015 IEEE international conference on robotics and automation (ICRA)*, pp. 440–447, IEEE, 2015.

[77] H. I. Ali, S. Noor, S. Bashi, and M. Marhaban, "A review of pneumatic actuators (modeling and control)," *Australian Journal of Basic and Applied Sciences*, vol. 3, no. 2, pp. 440–454, 2009.

[78] M. A. Salam, "Fundamentals of pneumatics and hydraulics," 2022.

[79] X. Brun, *Commandes linéaires et non linéaires en électropneumatique. Méthodologies et Applications*. PhD thesis, Insa Lyon, 1999.

[80] J. F. Carneiro and F. G. de Almeida, "Reduced-order thermodynamic models for servo-pneumatic actuator chambers," *Proceedings of the Institution of Mechanical Engineers, Part I: Journal of Systems and Control Engineering*, vol. 220, no. 4, pp. 301–314, 2006.

[81] E. Richer and Y. Hurmuzlu, "A high performance pneumatic force actuator system: part ii—nonlinear controller design," *Journal of dynamic systems, measurement, and control*, vol. 122, no. 3, pp. 426–434, 2000.

[82] Y. Tassa, T. Wu, J. Movellan, and E. Todorov, "Modeling and identification of pneumatic actuators," in *2013 IEEE International Conference on Mechatronics and Automation*, pp. 437–443, IEEE, 2013.

[83] E. Kelasidi, G. Andrikopoulos, G. Nikolakopoulos, and S. Manesis, "A survey on pneumatic muscle actuators modeling," in *2011 IEEE International Symposium on Industrial Electronics*, pp. 1263–1269, IEEE, 2011.

[84] N. Tsagarakis and D. G. Caldwell, "Improved modelling and assessment of pneumatic muscle actuators," in *Proceedings 2000 ICRA. Millennium Conference. IEEE International Conference on Robotics and Automation. Symposia Proceedings (Cat. No. 00CH37065)*, vol. 4, pp. 3641–3646, IEEE, 2000.

[85] D. Reynolds, D. Repperger, C. Phillips, and G. Bandry, "Modeling the dynamic characteristics of pneumatic muscle," *Annals of biomedical engineering*, vol. 31, no. 3, pp. 310–317, 2003.

[86] S. Davis and D. G. Caldwell, "Braid effects on contractile range and friction modeling in pneumatic muscle actuators," *The International Journal of Robotics Research*, vol. 25, no. 4, pp. 359–369, 2006.

[87] V. L. Nickel, J. Perry, and A. L. Garrett, "Development of useful function in the severely paralyzed hand," *JBJS*, vol. 45, no. 5, pp. 933–952, 1963.

[88] S. Ning and G. M. Bone, "Development of a nonlinear dynamic model for a servo pneumatic positioning system," in *IEEE International Conference Mechatronics and Automation, 2005*, vol. 1, pp. 43–48, IEEE, 2005.

[89] A. Ilchmann, O. Sawodny, and S. Trenn, "Pneumatic cylinders: modelling and feedback force-control," *International Journal of Control*, vol. 79, no. 06, pp. 650–661, 2006.

[90] D. G. Caldwell, G. A. Medrano-Cerda, and M. Goodwin, "Control of pneumatic muscle actuators," *IEEE Control Systems Magazine*, vol. 15, no. 1, pp. 40–48, 1995.

[91] D. X. Ba, T. Q. Dinh, and K. K. Ahn, "An integrated intelligent nonlinear control method for a pneumatic artificial muscle," *IEEE/ASME Transactions on Mechatronics*, vol. 21, no. 4, pp. 1835–1845, 2016.

[92] J. Zhao, J. Zhong, and J. Fan, "Position control of a pneumatic muscle actuator using rbf neural network tuned pid controller," *Mathematical Problems in Engineering*, vol. 2015, 2015.

[93] V. T. Jouppila, S. A. Gadsden, G. M. Bone, A. U. Ellman, and S. R. Habibi, "Sliding mode control of a pneumatic muscle actuator system with a pwm strategy," *International journal of fluid power*, vol. 15, no. 1, pp. 19–31, 2014.

[94] T. Acarman, C. Hatipoglu, and U. Ozguner, "A robust nonlinear controller design for a pneumatic actuator," in *Proceedings of the 2001 American Control Conference.(Cat. No. 01CH37148)*, vol. 6, pp. 4490–4495, IEEE, 2001.

[95] G. M. Bone and S. Ning, "Experimental comparison of position tracking control algorithms for pneumatic cylinder actuators," *IEEE/ASME Transactions on mechatronics*, vol. 12, no. 5, pp. 557–561, 2007.

[96] G. S. Choi, H. K. Lee, and G. H. Choi, "A study on tracking position control of pneumatic actuators using neural network," in *IECON'98. Proceedings of the 24th Annual Conference of the IEEE Industrial Electronics Society (Cat. No. 98CH36200)*, vol. 3, pp. 1749–1753, IEEE, 1998.

[97] A. Hildebrandt, O. Sawodny, R. Neumann, and A. Hartmann, "A cascaded tracking control concept for pneumatic muscle actuators," in *2003 European Control Conference (ECC)*, pp. 2517–2522, IEEE, 2003.

[98] H. Kazerooni, "Pneumatic force control for robotic systems," in *Proceedings of the IEEE International Conference on Mechatronics, 2004. ICM'04.*, pp. 231–236, IEEE, 2004.

[99] D. Ben-Dov and S. E. Salcudean, "A force-controlled pneumatic actuator for use in teleoperation masters," in *[1993] Proceedings IEEE International Conference on Robotics and Automation*, pp. 938–943, IEEE, 1993.

[100] M. Faudzi, N. D. Mustafa, and K. Osman, "Force control for a pneumatic cylinder using generalized predictive controller approach," *Mathematical Problems in Engineering*, vol. 2014, 2014.

[101] K. Khayati, P. Bigras, and L.-A. Dessaint, "A robust feedback linearization force control of a pneumatic actuator," in *2004 IEEE International Conference on Systems, Man and Cybernetics (IEEE Cat. No. 04CH37583)*, vol. 7, pp. 6113–6119, IEEE, 2004.

[102] I. Sardellitti, G. Palli, N. G. Tsagarakis, and D. G. Caldwell, "Antagonistically actuated compliant joint: Torque and stiffness control," in *2010 IEEE/RSJ International Conference on Intelligent Robots and Systems*, pp. 1909–1914, IEEE, 2010.

[103] B. Ugurlu, P. Forni, C. Doppmann, and J. Morimoto, "Torque and variable stiffness control for antagonistically driven pneumatic muscle actuators via a stable force feedback controller," in *2015 IEEE/RSJ International Conference on Intelligent Robots and Systems (IROS)*, pp. 1633–1639, IEEE, 2015.

[104] D.-y. Meng, G.-l. Tao, W. Ban, and P.-f. Qian, "Adaptive robust output force tracking control of pneumatic cylinder while maximizing/minimizing its stiffness," *Journal of Central South University*, vol. 20, no. 6, pp. 1510–1518, 2013.

[105] X. Shen and M. Goldfarb, "Independent stiffness and force control of pneumatic actuators for contact stability during robot manipulation," in *Proceedings of the 2005 IEEE International Conference on Robotics and Automation*, pp. 2697–2702, IEEE, 2005.

[106] X. Shen and M. Goldfarb, "Simultaneous force and stiffness control of a pneumatic actuator," *Journal of Dynamic Systems, Measurement, and Control*, vol. 129, no. 4, pp. 425–434, 2007.

[107] B. Taheri, D. Case, and E. Richer, "Force and stiffness backstepping-sliding mode controller for pneumatic cylinders," *IEEE/ASME Transactions on Mechatronics*, vol. 19, no. 6, pp. 1799–1809, 2014.

[108] Y. Zhu and E. Barth, "Impedance control of a pneumatic actuator for contact tasks," in *Robotics and Automation, 2005. ICRA 2005. Proceedings of the 2005 IEEE International Conference on*, pp. 987–992.

[109] T. Noritsugu and T. Tanaka, "Application of rubber artificial muscle manipulator as a rehabilitation robot," *IEEE/ASME Transactions on mechatronics*, vol. 2, no. 4, pp. 259–267, 1997.

[110] I. Sardellitti, J. Park, D. Shin, and O. Khatib, "Air muscle controller design in the distributed macro-mini (dm 2) actuation approach," in *2007 IEEE/RSJ international conference on intelligent robots and systems*, pp. 1822–1827, IEEE, 2007.

[111] V. Jouppila, S. Gadsden, and A. Ellman, "Modeling and identification of a pneumatic muscle actuator system controlled by an on/off solenoid valve," in *Proceeding 7th International Fluid Power Conference*, pp. 1–11, 2010.

[112] M. Takaiwa and T. Noritsugu, "Development of wrist rehabilitation equipment using pneumatic parallel manipulator," in *Proceedings of the 2005 IEEE International Conference on Robotics and Automation*, pp. 2302–2307, IEEE, 2005.

[113] E. T. Wolbrecht, D. J. Reinkensmeyer, and J. E. Bobrow, "Pneumatic control of robots for rehabilitation," *The International Journal of Robotics Research*, vol. 29, no. 1, pp. 23–38, 2010.

[114] R. Richardson, M. Brown, B. Bhakta, and M. Levesley, "Design and control of a three degree of freedom pneumatic physiotherapy robot," *Robotica*, vol. 21, no. 6, pp. 589–604, 2003.

[115] B. Yang, S. Roys, U.-X. Tan, M. Philip, H. Richard, R. P. Gullapalli, and J. P. Desai, "Design, development, and evaluation of a master–slave surgical system for breast biopsy under continuous mri," *The International journal of robotics research*, vol. 33, no. 4, pp. 616–630, 2014.

[116] K. B. Fite, T. J. Withrow, X. Shen, K. W. Wait, J. E. Mitchell, and M. Goldfarb, "A gas-actuated anthropomorphic prosthesis for transhumeral amputees," *IEEE Transactions on Robotics*, vol. 24, no. 1, pp. 159–169, 2008.

[117] F. Sup, A. Bohara, and M. Goldfarb, "Design and control of a powered transfemoral prosthesis," *The International journal of robotics research*, vol. 27, no. 2, pp. 263–273, 2008.

[118] P. Heo and J. Kim, "Power-assistive finger exoskeleton with a palmar opening at the fingerpad," *IEEE Transactions on Biomedical Engineering*, vol. 61, no. 11, pp. 2688–2697, 2014.

[119] B. Ugurlu, C. Doppmann, M. Hamaya, P. Forni, T. Teramae, T. Noda, and J. Morimoto, "Variable ankle stiffness improves balance control: Experiments on a bipedal exoskeleton," *IEEE/ASME Transactions on mechatronics*, vol. 21, no. 1, pp. 79–87, 2015.

[120] M. Hamaya, T. Matsubara, T. Teramae, T. Noda, and J. Morimoto, "Design of physical user–robot interactions for model identification of soft actuators on exoskeleton robots," *The International Journal of Robotics Research*, vol. 40, no. 1, pp. 397–410, 2021.

[121] V. Kumar, Z. Xu, and E. Todorov, "Fast, strong and compliant pneumatic actuation for dexterous tendon-driven hands," in *2013 IEEE international conference on robotics and automation*, pp. 1512–1519, IEEE, 2013.

[122] D. Shin, X. Yeh, and O. Khatib, "A new hybrid actuation scheme with artificial pneumatic muscles and a magnetic particle brake for safe human–robot collaboration," *The International Journal of Robotics Research*, vol. 33, no. 4, pp. 507–518, 2014.

[123] O. Mohseni, A. M. N. Rashty, A. Seyfarth, K. Hosoda, and M. A. Sharbafi, "Bioinspired legged robot design via blended physical and virtual impedance control," *Journal of Intelligent & Robotic Systems*, vol. 105, no. 1, pp. 1–15, 2022.

[124] D. Büchler, H. Ott, and J. Peters, "A lightweight robotic arm with pneumatic muscles for robot learning," in *2016 IEEE International Conference on Robotics and Automation (ICRA)*, pp. 4086–4092, IEEE, 2016.

[125] Festo, "Festo." `https://www.festo.com`, 2022.

[126] Shadowhand, "Shadowhand." `https://www.shadowrobot.com`, 2022.

[127] D. Shin, I. Sardellitti, Y.-L. Park, O. Khatib, and M. Cutkosky, "Design and control of a bio-inspired human-friendly robot," *The International Journal of Robotics Research*, vol. 29, no. 5, pp. 571–584, 2010.

[128] B. Vanderborght, B. Verrelst, R. Van Ham, and D. Lefeber, "Controlling a bipedal walking robot actuated by pleated pneumatic artificial muscles," *Robotica*, vol. 24, no. 4, pp. 401–410, 2006.

[129] T. Takuma and K. Hosoda, "Controlling the walking period of a pneumatic muscle walker," *The International Journal of Robotics Research*, vol. 25, no. 9, pp. 861–866, 2006.

[130] M. Van Damme, B. Vanderborght, B. Verrelst, R. Van Ham, F. Daerden, and D. Lefeber, "Proxy-based sliding mode control of a planar pneumatic manipulator," *The International Journal of Robotics Research*, vol. 28, no. 2, pp. 266–284, 2009.

[131] S. Sridar, C. J. Majeika, P. Schaffer, M. Bowers, S. Ueda, A. J. Barth, J. L. Sorrells, J. T. Wu, T. R. Hunt, and M. Popovic, "Hydro muscle-a novel soft fluidic actuator," in *2016 IEEE International Conference on Robotics and Automation (ICRA)*, pp. 4014–4021, IEEE, 2016.

[132] G. McCarthy, D. Effraimidis, B. Jennings, N. Corso, C. D. Onal, and M. Popovic, "Hydraulically actuated muscle (ham) exo-musculature," in *Robot Makers: The future of digital rapid design and fabrication of robots"(RoMa) Workshop, the*, 2014.

[133] A. Barth, J. Sorrells, S. Ueda, and J. Wu, "Hydro muscle control system," *A Major Qualifying Project, Primary Adviser: Marko B Popovic. Worcester Polytechnic Institute April*, vol. 15, 2015.

[134] C. Atkeson, J. Hale, F. Pollick, M. Riley, S. Kotosaka, S. Schaul, T. Shibata, G. Tevatia, A. Ude, S. Vijayakumar, E. Kawato, and M. Kawato, "Using humanoid robots to study human behavior," *IEEE Intelligent Systems and their Applications*, vol. 15, no. 4, pp. 46–56, 2000.

[135] S. O. Anderson and J. K. Hodgins, "Adaptive torque-based control of a humanoid robot on an unstable platform," in *2010 10th IEEE-RAS International Conference on Humanoid Robots*, pp. 511–517, IEEE, 2010.

[136] B. J. Stephens and C. G. Atkeson, "Push recovery by stepping for humanoid robots with force controlled joints," in *2010 10th IEEE-RAS International conference on humanoid robots*, pp. 52–59, IEEE, 2010.

[137] S.-H. Hyon, D. Suewaka, Y. Torii, and N. Oku, "Design and experimental evaluation of a fast torque-controlled hydraulic humanoid robot," *IEEE/ASME Transactions on Mechatronics*, vol. 22, no. 2, pp. 623–634, 2016.

[138] G. Nelson, A. Saunders, and R. Playter, "The petman and atlas robots at boston dynamics," *Humanoid Robotics: A Reference*, vol. 169, p. 186, 2019.

[139] G. Nelson, A. Saunders, N. Neville, B. Swilling, J. Bondaryk, D. Billings, C. Lee, R. Playter, and M. Raibert, "Petman: A humanoid robot for testing chemical protective clothing," *Journal of the Robotics Society of Japan*, vol. 30, no. 4, pp. 372–377, 2012.

[140] M. Johnson, B. Shrewsbury, S. Bertrand, T. Wu, D. Duran, M. Floyd, P. Abeles, D. Stephen, N. Mertins, A. Lesman, J. Carff, W. Rifenburgh, P. Kaveti, W. Straatman, J. Smith, M. Griffioen, B. Layton, T. de Boer, T. Koolen, P. Neuhaus, and J. Pratt, "Team ihmc's lessons learned from the darpa robotics challenge trials," *Journal of Field Robotics*, vol. 32, no. 2, pp. 192–208, 2015.

[141] C. G. Atkeson, P. W. B. Benzun, N. Banerjee, D. Berenson, C. P. Bove, X. Cui, M. DeDonato, R. Du, S. Feng, P. Franklin, M. Gennert, J. P. Graff, P. He, A. Jaeger, J. Kim, K. Knoedler, L. Li, C. Liu, X. Long, T. Padir, F. Polido, G. G. Tighe, and X. Xinjilefu, *What Happened at the DARPA Robotics Challenge Finals*, pp. 667–684. Cham: Springer International Publishing, 2018.

[142] J. Vorndamme, M. Schappler, A. Tödtheide, and S. Haddadin, "Soft robotics for the hydraulic atlas arms: Joint impedance control with collision detection and disturbance compensation," in *2016 IEEE/RSJ International Conference on Intelligent Robots and Systems (IROS)*, pp. 3360–3367, IEEE, 2016.

[143] D. Conner, S. Kohlbrecher, A. Romay, A. Stumpf, S. Maniatopoulos, M. Schappler, and B. Waxler, "Team vigir," tech. rep., TORC ROBOTICS LLC BLACKSBURG VA, 2015.

[144] M. Raibert, K. Blankespoor, G. Nelson, and R. Playter, "Bigdog, the rough-terrain quadruped robot," *IFAC Proceedings Volumes*, vol. 41, no. 2, pp. 10822–10825, 2008.

[145] T. Boaventura, C. Semini, J. Buchli, M. Frigerio, M. Focchi, and D. G. Caldwell, "Dynamic torque control of a hydraulic quadruped robot," in *2012 IEEE international conference on robotics and automation*, pp. 1889–1894, IEEE, 2012.

[146] T. Lenzi, J. Lipsey, and J. W. Sensinger, "The RIC arm—a small anthropomorphic transhumeral prosthesis," *IEEE/ASME Transactions on Mechatronics*, vol. 21, no. 6, pp. 2660–2671, 2016.

[147] Ottobock SE & Co. KGaA.

[148] R. Weir, M. Mitchell, S. Clark, G. Puchhammer, M. Haslinger, R. Grausenburger, N. Kumar, R. Hofbauer, P. Kushnigg, V. Cornelius, M. Eder, H. Eaton, and D. Wenstrand, "The intrinsic hand-a 22 degree of freedom artificial hand-wrist replacement," in *Proc Myoelectric Controls/Powered Prosthetics Symposium*, pp. 233–237, 2008.

[149] M. S. Johannes, E. L. Faulring, K. D. Katyal, M. P. Para, J. B. Helder, A. Makhlin, T. Moyer, D. Wahl, J. Solberg, S. Clark, R. S. Armiger, T. Lontz, K. Geberth, C. W. Moran, B. A. Wester, T. V. Doren, and J. J. Santos-Munne, "The modular prosthetic limb," in *Wearable Robotics*, pp. 393–444, Elsevier, 2020.

[150] Fillauer, "Reference for commercial prosthesis." `https://fillauer.com/`, 2021.

[151] Liberatingtech, "Reference for commercial prosthesis." `https://www.liberatingtech.com`, 2021.

[152] Ossur, "Reference for commercial prosthesis." `https://www.ossur.com/`, 2021.

[153] Keshen, "Reference for commercial prosthesis." `http://en.keshen.com/`, 2021.

[154] Mobiusbionics, "Reference for commercial prosthesis." `https://www.mobiusbionics.com/`, 2021.

[155] D. A. Bennett, J. E. Mitchell, D. Truex, and M. Goldfarb, "Design of a myoelectric transhumeral prosthesis," *IEEE/ASME Transactions on Mechatronics*, vol. 21, no. 4, pp. 1868–1879, 2016.

[156] M. R. Dawson, C. Sherstan, J. P. Carey, J. S. Hebert, and P. M. Pilarski, "Development of the bento arm: An improved robotic arm for myoelectric training and research," *Proc. of MEC*, vol. 14, pp. 60–64, 2014.

[157] J. Andrews and Y. Youm, "A biomechanical investigation of wrist kinematics," *Journal of Biomechanics*, vol. 12, no. 1, pp. 83–93, 1979.

[158] P. J. Kyberd, E. D. Lemaire, E. Scheme, C. MacPhail, L. Goudreau, G. Bush, and M. Brookeshaw, "Two-degree-of-freedom powered prosthetic wrist.," *Journal of Rehabilitation Research & Development*, vol. 48, no. 6, 2011.

[159] D. Bandara, R. Gopura, K. Hemapala, and K. Kiguchi, "Development of a multi-dof transhumeral robotic arm prosthesis," *Medical engineering & physics*, vol. 48, pp. 131–141, 2017.

[160] R. Damerla, Y. Qiu, T. M. Sun, and S. Awtar, "A review of the performance of extrinsically powered prosthetic hands," *IEEE Transactions on Medical Robotics and Bionics*, 2021.

[161] L. Resnik, S. L. Klinger, and K. Etter, "The deka arm: Its features, functionality, and evolution during the veterans affairs study to optimize the deka arm," *Prosthetics and orthotics international*, vol. 38, no. 6, pp. 492–504, 2014.

[162] C. O. Evans, "Patent: Us8449624b2," May 2013.

[163] M. M. Bridges, M. P. Para, and M. J. Mashner, "Control system architecture for the modular prosthetic limb," *Johns Hopkins APL Technical Digest*, vol. 30, no. 3, pp. 217–222, 2011.

[164] M. S. Johannes, J. D. Bigelow, J. M. Burck, S. D. Harshbarger, M. V. Kozlowski, and T. Van Doren, "An overview of the developmental process for the modular prosthetic limb," *Johns Hopkins APL Technical Digest*, vol. 30, no. 3, pp. 207–216, 2011.

[165] P. A. Parker and R. N. Scott, "Myoelectric control of prostheses.," *Critical reviews in biomedical engineering*, vol. 13, no. 4, pp. 283–310, 1986.

[166] I. Vujaklija, D. Farina, and O. C. Aszmann, "New developments in prosthetic arm systems," *Orthopedic research and reviews*, vol. 8, p. 31, 2016.

[167] N. A. Alshammary, D. A. Bennett, and M. Goldfarb, "Synergistic elbow control for a myoelectric transhumeral prosthesis," *IEEE Transactions on Neural Systems and Rehabilitation Engineering*, vol. 26, no. 2, pp. 468–476, 2017.

[168] M. A. Oskoei and H. Hu, "Myoelectric control systems—a survey," *Biomedical signal processing and control*, vol. 2, no. 4, pp. 275–294, 2007.

[169] T. A. Kuiken, G. Li, B. A. Lock, R. D. Lipschutz, L. A. Miller, K. A. Stubblefield, and K. B. Englehart, "Targeted muscle reinnervation for real-time myoelectric control of multifunction artificial arms," *Jama*, vol. 301, no. 6, pp. 619–628, 2009.

[170] P. Zhou, M. M. Lowery, K. B. Englehart, H. Huang, G. Li, L. Hargrove, J. P. Dewald, and T. A. Kuiken, "Decoding a new neural–machine interface for control of artificial limbs," *Journal of neurophysiology*, vol. 98, no. 5, pp. 2974–2982, 2007.

[171] C. Lauretti, A. Davalli, R. Sacchetti, E. Guglielmelli, and L. Zollo, "Fusion of m-imu and emg signals for the control of trans-humeral prostheses," in *2016 6th IEEE International Conference on Biomedical Robotics and Biomechatronics (BioRob)*, pp. 1123–1128, IEEE, 2016.

[172] R. Garcia-Rosas, Y. Tan, D. Oetomo, and C. Manzie, "On-line synergy identification for personalized active arm prosthesis: a feasibility study," in *2018 Annual American Control Conference (ACC)*, pp. 514–519, IEEE, 2018.

[173] J. Vogel, S. Haddadin, B. Jarosiewicz, J. D. Simeral, D. Bacher, L. R. Hochberg, J. P. Donoghue, and P. van der Smagt, "An assistive decision-and-control architecture for force-sensitive hand–arm systems driven by human–machine interfaces," *The International Journal of Robotics Research*, vol. 34, no. 6, pp. 763–780, 2015.

[174] L. R. Hochberg, M. D. Serruya, G. M. Friehs, J. A. Mukand, M. Saleh, A. H. Caplan, A. Branner, D. Chen, R. D. Penn, and J. P. Donoghue, "Neuronal ensemble control of prosthetic devices by a human with tetraplegia," *Nature*, vol. 442, no. 7099, pp. 164–171, 2006.

[175] D. K. Madusanka, R. Gopura, Y. Amarasinghe, and G. K. Mann, "Hybrid vision based reach-to-grasp task planning method for trans-humeral prostheses," *IEEE Access*, vol. 5, pp. 16149–16161, 2017.

[176] M. Gardner, C. S. Mancero Castillo, S. Wilson, D. Farina, E. Burdet, B. C. Khoo, S. F. Atashzar, and R. Vaidyanathan, "A multimodal intention detection sensor suite for shared autonomy of upper-limb robotic prostheses," *Sensors*, vol. 20, no. 21, p. 6097, 2020.

[177] R. Volkmar, S. Dosen, J. Gonzalez-Vargas, M. Baum, and M. Markovic, "Improving bimanual interaction with a prosthesis using semi-autonomous control," *Journal of neuroengineering and rehabilitation*, vol. 16, no. 1, pp. 1–13, 2019.

[178] B. Ugurlu, M. Nishimura, K. Hyodo, M. Kawanishi, and T. Narikiyo, "A framework for sensorless torque estimation and control in wearable exoskeletons," in *2012 12th IEEE international workshop on advanced motion control (AMC)*, pp. 1–7, IEEE, 2012.

[179] A. Ebrahimi, D. Gröninger, R. Singer, and U. Schneider, "Control parameter optimization of the actively powered upper body exoskeleton using subjective feedbacks," in *2017 3rd International Conference on Control, Automation and Robotics (ICCAR)*, pp. 432–437, IEEE, 2017.

[180] J. Rosen, J. C. Perry, N. Manning, S. Burns, and B. Hannaford, "The human arm kinematics and dynamics during daily activities-toward a 7 dof upper limb powered exoskeleton," in *ICAR'05. Proceedings., 12th International Conference on Advanced Robotics, 2005.*, pp. 532–539, IEEE, 2005.

[181] T. Nef, M. Mihelj, and R. Riener, "Armin: a robot for patient-cooperative arm therapy," *Medical & biological engineering & computing*, vol. 45, no. 9, pp. 887–900, 2007.

[182] H. S. Lo and S. S. Xie, "An upper limb exoskeleton with an optimized 4r spherical wrist mechanism for the shoulder joint," in *2014 IEEE/ASME International Conference on Advanced Intelligent Mechatronics*, pp. 269–274, IEEE, 2014.

[183] Y. Wang, B. Metcalfe, Y. Zhao, and D. Zhang, "An assistive system for upper limb motion combining functional electrical stimulation and robotic exoskeleton," *IEEE Transactions on Medical Robotics and Bionics*, vol. 2, no. 2, pp. 260–268, 2020.

[184] T. Chen, R. Casas, and P. S. Lum, "An elbow exoskeleton for upper limb rehabilitation with series elastic actuator and cable-driven differential," *IEEE Transactions on Robotics*, vol. 35, no. 6, pp. 1464–1474, 2019.

[185] C. Liu, H. Li, and Q. Zhang, "Configuration comparison and design of an upper limb exoskeleton for robot teleoperation," in *2019 IEEE International Conference on Mechatronics and Automation (ICMA)*, pp. 921–926, IEEE, 2019.

[186] A. Schiele and G. Hirzinger, "A new generation of ergonomic exoskeletons - the high-performance x-arm-2 for space robotics telepresence," in *2011 IEEE/RSJ International Conference on Intelligent Robots and Systems*, pp. 2158–2165, 2011.

[187] C. Carignan, J. Tang, and S. Roderick, "Development of an exoskeleton haptic interface for virtual task training," in *2009 IEEE/RSJ International Conference on Intelligent Robots and Systems*, pp. 3697–3702, IEEE, 2009.

[188] E. A. Kirchner, J. C. Albiez, A. Seeland, M. Jordan, and F. Kirchner, "Towards assistive robotics for home rehabilitation.," in *Biodevices*, pp. 168–177, 2013.

[189] M. Hessinger, M. Pingsmann, J. C. Perry, R. Werthschützky, and M. Kupnik, "Hybrid position/force control of an upper-limb exoskeleton for assisted drilling," in *2017 IEEE/RSJ International Conference on Intelligent Robots and Systems (IROS)*, pp. 1824–1829, IEEE, 2017.

[190] S. Moubarak, M. T. Pham, T. Pajdla, and T. Redarce, "Design and modeling of an upper extremity exoskeleton," in *World Congress on Medical Physics and Biomedical Engineering, September 7-12, 2009, Munich, Germany*, pp. 476–479, Springer, 2009.

[191] M. Dežman, T. Asfour, A. Ude, and A. Gams, "Exoskeleton arm pronation/supination assistance mechanism with a guided double rod system," in *2019 IEEE-RAS 19th International Conference on Humanoid Robots (Humanoids)*, pp. 559–564, 2019.

[192] R. Gopura and K. Kiguchi, "Mechanical designs of active upper-limb exoskeleton robots: State-of-the-art and design difficulties," in *2009 IEEE International Conference on Rehabilitation Robotics*, pp. 178–187, IEEE, 2009.

[193] R. Gopura, D. Bandara, K. Kiguchi, and G. K. Mann, "Developments in hardware systems of active upper-limb exoskeleton robots: A review," *Robotics and Autonomous Systems*, vol. 75, pp. 203–220, 2016.

[194] Y. Shen, P. W. Ferguson, J. Ma, J. Rosen, and R. Tong, "Upper limb wearable exoskeleton systems for rehabilitation: State of the art review and a case study of the exo-ul8—dual-arm exoskeleton system," in *Wearable Technology in Medicine and Health Care*, pp. 71–90, Academic Press, 2018.

[195] M. A. Gull, S. Bai, and T. Bak, "A review on design of upper limb exoskeletons," *Robotics*, vol. 9, p. 16, Mar. 2020.

[196] M. A. Vélez-Guerrero, M. Callejas-Cuervo, and S. Mazzoleni, "Artificial intelligence-based wearable robotic exoskeletons for upper limb rehabilitation: A review," *Sensors*, vol. 21, no. 6, p. 2146, 2021.

[197] M.-L. Olar, M. Leba, and M. Risteiu, "Exoskeleton-wearable devices. literature review," in *MATEC Web of Conferences*, vol. 342, EDP Sciences, 2021.

[198] A. Kapsalyamov, S. Hussain, and P. K. Jamwal, "State-of-the-art assistive powered upper limb exoskeletons for elderly," *IEEE Access*, vol. 8, pp. 178991–179001, 2020.

[199] T. Proietti, V. Crocher, A. Roby-Brami, and N. Jarrasse, "Upper-limb robotic exoskeletons for neurorehabilitation: a review on control strategies," *IEEE reviews in biomedical engineering*, vol. 9, pp. 4–14, 2016.

[200] J. Klein, S. Spencer, J. Allington, K. Minakata, E. Wolbrecht, R. Smith, J. Bobrow, and D. Reinkensmeyer, "Biomimetic orthosis for the neurorehabilitation of the elbow and shoulder (bones)," in *2008 2nd IEEE RAS & EMBS international conference on biomedical robotics and biomechatronics*, pp. 535–541, IEEE, 2008.

[201] M. Mistry, P. Mohajerian, and S. Schaal, "An exoskeleton robot for human arm movement study," in *2005 IEEE/RSJ International Conference on Intelligent Robots and Systems*, pp. 4071–4076, IEEE, 2005.

[202] A. Otten, C. Voort, A. Stienen, R. Aarts, E. van Asseldonk, and H. van der Kooij, "Limpact: a hydraulically powered self-aligning upper limb exoskeleton," *IEEE/ASME transactions on mechatronics*, vol. 20, no. 5, pp. 2285–2298, 2015.

[203] H.-C. Hsieh, D.-F. Chen, L. Chien, and C.-C. Lan, "Design of a parallel actuated exoskeleton for adaptive and safe robotic shoulder rehabilitation," *IEEE/ASME Transactions on Mechatronics*, vol. 22, no. 5, pp. 2034–2045, 2017.

[204] R. A. C. Gopura and K. Kiguchi, "Emg-based control of an exoskeleton robot for human forearm and wrist motion assist," in *2008 IEEE International Conference on Robotics and Automation*, pp. 731–736, IEEE, 2008.

[205] T. D. Lalitharatne, K. Teramoto, Y. Hayashi, and K. Kiguchi, "Evaluation of perception-assist with an upper-limb power-assist exoskeleton using emg and eeg signals," in *Proceedings of the 11th IEEE International Conference on Networking, Sensing and Control*, pp. 524–529, IEEE, 2014.

[206] T. Noda, N. Sugimoto, J. Furukawa, M.-a. Sato, S.-H. Hyon, and J. Morimoto, "Brain-controlled exoskeleton robot for bmi rehabilitation," in *2012 12th IEEE-RAS International Conference on Humanoid Robots (Humanoids 2012)*, pp. 21–27, 2012.

[207] R. Soltani Zarrin, A. Zeiaee, A. Eib, R. Langari, and R. Tafrershi, "Cleverarm: A novel exoskeleton for rehabilitation of upper limb impairments," 12 2017.

[208] B. Kim and A. D. Deshpande, "An upper-body rehabilitation exoskeleton harmony with an anatomical shoulder mechanism: Design, modeling, control, and performance evaluation," *The International Journal of Robotics Research*, vol. 36, pp. 414–435, Apr. 2017.

[209] S. Bai, S. Christensen, and M. R. U. Islam, "An upper-body exoskeleton with a novel shoulder mechanism for assistive applications," in *2017 IEEE International Conference on Advanced Intelligent Mechatronics (AIM)*, pp. 1041–1046, IEEE, 2017.

[210] H. I. Krebs, M. Ferraro, S. P. Buerger, M. J. Newbery, A. Makiyama, M. Sandmann, D. Lynch, B. T. Volpe, and N. Hogan, "Rehabilitation robotics: pilot trial of a spatial extension for mit-manus," *Journal of neuroengineering and rehabilitation*, vol. 1, no. 1, p. 5, 2004.

[211] K. Kiguchi and Y. Hayashi, "An emg-based control for an upper-limb power-assist exoskeleton robot," *IEEE Transactions on Systems, Man, and Cybernetics, Part B (Cybernetics)*, vol. 42, no. 4, pp. 1064–1071, 2012.

[212] W. Yu, J. Rosen, and X. Li, "Pid admittance control for an upper limb exoskeleton," in *Proceedings of the 2011 American control conference*, pp. 1124–1129, IEEE, 2011.

[213] S. Roderick, M. Liszka, and C. Carignan, "Design of an arm exoskeleton with scapula motion for shoulder rehabilitation," in *ICAR'05. Proceedings., 12th International Conference on Advanced Robotics, 2005.*, pp. 524–531, IEEE, 2005.

[214] P. R. Culmer, A. E. Jackson, S. Makower, R. Richardson, J. A. Cozens, M. C. Levesley, and B. B. Bhakta, "A control strategy for upper limb robotic rehabilitation with a dual robot system," *IEEE/ASME Transactions on Mechatronics*, vol. 15, no. 4, pp. 575–585, 2009.

[215] K. Anam and A. A. Al-Jumaily, "Active exoskeleton control systems: State of the art," *Procedia Engineering*, vol. 41, pp. 988–994, 2012.

[216] H. Mehdi and O. Boubaker, "Stiffness and impedance control using lyapunov theory for robot-aided rehabilitation," *International Journal of Social Robotics*, vol. 4, no. 1, pp. 107–119, 2012.

[217] G.-x. Pan, H.-q. Fu, X.-f. Zhang, and F.-l. Ma, "Research on bionic mechanism of shoulder joint rehabilitation movement," in *Wearable Sensors and Robots* (C. Yang, G. S. Virk, and H. Yang, eds.), (Singapore), pp. 181–194, Springer Singapore, 2017.

[218] D. Irimia, M. Poboroniuc, S. Hartopanu, and S. Florin, "Preliminary tests of a new hybrid fesex-oskeleton assisting device for the upper limb in stroke patients," *Buletinul Institutului Politehnic Din Iaşi*, vol. LXI (LXV), p. 79, 11 2015.

[219] Q. Wu, X. Wang, F. Du, and J. Xu, "Development and control of a bowden-cable actuated exoskeleton for upper-limb rehabilitation," in *2014 IEEE International Symposium on Robotic and Sensors Environments (ROSE) Proceedings*, pp. 7–12, IEEE, 2014.

[220] X. Cui, W. Chen, X. Jin, and S. K. Agrawal, "Design of a 7-dof cable-driven arm exoskeleton (carex-7) and a controller for dexterous motion training or assistance," *IEEE/ASME Transactions on Mechatronics*, vol. 22, no. 1, pp. 161–172, 2016.

[221] M. N. Castro, J. Rasmussen, M. S. Andersen, and S. Bai, "A compact 3-dof shoulder mechanism constructed with scissors linkages for exoskeleton applications," *Mechanism and Machine Theory*, vol. 132, pp. 264–278, 2019.

[222] J. Hunt, H. Lee, and P. Artemiadis, "A novel shoulder exoskeleton robot using parallel actuation and a passive slip interface," *Journal of Mechanisms and Robotics*, vol. 9, no. 1, 2017.

[223] S. J. Ball, I. E. Brown, and S. H. Scott, "Medarm: a rehabilitation robot with 5dof at the shoulder complex," in *2007 IEEE/ASME international conference on Advanced intelligent mechatronics*, pp. 1–6, IEEE, 2007.

[224] R. Soltani-Zarrin, A. Zeiaee, A. Eib, R. Langari, and R. Tafreshi, "Cleverarm: A novel exoskeleton for rehabilitation of upper limb impairments," *ArXiv preprint arXiv:1712.02322*, 2017.

[225] D. Sui, J. Fan, H. Jin, X. Cai, J. Zhao, and Y. Zhu, "Design of a wearable upper-limb exoskeleton for activities assistance of daily living," in *2017 IEEE International Conference on Advanced Intelligent Mechatronics (AIM)*, pp. 845–850, IEEE, 2017.

[226] J. C. Perry, J. Rosen, and S. Burns, "Upper-limb powered exoskeleton design," *IEEE/ASME transactions on mechatronics*, vol. 12, no. 4, pp. 408–417, 2007.

[227] Y. Shen, J. Ma, B. Dobkin, and J. Rosen, "Asymmetric dual arm approach for post stroke recovery of motor functions utilizing the exo-ul8 exoskeleton system: a pilot study," in *2018 40th annual international conference of the IEEE Engineering in Medicine and Biology Society (EMBC)*, pp. 1701–1707, IEEE, 2018.

[228] H. Seo and S. Lee, "Design and experiments of an upper-limb exoskeleton robot," in *2017 14th International Conference on Ubiquitous Robots and Ambient Intelligence (URAI)*, pp. 807–808, IEEE, 2017.

[229] P. Garrec, J.-P. Friconneau, Y. Measson, and Y. Perrot, "Able, an innovative transparent exoskeleton for the upper-limb," in *2008 IEEE/RSJ International Conference on Intelligent Robots and Systems*, pp. 1483–1488, IEEE, 2008.

[230] B. Kim and A. D. Deshpande, "Controls for the shoulder mechanism of an upper-body exoskeleton for promoting scapulohumeral rhythm," in *2015 IEEE International Conference on Rehabilitation Robotics (ICORR)*, pp. 538–542, IEEE, 2015.

[231] M. Xiloyannis, E. Annese, M. Canesi, A. Kodiyan, A. Bicchi, S. Micera, A. Ajoudani, and L. Masia, "Design and validation of a modular one-to-many actuator for a soft wearable exosuit," *Frontiers in Neurorobotics*, vol. 13, 2019.

[232] F. Missiroli, N. Lotti, M. Xiloyannis, L. H. Sloot, R. Riener, and L. Masia, "Relationship between muscular activity and assistance magnitude for a myoelectric model based controlled exosuit," *Frontiers in Robotics and AI*, vol. 7, p. 190, 2020.

[233] S. Lessard, P. Pansodtee, A. Robbins, L. B. Baltaxe-Admony, J. M. Trombadore, M. Teodorescu, A. Agogino, and S. Kurniawan, "Crux: A compliant robotic upper-extremity exosuit for lightweight, portable, multi-joint muscular augmentation," in *2017 International Conference on Rehabilitation Robotics (ICORR)*, pp. 1633–1638, IEEE, 2017.

[234] S. Lessard, P. Pansodtee, A. Robbins, J. M. Trombadore, S. Kurniawan, and M. Teodorescu, "A soft exosuit for flexible upper-extremity rehabilitation," *IEEE Transactions on Neural Systems and Rehabilitation Engineering*, vol. 26, no. 8, pp. 1604–1617, 2018.

[235] J. L. Samper-Escudero, A. Giménez-Fernandez, M. Á. Sánchez-Urán, and M. Ferre, "A cable-driven exosuit for upper limb flexion based on fibres compliance," *IEEE Access*, vol. 8, pp. 153297–153310, 2020.

[236] L. Grazi, E. Trigili, G. Proface, F. Giovacchini, S. Crea, and N. Vitiello, "Design and experimental evaluation of a semi-passive upper-limb exoskeleton for workers with motorized tuning of assistance," *IEEE Transactions on Neural Systems and Rehabilitation Engineering*, vol. 28, no. 10, pp. 2276–2285, 2020.

[237] R. Altenburger, D. Scherly, and K. S. Stadler, "Design of a passive, iso-elastic upper limb exoskeleton for gravity compensation," *Robomech Journal*, vol. 3, no. 1, pp. 1–7, 2016.

[238] T. Schmalz, J. Schändlinger, M. Schuler, J. Bornmann, B. Schirrmeister, A. Kannenberg, and M. Ernst, "Biomechanical and metabolic effectiveness of an industrial exoskeleton for overhead work," *International journal of environmental research and public health*, vol. 16, no. 23, p. 4792, 2019.

[239] Y. M. Zhou, C. Hohimer, T. Proietti, C. T. O'Neill, and C. J. Walsh, "Kinematics-based control of an inflatable soft wearable robot for assisting the shoulder of industrial workers," *IEEE Robotics and Automation Letters*, vol. 6, no. 2, pp. 2155–2162, 2021.

[240] E. Rashedi, S. Kim, M. A. Nussbaum, and M. J. Agnew, "Ergonomic evaluation of a wearable assistive device for overhead work," *Ergonomics*, vol. 57, no. 12, pp. 1864–1874, 2014.

[241] T. Butler and J. C. Gillette, "Exoskeletons used as a ppe for injury prevention," *Professional Safety*, vol. 64, no. 03, pp. 32–37, 2019.

[242] J. Rebelo, T. Sednaoui, E. B. Den Exter, T. Krueger, and A. Schiele, "Bilateral robot teleoperation: A wearable arm exoskeleton featuring an intuitive user interface," *IEEE Robotics & Automation Magazine*, vol. 21, no. 4, pp. 62–69, 2014.

[243] M. Mallwitz, N. Will, J. Teiwes, and E. A. Kirchner, "The capio active upper body exoskeleton and its application for teleoperation," in *Proceedings of the 13th Symposium on Advanced Space Technologies in Robotics and Automation. ESA/Estec Symposium on Advanced Space Technologies in Robotics and Automation (ASTRA-2015). ESA*, 2015.

[244] A. Schiele, H. Seiberth, P. Klär, and G. Hirzinger, "Mechatronics characterization of a novel high-performance ergonomic exoskeleton for space robotics telepresence," in *International Symposium on Artificial Intelligence, Robotics and Automation in Space*, pp. 499–506, 2010.

[245] R. Wei, S. Balasubramanian, L. Xu, and J. He, "Adaptive iterative learning control design for rupert iv," in *2008 2nd IEEE RAS & EMBS International Conference on Biomedical Robotics and Biomechatronics*, pp. 647–652, IEEE, 2008.

[246] D. Park, S. Toxiri, G. Chini, C. Di Natali, D. G. Caldwell, and J. Ortiz, "Shoulder-sidewinder (shoulder-side wearable industrial ergonomic robot): Design and evaluation of shoulder wearable robot with mechanisms to compensate for joint misalignment," *IEEE Transactions on Robotics*, 2021.

[247] A. Ebrahimi, "Stuttgart exo-jacket: An exoskeleton for industrial upper body applications," in *2017 10th International Conference on Human System Interactions (HSI)*, pp. 258–263, IEEE, 2017.

[248] W. Khalil and J. Kleinfinger, "A new geometric notation for open and closed-loop robots," in *Proceedings. 1986 IEEE International Conference on Robotics and Automation*, vol. 3, pp. 1174–1179, IEEE, 1986.

[249] B. Siciliano, O. Khatib, and T. Kröger, *Springer handbook of robotics*, vol. 200. Springer, 2008.

[250] C. Natale, *Interaction control of robot manipulators: six degrees-of-freedom tasks*, vol. 3. Springer Science & Business Media, 2003.

[251] W. Khalil and E. Dombre, *Modeling identification and control of robots*. CRC Press, 2002.

[252] E. Zupan and M. Saje, "Integrating rotation from angular velocity," *Advances in engineering software*, vol. 42, no. 9, pp. 723–733, 2011.

[253] A. Dietrich, X. Wu, K. Bussmann, M. Harder, M. Iskandar, J. Englsberger, C. Ott, and A. Albu-Schäffer, "Practical consequences of inertia shaping for interaction and tracking in robot control," *Control Engineering Practice*, vol. 114, p. 104875, 2021.

[254] A. Albu-Schäffer, C. Ott, U. Frese, and G. Hirzinger, "Cartesian impedance control of redundant robots: Recent results with the DLR -light-weight-arms," in *2003 IEEE International conference on robotics and automation (Cat. No. 03CH37422)*, vol. 3, pp. 3704–3709, IEEE, 2003.

[255] A. De Luca and R. Mattone, "Actuator failure detection and isolation using generalized momenta," in *2003 IEEE International Conference on Robotics and Automation (Cat. No.03CH37422)*, vol. 1, pp. 634–639 vol.1, 2003.

[256] S. Haddadin, *Towards Safe Robots: Approaching Asimov's 1st Law*. PhD thesis, RWTH Aachen, Oktober 2011.

[257] M. Schappler, J. Vorndamme, A. Tödtheide, D. C. Conner, O. von Stryk, and S. Haddadin, "Modeling, identification and joint impedance control of the atlas arms," in *2015 IEEE-RAS 15th International Conference on Humanoid Robots (Humanoids)*, pp. 1052–1059, IEEE, 2015.

[258] S.-H. Hyon, J. G. Hale, and G. Cheng, "Full-body compliant human–humanoid interaction: balancing in the presence of unknown external forces," *IEEE transactions on robotics*, vol. 23, no. 5, pp. 884–898, 2007.

[259] R. M. Murray, S. S. Sastry, and L. Zexiang, *A Mathematical Introduction to Robotic Manipulation*. USA: CRC Press, Inc., 1st ed., 1994.

[260] M. Chalon, W. Friedl, J. Reinecke, T. Wimboeck, and A. Albu-Schaeffer, "Impedance control of a non-linearly coupled tendon driven thumb," in *2011 IEEE/RSJ International Conference on Intelligent Robots and Systems*, pp. 4215–4221, IEEE, 2011.

[261] T. Wimböck, *Controllers for compliant two-handed dexterous manipulation*, vol. 17 of *Modellierung und Regelung komplexer dynamischer Systeme*. Shaker Verlag GmbH, 2013.

[262] A. Tödtheide, "Development, modeling and control of pneumatic drives for an anthropomorphic robot hand."

[263] A. Tödtheide, K. Hugo, and S. Haddadin, "Nonlinear disturbance observer for pneumatic systems: Algorithm and application to sliding mode force control," *(in preparation)*, 2022.

[264] C. Gaz, M. Cognetti, A. Oliva, P. Robuffo Giordano, and A. De Luca, "Dynamic identification of the franka emika panda robot with retrieval of feasible parameters using penalty-based optimization," *IEEE Robotics and Automation Letters*, vol. 4, no. 4, pp. 4147–4154, 2019.

[265] A. de Luca and R. Mattone, "Sensorless robot collision detection and hybrid force/motion control," in *Proceedings of the 2005 IEEE International Conference on Robotics and Automation*, pp. 999–1004, 2005.

[266] G. Zeng and A. Hemami, "An overview of robot force control," vol. 15, no. 5, pp. 473–482.

[267] A. Franchi, C. Secchi, H. I. Son, H. H. Bulthoff, and P. R. Giordano, "Bilateral teleoperation of groups of mobile robots with time-varying topology," *IEEE Transactions on Robotics*, vol. 28, no. 5, pp. 1019–1033, 2012.

[268] C. Secchi, A. Franchi, H. H. Bülthoff, and P. R. Giordano, "Bilateral teleoperation of a group of uavs with communication delays and switching topology," in *2012 IEEE International Conference on Robotics and Automation*, pp. 4307–4314, IEEE, 2012.

[269] O. Föllinger, "Regelungstechnik," *Hüthig*, vol. 7, 1992.

[270] S. Haddadin, "Towards safe robots: Approaching asimov's 1st law," *Springer Berlin / Heidelberg*, 2013.

[271] P. van der Smagt, M. Grebenstein, H. Urbanek, N. Fligge, M. Strohmayr, G. Stillfried, J. Parrish, and A. Gustus, "Robotics of human movements," *Journal of Physiology-Paris*, vol. 103, no. 3-5, pp. 119–132, 2009.

[272] M. Sasaki, A. Dutta, G. Obinata, I. Sato, K. Miyawaki, and T. Iwami, *Higher dimensional spatial expression of upper limb manipulation ability based on human joint torque characteristics*. INTECH Open Access Publisher, 2010.

[273] T. Hu, J. Kühn, and S. Haddadin, "Identification of human shoulder-arm kinematic and muscular synergies during daily-life manipulation tasks," in *2018 7th IEEE International Conference on Biomedical Robotics and Biomechatronics (Biorob)*, pp. 1011–1018, 2018.

[274] G. Averta, F. Barontini, V. Catrambone, S. Haddadin, G. Handjaras, J. P. O. Held, T. Hu, E. Jakubowitz, C. M. Kanzler, J. Kühn, O. Lambercy, A. Leo, A. Obermeier, E. Ricciardi, A. Schwarz, G. Valenza, A. Bicchi, and M. Bianchi, "U-Limb: A multi-modal, multi-center database on arm motion control in healthy and post-stroke conditions," *GigaScience*, vol. 10, 06 2021. giab043.

[275] G. Averta, F. Barontini, V. Catrambone, S. Haddadin, G. Handjaras, J. P. O. Held, T. Hu, E. Jakubowitz, C. Kanzler, J. Kühn, O. Lambercy, A. Leo, A. Obermeier, E. Ricciardi, A. Schwarz, G. Valenza, A. Bicchi, and M. Bianchi, "U-Limb," 2020.

[276] R. H. Krishnan, V. Devanandh, A. K. Brahma, and S. Pugazhenthi, "Estimation of mass moment of inertia of human body, when bending forward, for the design of a self-transfer robotic facility," *Journal of Engineering Science and Technology*, vol. 11, no. 2, pp. 166–176, 2016.

[277] R. Carvalho, E. Tudella, S. Caljouw, and G. Savelsbergh, "Early control of reaching: effects of experience and body orientation," *Infant Behavior and Development*, vol. 31, no. 1, pp. 23–33, 2008.

[278] P. DiZio and J. R. Lackner, "Congenitally blind individuals rapidly adapt to coriolis force perturbations of their reaching movements," *Journal of neurophysiology*, vol. 84, no. 4, pp. 2175–2180, 2000.

[279] D. W. Franklin, G. Liaw, T. E. Milner, R. Osu, E. Burdet, and M. Kawato, "Endpoint stiffness of the arm is directionally tuned to instability in the environment," *Journal of Neuroscience*, vol. 27, no. 29, pp. 7705–7716, 2007.

[280] D. M. Wolpert and J. R. Flanagan, "Motor prediction," *Current biology*, vol. 11, no. 18, pp. R729–R732, 2001.

[281] E. Burdet, R. Osu, D. W. Franklin, T. E. Milner, and M. Kawato, "The central nervous system stabilizes unstable dynamics by learning optimal impedance," *Nature*, vol. 414, no. 6862, pp. 446–449, 2001.

[282] P. C. Amadio, "Gliding resistance and modifications of gliding surface of tendon: clinical perspectives," *Hand clinics*, vol. 29, no. 2, pp. 159–166, 2013.

[283] M. Bartz, E. Uttich, and B. Bender, "Transfer of lightweight design principles from the musculoskeletal system to an engineering context," *Design Science*, vol. 5, 2019.

[284] T. E. Milner and D. W. Franklin, "Impedance control and internal model use during the initial stage of adaptation to novel dynamics in humans," *The Journal of physiology*, vol. 567, no. 2, pp. 651–664, 2005.

[285] M. Kawato, K. Furukawa, and R. Suzuki, "A hierarchical neural-network model for control and learning of voluntary movement," *Biological cybernetics*, vol. 57, no. 3, pp. 169–185, 1987.

[286] U. Proske and S. C. Gandevia, "The proprioceptive senses: their roles in signaling body shape, body position and movement, and muscle force," *Physiological reviews*, 2012.

[287] J. W. Krakauer, M.-F. Ghilardi, and C. Ghez, "Independent learning of internal models for kinematic and dynamic control of reaching," *Nature neuroscience*, vol. 2, no. 11, pp. 1026–1031, 1999.

[288] N. Hogan, "The mechanics of multi-joint posture and movement control," *Biological cybernetics*, vol. 52, no. 5, pp. 315–331, 1985.

[289] J. W. Sensinger and S. Dosen, "A review of sensory feedback in upper-limb prostheses from the perspective of human motor control," *Frontiers in Neuroscience*, vol. 14, 2020.

[290] C. Della Santina, C. Piazza, G. Grioli, M. G. Catalano, and A. Bicchi, "Toward dexterous manipulation with augmented adaptive synergies: The pisa/iit softhand 2," *IEEE Transactions on Robotics*, vol. 34, no. 5, pp. 1141–1156, 2018.

[291] M. Mitra, "Multi grasp prosthetic hand." `https://grabcad.com`, 2021.

[292] S. Lee, K. Yang, E. Shin, and H. Kim, "Development of 1-axis torque sensor with different shape of support and measurement spoke," in *2014 11th International Conference on Ubiquitous Robots and Ambient Intelligence (URAI)*, pp. 688–691, 2014.

[293] A. Schiele and G. Hirzinger, "A new generation of ergonomic exoskeletons-the high-performance x-arm-2 for space robotics telepresence," in *2011 IEEE/RSJ International Conference on Intelligent Robots and Systems*, pp. 2158–2165, IEEE, 2011.

[294] J. Vorndamme and S. Haddadin, "Rm-code: Proprioceptive real-time recursive multi-contact detection, isolation and identification," in *2021 IEEE/RSJ International Conference on Intelligent Robots and Systems (IROS)*, pp. 6307–6314, IEEE, 2021.

[295] A. E. Schultz, S. P. Baade, and T. A. Kuiken, "Expert opinions on success factors for upper-limb prostheses," *The Journal of Rehabilitation Research and Development*, vol. 44, no. 4, p. 483, 2007.

[296] J. S. Schofield, K. R. Schoepp, H. E. Williams, J. P. Carey, P. D. Marasco, and J. S. Hebert, "Characterization of interfacial socket pressure in transhumeral prostheses: A case series," *PLOS ONE*, vol. 12, p. e0178517, June 2017.

[297] L. V. McFarland, S. L. H. Winkler, A. W. Heinemann, M. Jones, and A. Esquenazi, "Unilateral upper-limb loss: Satisfaction and prosthetic-device use in veterans and servicemembers from vietnam and OIF/OEF conflicts," *The Journal of Rehabilitation Research and Development*, vol. 47, no. 4, p. 299, 2010.

[298] A. F. Mak, M. Zhang, and D. A. Boone, "State-of-the-art research in lower-limb prosthetic biomechanics-socket interface: a review," *Journal of rehabilitation research and development*, vol. 38, no. 2, pp. 161–174, 2001.

[299] L. Paterno, M. Ibrahimi, E. Gruppioni, A. Menciassi, and L. Ricotti, "Sockets for limb prostheses: A review of existing technologies and open challenges," *IEEE Transactions on Biomedical Engineering*, vol. 65, pp. 1996–2010, Sept. 2018.

[300] L. M. Mioton and G. A. Dumanian, "Targeted muscle reinnervation and prosthetic rehabilitation after limb loss," *Journal of Surgical Oncology*, vol. 118, pp. 807–814, Sept. 2018.

[301] B. Ricardo, C. Jessica, and V. J. Carlos, "A case report: Transhumeral amputee treatment with osseointegrated prosthesis and rehabilitation," *Journal of Hand Therapy*, vol. 33, pp. 263–268, Apr. 2020.

[302] A. Middleton and M. Ortiz-Catalan, "Neuromusculoskeletal arm prostheses: Personal and social implications of living with an intimately integrated bionic arm," *Frontiers in neurorobotics*, vol. 14, p. 39, 2020.

[303] "Human 3d model." `https://grabcad.com/library/tibial-intramedullary-nail-1`, 2021.

[304] F. Cordella, A. L. Ciancio, R. Sacchetti, A. Davalli, A. G. Cutti, E. Guglielmelli, and L. Zollo, "Literature review on needs of upper limb prosthesis users," *Frontiers in neuroscience*, vol. 10, p. 209, 2016.

[305] M. Tröbinger, C. Jähne, Z. Qu, J. Elsner, A. Reindl, S. Getz, T. Goll, B. Loinger, T. Loibl, C. Kugler, C. Calafell, M. Sabaghian, T. Ende, D. Wahrmann, S. Parusel, S. Haddadin, and S. Haddadin, "Introducing garmi - a service robotics platform to support the elderly at home: Design philosophy, system overview and first results," *IEEE Robotics and Automation Letters*, vol. 6, no. 3, pp. 5857–5864, 2021.

[306] Y. Zhu and E. J. Barth, "Passivity-based impact and force control of a pneumatic actuator," *Journal of Dynamic Systems, Measurement, and Control*, vol. 130, no. 2, p. 024501, 2008.